# Entangling, controlling, and detecting individual strontium atoms in optical tweezer arrays

Thesis by
Ivaylo Sashkov Madjarov

In Partial Fulfillment of the Requirements for the
Degree of
Doctor of Philosophy


CALIFORNIA INSTITUTE OF TECHNOLOGY
Pasadena, California

2021
Defended January 22, 2021

# ACKNOWLEDGEMENTS

The work behind this thesis has been in every aspect a collective effort of many talented teammates, whom I am grateful to have met, worked with, and laughed with. To my advisor Manuel, I thank you for seeing a physicist in me and for sculpting me into a better one. Above all, you have taught me how to properly ask scientific questions and how to properly answer them. I thank my teammates who were there from day one, Alex C and Alex B, who shared with me a passion for building our experiment and making it succeed, and with whom I enjoyed many a memorable times outside the lab. To Jake, who soon joined and wasted no time leaving a massive legacy of experimental excellence, I thank you for elevating — by example — my effectiveness as a physicist and as a researcher, and I thank you for your dedication to helping me grow as a professional. As my time with the group comes to a close, I am happy to know the experiment is left in the worthiest of hands. To Adam, it has been a pleasure co-piloting the experiment and fighting off lab goblins with you, and watching you leave your ever-growing mark on the future of the experiment. To Joonhee, you have brought the most unique perspectives to our lab and have continually shown no fear in performing exponentially sophisticated analysis in the face of exponentially complicating circumstances, with many of these efforts inspiring me to rethink what I previously called "unfeasable." To Xin, it has been a pleasure working on the finer points of optics with you, and learning from your diligent and thorough experimental approach. I thank Vlad, Hannes, Tai Hyun, Anant, Emily, Ryan, and Brian each for bringing unique and crucial contributions to our efforts. I give a special thank you to Xin, Joonhee, Adam, and Hannah for feedback on the content of this thesis. I also give a big thank you to the hardworking Loly, whose kindness and support have been invaluable to our group.

Finally, a big thank you to my mother and father, my sister Maya, my brother-in-law Barnaby, and my wonderful niece Sylvia and nephew Philip for their support, encouragement, and inspiration through the years. A special thank you to my mother for teaching me how to count, which has been a crucial component of this work.

# ABSTRACT

We present a novel experimental platform for quantum and precision science: single strontium atoms trapped in arrays of optical tweezers. We demonstrate development of this platform along three important fronts: single-atom trapping, imaging, and cooling; coherent control of the ultra-narrow clock transition; and inter-atom entanglement via Rydberg interactions.

In the context of single-atom physics, we demonstrate trapping in tweezer arrays of one- and two-dimensions as well as cooling to the motional ground state. We furthermore show high-fidelity single-atom imaging with extremely low loss, allowing us to image the same atoms thousands of times before losing them and in principle allowing for the assembly of defect-free atom arrays of several hundred sites.

Notably, we show these results in tweezers that are at a magic wavelength for strontium's clock transition. This feature allows us to perform high-fidelity state rotations on the clock transition. We also demonstrate operation of a single-site resolved atomic-array optical clock — a new atomic clock platform that combines several benefits of optical lattice and single-ion clocks.

From the metastable clock state, we drive the atoms to highly-excited Rydberg states to introduce interactions between nearby atoms. Using a Rydberg blockade in an assembled array of atom pairs, we demonstrate generation of two-atom entangled Bell states with a fidelity of >98%, or >99% with correction for state preparation and measurement errors. Furthermore, we demonstrate an auto-ionization state-detection scheme for Rydberg atoms which improves on the infidelity of previous Rydberg state-detection schemes by over an order of magnitude.

We conclude with several outlooks, including preliminary data on light-cone correlation spreading in a system of 17 interacting atoms. We also discuss prospects for implementing quantum gates, operating a spin-squeezed clock, increasing system size, quantifying many-body state fidelity, and reducing sources of infidelity.

# PUBLISHED CONTENT AND CONTRIBUTIONS

[1] Madjarov, I.S., Covey, J.P., Shaw, A.L. et al. *High-fidelity entanglement and detection of alkaline-earth Rydberg atoms*. Nature Physics **16**, 857–861 (2020). https://doi.org/10.1038/s41567-020-0903-z.

[2] Madjarov, I.S., Cooper, A., Shaw, A.L. et al. *An Atomic-Array Optical Clock with Single-Atom Readout*. Physical Review X **9**, 041052 (2019). https://doi.org/10.1103/PhysRevX.9.041052.

[3] Covey, J.P., Madjarov, I.S., Cooper, A. and Endres, M. *2000-Times Repeated Imaging of Strontium Atoms in Clock-Magic Tweezer Arrays*, Physical Review Letters **122**, 173201 (2019). https://doi.org/10.1103/PhysRevLett.122.173201.

[4] Cooper, A., Covey, J.P., Madjarov, I.S. et al. *Alkaline-Earth Atoms in Optical Tweezers*. Physical Review X **8**, 041055 (2018). https://doi.org/10.1103/PhysRevX.8.041055.

For all publications listed here, the author of this thesis contributed to the experimental design and build, data collection, data analysis, and modeling.

# TABLE OF CONTENTS

# Chapter 1

# INTRODUCTION

This work presents a new quantum platform based on strontium atoms trapped in arrays of optical tweezers. In this chapter, we present the motivation for such a platform (Sec. 1.1), the relevant body of work that has preceded it (Sec. 1.2), an overview of the experiment (Sec. 1.3), and a summary of the novel scientific results that we will present in later chapters (Sec. 1.4).

## 1.1 Motivation and goals

The goal of our work in general terms is to *engineer control over a large-scale quantum mechanical system*. What does this mean, why is it a worthwhile goal, and why do we want to use strontium atoms to accomplish it?

To answer these questions, we begin by considering the essential differences between a classical and quantum system. In each case, we consider an object that, when observed, can produce only one of two possible observations — say, up or down. Assuming no statistical uncertainty, in the classical case, the *state* of the object can only be one of two discrete values: up or down. In the quantum case, the object can also be in the states up or down, labeled as $|\uparrow\rangle$ or $|\downarrow\rangle$. However, these are not the only states available to the object under quantum mechanics. The principle of superposition demands that the object can also be in the state

$$|\psi\rangle = \cos\frac{\theta}{2}\,|\uparrow\rangle + e^{i\phi}\sin\frac{\theta}{2}\,|\downarrow\rangle \tag{1.1}$$

for any $\theta, \phi$ on the unit sphere. A convincing argument on *why* such a state space is necessary to describe objects in our universe can be found in a discussion of the foundational Stern-Gerlach experiment [1] in Chapter 1 of Ref. [2].

Computationally speaking, this means that the state of the classical object can be entirely represented by a single binary bit, whereas the state of the quantum object

needs two real numbers. We will henceforth call the classical object a *bit* and the quantum object a *qubit*.

The discrepancy in state representation becomes even greater when $N$ copies of the bit and qubit are considered. For the classical case, each state is now represented by $N$ binary bits — i.e., the system's information content scales linearly with the system size. For the qubits, one might be tempted to guess that there is a similar scaling. This *would* be the case if the qubits were completely independent systems. However, when they are all taken together as one system, quantum mechanics demands that we also allow for states of the system that are *entangled* amongst the various qubits. These are states that cannot be factorized into a product of single-qubit states. For example, the state $|\uparrow\downarrow\rangle + |\downarrow\uparrow\rangle$ is entangled. The existence of entangled states can be seen as an extension of the superposition principle to many-qubit states, and is required to explain observable phenomena such as violations of Bell's inequalities [3, 4].

With entangled states, the computational representation of a quantum state requires $2(2^N - 1)$ real numbers. This is an *exponential* scaling with number of qubits, and immediately suggests that numerically simulating a generic quantum system becomes impossible beyond some finite number of qubits. To get some sense of what this number might be, consider a real floating-point number computationally represented by $p$ bits, or $p/8$ bytes. The state of $N$ qubits then generically requires $\frac{p}{4}(2^N - 1)$ bytes to be represented. For a typical $p = 32$-bit representation, an $N = 40$ state already requires about 9 terabytes to be represented. For $N = 50$, the requirement is 9 petabytes.

The attitude of contemporary quantum science is to look at this situation in the opposite direction: instead of being an impossible simulation task, large quantum systems are an incredible computational resource. If one can map a certain computationally challenging real-life problem onto the state evolution of a quantum system — and if one had sufficient control over this state evolution — then one could use the quantum system to solve this problem. For large enough quantum systems, one could even solve problems that are impossible to solve on classical computers. This is the general goal of the related fields of *quantum computation* and *quantum simulation*. In the former, one attempts to implement an algorithm on a set of qubits using discrete operations, while in the latter, one attempts to evolve a certain physical Hamiltonian on a set of qubits.

One of the main difficulties with qubits is their necessarily analog nature, making

them susceptible to noise. Unlike classical bits, which can take on one of two very distinct values that are robust to noise, qubits can take on a continuum of values — and therefore a continuum of errors. In a classical electronic bit, applying 4.9 V instead of 5 V will not result in a state error: the bit will still read logical high. In a qubit, a similar imperfection in, for example, the phase angle $\phi$ *will* produce a commensurate error in the desired state. While there exist schemes for quantum *error correction* [5] where a more robust logical qubit is formed from a number of bare qubits, such schemes generally also require a very low error rate in their bare qubits.

The challenge of quantum science is therefore to engineer a system of qubits with two somewhat contradicting requirements: a large degree of control over the quantum state afforded to the experimentalist with simultaneously a large degree of isolation from the surrounding noisy environment. Several platforms have risen over the years to take on this challenge, with the leading platforms generally considered to be trapped ions [6–8] and superconducting qubits [9, 10].

The quantum platform that this work will detail is based on arrays of optically trapped neutral atoms. In particular, we will trap neutral strontium in arrays of *optical tweezers*, which are essentially tightly focused laser beams. Atoms have several desirable properties for quantum science. One is that atoms of the same species are, by design of nature, all completely identical. Furthermore, a gas of millions of them can be generated and trapped by laser light in some tens of milliseconds. Therefore, unlike with superconducting qubits, no fabrication is necessary, there is no issue with qubits being defective or inhomogeneous, and the qubit ensemble can be scaled and reconfigured on demand to the extent allowed for by the optics. Atoms are also typically non-interacting (at least at long range), which allows for an ease of scalability, reconfiguration, and single-particle control that may be otherwise difficult with ions, which are always strongly interacting at long range. In fact, a large component of this work and of recent work in neutral atom quantum science is *inducing* long-range electrostatic interactions (known as Rydberg interactions) in neutral atoms, as this is a necessary ingredient for generating entangled states.

Although this work is certainly not the first to develop neutral Rydberg atoms as a quantum platform (for a summary of such previous work, see Sec. 1.2.3), it is among the first to do so with *two-electron* atoms (in our case, with strontium). Two-electron atoms have two electrons in their outer valence shell, and are therefore similar in electronic structure to helium. But what benefits might a second valence

electron have for quantum science? In short, the gambit of this work is that the added complexity of a second electron will open up new techniques that produce significant advantage over one-electron atoms. These new opportunities include things such as better control over the atom's motion (Sec. 2.5), new pathways to long-range interactions (Sec. 4.1), and better schemes for reading out the atom's internal state (Sec. 4.1.3).

One more unique property of two-electron atoms — which will be the basis for a large component of this work on its own — is the existence of an *optical clock transition*. Atoms in general are extremely good metrological devices due to their identical nature and precise internal transitions. In fact, the current SI second is defined via a hyperfine transition in cesium. However, atomic clocks based on two-electron atoms such as strontium [11, 12] and ytterbium [13, 14] have significantly surpassed even the cesium standard in both accuracy and precision. This is primarily due to the existence of ultra-narrow clock transitions that are in the *optical* domain, and thus have a significantly higher frequency [15] than the microwave clock transitions found in one-electron atoms such as cesium. Although we are not in a position to advance the state-of-the-art in terms of atomic clock performance, we will exploit our new strontium array platform to demonstrate one of the first single-atom-resolved neutral atomic clocks (Sec. 3.4). The clock transition will play a large role in our research outside of clock operation as well, acting as an important state-preparation mechanism for entangling operations and as a potential qubit in itself. We will therefore give an in-depth discussion of this transition and of our efforts in driving it with a high degree of control. Finally, the combination of this thread of research with that of single-atom control and many-atom entanglement has the interesting prospect of creating a *spin-squeezed atomic clock* [16, 17] (Sec. 5.1.3), which leverages entanglement to beat classical limits of clock precision.

## 1.2 Landscape of previous work

Our work combines the advances of three vanguard fronts in modern atomic physics: (1) two-electron atoms, (2) the control and detection of single atoms, and (3) the generation of entanglement between atoms via long-range Rydberg interactions. In this section, we discuss the crucial previous work on these three fronts that has enabled our research.

### 1.2.1 Two-electron atoms

A magneto-optical trap (or MOT, the first step in generating a cold cloud of atoms in practically all atomic experiments) of strontium was reported alongside a calcium MOT in 1990 in Ref. [18], just three years after the first ever MOT [19] in 1987. However, the full potential of laser cooling in two-electron atoms was not realized until 1998 when the first ever *narrow-line* MOT was demonstrated in strontium [20]. Such a MOT exploits the narrow intercombination transitions in a two-electron atom (Sec. 2.1.2) and allows for cooling to the photon recoil limit [21]. This was an important advance as sub-Doppler cooling techniques that are otherwise readily available in alkali atoms [22] are not available in the ground states of two-electron atoms. For a more in depth review of the cooling of various two-electron atoms (including down to quantum degeneracy), we point the reader to Ref. [23].

In the mid 2000s, interest grew in two-electron atoms as an atomic reference for a new breed of optical lattice clocks [24–26] that were expected to eventually beat microwave-based clocks in systematic uncertainty. Although single-ion optical clocks had already surpassed this milestone [27], atomic optical lattice clocks promised to do so with significantly lower instability (see Sec. 3.3.2 for a definition of instability and systematic uncertainty). A development that was crucial in this effort was the elimination of systematic trap light shifts via a *magic wavelength*, or a wavelength that induces an equal shift in both states of a transition. In 2008, an optical lattice clock (based on strontium) was for the first time shown to have lower systematic uncertainty than the best microwave clocks [28]. Optical lattice clocks with two-electron atoms have since improved even further in terms of both instability and systematic uncertainty [11–14], although a single-ion clock currently holds the record for lowest systematic uncertainty [29].

In the mid 2010s, the first single-atom imaging of a two-electron atom (ytterbium) was done in optical lattices [30, 31].

### 1.2.2 Single-atom physics

The first single trapped neutral atom (cesium) was observed in 1994 at Caltech in a magneto-optical trap [32]. The first trapping and detection of single atoms in microscopic optical traps (having a confinement of $\lesssim 1$ $\mu$m) was performed in 2001 with cesium and rubidium [33, 34]. Perhaps even more importantly, Ref. [33] showed that loading of multiple atoms into a tight optical trap could be suppressed

by a collisional blockade process, significantly simplifying the process of preparing single atoms. In the early 2010s, optical cooling of single atoms to the motional ground state of optical tweezers was demonstrated with rubidium [35, 36].

In the meantime, several efforts were underway to trap and image multiple single atoms simultaneously*. This generally requires creating an optical trapping landscape that has multiple local potential minima, such that each minimum can be occupied by a single atom. One way to do this is with an optical lattice, which is generally created by retro-reflecting a far off-resonant beam such as to create a standing wave. Site-resolved imaging of a truly large scale lattice of single atoms was demonstrated in 2007 [37]. This was impressively done in a *three*-dimensional lattice with sequential imaging of different layers, and the lattice spacing was 4.9 $\mu$m. In the early to mid 2010s, optical resolution and single-atom imaging techniques were pushed to new highs in the development of the *quantum gas microscope* [30, 31, 38–43], which allowed for the site-resolved imaging of single atoms in 2D optical lattices with sub-micron lattice spacing.

Projected trap arrays are the other major class of large single-atom traps that have been developed. These are usually in the form of optical tweezer arrays, which can be generated via holographic projection via a spatial light modulator (SLM) [44–46], beam deflection with an acousto-optic deflector (AOD, which we will use in our work) [47, 48], or a microlens array [49]. An alternative to standard attractive potential arrays is the generation of an array via projection of repulsive beams [50, 51].

A crucial development for single-atom platforms in the context of quantum science was *rearrangement*, or sometimes called atom assembly. This is a technique that takes an initially randomly loaded trap array and rearranges the atoms into an arbitrary configuration, most usually into an array with no *defects*, or empty traps between atoms. This is important for quantum science applications, as one would like to have a fully connected qubit register with ideally zero randomness in the position of the qubits. The very first atom rearrangement was shown in 2006 with a dynamic optical tweezer moving atoms around in a static optical lattice [52]. Interest in atom rearrangement picked up again in the mid 2010s [46, 48, 53], this time directly in tweezer arrays. Rearrangement has also impressively been demonstrated in a 3D optical lattice via an entirely different technique of polarization rotation [54].

*It should be noted that when we discuss "single atoms," we do not mean working with literally only one atom, but instead we mean a circumstance where individual atoms can be resolved.

### 1.2.3 Entanglement via Rydberg interactions

In order to generate an entangled state between qubits, some kind of interactions between the qubits are necessary. Effectively zero-range interactions have been used to entangle atoms that are allowed to occupy the same trap [55] and to simulate many-body Hubbard models [38, 39, 56–58]. However, ground state atoms are typically non-interacting at long ($\gg$50 nm) range. Since our atoms will be in optical tweezers spaced at several $\mu$m apart, we must *induce* long-range interactions. One approach is to place the atoms in a cavity, which allows for photon-mediated interactions [59–63].

Our approach to long-range interactions will instead be to drive atoms to highly excited states, known as *Rydberg states* (Chap. 4). Atoms in these states can experience strong long-range induced dipole-dipole electrostatic interactions. Rydberg interactions were proposed as a potential entangling resource for neutral atoms in the early 2000s [64, 65]. Rydberg blockade, a mechanism for generating entanglement between atoms, was observed in 2009 [66, 67], and was soon after used to generate entanglement in hyperfine ground states [68, 69]. Rydberg interactions were later used in optical lattices [70, 71] and for entangling operations [72] and quantum simulation [73] in large arrays. Rydberg interactions have been most recently married with the technique of array rearrangement [74–78], allowing for the study of re-configurable, defect-free many-body entangled atomic arrays.

## 1.3 Overview of our experiment

We now summarize some key features of our new experiment. A more in-depth discussion can be found in App. A, and a detailed report from the earlier stages of our build can be found in Ref. [79]. See Fig. 1.1 for a brief visual overview.

All of our experimentation on atoms occurs in an ultra-high vacuum glass cell (App. A.1.2). Two high-resolution objectives (App. A.3) surround the cell and are responsible for both generating the optical tweezer arrays and for collecting fluorescence from the atoms. Although both of these can be done through one objective, having two objectives allows for the ability to image with one objective the tweezers that are generated through the other, and potentially also allows for imaging through both objectives simultaneously.

The general flow of our experimental cycles are as such:

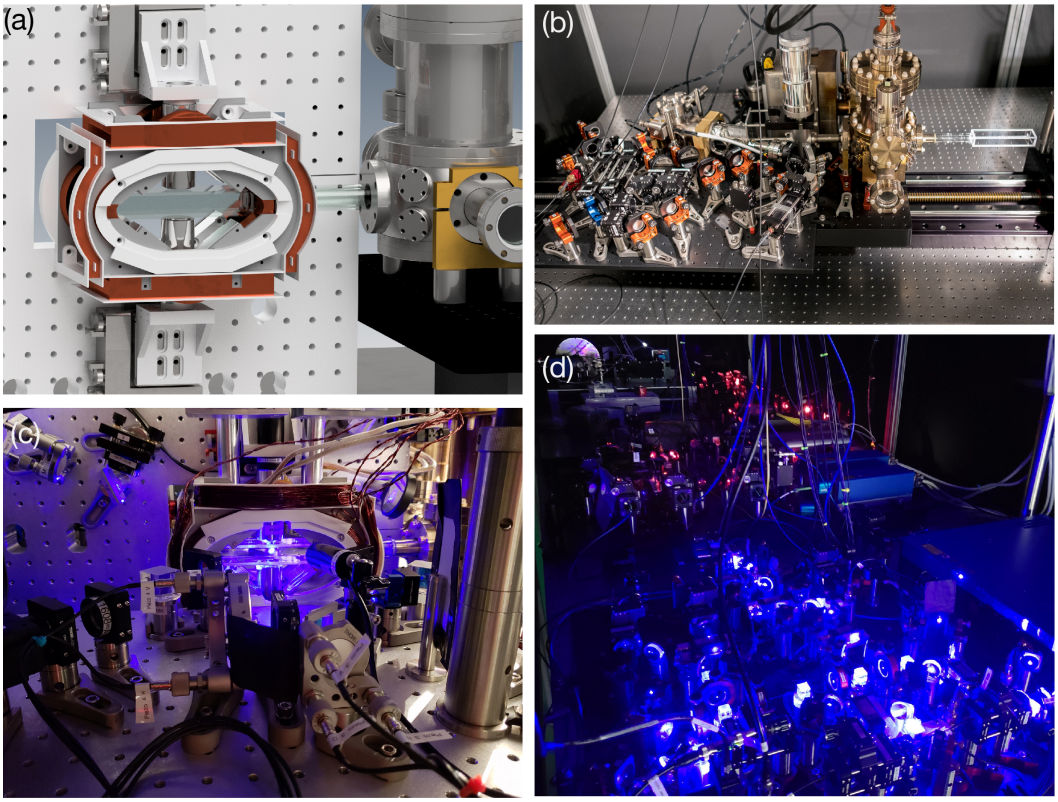


Figure 1.1: Overview of the experimental apparatus. **(a)** Rendering of the glass vacuum cell in which atom trapping occurs (see Fig. A.3 for more). **(b)** Our vacuum chamber along with relevant optics for the atom source (see App. A.1). The entire vacuum chamber is on a linear translation stage. **(c)** Glass cell with a blue magneto-optical trap of strontium, and surrounding optics. **(d)** Various lasers (see Sec. 2.1.2).

1. Generate a strontium MOT on the broad "blue" transition, then transfer it to a much colder and denser MOT on the narrow "red" transition (see Fig. 2.1).
2. Load atoms from the red MOT into the tweezer array (Sec. 2.4.1).
3. Perform pairwise loss to ensure no more than one atom is in each tweezer (Sec. 2.4.2).
4. (Optional) Re-load the array to increase filling fraction of atoms (Sec. 2.4.3).
5. Image the loaded array (while cooling, see Sec. 2.6) to determine which tweezers contain an atom.
6. Cool atoms to near the motional ground state (Sec. 2.5).
7. If desired, rearrange the atoms into a desired configuration (Sec. 2.7.3, Fig. 4.9), image again to verify success of rearrangement, and cool again.

8. At this point, the actual "science" occurs. We can, for example, interrogate the clock transition (Sec. 3.4) or perform Rydberg excitation to induce entanglement between atoms (Sec. 4.3).

9. Perform some state-selective detection operation. This can involve shelving the atoms into a metastable state (see end of Sec. 2.5.4), blasting atoms of a particular state out of the tweezers (Sec. 3.1.3), or auto-ionization (Sec. 4.1.3).

10. Image the remaining bright atoms. For each atom measured, this gives a binary value that, when averaged, informs on some state occupation probability that we are interested in.

11. Either repeat from Item 1, or in some cases (Sec. 3.4) atoms can be recycled such that we start again directly from Item 6.

The various laser beams that are used to accomplish these tasks are shown in Figs. 1.2–1.3.

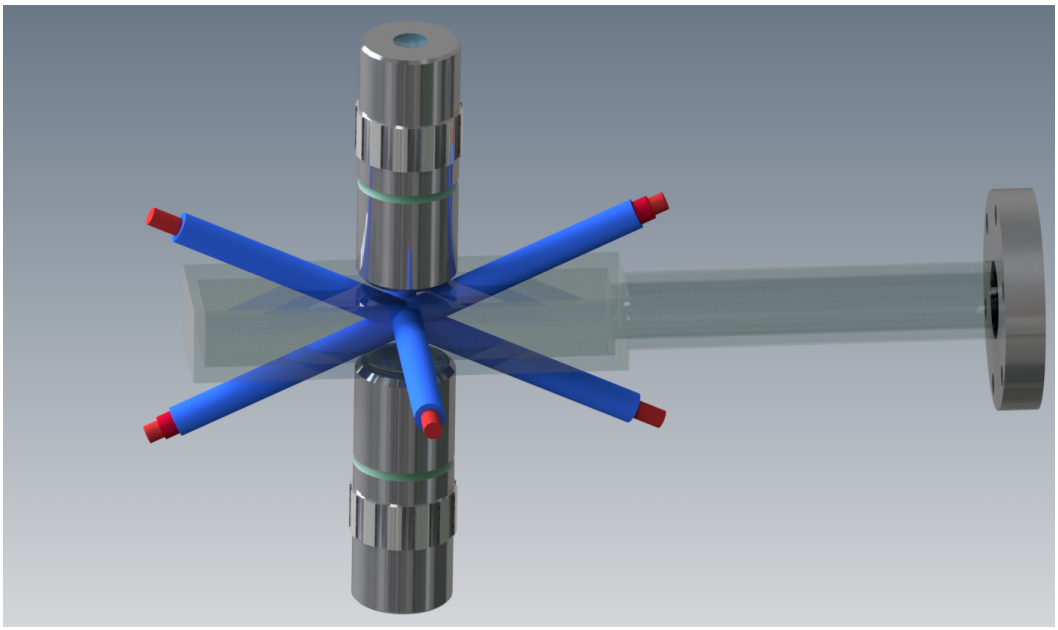

Figure 1.2: Beam configuration around our glass cell for our blue and red magneto-optical traps (MOTs). Circularly polarized beams are sent along three axes and retroreflected while passing twice through a quarter wave plate. We send in two beams at a shallow 65° angle to the vertical axis in order to avoid the objectives. For the position of our magnetic quadrupole coils, see Apps. A.1.2 & A.2.2. We overlap blue and red beams onto the same beampath using dichroic mirrors. A pair of repump beams at 679 nm and 707 nm are also overlapped with one of the diagonal axes (the one going down to up from left to right). Not shown: a pair of blue absorption imaging beams in the horizontal plane and at 45° to the MOT beam in that plane.

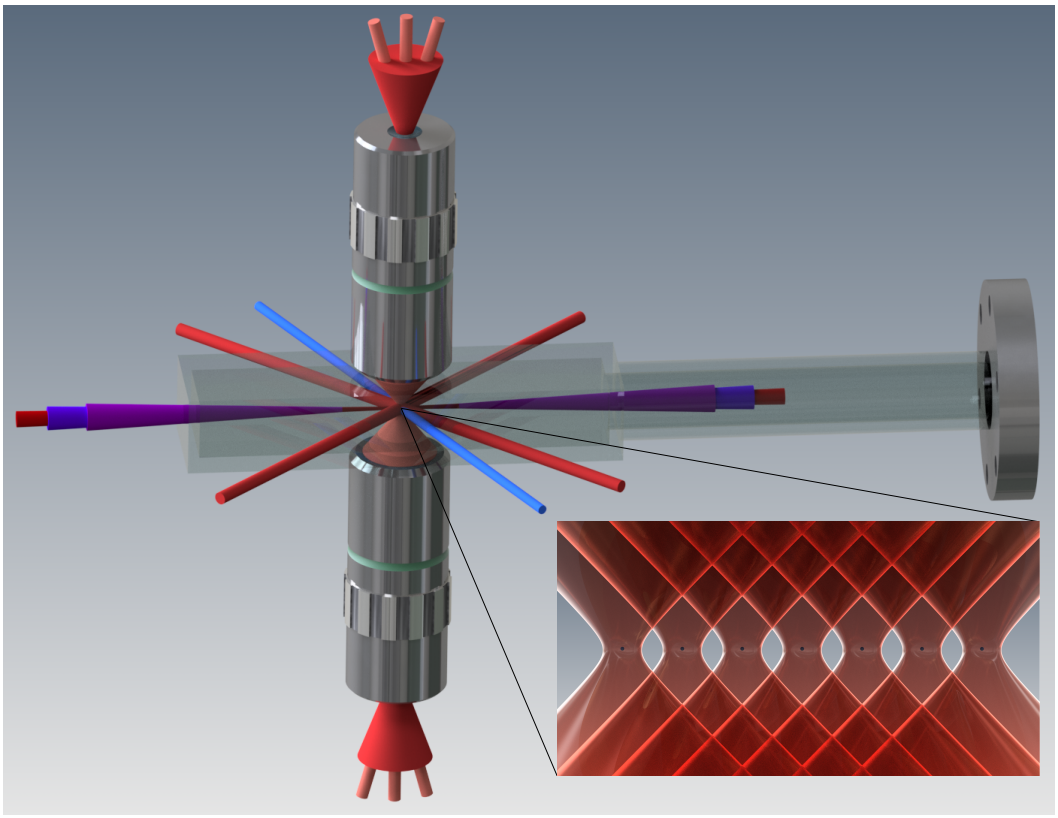

Figure 1.3: Beam configuration around our glass cell after atoms have been loaded into tweezers. Tweezer arrays are generated by sending beams with various angles (pink beams) through the input of one objective. Atoms are cooled with a set of three mutually orthogonal red beams: two in the horizontal plane at a 45° angle to the glass cell, and one vertical beam that is sent through the objective in such a way as to fill out the field of view. A blue beam in the horizontal plane is used for fluorescence imaging of single atoms. Through the front of the glass cell, we send in three converging beams, a Rydberg beam (light violet), an auto-ionization beam (dark violet), and a clock beam (red). The only beam that may be retroreflected here is the blue imaging beam, although this is not strictly necessary (Sec. 2.6.2). All beams shown that do not go through the objective are in the horizontal plane. Inset: an array of atoms trapped in optical tweezers in the focal plane of both objectives. Not shown: a repump beam with 679 nm, 707 nm, and potentially 688 nm light (shown in Fig. 1.2). In real life, laser beams don't cast shadows.

## 1.4 Summary of our novel results

We briefly highlight the most important novel results reported in this work:

**Single-atom physics**

1. The first single-atom imaging of strontium, the first trapping and imaging of single two-electron atoms in optical tweezers (Sec. 2.6.8), and the extension of these techniques to arrays of size up to $11 \times 11$ (Figs. 2.25 & 2.27).

2. An imaging scheme producing an imaging fidelity of 0.99991(1) and survival probability of 0.99932(8) (Sec. 2.6.8) — the latter of which is a record for single-atom imaging — allowing for thousands of repeated images of the same atoms.

3. Optical cooling of single strontium atoms to near the motional ground state of a tweezer (Sec. 2.5.4), and the experimental realization of a novel Sisyphus cooling mechanism (Secs. 2.5.2, 2.6.8).

4. Rearrangement of 1D strontium atom arrays (Fig. 2.24 & 4.9), including a fast and memory-efficient algorithm for rearrangement in 1D (Sec. 2.7.3).

5. Increased array loading via multiple filling cycles (Sec. 2.4.3).

6. Measurement of polarizabilities on strontium's intercombination line at $\lambda = 515.2$ nm (Sec. 2.3.4 & App. B).

**Clock state operations**

1. Operation of an atomic-array optical clock with single-atom resolution (Sec. 3.4), including a Monte-Carlo approach to modeling clock performance (Sec. 3.4.6).

2. Coherent excitation of the clock transition with an uncorrected $\pi$-fidelity of 0.985 (Sec. 3.2.4), with a total transfer fidelity of 0.998 possible with the addition of optical pumping (Sec. 4.1.1).

**Rydberg excitation and entanglement**

1. An auto-ionization Rydberg state-detection scheme with a state-detection fidelity of 0.9996(1), which improves on the infidelity of previous state-detection schemes by at least one order of magnitude (Sec. 4.1.3).

2. Excitation of a Rydberg qubit with an uncorrected (SPAM corrected) $\pi$-fidelity of 0.9951(9) (0.9967(9)) (Sec. 4.3).

3. Generation of entangled Bell pair states with an uncorrected (SPAM corrected) fidelity of $\geq$0.980(3) ($\geq$0.991(4)) via Rydberg blockade (Secs. 4.3.1 & 4.3.2), a leading value for Rydberg atoms.

4. Realization of light-cone correlation spreading across an assembled array of 17 atoms (Fig. 5.3).

# Chapter 2

# SINGLE-ATOM PHYSICS WITH STRONTIUM

In this chapter, we will look at the physics of trapping, cooling, and imaging single strontium atoms in optical tweezers.

## 2.1 Intro to strontium

Strontium (Sr) is an alkaline-earth (group 2) atom of atomic number $Z = 38$ with four stable and naturally occurring isotopes. In this section, we review relevant properties of strontium, its isotopes, its two-electron level structure, and certain key transitions.

### 2.1.1 Choice of isotope

All work in this thesis was done with **$^{88}$Sr**, a bosonic* isotope. The other naturally occurring isotopes are the fermionic $^{87}$Sr and the two other bosonic isotopes $^{84}$Sr and $^{86}$Sr.

$^{88}$Sr was chosen primarily for its large natural abundance (~83%) [80] as well as for the simplicity of its electronic structure. Whereas the fermionic isotope has a rather large nuclear spin of $I = 9/2$, all bosonic isotopes of Sr have $I = 0$, resulting in a lack of hyperfine structure. These two factors were favorable for a first study of single-atom Sr physics, but we will note here some features of the other isotopes that may be useful for future studies. $^{88}$Sr has a very small ground state scattering length of about $-1a_0$ [23] (where $a_0$ is the Bohr radius), making it challenging to evaporatively cool to degeneracy when compared to the other bosons which have much larger scattering lengths. This was not a concern for this study as no

*Letting $A$ be the mass number, one can see that neutral atoms for which $(-1)^{Z+A}$ is positive (negative) are bosons (fermions).

evaporative cooling was necessary, but it may be for other platforms. Furthermore, the lack of hyperfine structure has potentially negative implications for systematics during clock operation (Ch. 3.1.1) and precludes the use of nuclear states for certain quantum computation schemes [81] or studies of $SU(N)$ physics [82].

The spectral shifts between the four isotopes are within the range of acousto-optic modulators (AOMs), so it is in principle possible to work with all four isotopes with one apparatus and laser system [23]. Although we have to date worked with only $^{88}$Sr, we see no obvious reasons why the techniques presented in this thesis would not be adaptable to the other isotopes, especially the bosons.

### 2.1.2 Level structure

The most relevant property of Sr to us will be the level structure of its outer electronic shell, which importantly has two electrons in an $s^2$ configuration. This is a property shared by all of the alkaline earth atoms (Be, Mg, Ca, **Sr**, Ba, Ra), but is not exclusive to them. Helium, for example, is the quintessential and most basic two-electron atom. Ytterbium is another example, notable for having recently developed experimental techniques [83] that are similar to those we show in this work for Sr. Yet more examples are mercury [84] and cadmium [85]. See Ref. [23] for a broad review of work with two-electron atoms.

#### *Nomenclature*

Let $\vec{s}_i, \vec{l}_i$ be the spin and orbital angular momentum operators, respectively, for the $i^{th}$ outer-shell electron. We define $\vec{S} = \sum_i \vec{s}_i$, $\vec{L} = \sum_i \vec{l}_i$, and $\vec{J} = \vec{S} + \vec{L}$, with associated quantum numbers of, e.g., $|\vec{S}|^2$ denoted by the same symbol without an arrow, e.g., $S$. For two outer-shell electrons, we have $s_1 = s_2 = 1/2$, so the possible values of $S$ are 0 and 1. The $S = 0$ sector contains one $S^z$ state, so we call it a *singlet*, while the $S = 1$ sector contains three, so we call it a *triplet*.

We index states of Sr with the following notation:

$$n_1 l_1 n_2 l_2 \; {}^{2S+1}L_J \tag{2.1}$$

or, in the case of both electrons occupying the same orbital, by $nl^2 \; {}^{2S+1}L_J$, where we use the spectroscopic alphabet (s, p, d, f,...) to index $l$ and the same but with capital letters for $L$. So, for example, the ground state (which is a singlet) will be referred to as $5s^2 \; {}^1S_0$, while a triplet state might be $5s5p \; {}^3P_2$.

### *Intercombination lines*

This notation suggests that $l_i, L, S$, and $J$ are "good" quantum numbers, meaning that the energy eigenstates they apply to are either exact or approximate eigenstates of the operators associated with those quantum numbers. This arises when the dominant angular momentum coupling is given by $\vec{L} \cdot \vec{S}$, a situation that is called *LS coupling*. This is indeed the case for (relevant) states of Sr. Of these quantum numbers, however, only the total angular momentum quantum number $J$ is exact* for all states, and this is due to the overall rotational symmetry of the atom.

The fact that $S$ is a "good but not exact" quantum number is a key feature of two-electron atoms. Particularly, this becomes important when we look at electric dipole (E1) transitions between states, such as the ones induced by laser light. Strictly speaking, E1 transitions do not couple to electronic spin degrees of freedom, so we have the selection rule $\Delta S = 0$. One might then conclude that E1 transitions between singlet and triplet states are forbidden. However, mixing of atomic eigenstates of equal $J$ but different $S$ (due to weak $\vec{l}_i \cdot \vec{s}_i$ spin-orbit terms) makes some nominally triplet states have weak singlet character and vice versa, making transitions between the two sectors weakly allowed.

Practically what this means is that two-electron atoms have narrow E1 transitions between singlet and triplet sectors called *intercombination lines*. These lines are of great experimental utility as they allow for e.g. optical cooling to very low temperatures, precise spectroscopy, and optical clock transitions.

### *Transitions of interest*

Here we list some key transitions of Sr. These are also included in the level diagram of Fig. 2.1.

**Blue**

$5s^2\ {}^1S_0 \leftrightarrow 5s5p\ {}^1P_1$ | 460.9 nm | $\Gamma = 2\pi \times 30$ MHz ($\tau = 5.3$ ns) [86]

This is the primary "strong" singlet ground-to-excited transition of Sr. It is commonly used for slowing, first-stage magneto-optical traps (MOTs), and imaging. In this sense, it is similar to the $D_1$ and $D_2$ lines of alkali atoms; however, it is significantly broader by about a factor of 5. This means its Doppler temperature

*In the absence of external perturbing fields. In the case of nonzero nuclear spin $I$, only $F$ is exact for all states, where $\vec{F} = \vec{J} + \vec{I}$.

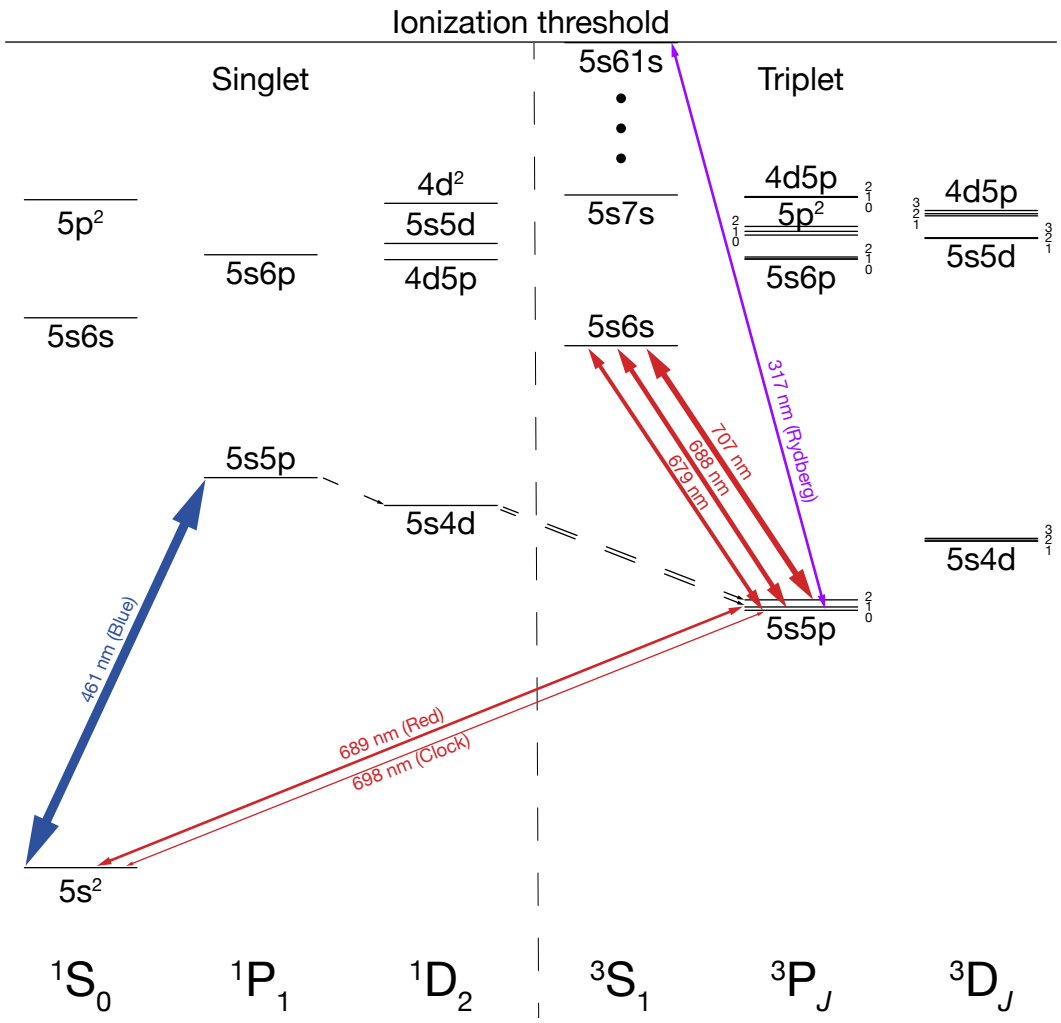


Figure 2.1: A to-scale energy level diagram of relevant states of Sr, with transitions of interest shown. We show all states with $L \in \{\mathrm{S},\ \mathrm{P},\ \mathrm{D}\}$ up to 5s7s $^3\mathrm{S}_1$ as well as our Rydberg state 5s61s $^3\mathrm{S}_1$ and the ionization threshold. If a state has fine structure, the $J$ values are listed to the side of the relevant states. Dashed arrows highlight an important decay channel (see Sec. 2.6.8). Not shown: the auto-ionizing state we use for Rydberg state detection (Sec. 4.1.3).

($T_d \sim 730\ \mu$K) is higher by the same factor, and furthermore there is no obvious way of achieving sub-Doppler cooling [22] on this transition as the 5s$^2$ $^1\mathrm{S}_0$ ground state has no fine or hyperfine structure. This would have made cooling Sr to sufficiently low temperatures impossible were it not for the red transition. The 5s5p $^1\mathrm{P}_1$ excited state has a weak decay channel into the 5s4d $^1\mathrm{D}_2$ state, which subsequently decays into the 5s5p $^3\mathrm{P}_{1,2}$ states. This is an important consideration for the blue MOT as well as for single-particle imaging, as will be discussed in Sec. 2.6.8.

**Red**

$5s^2\ {}^1S_0 \leftrightarrow 5s5p\ {}^3P_1$ | 689.4 nm | $\Gamma = 2\pi \times 7.5$ kHz ($\tau = 21\ \mu$s) [87]

This is an intercombination line (sometimes called *the* intercombination line) with a linewidth small enough for a Doppler temperature of $T_d \sim 180$ nK (although, unusually, its *recoil* temperature is higher at $T_r \sim 230$ nK), but still large enough for cooling to be practical. It does not scatter rapidly enough to make direct cooling of a thermal beam into a MOT very practical, so usually this transition is used for a second-stage red MOT after a blue MOT. Later, we will show that this transition is very useful for cooling (Sec. 2.5) and diagnostic spectroscopy in tweezers (Sec. 2.7.2). To actually take advantage of the narrow linewidth, one must use a narrow laser locked to a high-finesse cavity (App. A.4.2).

**Repumps**

$5s5p\ {}^3P_0 \leftrightarrow 5s6s\ {}^3S_1$ | 679.3 nm | $\Gamma = 2\pi \times 1.3$ MHz ($\tau = 120$ ns) [88]
$5s5p\ {}^3P_1 \leftrightarrow 5s6s\ {}^3S_1$ | 688.0 nm | $\Gamma = 2\pi \times 3.9$ MHz ($\tau = 41$ ns) [89]
$5s5p\ {}^3P_2 \leftrightarrow 5s6s\ {}^3S_1$ | 707.2 nm | $\Gamma = 2\pi \times 6.7$ MHz ($\tau = 24$ ns) [87]

These transitions allow for rapid incoherent population transfer between the $5s5p\ {}^3P_J$ states. For example, if it is desired to transfer population from ${}^3P_2$ to ${}^3P_1$, one can simultaneously turn on the transitions at 679 nm and 707 nm. Then, ${}^3P_1$ becomes the only dark state in the manifold and, after potentially several scattering events through $5s6s\ {}^3S_1$, it will be populated. This exact scheme is used to return atoms into the singlet blue transition cycle if they have decayed to $5s5p\ {}^3P_2$ through the weak $5s4d\ {}^1D_2$ channel. However, we will also find various other uses for these transitions that will be described when appropriate.

**Clock**

$5s^2\ {}^1S_0 \leftrightarrow 5s5p\ {}^3P_0$ | 698.4 nm | $\Gamma \to 0$ ($\tau \to \infty$) (See Sec. 3.1.1)

The ultra-narrow clock transition will be discussed at depth in Chap. 3. The practically zero decay rate of this transition is due to the $J = 0 \nrightarrow J' = 0$ and $\Delta S = 0$ electric dipole selection rules. We will refer to $5s5p\ {}^3P_0$ as the *clock state*.

**Rydberg**

$5s5p\ {}^3P_0 \leftrightarrow 5sns\ {}^3S_1$ | ~317 nm (Table. 4.2) | See Sec. 4.4.1 for decay rate

This is a series of transitions from the clock state to highly-excited (i.e., *Rydberg*) triplet states with $n \gtrsim 40$ that will be used to induce interactions and entanglement between atoms. These Rydberg transitions will be discussed at depth in Ch. 4. Note that the wavelength quoted here assumes excitation from the clock state $5s5p\ {}^3P_0$.

**Auto-ionization**

$5snsnsnsnsns\ ^3S_1 \leftrightarrow 5p_{3/2}ns_{1/2}$ | 407.9 nm | See Sec. 4.1.3 for discussion on decay rate

These are transitions from Rydberg states to states with an energy above the ionization threshold of the neutral Sr atom where both valence electrons are excited. Excitation of these transitions leads to rapid auto-ionization of the atom, which allows for high-fidelity detection of Rydberg states. Note that, unlike all states we have encountered so far, we use quantum numbers $j_i$ (the total angular momentum of each electron) to denote these auto-ionizing states. $J = 1, 2$ are possible for these states and are practically degenerate. However, $J = 1$ is most desirable for rapid auto-ionization, requiring some consideration of polarization (Sec. 4.1.3).

## 2.2 Optical tweezers

***Electric field conventions***

Differing electric field conventions are a common source of confusion, so here we state ours explicitly.

The real time-dependent electric field of a monochromatic wave is given by

$$\vec{E}(\vec{r}, t) = \mathrm{Re}\left\{\vec{\mathcal{E}}(\vec{r})e^{-i\omega t}\right\} \tag{2.2}$$

where $\vec{\mathcal{E}}$ is a complex vector. When $\vec{E}$ is understood to have a single, constant polarization across all space, we can work with just a scalar complex quantity $\mathcal{E}$ by writing $\vec{\mathcal{E}}(\vec{r}) = \hat{\epsilon}\mathcal{E}(\vec{r})$, where $\hat{\epsilon}$ is a unit complex vector. $\mathcal{E}$ is sometimes referred to as the *complex amplitude* of the electric field.

Intensity is then defined as

$$I = \tfrac{1}{2}c\varepsilon_0|\vec{\mathcal{E}}|^2 \tag{2.3}$$

with $c$ the speed of light and $\varepsilon_0$ the vacuum permittivity. Intensity has units of power per area and is the quantity most easily determined in a lab.

In a different convention, one may instead define the *positive frequency component* of the electric field as $\vec{\mathcal{E}}^{(+)} = \frac{1}{2}\vec{\mathcal{E}}$, and the negative frequency component $\vec{\mathcal{E}}^{(-)}$ by its complex conjugate. The positive and negative component convention is used heavily in Ref. [90], which we will cite often, and was used in our

published work Ref. [89]. However, we will *not* use it in this work, and instead use the complex amplitude everywhere.

Optical tweezers (or just *tweezers* for short) are optical dipole traps [91] with a small volume (typically $\lesssim 1\ \mu\text{m}^3$) that are formed by tightly focusing a far off-resonant beam of light through a high numerical aperture (NA) objective lens. The tight spatial extent of tweezers allows for preparation of single atoms (Sec.2.4.2) as well as for deep traps with large trap frequencies for relatively small optical powers.

We will analyze the optical profile of a tweezer by looking at how a lens focuses light. We will for now work in the scalar and paraxial regime of optics, where paraxial means that beams propagate only in small angles to the optical axis. In App. C, we will see how these approximations begin to break down for high NA systems. However, the corrections will be small, so for most purposes, a scalar paraxial treatment is sufficient. The reader is pointed to Ref. [92] for more in-depth discussions of the relevant derivations and approximations.

Consider an aberration-free lens of focal length $f$ illuminated by an input field with complex amplitude $\mathcal{E}_i(x', y')$. We let $\lambda = \frac{2\pi}{k}$ be the wavelength, $(x, y)$ and $(x', y')$ be coordinates in the focal and input planes, respectively, and $z$ be the distance from the focal plane. Then the output field near the focal plane of the lens is (up to an overall phase)

$$\mathcal{E}_o(x, y, z) = e^{ikz}\frac{k}{2\pi f}\iint \mathcal{E}_i(x', y')e^{-ik\frac{xx'+yy'}{f}}e^{-ikz\frac{x'^2+y'^2}{2f^2}}dx'dy' \tag{2.4}$$

The integral is the *Fourier transform of the input field* times a radially quadratic phase that scales linearly with $z$. This formula follows from Fresnel diffraction up to a few approximations. Note that $\mathcal{E}_o(x, y, z)$ satisfies the *paraxial Helmholtz equation*: $(\nabla_\perp^2 + 2ik\partial_z + 2k^2)\mathcal{E} = 0$. The solutions of this equation are often written in terms of a basis of Gaussian modes, such as *Hermite-Gaussian* modes in Cartesian coordinates or *Laguerre-Gaussian* modes in cylindrical coordinates. The lowest order mode of both of these bases is the simple Gaussian beam, which we will soon see is a close approximation of a tweezer.

When the input field has symmetry around the optical axis, we can simplify the expression by working in cylindrical coordinates:

$$\mathcal{E}_o(r, z) = e^{ikz}\frac{k}{f}\int_0^\infty r'\mathcal{E}_i(r')J_0(\tfrac{k}{f}rr')e^{-ikz\frac{r'^2}{2f^2}}dr' \tag{2.5}$$

where $r = \sqrt{x^2 + y^2}$, $r' = \sqrt{x'^2 + y'^2}$, and $J_n$ is the order $n$ Bessel function of the first kind. In the context of optical aberration theory, the quadratic phase in the integral of Eq. 2.5 can be interpreted as a *defocus aberration*. It is in some sense not a "true" aberration as it only represents a displacement from the focal plane. However, higher order aberrations which are not trivial can be similarly represented by more complex phase patterns (such as spherical aberrations, represented by fourth order phase curvature). One often uses *Zernike polynomials* in this context, which form an orthonormal basis for optical aberrations of all orders [93].

To form an optical tweezer, we send a Gaussian beam of waist $w_i$ and central complex amplitude $\mathcal{E}_{0,i}$ through a lens with aperture radius* $R$. Then the electric field of the tweezer is given by

$$\mathcal{E}_t(r, z) = e^{ikz} \frac{k\mathcal{E}_{0,i}}{f} \int_0^R r' e^{-\frac{r'^2}{w_i^2}} J_0(\tfrac{k}{f} r r') e^{-ikz\frac{r'^2}{2f^2}} dr' \tag{2.6}$$

There is generally not a clean analytical solution to this integral for finite apertures, but the limits $\frac{w_i}{R} \gg 1$ and $\frac{w_i}{R} \ll 1$ are tractable and instructive. For $\frac{w_i}{R} \gg 1$, the Gaussian input becomes approximately uniform on the aperture (although most of the input power is not transmitted) and we drop the first Gaussian factor in Eq. 2.6. For $z = 0$, this can be evaluated to give

$$\mathcal{E}_t(r, 0)|_{\frac{w_i}{R} \gg 1} = \mathcal{E}_{0,i} \frac{R}{r} J_1(\tfrac{kR}{f} r) \tag{2.7}$$

This output pattern is called an *Airy disk* and is generally the "smallest" feature that a lens can produce. It is very closely Gaussian near the center, but has rings on the outside, the first and most prominent of which is peaked at $r \sim 5.14\frac{f}{kR}$. Note that $\lim_{r\to 0} \mathcal{E}_t(r, 0)|_{\frac{w_i}{R} \gg 1} = \mathcal{E}_{0,i} \frac{kR^2}{2f}$.

For $\frac{w_i}{R} \ll 1$, the input Gaussian is much smaller than the aperture and practically all input power goes through. To evaluate this, we let the upper bound of the integral

*For a compound microscope objective, usually NA is specified instead of $R$. Then, we have $R = f \times NA$, where $f$ is the *effective focal length* of the objective.

in Eq. 2.6 go to infinity. The result is simply another Gaussian:

$$\mathcal{E}_t(r,z)|_{\frac{w_i}{R}\ll 1} = \mathcal{E}_0 \frac{w_0}{w(z)} \exp\Big(-\frac{r^2}{w(z)^2}\Big) \exp\Big(ikz + ik\frac{r^2}{2R(z)} - i\psi(z)\Big) \tag{2.8}$$

$$w_0 = \frac{2f}{kw_i} \tag{2.9}$$

$$\mathcal{E}_0 = \frac{w_i}{w_0}\mathcal{E}_{0,i} \tag{2.10}$$

$$z_R = \tfrac{1}{2}kw_0^2 \tag{2.11}$$

$$w(z) = w_0\Big(1 + \Big(\frac{z}{z_R}\Big)^2\Big)^{\frac{1}{2}} \tag{2.12}$$

$$R(z) = z\Big(1 + \Big(\frac{z_R}{z}\Big)^2\Big) \tag{2.13}$$

$$\psi(z) = \arctan\Big(\frac{z}{z_R}\Big) \tag{2.14}$$

This is indeed the general formula for any Gaussian beam, with *waist* $w_0$, *Rayleigh range* $z_R$, *Radius of curvature* $R(z)$, and *Gouy phase* $\psi(z)$.

For a general choice of $\frac{w_i}{R}$, the integral is not analytically tractable, but we can study it numerically [94]. We will see in Sec. 2.3 that a far off-resonant optical beam creates energy shifts proportional to its intensity*, gradients of which can create trapping motional potentials. For trapping, what is most relevant is what happens near the point of maximum intensity. In particular, we are interested in a *trap depth* $U_0 \equiv -U(\vec{r}=0) \propto |\mathcal{E}_0|^2$, where $U(\vec{r})$ is the optical potential, as well as the *trap frequencies* $\omega_i \equiv \sqrt{\frac{1}{m}\partial_i^2 U|_{\vec{r}=0}}$, where $m$ is the atomic mass. We can numerically compute these quantities for a real tweezer as a function of $\frac{w_i}{R}$ at fixed input power, with results shown in Fig. 2.2. Making a tight and deep tweezer with a Gaussian input is a competition between getting high power transmission (which favors *smaller* input waist) and a tight tweezer waist (which favors *larger* input waist). A compromise is reached at about $\frac{w_i}{R} \sim 1$, though we see that radial trap frequency, axial trap frequency, and depth have slightly different optima. We will thus choose to work in a regime of $\frac{w_i}{R} \sim 1$, so these tweezers will be something in between an Airy disk and a Gaussian.

When considering trapping, we will choose to model a tweezer potential as purely Gaussian. We will assume an experimentally determined trap depth $U_0$, along with a fitted waist $w_0$ and Rayleigh range $z_R$, which we will in general *not* constrain by Eq. 2.11. The only time in which this approximation may not be sufficient is when

*Up to small, usually unimportant caveats discussed in Sec. 2.3.3 and Sec. 3.1.2

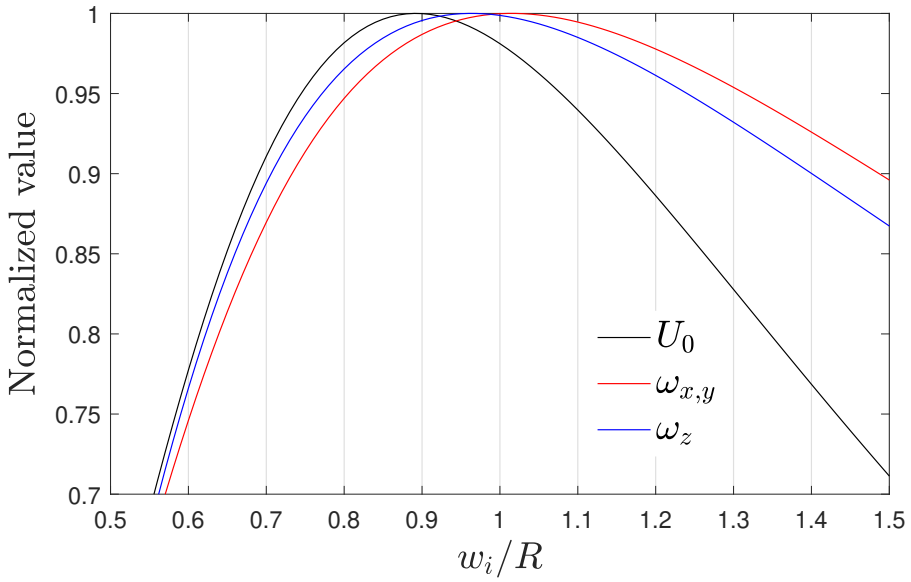


Figure 2.2: Trap depth and trap frequencies for a tweezer generated by an input Gaussian of waist $w_i$ through an aperture of radius $R$, under the paraxial approximation. The total power of the input beam before the aperture is kept fixed.

we consider two tweezers close together such that the non-Gaussian outer rings of one overlap with the central region of the other. The outer structure of a real tweezer is compared with that of a Gaussian and an Airy disk in Fig. 2.3.

Within the Gaussian approximation, the optical potential is given by

$$U(r,z) = \frac{-U_0}{1+z^2/z_R^2} \exp\left(\frac{-2r^2}{w_0^2(1+z^2/z_R^2)}\right) \tag{2.15}$$

and we have the following useful formulas for radial and axial trap frequencies:

$$\omega_{x,y} = \sqrt{\frac{4U_0}{mw_0^2}} \tag{2.16}$$

$$\omega_z = \sqrt{\frac{2U_0}{mz_R^2}} \tag{2.17}$$

It is often useful in the lab to be able to compute the central intensity $I_0$ of a Gaussian beam given $w(z)$ and the total power of the beam $P$. This is given by:

$$I_0(z) = \frac{2P}{\pi w(z)^2} \tag{2.18}$$

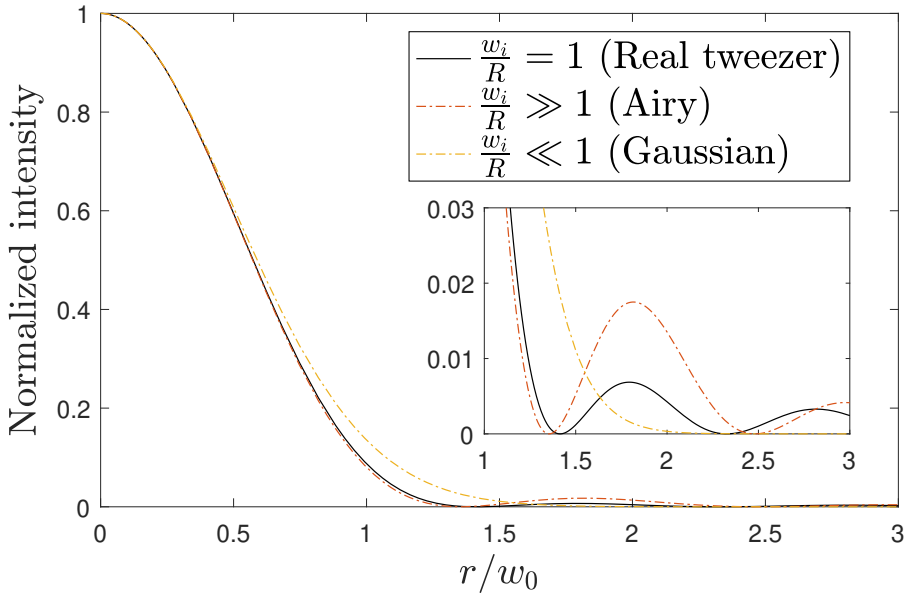


Figure 2.3: Comparison between "Real tweezer", Airy, and Gaussian intensity profiles at long distances, under the paraxial approximation. Note that these do *not* result from the same input beam, but are rather constrained to the same peak intensity and the same second derivative at zero. The purpose of this is to compare different trap models far from the center under the same central conditions (i.e. the same trap depth and trap frequency). The x-axis is in units of Gaussian waists. Inset: A zoom-in around the outer ring features.

## 2.3 Light shifts & optical trapping

In this subsection, we will compute how a far off-resonant beam of light creates energy shifts called *light shifts* in the atomic level structure proportional to the light's intensity. This allows us to directly interpret the intensity profile of a tweezer (explored in Sec. 2.2) as a motional potential that we can use to trap an atom.

### 2.3.1 Polarizability

Within the electric dipole approximation, the Hamiltonian describing the interaction of light with an atom at a particular point in space is

$$H_d(t) = -\vec{d} \cdot \vec{E}(t) \tag{2.19}$$

where $\vec{d} = -|e|\vec{r}$ is the vector dipole operator. Note that if we choose our basis $\{|i\rangle\}$ to be eigenstates of parity (as atomic energy eigenstates are), then $\langle i|\vec{d}|i\rangle = 0$. We will assume henceforth that such a basis is used. We will assume that $\vec{E}$ is monochromatic with $\omega$ far off-resonant from any atomic transitions of the states that

we are interested in. Under this assumption, we will evaluate the dipole interaction with perturbation theory. As our basis consists of parity eigenstates, first-order energy perturbations vanish, so the leading perturbations will be second-order.

An important takeaway from this subsection will be that the second-order perturbation generically leads to more than just an energy shift: *one must also consider mixing of states within the same (near-)degenerate manifold*. For example, if we consider the perturbation on a state $|5s5p\ ^3P_1\ m_J = 0\rangle$, we should not only ask how the energy of this state shifts, but also how it mixes with $|5s5p\ ^3P_1\ m_J = \pm 1\rangle$. Such state mixing generally happens when the electric field vector $\hat{\epsilon}$ is not parallel to the quantization axis, which might be fixed as parallel to a magnetic field.

The process that leads to an energy shift can be interpreted as a two-photon process from a state $|i\rangle$ to a series of intermediate states $|j\rangle$ and then back to $|i\rangle$. Such processes are captured in second-order perturbation theory by terms such as $\langle i|H_d|j\rangle\langle j|H_d|i\rangle$. If we let $|i'\rangle$ be another state in the same manifold as $|i\rangle$, the process $\langle i|H_d|j\rangle\langle j|H_d|i'\rangle$ may also be allowed and will produce an admixture between these states. In principle, such a two-photon state admixture can happen between *any* two states when allowed by selection rules, but admixtures between *different* non-degenerate manifolds are usually strongly energetically suppressed and can be ignored.

Therefore, we will compute more than just second-order *energy shifts*; we will in fact compute an entire *effective second-order perturbative Hamiltonian* $H_d^{\text{eff}}$ for a degenerate manifold of states. We state the final result and refer the reader to Ref. [90] Chapter 7.7 for a thorough derivation. First we define the *Cartesian tensor polarizability operator* for a degenerate manifold of states $|i\rangle$:

$$\alpha_{\mu\nu} = \sum_j \frac{2\omega_{ji}}{\hbar(\omega_{ji}^2 - \omega^2)} d_\mu |j\rangle\langle j| d_\nu \tag{2.20}$$

where $\mu, \nu$ are Cartesian coordinate indices, $d_\mu$ is the $\mu$ component of the vector dipole operator $\vec{d}$, and $\omega_{ji} = \frac{1}{\hbar}(\mathscr{E}_j - \mathscr{E}_i)$ where $\mathscr{E}_i$ is the unperturbed atomic energy of the degenerate manifold to which $|i\rangle$ belongs.

Then the effective second-order perturbative Hamiltonian is

$$H_d^{\text{eff}} = -\frac{I}{2c\varepsilon_0} \sum_{\mu,\nu} \alpha_{\mu\nu} \epsilon_\mu^* \epsilon_\nu \tag{2.21}$$

where $I$ is the intensity and $\epsilon_\mu$ is the $\mu$ component of the complex unit polarization vector. Note that the time dependence of the original $H_d(t)$ is gone.

### 2.3.2 Spherical tensor decomposition

While Eqs. 2.20 & 2.21 in principle give the desired result, they can be rewritten in a more elegant and insightful way. In particular, Eq. 2.20 requires one to choose a coordinate basis in which to evaluate dipole matrix elements and is not immediately transparent as to its dependence on polarization. We will remedy this by "factoring out" an angular dependence, such that the final expression separates into something that depends only on polarization and something that depends only on *radial* atomic structure (which can be obtained from atomic data references, see Sec. 2.3.2).

The strategy will be to decompose $\alpha_{\mu\nu}$ into spherical tensor components. A rank-2 *Cartesian* tensor such as $\alpha_{\mu\nu}$ can be decomposed into rank-0,1, and 2 *spherical* tensors known as the *scalar, vector*, and *tensor* components, respectively.

We will denote with Greek letters the parts of a state vector that refer to all but the magnetic sub-level. That is, the full state can be specified by $|\beta\ m_J\rangle$, where $m_J$ is the magnetic quantum number.

The *Wigner-Eckart theorem* allows us to decompose the dipole matrix element between two states $|\beta\ m_J\rangle$ and $|\beta'\ m'_J\rangle$ with respective total angular momentum* quantum numbers $J$ and $J'$ as:

$$\langle \beta\ m_J | d_q | \beta'\ m'_J \rangle = \frac{1}{\sqrt{2J+1}} \langle \beta || d || \beta' \rangle \langle J\ m_J | J'\ m'_J; 1\ q \rangle \tag{2.22}$$

Here, $\langle J\ m_J | J'_\beta\ m'_J; 1\ q\rangle$ is a Clebsch-Gordan coefficient and $q \in \{-1, 0, 1\}$ is a spherical component index†. The quantity $\langle \beta || d || \beta' \rangle$ is called the *reduced dipole matrix element* (RDME), and is independent of polarization and quantization axis. The RDME is in principle computed by an integral between radial wavefunctions, and in practice determined experimentally (Sec. 2.3.2). Note that there is a difference in convention of definition of the RDME between this work and Ref. [90], where our definition has an additional factor of $\frac{1}{\sqrt{2J+1}}$ in the right-hand side of Eq. 2.22. This makes the RDME more symmetric in exchange of $\beta$ and $\beta'$, and also makes it consistent with our own work Ref. [89]. The final result for polarizabilities, however, will agree and the formulas for polarizabilities will be modified to ensure this.

Now we are ready to give the spherical tensor decomposition of $\alpha_{\mu\nu}$. We assume that $\alpha_{\mu\nu}$ is an operator defined on a degenerate manifold $|\beta\rangle$ of total angular momentum

*All discussions in this section apply equally to atoms with hyperfine structure; one just needs to substitute $J \to F$.

†We decompose $\vec{d}$ into spherical components $d_q$ such that $d_0 = d_z$ and $d_{\pm 1} = \mp(d_x \pm i d_y)/\sqrt{2}$.

quantum number $J$. We will again simply state the result and refer to Ref. [90] Chapter 7.7 for derivation:

$$\alpha_{\mu\nu} = \alpha_{\mathrm{s}}\delta_{\mu\nu} + \frac{i\alpha_{\mathrm{v}}}{J}\varepsilon_{\sigma\mu\nu}J_\sigma + \frac{\alpha_{\mathrm{t}}}{2J(2J-1)}\Big(3(J_\mu J_\nu + J_\nu J_\mu) - 2J(J+1)\delta_{\mu\nu}\Big) \quad (2.23)$$

where

$$\alpha_{\mathrm{s}} = \frac{2}{3(2J+1)}\sum_{\beta'}\frac{\omega_{\beta'\beta}|\langle\beta||d||\beta'\rangle|^2}{\hbar(\omega_{\beta'\beta}^2-\omega^2)} \quad (2.24)$$

$$\alpha_{\mathrm{v}} = \sqrt{\frac{6J}{(J+1)(2J+1)}}\sum_{\beta'}(-1)^{J+J'+1}\begin{Bmatrix}1 & 1 & 1\\ J & J & J'\end{Bmatrix}\frac{\omega_{\beta'\beta}|\langle\beta||d||\beta'\rangle|^2}{\hbar(\omega_{\beta'\beta}^2-\omega^2)} \quad (2.25)$$

$$\alpha_{\mathrm{t}} = \sqrt{\frac{40J(2J-1)}{3(J+1)(2J+1)(2J+3)}}\sum_{\beta'}(-1)^{J+J'}\begin{Bmatrix}1 & 1 & 2\\ J & J & J'\end{Bmatrix}\frac{\omega_{\beta'\beta}|\langle\beta||d||\beta'\rangle|^2}{\hbar(\omega_{\beta'\beta}^2-\omega^2)} \quad (2.26)$$

Here, $J_\nu$ is the unitless spin-$J$ operator along the $\nu$ direction, $\delta_{\mu\nu}$ is a Kronecker delta, $\varepsilon_{\sigma\mu\nu}$ is a Levi-Civita symbol, and $\begin{Bmatrix}\dots\end{Bmatrix}$ is a Wigner 6-$j$ symbol. The quantities $\alpha_{\mathrm{s}}$, $\alpha_{\mathrm{v}}$, and $\alpha_{\mathrm{t}}$ are known as the scalar, vector, and tensor polarizabilities, respectively. They are functions of the light frequency $\omega$ and are specific to each degenerate atomic manifold $|\beta\rangle$. Importantly, they do not depend on polarization of the light.

Finally, this allows us to write $H_d^{\mathrm{eff}}$ in the following coordinate-invariant form:

$$H_d^{\mathrm{eff}} = -\frac{I}{2c\varepsilon_0}\left(\alpha_{\mathrm{s}} + \frac{i\alpha_{\mathrm{v}}}{J}(\hat{\epsilon}^*\times\hat{\epsilon})\cdot\vec{J} + \frac{\alpha_{\mathrm{t}}}{2J(2J-1)}\Big(3\{\hat{\epsilon}\cdot\vec{J},\hat{\epsilon}^*\cdot\vec{J}\} - 2J(J+1)\Big)\right) \quad (2.27)$$

where $\{\cdot,\cdot\}$ is the anticommutator. Note that the cross product here is computed with the standard algorithm $(\vec{a}\times\vec{b})_\sigma = \sum_{\mu,\nu}\varepsilon_{\sigma\mu\nu}a_\mu b_\nu$, and no conjugation is implied.

It is often convenient to write the term proportional to the vector polarizability as that of an *effective magnetic field* $\vec{B}_{\mathrm{eff}}$ as its contribution to the Hamiltonian is identical to that of a real magnetic field (when restricted to the degenerate manifold in question). This can be done by defining

$$\vec{B}_{\mathrm{eff}}(\alpha_{\mathrm{v}}) \equiv -\frac{i\alpha_{\mathrm{v}}I}{2c\varepsilon_0\mu_{\mathrm{B}}g_J J}(\hat{\epsilon}^*\times\hat{\epsilon}) \quad (2.28)$$

where $\mu_{\mathrm{B}}$ is the Bohr magneton and $g_J$ is the Landé $g$-factor*. Then the part of $H_d^{\mathrm{eff}}$ proportional to $\alpha_{\mathrm{v}}$ can be written as $\mu_{\mathrm{B}}g_J\vec{B}_{\mathrm{eff}}(\alpha_{\mathrm{v}})\cdot\vec{J}$. This observation makes

*The Landé $g$-factor is $g_J = g_L\frac{J(J+1)-S(S+1)+L(L+1)}{2J(J+1)} + g_S\frac{J(J+1)+S(S+1)-L(L+1)}{2J(J+1)}$, where $g_L \approx 1$ is the orbital $g$-factor and $g_S \approx 2$ is the electron spin $g$-factor.

an intuitive connection between vector polarizability and magnetic fields. We note that $\vec{B}_{\text{eff}}$ can only be nonzero when the polarization is not linear; i.e. when it has a circular component. Note that, like a magnetic field, a circular polarization is anti-symmetric under time reversal.

$H_d^{\text{eff}}$ is directly proportional to the intensity. So, at a fixed polarization and for a particular eigenstate $|A\rangle$ of $H_d^{\text{eff}}$, it makes sense to speak of a single, *total* polarizability $\alpha_A$, such that the energy shift of the eigenstate is $\Delta\mathscr{E}_A = -\frac{1}{2c\varepsilon_0}\alpha_A I$. This energy shift is a *light shift*. A spatial gradient of such a shift (as would be produced by, e.g., a tweezer) produces a motional potential for an atom. As we will be trapping atoms in intensity *maxima*, negative shifts (and positive polarizabilities) will be needed to produce trapping potentials.

When $H_d^{\text{eff}}$ is diagonal in the angular momentum basis $|J\ m_J\rangle$, the vector part produces shifts proportional to $m_J$ (indeed, as a magnetic field does) while the tensor part produces shifts proportional to $m_J^2$ (as a DC electric field does). The scalar part shifts all sub-levels identically.

However, $H_d^{\text{eff}}$ is sometimes not diagonal in *any* angular momentum basis. For strictly elliptical polarization and finite tensor polarizability, there is in fact no choice of quantization axis for which $H_d^{\text{eff}}$ is diagonal in the angular momentum basis. Another way to say this is that, in such cases, there is no choice of $\hat{z}$ for which $[\vec{J}\cdot\hat{z}, H_d^{\text{eff}}] = 0$. To gain intuition as to why, note that an ellipse has no axis of rotational symmetry. When the polarization is linear or circular, a diagonal choice of $\hat{z}$ does exist, but other fields — such as an external magnetic field — may point in a different direction and make the total Hamiltonian again not diagonalizeable with angular momentum states. We will explore diagonalization of $H_d^{\text{eff}}$ and talk about subtleties of adding in magnetic fields in Sec. 2.3.3.

***Reduced dipole matrix elements***

Reduced dipole matrix elements are listed in various ways in the wider literature and it is often confusing to convert from one convention to the other. We will not give a comprehensive review of all of them here (the reader is pointed to Refs. [80] for more), but we will at least relate the RDME as defined in Eq. 2.22 to an unambiguous experimental quantity: the decay rate.

For an allowed transition $|\beta\rangle \leftrightarrow |\beta'\rangle$ where $|\beta'\rangle$ is higher in energy, there is generally some decay rate $\Gamma_{\beta'\to\beta}$ from $|\beta'\rangle$ to $|\beta\rangle$ (in NIST databases, $\Gamma_{\beta'\to\beta}$ is denoted by $A_{ki}$). Note that this decay rate does not depend on magnetic sub-level. Also, note that this may not be the *total* decay rate of $|\beta'\rangle$ if it decays to states other than $|\beta\rangle$. Then the squared RDME between the two states is given by:

$$|\langle\beta||d||\beta'\rangle|^2 = \frac{3\pi\varepsilon_0\hbar c^3}{\omega_{\beta'\beta}^3}(2J'+1)\Gamma_{\beta'\to\beta} \text{ [for } E_{\beta'} > E_\beta\text{]} \tag{2.29}$$

Like for Eq. 2.22, note that our convention has a factor of $(2J'+1)$ which is not found in some other conventions, e.g. in that of Ref. [90]. See App. D for further discussion on RDMEs in the context of Rydberg states, of particular interest being how RDMEs relate to radial wavefunctions.

### 2.3.3 Polarizability tuning

The wavelength of light is the most important factor in the polarizability of a state. Wavelengths tend to create positive polarizabilities (and trapping shifts) when they are red-detuned from nearby atomic transitions, and tend to create negative polarizabilities (and *anti*-trapping shifts) when they are blue-detuned from nearby transitions. Of particular interest are wavelengths that give the same shifts for two different states — these are so-called *magic* wavelengths.

However, commercially available high-power lasers may not always be available at the exact wavelength that gives a desired set of shifts. Furthermore, it might be necessary to dynamically tune the light shift of a state mid-experiment without having to tune a laser over many nanometers, which is usually the scale on which polarizabilities appreciably change. On the other hand, it may also be desirable to have light shifts that are *insensitive* to parameters that may have fluctuations or inhomogeneities. In either case, it is important to study how polarizability can be tuned by polarization and magnetic fields.

We will consider a beam propagating in the $+\hat{z}$ direction and assume that it has a constant complex unit polarization $\hat{\epsilon}$. This latter assumption breaks down slightly near the focal plane for high-NA systems (see App. C), but for most purposes this is unimportant. We will parametrize the polarization as

$$\hat{\epsilon}(\gamma) = \cos(\gamma)\hat{x} + i\sin(\gamma)\hat{y} \tag{2.30}$$

where $\gamma \in [-\frac{\pi}{4}, \frac{\pi}{4}]$ is an ellipticity parameter. Linear polarization (in $\hat{x}$) is given by $\gamma = 0$ and fully circular polarization is given by $\gamma = \pm\frac{\pi}{4}$, with opposite handedness for plus and minus. Note that this parametrization assumes that the polarization major axis is along $\hat{x}$, which is an arbitrary choice if we allow the external magnetic field $\vec{B}$ to have components in all directions, which we will.

The first observation to make is that we can relate the effective magnetic field $\vec{B}_{\text{eff}}$ (Eq. 2.28) to $\gamma$ as

$$\vec{B}_{\text{eff}} = \frac{\alpha_{\text{v}} I}{2c\varepsilon_0 \mu_{\text{B}} g_J J} \sin(2\gamma)\hat{z} \tag{2.31}$$

However, remember that $\vec{B}_{\text{eff}}$ is just a convenient way of writing the vector polarizability component already included in $H_d^{\text{eff}}$ and that it is not an effect in addition to it. We can write the full $H_d^{\text{eff}}$ in terms of $\gamma$ as

$$\begin{aligned} H_d^{\text{eff}}(\gamma) = -\frac{I}{2c\varepsilon_0}\Bigg(&\alpha_{\text{s}} + \frac{\alpha_{\text{v}}}{J}\sin(2\gamma)J_z \\ &+\frac{\alpha_{\text{t}}}{J(2J-1)}\Big(3\big(\cos^2(\gamma)J_x^2 + \sin^2(\gamma)J_y^2\big) - J(J+1)\Big)\Bigg) \end{aligned} \tag{2.32}$$

***Polarization ellipticity***

Here we will look at the eigenstates of $H_d^{\text{eff}}$ as a function of the ellipticity parameter $\gamma$. We see that $\vec{B}_{\text{eff}}$ is zero for linear polarization (Eq. 2.31), so the vector polarizability only matters when the polarization is not linear. For a manifold with no tensor polarizability, $\vec{B}_{\text{eff}}$ and the scalar polarizability are the end of the story and we would expect the magnetic sub-levels $|J\ m_J\rangle$ to shift with ellipticity as they would under the usual Zeeman shift [95].

For nonzero tensor polarizability, however, ellipticity has further effects [89, 96]. Here, we will show results only for $J = 1$ state manifolds. One reason for this is that $J = 1$ is the simplest case where all of the scalar, vector, and tensor polarizabilities are nonzero ($J = 0$ has only scalar polarizability while $J = 1/2$ has only scalar and vector), so it is the simplest fully non-trivial case. Another reason is that for Sr, the state for which this discussion will be most relevant is 5s5p $^3\text{P}_1$, which has $J = 1$.

In the absence of an external magnetic field, the eigenenergies of $H_d^{\text{eff}}$ for $J = 1$ are

given by

$$\mathscr{E}_{\mathrm{A}}(\gamma) = -\left(\alpha_{\mathrm{s}} - \tfrac{1}{2}\left(\alpha_{\mathrm{t}} + f(\gamma)\right)\right)\frac{I}{2c\varepsilon_0} \tag{2.33}$$

$$\mathscr{E}_{\mathrm{B}}(\gamma) = -\left(\alpha_{\mathrm{s}} - \tfrac{1}{2}\left(\alpha_{\mathrm{t}} - f(\gamma)\right)\right)\frac{I}{2c\varepsilon_0} \tag{2.34}$$

$$\mathscr{E}_{\mathrm{C}} = -(\alpha_{\mathrm{s}} + \alpha_{\mathrm{t}})\frac{I}{2c\varepsilon_0} \tag{2.35}$$

where

$$f(\gamma) = \mathrm{sgn}(\alpha_{\mathrm{t}})\sqrt{9\alpha_{\mathrm{t}}^2\cos^2(2\gamma) + 4\alpha_{\mathrm{v}}^2\sin^2(2\gamma)} \tag{2.36}$$

We see that one of the eigenenergies ($\mathscr{E}_{\mathrm{C}}$) is insensitive to polarization ellipticity. For linear polarization ($\gamma = 0$), the tensor polarizability splits $\mathscr{E}_{\mathrm{A}}$ from $\mathscr{E}_{\mathrm{B}}$ and $\mathscr{E}_{\mathrm{C}}$. For circular polarization ($\gamma = \pm\frac{\pi}{4}$), the tensor polarizability splits $\mathscr{E}_{\mathrm{C}}$ from $\mathscr{E}_{\mathrm{A}}$ and $\mathscr{E}_{\mathrm{B}}$, while the vector polarizability splits $\mathscr{E}_{\mathrm{A}}$ from $\mathscr{E}_{\mathrm{B}}$.

The polarization ellipticity is thus a potential knob for tuning light shifts. We can define $\alpha_{\mathrm{A,B,C}}(\gamma) \equiv -\mathscr{E}_{\mathrm{A,B,C}}(\gamma)/\frac{I}{2c\varepsilon_0}$ as the total polarizability of the corresponding eigenstate for the given ellipticity.

For finite $\alpha_{\mathrm{t}}$ and non-circular polarization, analytical formulas for the corresponding eigenstates are given by

$$|\mathrm{A}(\gamma)\rangle = \left(g_-(\gamma)|m_J^z = +1\rangle - |m_J^z = -1\rangle\right)/\left(g_-^2(\gamma) + 1\right)^{1/2} \tag{2.37}$$

$$|\mathrm{B}(\gamma)\rangle = \left(g_+(\gamma)|m_J^z = +1\rangle + |m_J^z = -1\rangle\right)/\left(g_+^2(\gamma) + 1\right)^{1/2} \tag{2.38}$$

$$|\mathrm{C}\rangle = |m_J^z = 0\rangle \tag{2.39}$$

where

$$g_\pm(\gamma) = \frac{f(\gamma) \pm 2\alpha_{\mathrm{v}}\sin(2\gamma)}{3\alpha_{\mathrm{t}}\cos(2\gamma)} \tag{2.40}$$

and $m_J^\mu$ is the magnetic quantum number projected in the $\mu$ direction. The $|\mathrm{C}\rangle = |m_j^z = 0\rangle$ eigenstate is independent of ellipticity similarly to its corresponding eigenvalue. Note that for strictly elliptical polarization and finite tensor polarizability, $|\mathrm{A}(\gamma)\rangle$ and $|\mathrm{B}(\gamma)\rangle$ are not eigenstates of angular momentum for any choice of quantization axis.

For circular polarization, or any polarization when $\alpha_{\mathrm{t}} = 0$, the eigenstates are

$$|\mathrm{A_{circ}}\rangle = |m_J^z = \pm 1\rangle \tag{2.41}$$

$$|\mathrm{B_{circ}}\rangle = |m_J^z = \mp 1\rangle \tag{2.42}$$

$$|\mathrm{C}\rangle = |m_J^z = 0\rangle \tag{2.43}$$

For linear polarization, $|B\rangle$ and $|C\rangle$ are degenerate, so we are free to rotate our eigenbasis in this subspace. Here, it will be most convenient to choose a quantization axis that is along the polarization ($\hat{x}$). For this choice — and with appropriate rotation in the degenerate subspace — our eigenstates are

$$|\mathrm{A}_{\mathrm{lin}}\rangle = |m_J^x = 0\rangle \tag{2.44}$$

$$|\mathrm{B}_{\mathrm{lin}}\rangle = |m_J^x = \pm 1\rangle \tag{2.45}$$

$$|\mathrm{C}_{\mathrm{lin}}\rangle = |m_J^x = \mp 1\rangle \tag{2.46}$$

***Competing magnetic and optical eigenstates***

In the presence of an external magnetic field $\vec{B}$, the optical plus magnetic Hamiltonian is $H = H_d^{\mathrm{eff}} + \mu_{\mathrm{B}} g_J \vec{B} \cdot \vec{J}$.

When the polarization is elliptical, or when the external magnetic field is not parallel to a linear polarization, or when the field is not in the $\hat{z}$ direction under circular polarization, the optical part and the magnetic part of the Hamiltonian generically do not commute. When this happens and the Zeeman shift from the field is weak compared to the maximum light shift, the eigenstates of the combined optical and magnetic Hamiltonian may change significantly between the outside of an optical beam (where the magnetic field dominates) and the center of that beam (where the light dominates). In this scenario, not only is the intensity changing, but the eigenstates themselves are changing with intensity. This effectively leads to a light shift that is not linear in the intensity, and may in fact change the *shape* of a trap. Similar effects will also be discussed in App. C.

We will henceforth assume that we work in a regime where optical and magnetic eigenstates are not competing, either because the optical and magnetic eigenstates align, or because the magnetic field is everywhere dominant.

***Dominant magnetic field***

Now we assume an external magnetic field $\vec{B} = B\hat{z}'$, where $\hat{z}'$ is arbitrary and $B$ is large enough to produce a shift that is significantly larger than the maximal light shift. In this case, we know *a priori* that the eigenstates are very nearly $|m_J^{z'} = 0, \pm 1\rangle$ everywhere, that they experience a Zeeman shift of $\Delta\mathscr{E}_{\mathrm{Z}} = \mu_{\mathrm{B}} g_J B m_J^{z'}$, and that optical mixing between them is negligible regardless of the polarization.

In this scenario, we are justified in computing light shifts by simply taking the expectation value $\Delta\mathscr{E}_{\rm ls}(m_J^{z'}) = \langle m_J^{z'}|H_d^{\rm eff}|m_J^{z'}\rangle$. Let us for brevity drop the $z'$ in the magnetic quantum number, define $\cos^2(\theta) = |\hat{\epsilon}\cdot\hat{z}'|^2$ and $\cos(\phi) = \hat{z}\cdot\hat{z}'$ where $\hat{z}$ is still the direction of propagation of the light. Then, we get the following light shifts:

$$\Delta\mathscr{E}_{\rm ls}(m_J) = -\Bigg(\alpha_{\rm s} - \frac{\alpha_{\rm v}}{J}\sin(2\gamma)\cos(\phi)m_J + \frac{\alpha_{\rm t}}{2J(2J-1)}\Big(3\big(\cos^2(\theta)(3m_J^2-2) - m_J^2 + 2\big) - 2J(J+1)\Big)\Bigg)\frac{I}{2c\varepsilon_0} \tag{2.47}$$

This expression varies with the direction of the magnetic field, but not with its magnitude. We stress again, however, that this is only valid when the eigenstates are known *a priori* to be angular momentum eigenstates in $\hat{z}'$, which happens in the limit of large magnetic field magnitude ($\Delta\mathscr{E}_{\rm Z} \gg \Delta\mathscr{E}_{\rm ls}$). If there is doubt about the magnitude of a field not being sufficient, then diagonalization of the combined optical plus magnetic Hamiltonian is recommended. Note that when the polarization is linear, the parameter $\theta$ can be interpreted as the angle between the polarization and the magnetic field. However, $\theta$ is defined even in the case of elliptical polarization where this geometric interpretation is not as well-defined.

### *Stability considerations*

Experimentally, it is ideal to work with conditions that not only achieve the desired light shifts, but are also robust to fluctuations in parameters. With this in mind, one finds practically that maintaining a constant polarization across various optics is challenging — especially for arrays of tweezers. In fact, it is ideal if the trapping light passes through a polarizing optic close to the entrance of the focusing objective. Therefore, tuning polarizability with ellipticity is not recommended for large arrays.

Tuning with a magnetic field [31, 97], when possible, does turn out to be more convenient as magnetic fields can easily be made homogeneous across the extent of a tweezer array (a few hundred microns). Furthermore, they are much easier to change on the fly, with settling times of milliseconds or less. When working in the regime of a dominant magnetic field, it is also most prudent to work with the $|m_J = 0\rangle$ state, as its energy is insensitive to fluctuations in the magnetic field magnitude. It is worth writing down the light shift explicitly for $|J = 1\ m_J = 0\rangle$

under a large field:

$$\Delta\mathscr{E}_{\mathrm{ls}}(J=1, m_J=0) = -\Big(\alpha_{\mathrm{s}} + \alpha_{\mathrm{t}}\big(1 - 3\cos^2(\theta)\big)\Big)\frac{I}{2c\varepsilon_0} \tag{2.48}$$

When $\theta = 0$, $\Delta\mathscr{E}_{\mathrm{ls}}(\theta = 0) = -(\alpha_{\mathrm{s}} - 2\alpha_{\mathrm{t}})\frac{I}{2c\varepsilon_0}$, and this is the same as $\mathscr{E}_{\mathrm{A}}$ of Eq. 2.33 at linear polarization. When $\theta = \frac{\pi}{2}$, $\Delta\mathscr{E}_{\mathrm{ls}}(\theta = \frac{\pi}{2}) = -(\alpha_{\mathrm{s}} + \alpha_{\mathrm{t}})\frac{I}{2c\varepsilon_0}$, and this is the same as $\mathscr{E}_{\mathrm{B}}$ of Eq. 2.34 at linear polarization and also the same as $\mathscr{E}_{\mathrm{C}}$ of Eq. 2.35 at any ellipticity.

Ideal insensitivity to polarization occurs for the $|m_J = 0\rangle$ state with a large magnetic field in the direction of propagation of the light (i.e. $\theta = \frac{\pi}{2}$, $\phi = 0$). Then, the light shift is insensitive* to both polarization direction and ellipticity. However, this configuration also precludes any field tunability, and if a magic condition is required, then the wavelength is the only knob available. Such a condition occurs for the red transition of Sr at 914 nm [98]. Another such condition is predicted to occur at 500.65(50) nm [89] (Sec. 2.3.4). However, to our knowledge, this latter wavelength has not been used for Sr trapping yet.

### 2.3.4 Polarizability in strontium

For Sr, the polarizabilities of the following states are of particular importance:

$5s^2\ {}^1S_0$: As this is the absolute ground state of Sr, the atom will be here "by default" and this state must of course be sufficiently trapped (i.e. sufficiently positive polarizability). As it is $J = 0$, only a scalar contribution will enter.

$5s5p\ {}^3P_1$: Cooling will be done by driving to this state on the red transition. We will see in Sec. 2.5 that the polarizability of this state relative to that of absolute ground state has important implications for cooling. In fact, most of the discussion of light shift tunability so far has been with this state in mind.

$5s5p\ {}^3P_0$: This is the clock state, and for coherently driving the ultra-narrow clock transition it is important that the light shift of this state is equal to that of the absolute ground state. This state also only has a scalar contribution; however, with ultra-narrow spectroscopy, it is in fact possible to resolve *hyperpolarizability* effects on this state, which are fourth-order in perturbation theory. These are beyond the scope of this section and will be discussed more in Sec. 3.1.2.

*However, it is sensitive to drifts or inhomogeneities of the *field* direction or of the direction of trap light propagation, but these are easier to control. Ultimately, there is no configuration that is 100% robust to everything.

5s5p $^3P_2$: This is another metastable state. While its exact polarizability is not hugely important, it is important for it to be sufficiently trapped as the atom will often have to occupy this state.

5s4d $^1D_2$: This is a long-lived (few hundred $\mu$s) state which is a weak decay channel for the blue transition. We will see in Sec. 2.6 that it is important for it to be trapped in order to achieve high-survival imaging. This consideration unfortunately is incompatible with the convenient trapping wavelengths 515 nm and 532 nm.

5s5p $^1P_1$: This is the excited state which we will use for imaging. Its polarizability is ultimately not too important — even if it is anti-trapped — because its lifetime is very short (few ns). However, it is useful to know its polarizability relative to the ground state so as to know how the trap shifts the blue transition.

5s6s $^3S_1$: This is the excited state which we will use for pumping atoms between the 5s5p $^3P_J$ triplet states. Its polarizability is also not hugely important due to its short lifetime, but may play a role in heating during pumping. It is also useful to know how the trap shifts the various repump transitions.

We will examine polarizabilities of Sr near the trapping wavelengths 515 nm and 813 nm, which are the two wavelengths used in this work. We will focus particularly on the states involved in the red cooling transition, but we will mention other polarizabilities as well. We will also note other wavelengths of interest, such as 500 nm, 532 nm, 914 nm, 1030 nm, and 1064 nm, where appropriate. App. B discusses the data sources and methodology of our calculations.

***Near 515 nm***

515 nm is an interesting wavelength for trapping Sr because it is available at high power (~10 W) and is also power efficient due to being a relatively short wavelength (leading to a tight tweezer waist) and having large ground state polarizability. Furthermore, it offers transitions to both more weakly and more strongly trapped sub-levels of 5s5p $^3P_1$. If desired, 515 nm traps can also be tuned to a magic condition for the red transition with polarization [89] or fields [97]. However, we will see here and in Sec. 2.6 that 515 nm tweezers have unavoidable issues that lead to atom loss at the percent level during imaging. Finally, 515 nm is not magic for the clock transition (and cannot be made so), so highly coherent clock operation with 515 nm traps is ruled out — however, see Ref. [99] for a hybrid 515 nm and 813.4 nm system.

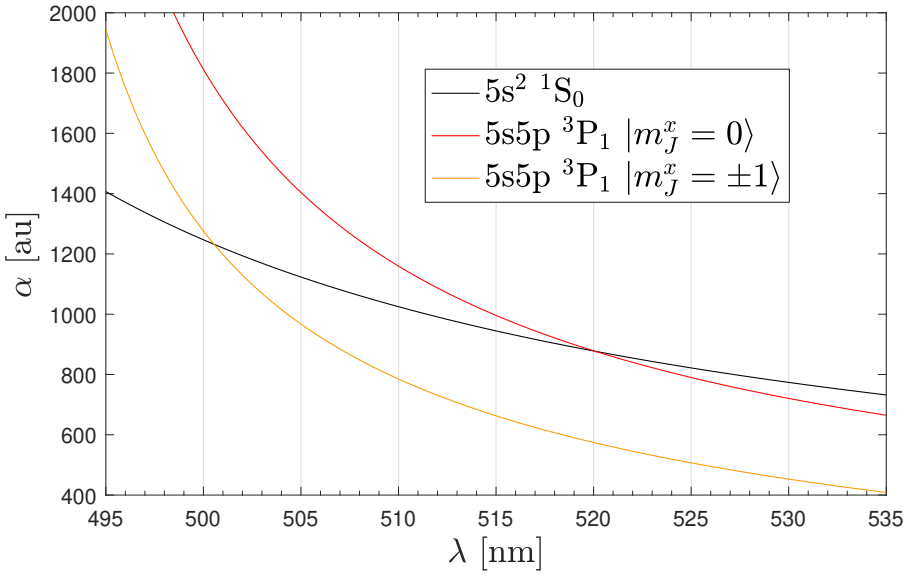


Figure 2.4: Total polarizabilities near 515 nm for the states involved in the red transition at zero magnetic field and linear polarization along $\hat{x}$, which is taken to be the quantization axis. Magic wavelengths are predicted — but have not been observed — at 500.65(50) nm and 520(2) nm [89].

We first look at the polarizabilities of the states involved in the red transition: $5s^2\ {}^1S_0$ and $5s5p\ {}^3P_1$, shown in Fig. 2.4 for linear polarization. We see that our modified sum-over-states model (App. B) closely reproduces the magic wavelengths predicted at 500.65(50) nm and 520(2) nm in Ref. [89].

One of the main problems with 515 nm is the polarizability of the $5s4d\ {}^1D_2$ state, which is populated via a small branching ratio decay of $5s5p\ {}^1P_1$. It unfortunately turns out that 515 nm is *very* close to a transition of that state, particularly the $5s4d\ {}^1D_2 \leftrightarrow 5s4f\ {}^1F_3$ transition at 515.75 nm. This makes the $5s4d\ {}^1D_2$ state have large divergences in its polarizability at this wavelength, the implications of which will be discussed in Sec. 2.6.8. Coincidentally, the same problem occurs near 532 nm, another convenient high power wavelength: the $5s4d\ {}^1D_2 \leftrightarrow 5s7p\ {}^1P_1$ transition occurs at 533.13 nm. These divergences are illustrated in Fig. 2.5.

We summarize the polarizabilities of these and other relevant states at 515.2 nm in Table 2.1.

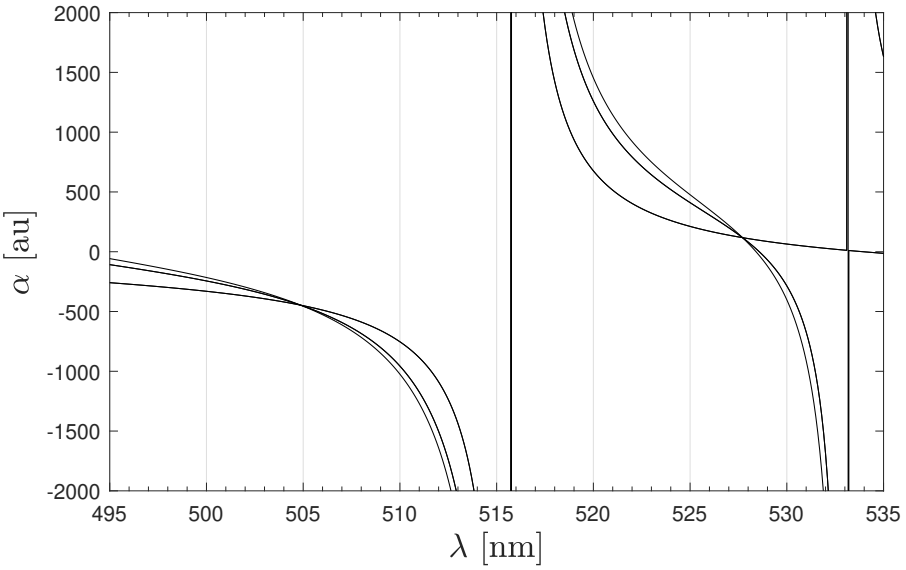


Figure 2.5: Total polarizabilities near 515 nm for the various 5s4d $^1D_2$ sub-states at zero magnetic field and linear polarization. Note the divergences at the transition wavelengths of 515.75 nm and 533.13 nm.

| State | $\lvert m_J^x \rvert$ | Total polarizability @ 515.2 nm [au] |
|---|---|---|
| $5s^2\ ^1S_0$ | 0 | 941.8 |
| 5s5p $^3P_0$ | 0 | 656.2 |
| 5s5p $^3P_1$ | 0 | 990.4 |
| | 1 | 658.9 |
| 5s5p $^3P_2$ | 0 | 607.9 |
| | 1 | 728.6 |
| | 2 | 1091 |
| 5s4d $^1D_2$ | 0 | $-1.166 \times 10^4$ |
| | 1 | $-1.041 \times 10^4$ |
| | 2 | -6644 |
| 5s5p $^1P_1$ | 0 | -1335 |
| | 1 | -302.6 |
| 5s6s $^3S_1$ | 0 | 160.2 |
| | 1 | 158.0 |

Table 2.1: Summary of polarizabilities at 515.2 nm, linear polarization in $\hat{x}$, and zero magnetic field. Calculation methodology follows that described in App. B and Table. B.1.

***Near 813 nm and beyond***

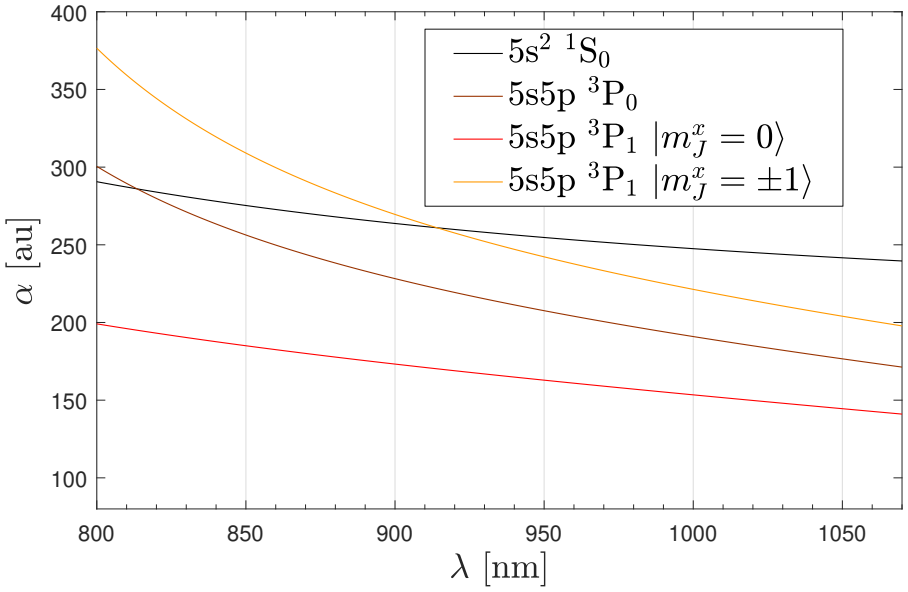


Figure 2.6: Total polarizabilities near and beyond 813 nm for the states involved in the clock and red transitions at zero magnetic field and linear polarization along $\hat{x}$, which is taken to be the quantization axis. The magic wavelength for the clock transition is at 813.4 nm [88]. There is also a magic wavelength for the red transition at 914 nm [98].

813.4 nm is particularly interesting for one key reason: it is a magic wavelength for the clock transition. It is usually generated by titanium sapphire (Ti:sapph) lasers with a typical maximum output power of 6 W. We will see that the ground state polarizability at 813 nm is about 30% of that at 515 nm. Combined with the longer wavelength (leading to less tight tweezer waist), one can expect overall only about 12% of the trap depth for an equivalent power at 813 nm as compared to 515 nm. Nevertheless, 813 nm turns out to be a particularly good wavelength for Sr trapping for many reasons (Sec. 2.6.8), beyond just its clock magic property. One of these is the fact that 5s4d $^1$D$_2$ and practically all states except the short-lived 5s6s $^3$S$_1$ are trapped.

The polarizabilities of the states involved in the clock and red transitions are plotted in Fig. 2.6 for linear polarization. We summarize the polarizabilities of these and other relevant states at 813.4 nm in Table 2.2.

We plot polarizabilities going well beyond 813 nm up to 1070 nm for a couple of reasons. One is that we would like to highlight the magic wavelength for the red

transition at 914 nm [98], which is similar to the one predicted at 500 nm in that it is valid for all polarization ellipticities. The other reason is that high power (>100 W) lasers exist at 1030 nm as well as 1064 nm, and these may be good alternatives to 813 nm if its clock magic nature is not required. At 1064 nm, the ground state polarizability is ×0.84 that at 813.4 nm. Another factor of about 0.58 is lost due to the larger waist, leading to a total loss of trap depth of ×0.49. However, power availability at 1064 nm should more than make up for this. No transitions exist between 813 nm and 1064 nm for all relevant states, so no divergences exist in the polarizabilities in this range and all states that are trapped at one wavelength are also trapped at the other. However, all 5s5p $^3P_1$ sub-levels have lower polarizabilities than that of 5s$^2$ $^1S_0$ at all wavelengths beyond 914 nm for linear polarization (Fig. 2.6). This may have unfavorable implications for cooling (Sec. 2.5.2). However, it is also possible with ellipticity to make one sub-level of 5s5p $^3P_1$ attain an equal (magic) or larger polarizability than that of 5s$^2$ $^1S_0$ at 1064 nm (Fig. 2.8), which could remedy this situation if it is found to be unfavorable.

| State | $\lvert m_J^x \rvert$ | Total polarizability @ 813.4 nm [au] |
|---|---|---|
| 5s$^2$ $^1S_0$ | 0 | 286.0 |
| 5s5p $^3P_0$ | 0 | 286.0 |
| 5s5p $^3P_1$ | 0 | 195.1 |
| | 1 | 353.9 |
| 5s5p $^3P_2$ | 0 | 464.3 |
| | 1 | 391.6 |
| | 2 | 173.8 |
| 5s4d $^1D_2$ | 0 | 256.8 |
| | 1 | 522.2 |
| | 2 | 1318 |
| 5s5p $^1P_1$ | 0 | 708.4 |
| | 1 | 737.8 |
| 5s6s $^3S_1$ | 0 | -494.1 |
| | 1 | -481.9 |

Table 2.2: Summary of polarizabilities at 813.4 nm, linear polarization in $\hat{x}$, and zero magnetic field. Calculation methodology follows that described in App. B and Table. B.1.

### *Tunability of* 5s5p $^3P_1$

The red transition 5s$^2$ $^1S_0 \leftrightarrow$ 5s5p $^3P_1$ has a particularly narrow linewidth of 7.5 kHz. Trap light shifts are usually larger than this, so a *differential* polarizability between

these two states can usually be well-resolved. It is often useful (e.g. for spectroscopy) to work with zero differential polarizability (i.e. magic conditions). Furthermore, the differential polarizability between the states of the red transition has qualitative consequences for cooling (Sec. 2.5). Therefore, the tunability of differential polarizability of the red transition is of particular importance. While $5s^2\ {}^1S_0$ has no angular structure and no tunability besides with wavelength, the polarizability of $5s5p\ {}^3P_1$ can be tuned with either ellipticity or field.

A large component of the studies in Ref. [89] was the dependence of the polarizability of $5s5p\ {}^3P_1$ on polarization ellipticity. Although we ultimately found such tunability inferior to magnetic tuning for tweezer arrays (Sec. 2.3.3), it is still instructive to understand how it works. Furthermore, we will see that there are situations where ellipticity offers tunability that a magnetic field does not and vice-versa. Fig. 2.7 plots the polarizabilities of the states in the red transition near 515 nm under the magic ellipticity angle for 515.2 nm and zero field. A large range of wavelengths between the two linearly polarized magic wavelengths can be made magic by ellipticity tuning (though not quite the entire range). Fig. 2.8 plots the polarizabilities of the states in the clock and red transitions near 813 nm and beyond under *circular* polarization and zero field. We see that here ellipticity actually gives one of the sub-states *larger* polarizability, making it have a larger polarizability than the ground state for wavelengths at least up to 1070 nm.

Tunability with ellipticity and field is plotted in Fig. 2.9 at 515.2 nm and 813.4 nm. We see that polarizabilities at one wavelength shift in the opposite direction as compared to those at the other wavelength. While a magic ellipticity exists at zero field for the red transition at 515.2 nm, one does not exist at 813.4 nm. However, a magic *field* angle exists for both. Generally, a field angle can tune the polarizability of the $|m_J = 0\rangle$ state (with quantization axis defined by the field, assumed to be dominant) anywhere from the polarizability of the $|m_J^x = 0\rangle$ state up to that of the $|m_J^x = \pm 1\rangle$ states (for zero field and linear polarization in $\hat{x}$). At 1030 nm and 1064 nm, there are no magic field angles for $|m_J = 0\rangle$, but there are magic ellipticities at zero field.

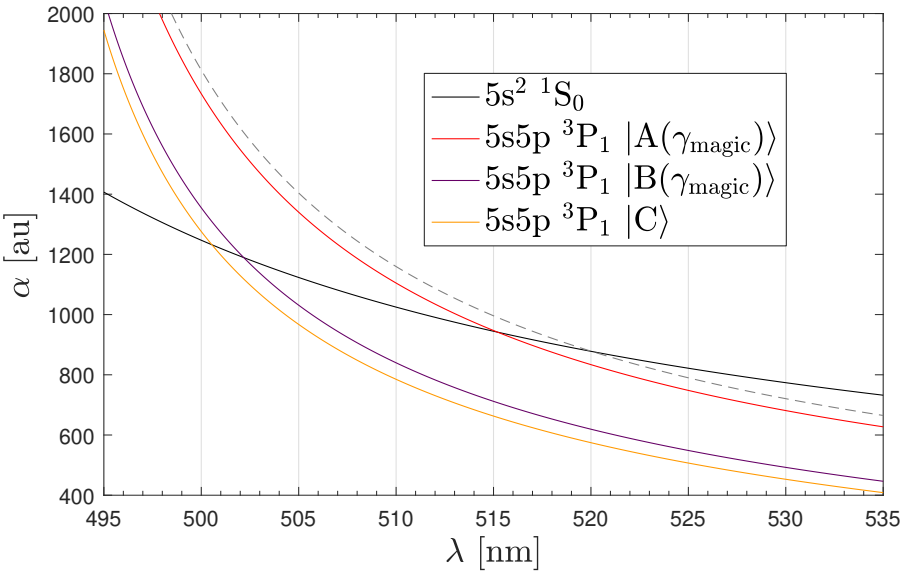


Figure 2.7: Total polarizabilities near 515 nm for the states involved in the red transition at zero magnetic field and at the magic polarization ellipticity for 515.2 nm. Eigenstates for this configuration are not all angular momentum eigenstates, so we label states with letters as in Eqns. 2.37-2.39. Note the splitting of the previously degenerate B and C states, where the C state is insensitive to ellipticity. The grey dashed line represents the polarizability of the $|m_J^x = 0\rangle$ state under linear polarization, as in Fig. 2.4.

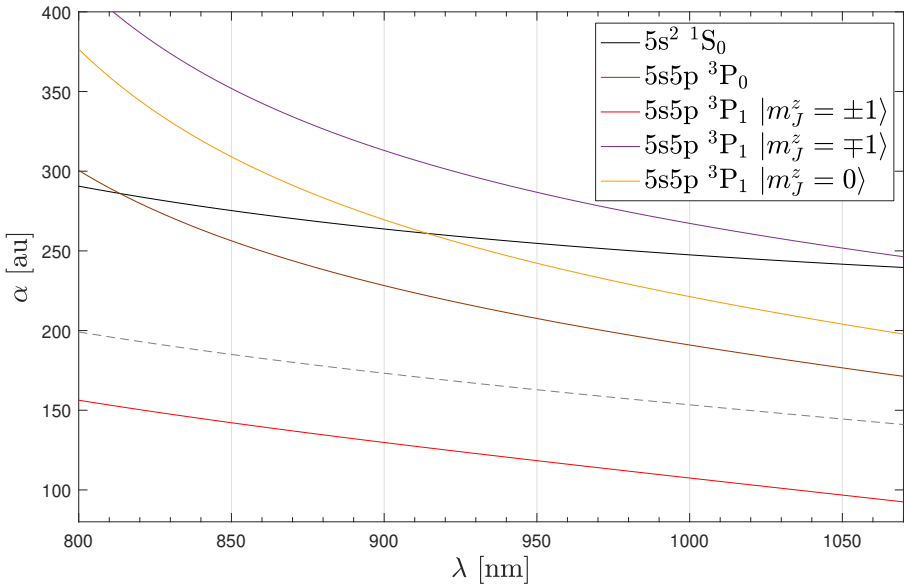


Figure 2.8: Total polarizabilities near and beyond 813 nm for the states involved in the clock and red transitions at zero magnetic field and *circular* polarization ($\gamma = 45°$), showing the full range of tunability. Here, the quantization axis is the direction of propagation $\hat{z}$. The grey dashed line represents the polarizability of the $|m_J^x = 0\rangle$ state under linear polarization, as in Fig. 2.6.

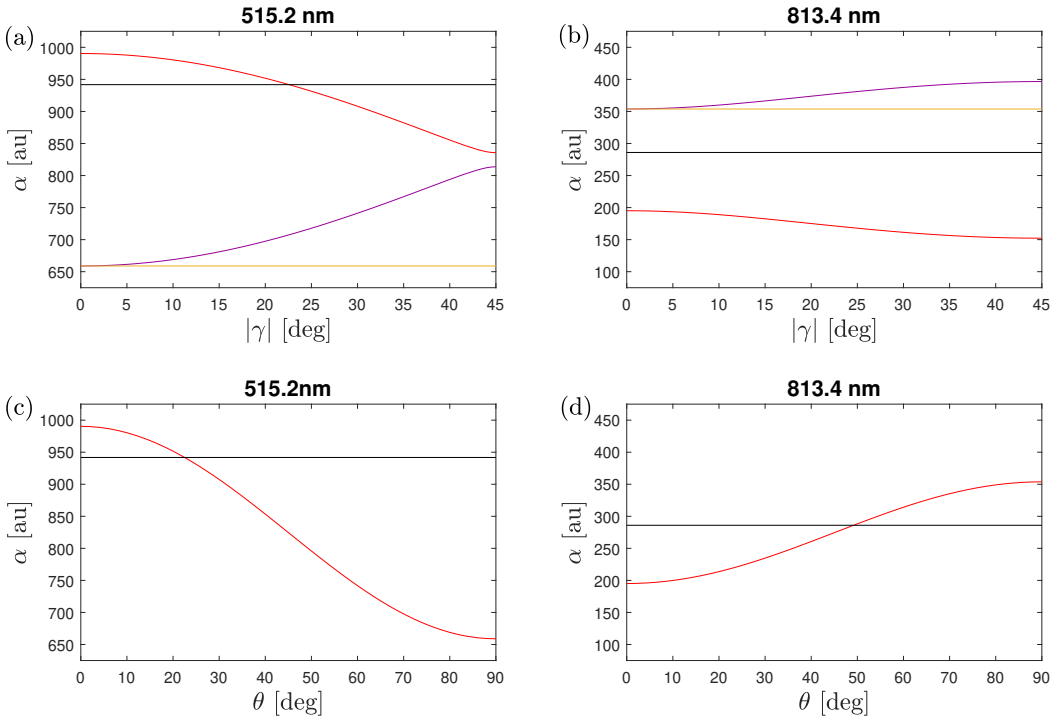


Figure 2.9: Tunability of polarizabilities involved in the red transition with ellipticity and magnetic field direction. **(a,b)** Total polarizabilities of $5s^2\ {}^1S_0$ (black) and all sub-states of $5s5p\ {}^3P_1$ (various colors) as a function of absolute ellipticity parameter $|\gamma|$ at zero magnetic field at (a) 515.2 nm and (b) 813.4 nm. The color scheme is consistent with that used in Figs. 2.7 & 2.8. We see that for 515.2 nm, a magic condition is computed at $|\gamma| = 22.6°$ (measured as $|\gamma| = 24°$ [89]). However, no such condition exists for 813.4 nm. **(c,d)** Total polarizabilities of $5s^2\ {}^1S_0$ (black) and $5s5p\ {}^3P_1\ |m_J = 0\rangle$ (red) under a dominant magnetic field that defines the quantization axis at (c) 515.2 nm and (d) 813.4 nm. $\theta$ is the parameter from Eq. 2.47 which can be interpreted as the angle between field and polarization in case of linear polarization. A magic angle is computed at 22.5° for 515.2 nm (measured as 24(1)° for 515.13 nm [97]). A magic angle is computed at 49.2° for 813.4 nm (measured as 49° [100]).

## 2.4 Preparing single atoms

A key feature of optical tweezer platforms is the ability to isolate only one atom per tweezer. Not having to worry about short-range collisional or molecular interactions or hopping from site to site makes the relevant physics relatively "clean." Furthermore, having one atom per site makes natural the treatment of tweezer arrays as qubit registers (in a fashion similar to ion chains).

First, we will describe the loading of multiple atoms from a Sr red MOT into tweezers (Sec. 2.4.1). Then, we will describe a technique for inducing pairwise loss such that tweezers end up loaded with either one or zero atoms (Sec. 2.4.2). From here, defect-free arrays can be assembled via rearrangement (Sec. 2.7.3). We will conclude with some potential techniques for beating the standard 50% filling fraction limit of pairwise loss (Sec. 2.4.3).

### 2.4.1 Loading multiple atoms from a MOT

We load atoms into tweezers from the "red" MOT of Sr, which is usually generated as a second-stage MOT after a larger, hotter, and less dense "blue" MOT. The techniques for generating these MOTs are well established and we point the reader to Refs. [20, 23] for a further discussion on the preparation and subtleties of a Sr red MOT.

#### *Thermal considerations*

It is illuminating to estimate the number of atoms in a MOT that end up within the trapped phase space of a tweezer if the tweezer is instantaneously turned on. While in principle any atom with negative motional energy will be trapped, it is sensible to require a more stringent condition for trapping that will allow us to consider only deeply trapped atoms localized close to the center of the tweezer. We will consider only points in phase space with an energy below $-(1-\kappa)U_0$ where $U_0$ is the (positive) trap depth and $\kappa$ is a cutoff parameter.

Considering the classical Hamiltonian $H(r,z,p) = \frac{p^2}{2m} + U(r,z)$ with $U(r,z)$ being the tweezer potential from Eq. 2.15, we get the following bounds on the phase space

variables for a cutoff parameter $\kappa$:

$$p_{\max} = \sqrt{2mU_0\kappa} \tag{2.49}$$

$$z_{\max}(p) = z_R\sqrt{\frac{p_{\max}^2}{\kappa p^2 + (1-\kappa)p_{\max}^2} - 1} \tag{2.50}$$

$$r_{\max}(p,z) = w_0\sqrt{\tfrac{1}{2}(1+z^2/z_R^2)\ln\left(\frac{1+z_{\max}^2(p)/z_R^2}{1+z^2/z_R^2}\right)} \tag{2.51}$$

We will assume that the momentum distribution in the MOT is thermal with a temperature $T_M$. We will further assume that the cutoff $\kappa$ is chosen sufficiently small such that the tweezer volume is small as compared to the scale of density variations of the MOT, such that we can assume that its atom number density is a constant denoted by $n(T_M)$. This is possible for a wide range of cutoff parameters as the length scale of a tweezer is on the order of 1 $\mu$m or smaller, whereas a MOT typically has a size of $> 100$ $\mu$m. We do not provide an explicit functional form of $n(T_M)$ as the dependence on $T_M$ may be nontrivial — we only assume that $n(T_M)$ has been experimentally determined at the temperature(s) of interest. Then the number of atoms within the cut-off phase space upon instantaneous turn-on of the tweezer is

$$N^{\text{inst}} = \frac{8\pi^2 n(T_M)}{(2\pi m k_{\text{B}} T_M)^{3/2}}\int_0^{p_{\max}} dp\; p^2 \exp\left(\frac{-p^2}{2mk_{\text{B}}T_M}\right)\int_0^{z_{\max}(p)} dz\; r_{\max}^2(p,z) \tag{2.52}$$

This formula is not analytically tractable, but can be evaluated numerically. We will assume "typical" tweezer parameters of $U_0 = k_{\text{B}} \times 500$ $\mu$K, $w_0 = 800$ nm, and $z_R = 2.5$ $\mu$m, and choose our cutoff to be $\kappa = 1/2$. For the Sr red MOT, a typical temperature and density are $T_M = 1$ $\mu$K and $n = 10^{11}$ cm$^{-3}$. We can evaluate Eq. 2.52 directly at these parameters to get $N^{\text{inst}} \sim 0.25$.

Another approach would be to note that $T_M \ll \kappa U_0$, in which case we can work in the $T_M \to 0$ limit. Here, we essentially evaluate $N^{\text{inst}}$ by multiplying the MOT density by the cut-off volume of the tweezer. We obtain

$$\begin{aligned} N_{T_M\to 0}^{\text{inst}} =& 2\pi n(0)\int_0^{z_{\max}(0)} dz\; r_{\max}^2(0,z) \\ =& \frac{2\pi}{9}w_0^2 z_R\left(\left(\frac{\kappa}{1-\kappa}\right)^{3/2} + 6\left(\frac{\kappa}{1-\kappa}\right)^{1/2} - 6\arctan\left(\left(\frac{\kappa}{1-\kappa}\right)^{1/2}\right)\right)n(0) \qquad (2.53) \\ \to& \frac{(14-3\pi)\pi}{9}w_0^2 z_R n(0)\ \text{[for } \kappa \to 1/2\text{]} \qquad (2.54) \end{aligned}$$

Note that $N_{T_M\to 0}^{\text{inst}}/n(0)$ is simply the volume of space in a tweezer with a potential energy less than $-(1-\kappa)U_0$. Evaluating Eq. 2.54 at the parameters listed above indeed gives a very similar answer of $N_{T_M\to 0}^{\text{inst}} \sim 0.26$.

These numbers, although non-negligible, are much smaller than what can be achieved if atoms are made to *thermalize* in the tweezer potential. Perhaps the most important thermalization mechanism is laser cooling in the trap, which we will discuss shortly. Collisional thermalization between atoms in the tweezers and atoms in the MOT is in principle also possible, though could be slow for $^{88}$Sr given its small ground state scattering length. However, Ref. [101] used collisional thermalization between atoms in a light-shifted optical trap and atoms in a red MOT to achieve a $^{84}$Sr BEC. Adiabatic turn-on of the tweezer may also lead to thermalization, but we have never found this to be necessary or beneficial.

Regardless of the thermalization mechanism, let us suppose it happens and that it results in a temperature $T_t$ inside the tweezer. Assuming no atom-atom interactions, such thermalization can be accounted for by modifying the formerly spatially constant density $n(T_M)$ by a Boltzmann factor from the tweezer potential, such that the density in the tweezer is now $e^{-\frac{U(r,z)}{k_B T_t}} n(T_M)$. We will eventually show that the red transition leads to tweezer temperatures similar to those in a red MOT, such that $T_t$ can be assumed to be on an order similar to $T_M$. As tweezers can easily be made much deeper than these temperatures ($U_0 \sim$ 100's of $\mu$K and beyond), we see that this Boltzmann factor can easily be made enormous — so large as to essentially load all atoms of the MOT into the tweezer.

This is of course not a guarantee that thermalization will happen, as many things can prevent thermalization or make it too slow. One of these, as previously mentioned, is differential light shifts due to the trap that can detune the cooling transition. More generally, effects from the trap such as motional sidebands may qualitatively change the cooling mechanism. Finally, the very high densities achievable in a tweezer make atom-atom collisions and interactions highly non-negligible.

For the first two potential problems mentioned above, several solutions are possible. One is to work with a magic condition on the red transition such that differential light shifts are nullified. Another is to work with traps shallow enough such that light shifts are small. This also mitigates worries about cooling mechanisms being qualitatively different. We have empirically found that the most efficient loading from a red MOT into $\lambda = 813.4$ nm tweezers, without using any additional beams or detunings not already used for the MOT, occurs at about $U_0 \sim 30$ $\mu$K. Here, radial motional sidebands are at $\omega_r \sim 2\pi \times 20$ kHz and light shifts are approximated to be 170 kHz (though it is unclear how the magnetic gradient of the MOT affects these shifts). A final strategy, if loading into deeper traps, is to use a separate beam (one

is usually sufficient) detuned to an appropriate tweezer cooling frequency. We have found all of these strategies to work well and ultimately find loading into tweezers to be robust (assuming good MOT-tweezer overlap, see Sec. 2.4.1) even for small MOT atom numbers.

As to atom-atom collisions and interactions, these likely eventually limit the number of atoms that can be loaded into a trap. However, these are also the same mechanisms that we will exploit to prepare single atoms, so their presence is overall welcome. At least for $^{88}$Sr, we have found that numerous (see Sec. 2.4.1 for discussion on a lower bound for such a number) atoms can be loaded into a tweezer simultaneously for practically any tweezer parameters that we have used ($\lambda = 515.2$ nm at $U_0 = 1.4$ mK and $\lambda = 813.4$ nm at $U_0$ as low as 30 $\mu$K to as high as 500 $\mu$K).

***Overlapping tweezers with a red MOT***

The low temperature and high density of a red MOT allows for efficient loading into shallow tweezers. However, the red MOT is also only a few 100's of $\mu$m in size and must be well-aligned with the center of optical tweezers. This requirement becomes even more stringent when an array of tweezers is used, which can have a size of a similar length scale.

The best way to achieve and maintain alignment (after coarse alignment with optics) is to use an externally applied magnetic field that can be tuned along all three spatial dimensions. The magnetic quadrupole gradient used for the red MOT is usually on the order of $\partial B \sim 3$ G/cm or less (along the strong direction of the quadrupole, 1/2 as strong in the other two orthogonal directions). As the red MOT is centered at the zero of the quadrupole field, applying an external field will shift the zero of the quadrupole and thus the position of the red MOT. The magnitude of the gradient $\partial B$ determines the sensitivity of the position to an external field and therefore the level of field stability required. If a spatial stability of $\delta x$ is desired, a field stability of $\delta B = \partial B \, \delta x$ is required. For $\delta x = 10\mu$m and $\partial B = 3$ G/cm, a field stability of $\delta B = 3$ mG should be ensured. With appropriate magnetic coils (see App. A.2), this is easily achievable with commercially available current sources. Furthermore, a dynamic range of at least 10 G should still be possible at these levels of stability, allowing for position tuning of the red MOT up to ~3 cm, well beyond what is usually required.

***Experimental results & atom number estimates***

We find that atoms are robustly loaded into tweezers for a wide range of trapping parameters. The presence of atoms in tweezers is determined by fluorescence imaging, which will be thoroughly discussed in Sec. 2.6 and is only briefly summarized here. In short, a trap is determined as occupied when the signal at its position on the camera image surpasses some threshold, which is chosen to be sufficiently above some background level (Sec. 2.6.6).

One may expect that the number of atoms in a trap can be measured by the magnitude of the signal detected on a camera. While correlation between signal and atom number is likely, we have found that peaks in the signal histogram from different atom numbers are generally not well-resolved, likely due to the effects of light-induced pairwise loss (Sec. 2.4.2) or other multi-body loss effects. Therefore, the only reliable conclusion that we make from a single image is binary: the trap is either occupied (with one or more atom) or not.

Nonetheless, we are able to put a lower bound on the average number of loaded atoms via an assumption on the loading statistics. This assumption is that the number of atoms that are loaded from the MOT into a tweezer follows a Poisson distribution [33] — at least before any multi-body loss takes effect. For a Poisson distribution of mean atom number $\bar{N}$, the probability of loading zero atoms is $P(0) = e^{-\bar{N}}$. Experimentally, the fraction of images determined to contain an unoccupied tweezer give an upper bound on $P(0)$ (so long as false positives are not significant). This measurement is generally an upper bound on $P(0)$ as multiple atoms can be rapidly lost before they scatter enough photons to be imaged. Via this upper bound on $P(0)$, we get a *lower* bound on the mean occupation number via $\bar{N} = -\ln\big(P(0)\big)$. In Ref. [89], which used $\lambda = 515.2$ nm and 1.4 mK deep tweezers, we reported $P(0) < 5 \times 10^{-4}$. This placed a lower bound of $\bar{N} > 7.6$. Finally, we will see in Sec. 2.4.2 that the filling fraction observed *after* pairwise loss can also be used as an estimate of a lower bound for $\bar{N}$.

## 2.4.2 Pairwise loss

Our ultimate goal is to prepare one atom per tweezer. One strategy for this might be to fine-tune the density of the red MOT or some other loading parameter such as to maximize the probability of loading only one atom. While this is possible, weakly-interacting atoms fill traps stochastically, usually following a Poisson dis-

tribution [33]. The maximum possible probability of loading a single atom under Poissonian statistics is only about 37% (occurring at a mean atom number of $\bar{N} = 1$). For the rest of the tweezers, 37% would be empty and 26% would be loaded with multiple atoms.

A more robust way of preparing single atoms is to initially fill tweezers with many atoms and from there eliminate excess atoms. An ideal mechanism would expel atoms one-by-one, but stop as soon as only one atom is left. While such schemes have been realized to some extent in alkali atoms [102–105] and will be speculated upon for Sr in Sec. 2.4.3, they involve a high degree of fine-tuning.

A mechanism which instead is most ubiquitously found in single-atom physics is *pairwise loss* [33, 39, 48, 106, 107]. Pairwise loss is the simultaneous loss of pairs of atoms, such that $N \rightarrow (N-2)$. One can therefore see that the ultimate result of pairwise loss is $N_f = N_i \bmod 2$, where the subscripts stand for "final" or "initial". In other words, odd initial atom numbers end up at one, and even initial atom numbers end up at zero. This is why the end result of pairwise loss is also sometimes called *parity projection*.

The average number of atoms remaining at the end of pairwise loss is therefore $\bar{N}_f = p_i^{\text{odd}}$, where $p_i^{\text{odd}}$ is the probability of initially having an odd number of atoms. Assuming $N_i$ follows Poissonian statistics, this becomes

$$\bar{N}_f = \tfrac{1}{2}(1 - e^{-2\bar{N}_i}) \tag{2.55}$$

This tends to $\frac{1}{2}$ for increasing values of $\bar{N}_i$, and already for $\bar{N}_i = 4$ there is only a $1.7 \times 10^{-4}$ difference from $\bar{N}_f = \frac{1}{2}$. By inverting this equation, one can also estimate $\bar{N}_i$ (realistically, for values of $\bar{N}_f$ close to 0.5, this would give a lower bound limited by the statistical error of the measurement).

In the context of a tweezer array, pairwise loss in the large $\bar{N}_i$ regime means each trap will have a probability of $\frac{1}{2}$ of ending up with a single atom or otherwise being empty. If we then ask how many total single-atom filled tweezers we expect to have in an array of $N_{\text{traps}}$ traps, the answer will be a binomial distribution with a mean of $N_{\text{traps}}/2$. This distribution has a standard deviation of $\sqrt{N_{\text{traps}}}/2$.

The mechanism for pairwise loss in neutral atoms is usually excitation to two-atom molecular states [108]. The specifics and subtleties of this process vary between atoms and transitions, but an overall theme is that a pair of atoms in an electronically excited molecular state gain a large amount of kinetic energy upon decay to the electronic ground state — enough kinetic energy such that both atoms exit the trap.

In experiment, we see evidence for pairwise loss when driving at certain frequencies on the red transition [89]. In particular, we observe that a tweezer which is initially occupied with very large probability (by, very likely, several atoms) is only occupied 50% of the time after appropriate driving on the red transition for a few 10's of ms (Fig. 2.10). Furthermore, the occupation saturates to this value and does not reduce any further (at least not on any comparable timescales). This observation is consistent with pairwise loss and strongly suggests that the end result is a single atom.

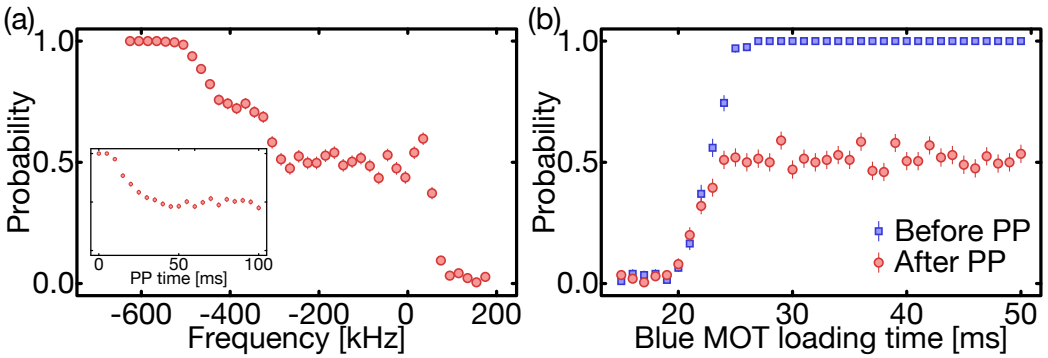


Figure 2.10: Pairwise loss (i.e. parity projection (PP)) for strontium in tweezers. Data was produced by driving atoms on the red transition in a ~1.4 mK magic-ellipticity tweezer at $\lambda = 515.2$ nm with a radial trapping frequency of $\omega_r = 2\pi \times 211$ kHz. **(a)** Probability of finding an occupied tweezer after PP as a function of drive frequency, with a pulse time of 60 ms. The horizontal axis is the frequency offset ($\delta/(2\pi)$ in the language of Eq. 2.57) from the free-space resonance of the red transition. Inset: Probability of finding an occupied tweezer as a function of time while driving at -226 kHz. **(b)** Probability of finding an occupied tweezer before (blue) and after (red) a PP pulse, as a function of MOT loading time.

While we do not have a fully satisfactory model for the microscopic mechanism of pairwise loss, we hypothesize that the molecular state at a frequency of $-435$ kHz [109] plays a role. It is possible that cooling plays an important role during pairwise loss (as a mechanism to increase phase-space density), thus biasing the optimal frequency toward the trap frequency (where low-order motional sidebands can be driven, see Sec. 2.5).

### 2.4.3 Schemes for increased filling

Here we discuss some potential strategies for obtaining single-atom array filling fractions beyond the 0.5 provided by pairwise loss. We will present two distinct

approaches: (1) loading the array multiple times (Sec. 2.4.3) and (2) a speculative approach based on fine-tuning of molecular dynamics (Sec. 2.4.3). We have had preliminary success with implementing strategy (1), while we only speculate on strategy (2) for now based on previous work in alkali [102–105].

***Approach 1: multiple loading cycles***

In this approach*, we load the array and perform pairwise loss as usual, and then proceed to re-load any remaining empty tweezers while preserving the single atoms in the tweezers already filled.

A procedure for accomplishing this is the following:

1. Load atoms into the array from a red MOT.
2. Perform pairwise loss.
3. Image the array to see which tweezers are empty.
4. Transfer atoms to the clock state (Sec. 4.1.1).
5. Decrease the depth of *only* the tweezers that contain an atom. This can be done via altering the AOD signal (Eq. 2.122).
6. Load atoms into the array from a red MOT again.
7. Illuminate the array with both imaging (Sec. 2.6) and cooling (Sec. 2.5) light. The imaging light will heat all atoms except the ones transferred to the clock state. The cooling will prevent atoms in deep traps from being lost due to heating, but will not prevent the loss of ground state atoms in shallow traps.
8. Return all tweezers to normal depth and perform pairwise loss (which may already have been partially performed by Item 7).
9. Optional: repeat the procedure starting from Item 3.

Here, Item 7 crucially eliminates any new atoms that are loaded into tweezers that were already prepared with a single atom in the previous loading cycle. It also does so without removing those previously prepared atoms as they are in the clock state

*We acknowledge Adam L. Shaw and Brandon Grinkemeyer for useful conversations regarding these ideas.

and therefore dark to the imaging light. Furthermore, Item 7 does not remove all the atoms that were newly loaded into previously empty tweezers as those tweezers are at the proper depth to experience effective cooling. It is possible to use tweezer depth as a selective factor in this way for two reasons: one is that a trap light shift can move the resonance of the cooling transition (see Eq. 2.81) and the other is that atoms in shallower traps can be heated out faster.

Item 5 actually plays a double role in this scheme in both allowing for the aforementioned depth selection as well as extending the lifetime of atoms in the clock state. One wants to minimize the depth as to minimize Raman scattering that can transfer atoms out of the clock state (see Sec. 3.2.2). Typically, the process of creating and loading from a red MOT lasts about ~200 ms, so the lifetime of atoms in the clock state needs to be significantly longer than this.

This scheme alone is enough to increase array loading, but there are also some further tweaks that can improve the performance. One is to rearrange the initially loaded array (see Sec. 2.7.3) such that all the loaded atoms are on one side. Then, one can fine tune the position of the red MOT (see Sec. 2.4.1) during the next loading cycle such that it overlaps mostly with the empty tweezers and avoids the already filled tweezers. The red MOT is typically small enough (few hundred $\mu$m) to be able to discriminate between one side of the array and the other. Finally, one can use a red loading beam that has its detuning optimized to load into deep tweezers (see discussion at end of Sec. 2.4.1).

We can quantify the performance of this scheme by asking what we expect the array filling fraction to be after $N_L$ loading cycles. We can make two reasonable simplifying assumptions: that all empty tweezers are loaded with a probability of 0.5 at any loading cycle and that no new atoms are loaded into tweezers that were previously loaded (Item 7 ideally ensures this). Then the performance of the scheme can be parametrized by a single variable $p_s$ that is the probability that an initially loaded atom remains in the trap until the end of the next loading cycle (atoms may be lost by e.g., losses during imaging, unsuccessful transfer to the clock state, undesired transfer out of the clock state, heating in the trap, etc.). Then, the average filling fraction after $N_L$ loading cycles is:

$$\bar{f}(N_L) \equiv \frac{\bar{N}_f(N_L)}{N_{\text{traps}}} = \frac{1 - (p_s - \frac{1}{2})^{N_L}}{3 - 2p_s} \tag{2.56}$$

Note that $\bar{N}_f$ should be interpreted as the average of a binomial distribution and that statistical fluctuations of $N_f$ and $f$ will be present from run to run. An interesting

limit is that of $N_L \to \infty$ where $\bar{f}(\infty) = \frac{1}{3-2p_s}$. Another is that of $p_s \to 1$ where $\lim_{p_s \to 1} \bar{f}(N_L) = 1 - 2^{-N_L}$.

As a preliminary result, we measure a filling fraction of $\bar{f}(2) = 0.68$ after two loading cycles, suggesting that our $p_s = 0.86$. We thus expect our filling fraction to saturate to $\bar{f}(\infty) = 0.78$ after many loading cycles with this level of performance. Optimization of this performance is a matter of ongoing work.

The downside of this scheme is that it significantly increases the experimental cycle time (unlike the speculative scheme we will present in Sec. 2.4.3) and that there are diminishing returns with each added loading cycle. Weighing the importance of having more atoms in the array versus that of having a fast cycle time depends on the application and on the experimentalist's discretion.

***Approach 2 (speculative): molecular dynamics***

Refs. [102–105] report the experimental realization of single-atom filling fractions of greater than 0.5, reaching as high as $\sim 0.9$ [103, 105]. These results are done with alkali atoms and exploit molecular interactions. They start by loading traps with more than one atom, just as we do before inducing pairwise loss. However, they are able to then excite molecular states that, upon decay, release just enough kinetic energy relative to the trap depth such that there is enough energy for one atom to leave the trap but not both. This dynamical process requires finite center-of-mass motion of the atom pair in order to bias the energy release into expelling only one atom.

Such schemes have not currently been realized for Sr, but further study into this topic may be fruitful. It may be particularly interesting to consider the molecular states of a pair of atoms in the $5s^2\ {}^1S_0$ – $5s5p\ {}^3P_1$ pair state, which are given in Ref. [109]. We hypothesize that the most weakly-bound bound state at -435 kHz plays a role in our pairwise loss (Sec. 2.4.2) and that it could be exploited to produce filling fractions greater than 0.5. In particular, we foresee a possibility of tuning the trap depth such that the energy released upon decay from such a state allows for expelling only one of two atoms. Since atomic temperatures in Sr are typically lower than those for alkali, it may be necessary to intentionally heat the atoms to induce the finite center-of-mass motion necessary for such a process. We leave further exploration of this topic to future work.

## 2.5 Cooling in a tweezer

Having an atom that is not only trapped but also *cold* is of utmost importance for practically every purpose. In this section, we will discuss how we use the red transition to reach temperatures in a tweezer on the order of a few $\mu$K — giving significant motional ground state occupation. We will discuss the various mechanisms at play, how to measure temperature, and practical factors that limit temperature.

We cool strontium by driving the narrow red transition. This transition already allows us to reach $\sim$1 $\mu$K temperatures in the red MOT via Doppler cooling. In this section, we will show how cooling on the red transition works in a trap. We begin in Sec. 2.5.1 by exploring sideband cooling in a magic trap. The narrow linewidth of the red transition will allow us to excite resolved sidebands with a *single-photon* excitation to an optically excited state, similarly to certain ion trap experiments [110]. This is to be contrasted with sideband cooling via a two-photon Raman transition between ground hyperfine states, which is typically used in alkali atoms [35], but has also been utilized in ion traps [111].

In Sec. 2.5.2, we will see that a Sisyphus cooling mechanism occurs in non-magic traps.

### 2.5.1 Sideband cooling

#### *Motional transitions*

We begin by considering a two-level atom in a trap of potential $U(\vec{r})$ and driven by a spatially uniform wave with wavevector $\vec{k}$, Rabi frequency $\Omega$, and detuning $\Delta$. In this section, we will assume the trap is magic, meaning that the trap potential is the same in both the ground and excited state. We will see in Sec. 2.5.2 the implications of having a *non*-magic trap.

Under these assumptions, the motional plus internal Hamiltonian (which does not include excited state decay) in the rotating frame is given by

$$H = \frac{\vec{p}^2}{2m} + U(\vec{r}) - \hbar\Delta|e\rangle\langle e| + \tfrac{1}{2}\hbar\Omega\left(e^{i\vec{k}\cdot\vec{r}}|e\rangle\langle g| + \text{H.c.}\right) \tag{2.57}$$

We now assume that $U(\vec{r})$ is approximately harmonic near $\vec{r} = 0$ (which is true for tweezers) and that the atom is near this region. In this case, the 3D trap will

have three geometric principal axes along which we can define trap frequencies $\omega_i \equiv \sqrt{\frac{1}{m}\partial_i^2 U|_{\vec{r}=0}}$. Let us further assume one of these axes is parallel to $\vec{k}$, and let us call it $\hat{x}$. The Hamiltonian in this harmonic region will now separate into a sum of components along each direction, with only the component in $\hat{x}$ having non-trivial coupling between motion and internal state. We define the harmonic ladder operators as $a_i \equiv \sqrt{\frac{m\omega_i}{2\hbar}}(r_i + \frac{i}{m\omega_i}p_i)$ and the dimensionless *Lamb-Dicke parameters* $\eta_i \equiv k_i\sqrt{\frac{\hbar}{2m\omega_i}}$. Focusing only on the $\hat{x}$ component of the Hamiltonian and dropping subscripts, we get

$$H_x = \hbar\omega\left(a^\dagger a + \tfrac{1}{2}\right) - \hbar\Delta|e\rangle\langle e| + \tfrac{1}{2}\hbar\Omega\left(e^{i\eta(a+a^\dagger)}|e\rangle\langle g| + \text{H.c.}\right) \tag{2.58}$$

The most interesting term in this Hamiltonian is $e^{i\eta(a+a^\dagger)}$. One may recognize this as the operator which displaces a wavefunction by $\vec{k}$ in momentum space. Here, this is the result of a photon recoil. To see how this term affects the dynamics in a trap, we can evaluate its matrix elements on a basis of eigenstates of $n \equiv a^\dagger a$. The result is given in Eq. 31 of Ref. [112] as*:

$$\langle n'|e^{i\eta(a+a^\dagger)}|n\rangle = \sqrt{\frac{n_<!}{(n_< + |n'-n|)!}}(i\eta)^{|n'-n|}e^{-\frac{1}{2}\eta^2}L_{n_<}^{|n'-n|}\left(\eta^2\right) \tag{2.59}$$

where $n_< = \min(n, n')$ and $L_\beta^\alpha(y)$ is a generalized/associated Laguerre polynomial function with argument $y$.

It is instructive to evaluate this particularly for the case of $n = n'$ (so-called *carrier* transitions) and for $n = n' \pm 1$ (so-called *first blue/red sidebands*). Exact results are plotted in Fig. 2.11, and expansions in powers of $\eta$ are given below:

$$\langle n|e^{i\eta(a+a^\dagger)}|n\rangle = 1 - \tfrac{1}{2}\eta^2(2n+1) + O(\eta^4) \text{ [carrier]} \tag{2.60}$$

$$\langle n-1|e^{i\eta(a+a^\dagger)}|n\rangle = i\eta\sqrt{n} + O(\eta^3) \text{ [first red sideband]} \tag{2.61}$$

$$\langle n+1|e^{i\eta(a+a^\dagger)}|n\rangle = i\eta\sqrt{n+1} + O(\eta^3) \text{ [first blue sideband]} \tag{2.62}$$

Note that only *even* powers of $\eta$ enter into parity-*preserving* transitions [$(-1)^n = (-1)^{n'}$] while only *odd* powers of $\eta$ enter into parity-*reversing* transitions [$(-1)^n \neq (-1)^{n'}$]. Also note that the physical parity $P$ of these states is indeed given by the mathematical parity of $n$ by $P|n\rangle = (-1)^n|n\rangle$.

The term $-\hbar\Delta|e\rangle\langle e|$ in the Hamiltonian of Eq. 2.58 also plays an important role by allowing one to energetically target certain motional transitions by detuning the driving laser. In particular, one can create a resonance condition for $|n, g\rangle \rightarrow |n+m, e\rangle$ transitions by choosing $\Delta = m\omega$.

*Ref. [112] is also generally a very good review of this topic.

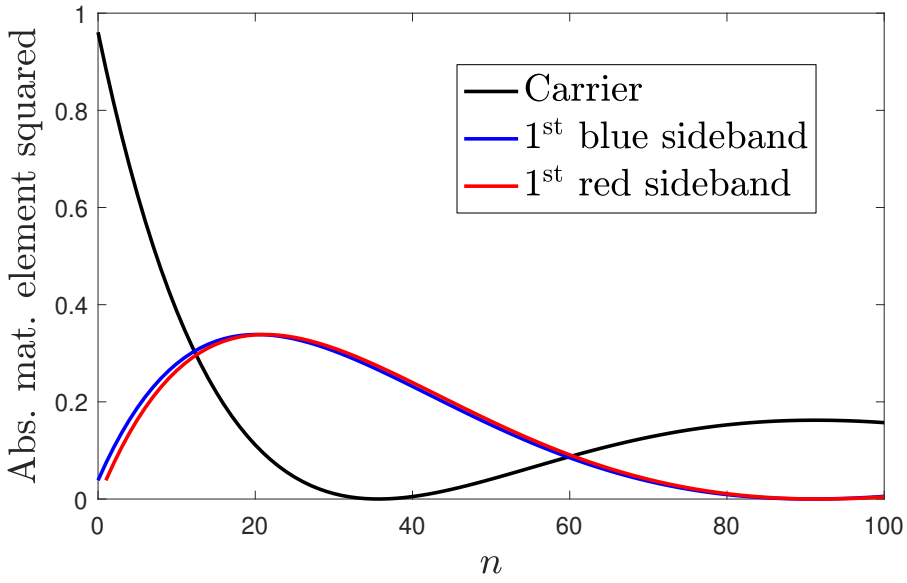


Figure 2.11: Absolute matrix elements squared $|\langle n'|e^{i\eta(a+a^\dagger)}|n\rangle|^2$ for the carrier ($n \rightarrow n$), first blue sideband ($n \rightarrow n+1$), and first red sideband ($n \rightarrow n-1$), with $\eta = 0.2$.

***Decay and cooling***

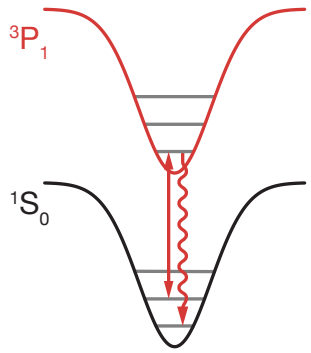


Figure 2.12: Illustration of sideband cooling on the Sr red transition. A coherent transition on the first red sideband drives the atom to a reduced motional state in the electronic excited state. Upon spontaneous decay in the Lamb-Dicke regime ($\eta \ll 1$), this atom returns to the same reduced motional state in the electronic ground state.

A crucial element of sideband cooling we have not yet considered is spontaneous decay. Let us now assume that $|e\rangle$ decays to $|g\rangle$ with a rate $\Gamma$. This can be modeled

by the master equation

$$i\hbar\partial_t\rho = (H_\Gamma\rho - \rho H_\Gamma^\dagger) + i\hbar\Gamma\int d\Omega D(\theta,\phi)c_{\theta,\phi}\rho c_{\theta,\phi}^\dagger \tag{2.63}$$

$$H_\Gamma = H - \frac{i}{2}\hbar\Gamma|e\rangle\langle e| \tag{2.64}$$

$$c_{\theta,\phi} = e^{-i|k|\hat{u}(\theta,\phi)\cdot\vec{r}}|g\rangle\langle e| \tag{2.65}$$

Here, $\rho$ is the density matrix of the electronic and motional state, $H_\Gamma$ is an effective non-Hermitian Hamiltonian, $c_{\theta,\phi}$ is a *jump operator* representing spontaneous emission in a particular direction, $D(\theta,\phi)$ is a dipole radiation pattern (discussed more in Sec. 2.6.3) and $\hat{u}(\theta,\phi)$ is a unit vector along the given direction. The jump operators not only de-excite the atom, they also apply a momentum kick in a random (dipole pattern distributed) direction. These random momentum kicks are an intrinsic source of heating and play a role in the temperature limit of sideband cooling (Sec. 2.5.1).

The final requirements for sideband cooling are certain conditions between $\omega, \Omega, \Gamma$, and $\eta$. Firstly, we would like to be able to tune $\Delta$ such that we can target a specific $n \to n+m$ transition and to have all others be off-resonant. This requires us to be in the *sideband-resolved regime*, which means that the separation between motional levels is significantly larger than the power-broadened linewidth of the transition, or $\omega \gg \sqrt{2\Omega^2+\Gamma^2}$. Secondly, we would like the momentum kick of the spontaneously emitted photon to be small. In particular, we would like the kick to be small enough such that its $n \to n$ matrix element is much larger than all other matrix elements that change the motional state (at least for small $n$). We can see from Eq. 2.59 and its various approximations in Eqs. 2.60–2.62 that this is achieved when $\eta \ll 1$. This is known as the *Lamb-Dicke regime*, and is similar to the Mössbauer effect in lattices [112]. Note that the sideband-resolved and Lamb-Dicke regimes can both be satisfied by having a sufficiently large $\omega$, but they are *not* equivalent, and one may be satisfied without the other being satisfied. We note finally that these two requirements are essentially the major distinctions between sideband cooling and Doppler cooling — in fact, Eq. 2.63 could just as well be used to model light-induced forces in free-space by setting $U = 0$ in the Hamiltonian.

We can now present the full cycle of sideband cooling: an atom in $|n, g\rangle$ is resonantly excited by light detuned at $\Delta = -m\omega$ to the state $|n-m, e\rangle$, with $m > 0$. We can do this without resonantly exciting other motional transitions as we are in the sideband resolved regime. Eventually, the atom spontaneously emits a photon while in

$|n-m,e\rangle$, and since it is in the Lamb-Dicke regime, it decays to $|n-m,g\rangle$ with high probability (again, this is true mainly for small $n$). The cycle then repeats to $|n-2m,g\rangle$ and so on until a state $|n'<m,g\rangle$ is reached. This is now a dark state, as there is no longer a state with quantum number $n'-m$, and cooling stops. If we wish to reach the motional ground state, we must ultimately choose $m=1$ such that the dark state that we reach is $|0,g\rangle$. Such a cycle is illustrated in Fig. 2.12.

For a 3D trap, performing this process will cool the dimension along which the beam is pointed. However, the spontaneous decay will produce momentum kicks in all three directions, producing an overall heating effect in non-cooled directions [113]. In practice, this is mitigated by alternating cooling in all three directions (Sec. 2.5.4), where pulses are alternated to avoid interference between beams.

### *Fundamental temperature limit*

The sideband cooling cycle just described makes the approximation that the motional and electronic ground state $|0,g\rangle$ is completely dark to excitation as no red sideband exists for this state. However, slow off-resonant excitation of the carrier and of blue sidebands can still occur. Excitation of such transitions can lead to decay that does not preserve the initial ground motional state. This creates a fundamental lower-bound limit on the achievable motional energy (which we will measure by the average vibrational number $\bar{n}$).

Ref. [22] Sec. VE1 computes this limit for sideband cooling as $\bar{n}=\frac{5}{16}\frac{\Gamma^2}{\omega^2}$. This is achieved at $\delta=-\omega$ and $\Omega\ll\Gamma$, as this configuration minimizes off-resonant excitation. However, this result assumes that the atom is unpolarized and that there is collision-induced thermalization between all three motional degrees of freedom. In our case, both of these assumptions are incorrect as we excite the atom to a well-defined rotational sub-level and there is no collisional thermalization for single atoms.

To compute the true limit in our configuration, we have to take into account the dipole radiation pattern $D(\theta,\phi)$ of spontaneously emitted photons and assume no thermalization between motional directions. This is already done by Eq. 2.63. We find the steady-state $\bar{n}$ by numerically computing the $\rho$ that satisfies $\partial_t\rho=0$. Assuming a linear polarization orthogonal to the direction of motion and $\Omega\ll\Gamma$,

we numerically find that the fundamental limit to $\bar{n}$ under these assumptions is

$$\bar{n} \approx 0.17 \times \frac{\Gamma^2}{\omega^2} \tag{2.66}$$

Note, as mentioned in the previous section, that cooling only along one direction will lead to heating in the orthogonal directions.

***Conversions between thermal quantities***

It is useful to be able to convert back and forth between various thermal quantities: the ground state population $p_0$, the mean vibrational occupation $\bar{n}$, and the temperature $T$. Here we give conversions between each (assuming thermal equilibrium):

$$p_0(\bar{n}) = \frac{1}{1+\bar{n}} \tag{2.67}$$

$$p_0(T) = 1 - e^{-\frac{\hbar\omega}{k_B T}} \tag{2.68}$$

$$\bar{n}(p_0) = \frac{1}{p_0} - 1 \tag{2.69}$$

$$\bar{n}(T) = \frac{1}{e^{\frac{\hbar\omega}{k_B T}} - 1} \tag{2.70}$$

$$T(p_0) = -\frac{\hbar\omega}{k_B \ln\left(1 - p_0\right)} \tag{2.71}$$

$$T(\bar{n}) = \frac{\hbar\omega}{k_B \ln(1 + \frac{1}{\bar{n}})} \tag{2.72}$$

### 2.5.2 A Sisyphus mechanism in a differential trap

We will now examine what happens when the ground and excited state have *different* trapping potentials. This happens e.g. in Sr on the red transition when the trap is not at a magic condition (Sec. 2.3.4). Two essential effects occur for an optically driven atom in a non-magic trap: (1) a state-dependent potential and (2) a position-dependent detuning, originating from a position-dependent differential light shift. This situation is reminiscent of Sisyphus cooling schemes in alkali atoms [22], except that in our case we have a detuning gradient instead of a polarization gradient. The situation in our case was recognized as a Sisyphus mechanism and studied theoretically in Refs. [114, 115].

***Trap-induced motional transitions***

We will begin our analysis by re-writing the Hamiltonian of Eq. 2.57 with differential trapping:

$$H = \frac{\vec{p}^2}{2m} + U_g(\vec{r})|g\rangle\langle g| + U_e(\vec{r})|e\rangle\langle e| - \hbar\Delta|e\rangle\langle e| + \tfrac{1}{2}\hbar\Omega\big(e^{i\vec{k}\cdot\vec{r}}|e\rangle\langle g| + \text{H.c.}\big) \quad (2.73)$$

We can once again make the harmonic approximation, this time with separate trap frequencies and corresponding ladder operators for the ground and excited electronic states. We will again assume that the interrogation beam is along one of the principle axes $\hat{x}$, but this time we will keep all three dimensions in our expression as we will eventually see that all three dimensions have non-trivial dynamics:

$$\begin{aligned} H = \sum_{j=1}^{3} \Big(\hbar\omega_g^j\big(a_g^{j\dagger}a_g^j + \tfrac{1}{2}\big)|g\rangle\langle g| + \hbar\omega_e^j\big(a_e^{j\dagger}a_e^j + \tfrac{1}{2}\big)|e\rangle\langle e|\Big) \\ -\hbar\Delta|e\rangle\langle e| + \tfrac{1}{2}\hbar\Omega\big(e^{i\eta_g^x(a_g^x + a_g^{x\dagger})}|e\rangle\langle g| + \text{H.c.}\big) \end{aligned} \quad (2.74)$$

Dropping coordinate indices, we can relate $a_g$ to $a_e$ by a *Bogoliubov transformation*. The easiest way to do this is to note that the position and momentum operators are the same in both the ground and excited electronic states, so we have $r = \sqrt{\frac{\hbar}{2m\omega_g}}(a_g + a_g^\dagger) = \sqrt{\frac{\hbar}{2m\omega_e}}(a_e + a_e^\dagger)$ and $p = i\sqrt{\frac{\hbar m\omega_g}{2}}(a_g^\dagger - a_g) = i\sqrt{\frac{\hbar m\omega_e}{2}}(a_e^\dagger - a_e)$. Solving these equations gives

$$a_e = \frac{1}{2}\Big((\omega_e/\omega_g)^{1/2}(a_g + a_g^\dagger) + (\omega_g/\omega_e)^{1/2}(a_g - a_g^\dagger)\Big) \quad (2.75)$$

Note that $\eta_g(a_g + a_g^\dagger) = \eta_e(a_e + a_e^\dagger)$, so either factor can be used in the exponential in Eq. 2.74.

We now compute the state overlaps $\langle n_g|n_e\rangle$, where it should be understood that this corresponds to the quantum numbers along only one dimension — with the full 3D overlap given by the product of the overlap of each dimension. The strategy for finding these is to first apply the excited annihilation operator to the excited ground state, which must yield zero: $a_e|0_e\rangle = 0$. By using the Bogoliubov transformation of Eq. 2.75 and the normalization condition $\sum|\langle n_g|0_e\rangle|^2 = 1$, we obtain:

$$\langle 0_g|0_e\rangle = \left(\sum_{m=0}^{\infty}\frac{(2m-1)!!}{(2m)!!}\Big(\frac{\omega_e - \omega_g}{\omega_e + \omega_g}\Big)^{2m}\right)^{-1/2} \quad (2.76)$$

$$\langle n_g|0_e\rangle = (-1)^{n_g/2}\sqrt{\frac{(n_g-1)!!}{(n_g)!!}}\Big(\frac{\omega_e - \omega_g}{\omega_e + \omega_g}\Big)^{n_g/2}\langle 0_g|0_e\rangle \text{ [if } n_g \text{ even]} \quad (2.77)$$

$$\langle n_g|0_e\rangle = 0 \text{ [if } n_g \text{ odd]} \quad (2.78)$$

We can then find overlaps for higher $n_e$ by repeated application of the raising operator $a_e^\dagger$. The result can be stated in recursive form as

$$\langle n_g|n_e\rangle = \frac{1}{2\sqrt{n_e}}\left(\alpha_+\sqrt{n_g}\langle n_g-1|n_e-1\rangle + \alpha_-\sqrt{n_g+1}\langle n_g+1|n_e-1\rangle\right) \tag{2.79}$$

where we define

$$\alpha_\pm \equiv \left(\sqrt{\frac{\omega_e}{\omega_g}} \pm \sqrt{\frac{\omega_g}{\omega_e}}\right) \tag{2.80}$$

Note again that there is only mixing between states of the same parity, i.e. $\langle n_g|n_e\rangle = 0$ if $(-1)^{n_g} \neq (-1)^{n_e}$. One can now go on to evaluate the matrix elements of the exponential drive using a basis transformation and the result in Eq. 2.59. However, the general result is overly cumbersome. In general, one can expect the matrix elements we previously computed (e.g. in Fig. 2.11) to be modified.

Instead of computing how all matrix elements of the drive are modified, we will focus on a *qualitatively* new phenomenon: the coupling of different motional states that exists even in the limit of $\eta = 0$. When we take $\lim_{\eta\to 0} e^{i\eta(a+a^\dagger)} = 1$, the only coupling between different motional states arises from state overlaps $\langle n_g|n_e\rangle$ (analogous to Franck-Condon factors in molecular states), which as we have seen are generically nonzero for a non-magic trap. This is in contrast to sideband transitions in a magic trap (Sec. 2.5.1), where a nonzero $\eta$ is required for motional-state-changing transitions. One can say that these $\eta$-dependent sideband transitions result from a momentum transfer between the driving beam and the atom. When the trap is non-magic, however, an atom that is electronically driven can experience motional-state-changing transitions *without* momentum transfer from the driving beam, with the "force" arising instead from differential trapping.

We will broadly call such differential-trapping-induced and $\eta$-independent motional effects *Sisyphus* mechanisms. An important observation is that *Sisyphus mechanisms are independent of the direction of the driving beam* and affect motional dynamics in all directions — even if the driving beam points along only one of the principal axes of the trap. Note that when a trap is non-magic and when $\eta \neq 0$, *sideband and Sisyphus mechanisms are both present* and arise from the same Hamiltonian. In this case, it is difficult to treat them as separate phenomena.

It is nevertheless worth investigating dynamics when $\eta \to 0$ so that we can get some insight into "purely Sisyphus" dynamics. Taking $\eta \to 0$ means taking either $\omega \to \infty$ or $k \to 0$. The former can be done experimentally by using a tighter trap, and we note that doing so does *not* change the state overlaps in Eqs 2.76–2.80

and therefore also does not change the Sisyphus contributions to the drive matrix elements — whereas it *decreases* the sideband contributions. The latter method ($k \to 0$) can be artificially realized by driving the atom with a beam orthogonal to the relevant direction of motion (though note that spontaneous decay will still lead to momentum kicks in all directions).

Let us now assume an $\eta = 0$ regime. If the trap is non-magic, we can drive parity-preserving Sisyphus transitions $n_g \to (n + 2m)_e$ in all directions, where $m$ is any integer, with a drive strength proportional to the 3D product of the state overlaps in Eqs 2.76–2.80. By choosing $m$ to be negative and detuning the laser to drive that transition on resonance (assuming we are in a regime where these transitions are energetically resolved), we can drive the atom to an electronic excited state with reduced motional energy. For an $\frac{\omega_e}{\omega_g}$ ratio that is reasonably close to 1 and for states near the ground state, the $\langle n_e | n_g \rangle$ matrix element with $n_e = n_g$ will be dominant, so the dominant decay process will preserve the lowered motional state.

Therefore, Sisyphus mechanisms can be exploited for cooling in a way similar to sideband cooling, and can produce cooling in any direction regardless of the orientation of the drive beam. A significant difference, however, is that Sisyphus transitions cannot change the parity of a motional state, so if an atom is "stuck" in an odd parity motional state, a Sisyphus transition cannot bring it to the ground state.

***State-dependent resonance conditions***

Another major *difference* that appears between magic and non-magic traps is that the resonance condition for an $n_g \to (n+m)_e$ transition depends not only on $m$, but also on $n$. Indeed the resonance condition is given by

$$\Delta^{\text{res}}_{n_g \to (n+m)_e} = n_g(\omega_e - \omega_g) + m\omega_e + \left[\tfrac{1}{2}(\omega_e - \omega_g) + \big(U_e(0) - U_g(0)\big)/\hbar\right] \quad (2.81)$$

where the second term in brackets is a state-independent overall light-shift that includes both the difference in zero-point energies as well as the difference in trap depth (which we neglected in Eq. 2.74). When the trap is magic, $\omega_e = \omega_g$ and $U_e = U_g$, and we return to the magic sideband resonance condition $\Delta^{\text{res}} = m\omega$. Note that this resonance condition is true for *all* motional transitions, whether they be sidebands, Sisyphus transitions, or some combination.

Practically, this means that for non-magic traps, there is no single laser detuning that produces optimal cooling for all motional states. Whether this is a practical

problem for cooling depends entirely on the severity of the situation. With the typical parameters used in this work and sufficient array uniformity (Sec. 2.7.2), we find that differential trapping is not a major hindrance to cooling even when using only one static frequency, and going to magic conditions does not produce significantly lower temperatures. However, this should not be taken as a definitive statement for all parameters (note that laser noise plays a large role in our practical cooling limit, see Sec. 2.5.3), and having access to magic conditions may in some cases be beneficial for cooling. Finally, we note the possibility of using frequency sweeps and/or multi-step cooling schemes with different frequencies.

Inversely, if a spectrum of motional states is measured on a thermal ensemble of atoms, that spectrum will show smearing between different motional states. For excited states that are more tightly trapped than the ground state ($\omega_e > \omega_g$), the spectrum exhibits an overall shift to negative detunings and thermally smears toward positive detunings, with the opposite true for $\omega_e < \omega_g$. The overall shift — especially on narrow transitions like the red transition — can be very useful for measuring the trap depth of a tweezer, which is especially useful for uniformizing an array [89] (Sec. 2.7.2). The spectral smear can potentially be useful for measuring the motional state of the ensemble, even without assumptions of thermal equilibrium.

#### *Attractive and repulsive Sisyphus cooling*

It is found experimentally and numerically that cooling in a non-magic trap produces either an "attractor" or "repeller" in energy space. An attractor at a certain energy tends to cool atoms above that energy, but tends to *heat* atoms below that energy, hence "attracting" atoms towards itself. A repeller does the opposite: it heats atoms above its energy and cools atoms below its energy, thus "repelling" atoms away from itself. The location of the attrator/repeller in energy space is approximately proportional to the detuning of the drive beam [89]. Note that this is not an additional effect on top of the dynamics already discussed, but rather a heuristic effect resulting from them.

For a more tightly trapped excited state ($\omega_e > \omega_g$), an *attractor* is present [116], and vice versa: for a less tightly trapped excited state ($\omega_e < \omega_g$), a *repeller* is present [89]. For practical cooling purposes, it therefore may be preferable to have a more tightly trapped excited state rather than a more weakly trapped one, as this is generally more stable in that it will not uncontrollably heat an atom out of a trap

if it is on the "wrong" side of the repeller.

### 2.5.3 Heating sources & practical cooling limits

In this sub-section, we give a non-exhaustive list of common non-intrinsic experimental sources of heating that go beyond fundamental limits.

#### *Cooling laser phase/frequency noise*

So far we have assumed that we can tune the $\Delta$ of our cooling laser with exact precision and no noise. However, all lasers have frequency noise, and this becomes especially important for the kinds of narrow transitions that we use for cooling. To quantify frequency noise, we will need a power spectral density (PSD) of the laser detuning fluctuations $\delta\nu(t) = \delta\Delta(t)/(2\pi)$, which we will denote by $S_{\delta\nu}(f)$. We will also assume that we can produce representative noisy time traces $\Delta(t) = \Delta + \delta\Delta(t)$ from this PSD (Ref. [117] and Sec. 3.4.6), such that we can perform Monte Carlo simulations of cooling dynamics under a noisy laser.

We measure the frequency noise PSD by passing the in-loop error signal of the laser lock through a spectrum analyzer [117]. However, the directly measured error signal is attenuated at high modulation frequencies by a cavity roll-off factor, which depends on the cavity linewidth (Ref. [118] Eq. 1.42). We therefore divide our measured power spectral density by (the square of) this factor to obtain the true frequency noise PSD.

The *un*corrected PSD is still useful, however, as it directly tells us what frequency PSD we can expect if we use the cavity transmission to seed a second laser that is then used for cooling. Such a scheme would use the cavity as a filter to reduce frequency noise [119]. While we have not yet implemented such a scheme, it is an interesting future outlook.

Fig. 2.13 shows the measured $S_{\delta\nu}(f)$ of the laser we use for cooling on the red transition. We see that a significant amount of frequency noise exists at modulation frequencies near ~100 kHz, which is on the same order as typical trap frequencies. One may reasonably expect that this would be bad for cooling in a trap, as the light will have frequency components at the trap frequency and may excite unwanted motional transitions. Fig. 2.13 also shows our prediction for how much this noise may be reduced via cavity filtering.

We note that such noise at high frequency is typically poorly captured in a measure such as the laser linewidth, which is more sensitive to noise at lower modulation frequencies (see Ref. [120]).

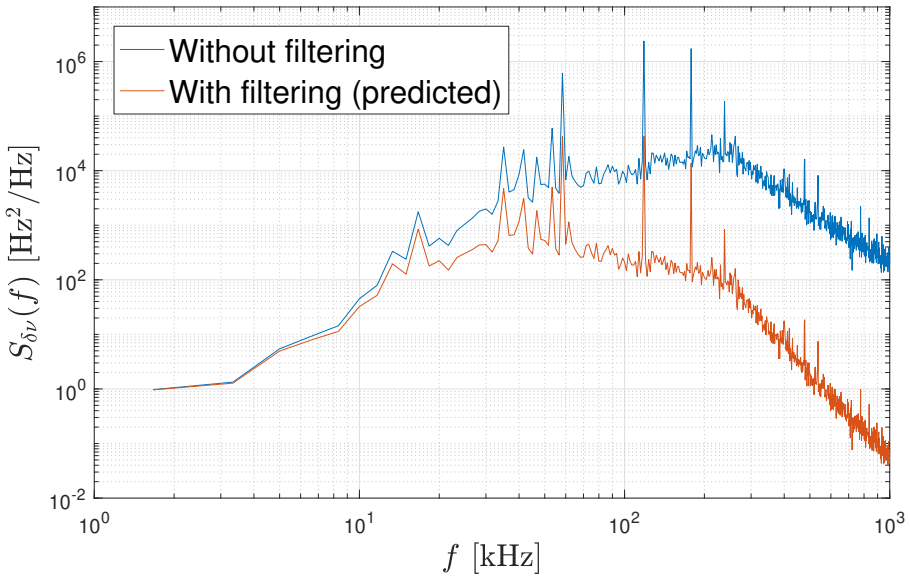


Figure 2.13: One-sided power spectral density $S_{\delta\nu}(f)$ of frequency noise for the laser used for cooling on the red transition, measured via the in-loop error signal of the laser lock [117]. The blue curve is the currently present noise, while the red curve shows a potential improvement possible by cavity filtering [119]. The resolution bandwidth is 100 Hz.

To quantify the effect of such noise on cooling, we numerically evolve the sideband cooling master equation (Eq. 2.63) and average over an ensemble of laser noise trajectories in the time domain generated from the measured power spectral density [117]. The results are summarized in Table. 2.3.

| Model | Predicted $\bar{n}$ |
|---|---|
| Without filtering | $9.9 \times 10^{-2}$ |
| With filtering | $5.4 \times 10^{-3}$ |
| No noise | $2.9 \times 10^{-3}$ |

Table 2.3: Simulated steady-state values of $\bar{n}$ for sideband cooling under the laser frequency noise given in Fig. 2.13. The cooling parameters are $\omega = 2\pi \times 78$ kHz, $\delta = -\omega$, $\Omega = 2\pi \times 16.8$ kHz, and magic trapping conditions. $\Gamma = 2\pi \times 7.5$ kHz for the red transition. We choose $\Omega \gtrsim \Gamma$, which does not produce the optimal $\bar{n}$ for each configuration, but rapidly achieve a steady state that can be compared between configurations.

We see that the laser frequency noise is predicted to significantly contribute to a non-fundamental cooling limit, and that filtering is expected to reduce this limit by more than an order of magnitude in $\bar{n}$. We leave experimental confirmation of this prediction to future work. We note that our actual measured temperature (Sec. 2.5.4) after cooling is still about a factor of 2.4 higher than predicted in the "without filtering" model, suggesting that we are either underestimating our laser noise or that there is another unexplained factor affecting our temperature limit.

### *Trap intensity noise*

An optical trap with intensity fluctuations* can induce heating. A full treatment of this kind of heating is given in Ref. [121] (including a treatment of heating due to trap position fluctuations). Here we restate the main result, obtained via leading order perturbation theory for a harmonic oscillator: fluctuations of the trap intensity at *twice* the trap frequency create a heating rate proportional to $\bar{n}$, such that

$$\frac{d}{dt}\bar{n} = \Gamma_I(\bar{n} + \tfrac{1}{2}) \tag{2.82}$$

$$\Gamma_I = \pi^2 \nu^2 S_{\delta I}(2\nu) \tag{2.83}$$

where $\nu = \omega/(2\pi)$ and $S_{\delta I}(f)$ is the one-sided power spectral density of the fluctuations in the intensity. Eq. 2.82 implies that heating will proceed exponentially: $\bar{n}(t) = \left(\bar{n}(0) + \frac{1}{2}\right)e^{\Gamma_I t} - \frac{1}{2}$. Eq. 2.83 implies that this heating is only nonzero for intensity noise fluctuating at twice the trap frequency. However, keep in mind that this result is only up to the leading order in perturbation theory.

### *Scattering*

When an atom scatters a photon, it is liable to heat. Scattering may come either from a near-resonant beam such as one used to image an atom, or from a far-off-resonant beam such as the trap. An analytic treatment will be beyond the scope of this work, and ultimately a numerical treatment (via master equation, quantum jump [113], or semiclassical treatment [122, 123]) is often the most useful. Here we give some guidance as to how to model heating from scattering.

A full model of near-resonant scattering should incorporate the effects of momentum transfer from the drive beam, momentum transfer from spontaneous emission, and

*Sometimes called *relative intensity noise* or RIN.

differential trapping of the excited state. We note that such a model is essentially identical to the ones already discussed by e.g. the master equation approach of Eq. 2.63. These equations were first used to show *cooling*, so it is apparent that no blanket statement can be made as to how a scattering event will affect temperature, and that the resulting dynamics are highly dependent on parameters. This potentially includes beam geometry, such as whether or not the drive beam is retro-reflected. The presence or absence of a retro beam tends to become important when the scattering rate is significantly higher than the trap frequency along the direction of interrogation (see discussion in Sec. 2.6.2).

We note that all such heating from near-resonant scattering is proportional to the scattering rate. For an effective two-level system, this is given by

$$\Gamma_s = \frac{\Gamma}{2}\frac{s}{1+s+\frac{4\Delta^2}{\Gamma^2}} \tag{2.84}$$

where

$$s = |\hat{\epsilon}\cdot\hat{e}_q|^2 I/I_s \tag{2.85}$$

is the *saturation parameter*. Here, we assume a $m_J \rightarrow m_J + q$ transition and $\hat{\epsilon}\cdot\hat{e}_q$ is the projection of the polarization onto the $q^{\text{th}}$ spherical basis vector (see footnote following Eq. 2.22). We also use the *saturation intensity*

$$I_s = \frac{2\pi^2\hbar c\Gamma}{3\lambda^3} \tag{2.86}$$

defined for the transition in question [21].

For far-off-resonant scattering such as from a trap, we point the reader to Refs. [91], which argues that each scattering event heats the atom by $2E_r$, where $E_r = \frac{\hbar^2k^2}{2m}$ is the recoil energy with $k$ the wavevector of the beam. Ref. [124] is also a good resource for computing trap scattering rates.

### 2.5.4 Temperature measurement and experimental results

There is one *de facto* "gold standard" for measuring near-ground-state temperatures: sideband spectroscopy [35]. The true value of sideband spectroscopy is that it is insensitive to a wide array of experimental parameters and that its analysis is simple and depends on very few assumptions. A number of other techniques exist, such as release-and-recapture (Sec. 4.4.2) and adiabatic rampdown [36, 125–128], which we

have used in our experiment [89, 116]. While we find such techniques to be useful for *comparisons* of temperature when, e.g., optimizing cooling parameters, their exact results are often sensitive to the details of the trap outside its harmonic region as well as to details of the procedure used (i.e. how fast the trap is turned/ramped up and down). Furthermore, they convolve energy distributions along all three dimensions (with release-and-recapture more sensitive to directions of tighter trapping and adiabatic rampdown more sensitive to directions of weaker trapping), while sideband spectroscopy can give information along all directions separately.

In this section, we will use spectroscopy of sidebands on a transition with no differential light shift (i.e. with a trap that is magic for the given transition) to determine temperature under an assumption of thermal equilibrium. We note that similar techniques are possible for non-magic conditions with potentially greater insight into the energy distribution in the trap, but the analysis of such situations is more complicated and we will leave them beyond the scope of this work (though see Appendix B2 of Ref. [89] for further discussion).

We perform spectroscopy on the red and blue motional sidebands and compare their amplitude. In principle, all sidebands (and even the carrier, see Sec. 3.2.1) can provide information about the motional state, but for simplicity here we will use only the first red and first blue motional sidebands. For now, we will assume that all spectroscopy is coherent, i.e., that there is no spontaneous decay while driving the sidebands. We will come back to situations with spontaneous decay later.

Let $P_b$ be the probability of exciting the first blue sideband at detuning $\Delta$, and let $P_r$ be the probability of exciting the first red sideband for the same interrogation time and intensity, but at a detuning of $-\Delta$. Then we have

$$\frac{P_r}{P_b} = \frac{\sum_{n=1}^{\infty} p_n P_{n\to(n-1)}(-\Delta)}{\sum_{n=0}^{\infty} p_n P_{n\to(n+1)}(\Delta)} \tag{2.87}$$

where $P_{n\to m}(\Delta)$ is the probability of exciting an atom with vibrational number $n$ to $m$ at a detuning $\delta$. Note that the sum in the numerator only starts from $n = 1$ as there is no red sideband for $n = 0$. Now, note that $P_{n\to(n+1)}(\Delta) = P_{(n+1)\to n}(-\Delta)$ as we are assuming coherent dynamics and the r.h.s. is simply the reverse process. Next, under the *assumption* of thermal equilibrium* in a harmonic trap, we have $p_{n+1} = e^{-\frac{\hbar\omega}{k_B T}} p_n$. By changing the sum index in the numerator to $n' = n - 1$ and

*We point the reader to Ref. [129] for an illuminating study of the excitation dynamics of sidebands in non-thermal states.

plugging the two aforementioned results into Eq. 2.87, the sum drops out and we are left with

$$\frac{P_r}{P_b} = e^{-\frac{\hbar\omega}{k_B T}} \tag{2.88}$$

$$= \frac{\bar{n}}{\bar{n}+1} \tag{2.89}$$

or, inverting:

$$\bar{n} = \frac{1}{\frac{P_b}{P_r} - 1} \tag{2.90}$$

Note that we made no assumptions on the interrogation time, intensity, or even $\Delta$, so long as the red sideband and blue sideband are interrogated at precisely opposing detunings. For maximal signal, one should practically choose an interrogation time that gives maximal excitation on the first red sideband. If $\Omega$ is the bare Rabi frequency as defined in, e.g., Eq. 2.58, then to first order in $\eta$ and for small $\bar{n}$ this optimal interrogation time is approximately given by $t = \frac{\pi}{\eta\Omega}$. Furthermore, it is possible to interrogate the red and blue sidebands at multiple $|\Delta|$ and take $P_r$ and $P_b$ to be integrated values, i.e. the area under the red and blue peaks — so long as this is done symmetrically around $\Delta = 0$. For this, it is useful to first ascertain the position of the carrier. Note that when integrating experimental data, it is important to first subtract off any constant baseline (due to readout infidelity or etc.). For our readout method on the clock transition (destructive method detailed in Sec. 3.1.3), the baseline is negligibly small, so we can skip this step.

In Sr, we have pursued two ways of performing sideband spectroscopy. One, which has proven to be the most useful, is by using the clock transition in an 813.4 nm clock-magic trap. Here, the process is highly coherent and the achievable sideband resolution is extremely high. Linewidths can be kHz or much less, whereas typical trap frequencies are tens of kHz. Readout can be done either by shelving excited atoms in the clock state (in a non-destructive readout scheme like the one shown in Ref. [116]), or by destructively blasting out ground state atoms with a strong resonant beam on the blue transition.

Fig. 2.14 shows a typical sideband spectrum on the clock transition with read out done via the blast-out scheme. It measures a radial temperature of $\bar{n}_r = 0.24$, which is a typical value reached after optimization. A typical cooling procedure used to achieve such temperatures is a set of 100 $\mu$s pulses on the red transition alternating between cooling in one radial direction, the orthogonal radial direction, and the axial

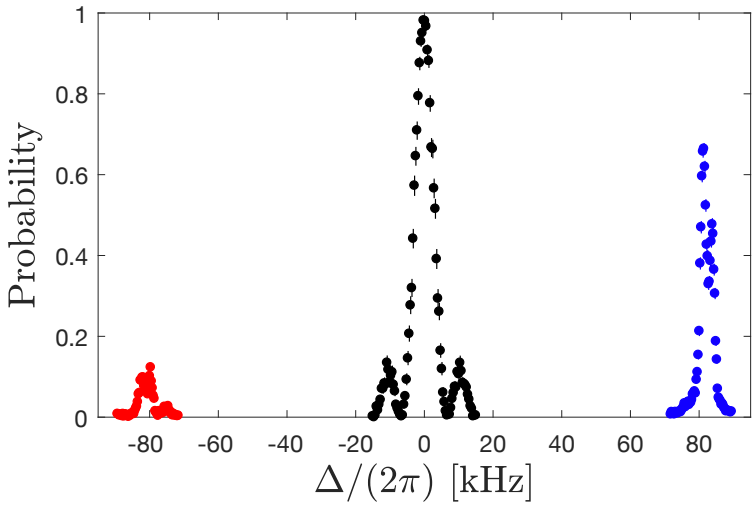


Figure 2.14: Sideband spectrum on the clock transition in clock-magic $\lambda = 813.4$ nm tweezers. Red/blue data are the red/blue sidebands, respectively, and black is the carrier (taken in a separate dataset and at a different interrogation time corresponding to its $\pi$-time). The carrier Rabi frequency is $\Omega = 2\pi \times 4$ kHz, while the radial trap frequency is $\omega \sim 2\pi \times 82$ kHz. The measured radial temperature is $\bar{n}_r = 0.24$. Note that this includes contributions from two slightly non-degenerate orthogonal radial directions, as can be seen from a double peak split by ~2.5 kHz on the sidebands. Data is averaged over a 61-tweezer array with 50% stochastic filling. No correction or rescaling is performed for the vertical axis.

direction of the tweezer (with a collimated red beam sent through the objective). This set of three alternating pulses is repeated ~50 – 100 times. The detuning and intensity of each beam is experimentally optimized. The results shown in Fig. 2.14 were achieved in a $\lambda = 813.4$ nm tweezer by exciting to a sub-state of the red transition with a polarizability equal to that of the $|m_J^x = \pm 1\rangle$ states of Fig. 2.6. That is, cooling was done under non-magic conditions such that the excited state is more strongly trapped than the ground state. We do not find that going to magic conditions improves the achievable temperature significantly (see a discussion about uniformity in Sec. 2.7.2). We note that the temperature achieved is more than a factor of two higher than the predicted temperature limit from our measured laser noise (Sec. 2.5.3). It is unclear what accounts for this discrepancy.

The other method we have used for sideband spectroscopy is directly with the red transition itself [89]. This method is complicated by the presence of spontaneous decay, however, and does not provide as much sideband resolution as the clock transition. Interpreting the results of such a scheme requires referencing with numerical simulations that include decay [89, 97]. Readout is done by rapidly

shelving excited atoms to the clock state via the 688 nm and 707 nm transitions and imaging without repumping the clock state [89]. Fig. 2.15 shows sideband spectra on the red transition for both a radial and axial direction [89].

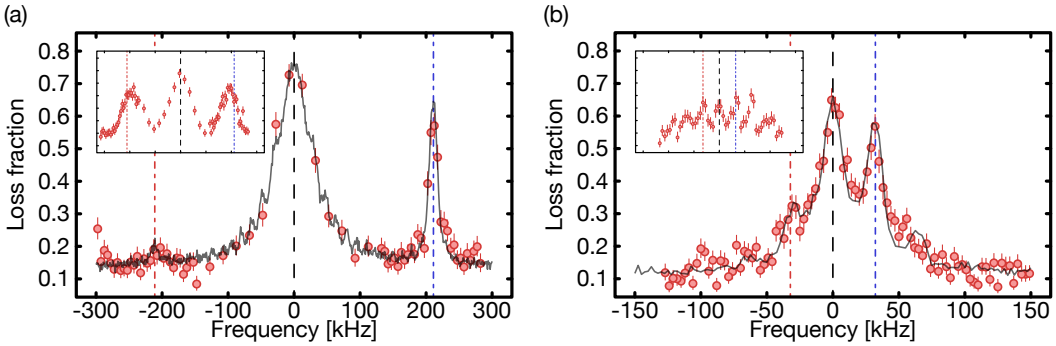


Figure 2.15: Sideband spectra on the red transition in $\lambda = 515.2$ nm tweezers under a magic ellipticity angle. Data is for a single tweezer. Insets show the same spectra but before cooling. Red/blue and black dashed lines indicate the red/blue sidebands and the carrier, respectively. Gray solid lines show results of comparison to numerical simulations. For details on the interrogation sequence and the numerical analysis, see Ref. [89]. **(a)** A radial sideband spectrum showing a temperature of $\bar{n}_r = 0.25$. **(b)** An axial sideband spectrum showing a temperature of $\bar{n}_a = 0.92$. In both plots, the horizontal axis is $\Delta/(2\pi)$.

## 2.6 Single-atom imaging

We will now discuss our method of detecting trapped atoms: fluorescence imaging. This is a ubiquitous technique in atomic physics and specifically in single-atom physics [30, 31, 33, 37–43]. Here we show its extension to single-atom physics with strontium in particular. We will seek to do two things with very high fidelity: (1) determine the presence or absence of an atom while (2) making sure that this detection does not expel the atom from the trap. Point (2) will be highly important to our ability to generate large, defect-free arrays (Sec. 2.7.3). Imaging a single atom is a delicate process where every photon counts, and this requires us to think about certain concepts more deeply than one would when imaging, for example, a bulk gas.

### 2.6.1 Transitions

For a trapped atom to be detected with high fidelity, it needs to scatter a sufficient amount of photons into an imaging system so as to be well-distinguished from a background signal. Two processes can prevent this from happening: (1) leaving the trap due to heating from fluorescence scatter and (2) the population of sufficiently long lived dark and/or un-trapped states. Therefore, in addition to addressing the atom with an imaging beam, we need to provide a mechanism for cooling as well as one for ensuring that no unwanted states are populated.

Fig. 2.16 shows a typical imaging setup. Fluorescence is induced by a 461 nm beam near-resonant with the blue transition while simultaneous cooling is done by a beam at 689 nm. As argued in Sec 2.5.2, a single non-retroreflected cooling beam is sufficient to cool all directions during imaging. Multiple (and possibly retro-reflected) beams can be used [89], but care must be taken that interference does not occur (by e.g. piezo modulating a mirror).

A repump beam at 707 nm is used to repump atoms out of the 5s5p $^3P_2$ metastable state into the 5s5p $^3P_1$ state, which decays back into the imaging cycle. 5s5p $^3P_2$ is populated via decay from 5s4d $^1D_2$, which is in turn populated by a weak decay channel from the excited state of the blue transition 5s5p $^1P_1$. We will see in Secs. 2.6.8 and 2.6.8 that the polarizability of 5s4d $^1D_2$ at the trapping wavelength is important. If this state is not sufficiently trapped, the atom can leave the trap before it decays out of this state. Since 5s5p $^3P_2$ is repumped via 5s6s $^3S_1$, part of the population ends up in 5s5p $^3P_0$, so a 679 nm repump is needed to excite

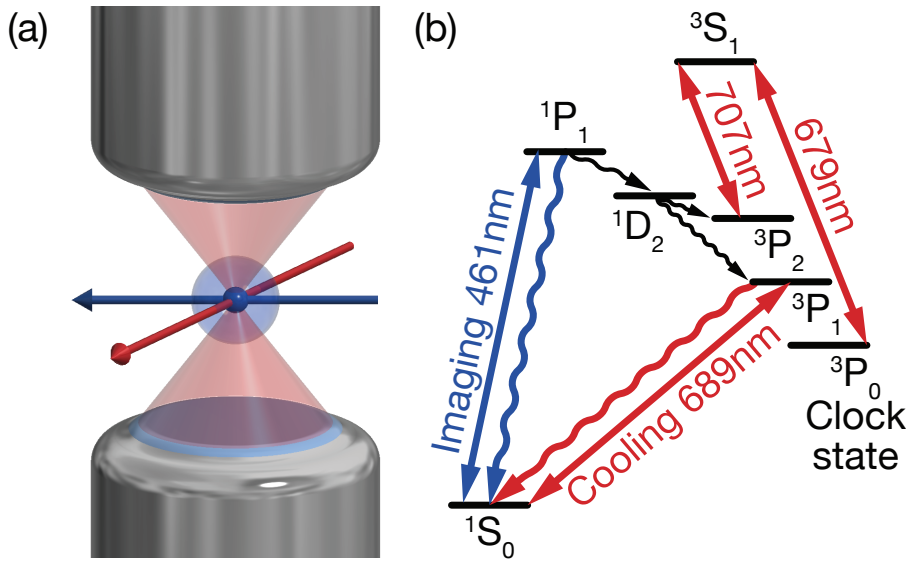


Figure 2.16: Imaging setup. **(a)** An atom in a tweezer is illuminated by a blue (461 nm) imaging beam while being cooled by a red (689 nm) cooling beam. The imaging beam may be retro-reflected or not (Sec. 2.6.2). One objective creates the tweezer, and fluorescence can be imaged through either or both objectives. Not shown: repump beams. **(b)** A level structure indicating the relevant transitions during imaging. In addition to the imaging and cooling beams, two beams at 679 nm and 707 nm are used to repump atom out of the 5s5p $^3P_2$ and 5s5p $^3P_0$ metastable states.

these atoms back to 5s6s $^3S_1$. The combination of the 707 nm and 679 nm beams eventually repumps all population in the metastable 5s5p $^3P_{0,2}$ states back to the imaging/cooling cycle, typically on the timescale of a few $\mu$s. We further note that both of these repump wavelengths are also necessary when exciting the red (689 nm) transition in a trap, as the trap light can cause Raman scattering between the various states of the 5s5p $^3P_J$ manifold.

Finally, we note that it is entirely possible to use the red cooling beam as *both* a cooling and imaging beam, i.e. such that red fluorescence is collected instead of blue. This particularly simple imaging scheme will be discussed in Sec. 2.6.8.

### 2.6.2 Imaging beam

Here we give a few considerations for the blue imaging beam. First, we consider whether it needs to be retro-reflected. One may suspect that a sideband-unresolved beam pointed along only one direction can create an "unbalanced" radiation pressure force $F = \hbar k \Gamma_s$ on the atom (with with $\Gamma_s$ the scattering rate) such that the atom is

pushed away from the tweezer in that direction. However, we have found that for the scattering rates we typically use that retro-reflection is not important. Classically, such a force applied to a harmonically trapped particle simply shifts its equilibrium position by $\Delta x = \frac{\hbar k \Gamma_s}{m\omega^2}$. If $\Delta x$ is small enough, this effect is unimportant. Nonetheless, this fact makes it prudent to point the imaging beam along the radial tweezer direction (as in Fig. 2.16) so as to not apply a force along the weakly trapped axial direction. In our typical regime, $\Gamma_s \lesssim 50 \times 10^3$ s$^{-1}$ (limited to such values by other heating mechanisms) is not large enough to necessitate retro-reflection. Indeed, we find there to be little difference between imaging with and without retro-reflection. If retro-reflection is used, care should be taken that no interference occurs by e.g. modulating a piezo mirror.

We generally choose a detuning for the blue imaging beam of $\sim 2\pi \times 30$ MHz *from the resonance condition at the center of the trap*. Furthermore, the sign of this detuning is chosen to be such that when the atom heats and attains a higher energy in the trap, its scattering rate goes *down*. This is heuristically done to reduce heating for higher-temperature atoms. The actual sign of detuning that fulfills this condition depends on the differential polarizability of the blue transition. At a trap wavelength of 813.4 nm, the blue excited state 5s5p $^1$P$_1$ is more strongly trapped than the ground state, so a red detuning is used. At 515.2 nm, the situation is reversed, and in fact here the excited state is anti-trapped. We point the reader to Refs. [40, 123] for further discussion on why a large detuning is beneficial for an un- or anti-trapped excited state. A larger magnitude detuning also provides greater uniformity of the scattering rate across different positions in the trap (assuming it is non-magic for the blue transition). However, a larger detuning also requires greater intensity to achieve the same scattering rate (Eq. 2.84) so background scatter off of nearby surfaces may increase. Ultimately, we find the detuning of the blue imaging beam to be a relatively unimportant factor, and many choices of detuning can be made to work.

As to the size of the beam, it is recommended to choose a beam large enough such that it illuminates the entire tweezer array uniformly. However, larger beams also produce greater background scatter. If possible, the beam should be made to avoid scattering off of surfaces near the imaging objective.

For polarization considerations, see Sec. 2.6.3.

### 2.6.3 Dipole radiation pattern

The scattering of fluorescence photons is not isotropic. The *dipole radiation pattern* $D(\theta, \phi)$ is a function defined on a sphere giving the probability that an atom will scatter a photon in a particular direction. We note that the results presented here are essentially identical to those of classical electrodynamics, particularly in the context of electromagnetic radiation from oscillating dipoles.

We will follow a treatment given in Ref. [90] Chapter 7.6. For an excited state with total angular momentum quantum number $J_e$ decaying into a ground state with $J_g$, we define a dipole radiation pattern *operator* on the subspace of the excited manifold as

$$\mathcal{D}(\theta,\phi) = \left(\frac{2J_e+1}{2J_g+1}\right) \sum_{q,q'\in\{0,\pm1\}} f_{qq'}(\theta,\phi) \sum_{m_e} |J_e\ m_e\rangle\langle J_e\ m_e+q-q'| \times \ldots \\ \cdots \times \langle J_g\ m_e+q|J_e\ m_e+q-q';1\ q'\rangle\langle J_g\ m_e+q|J_e\ m_e;1\ q\rangle \tag{2.91}$$

where

$$f_{qq'}(\theta,\phi) = \frac{1}{4\pi}\left(\delta_{qq'} - (-1)^q\sqrt{6\pi}\begin{pmatrix} 1 & 1 & 2 \\ -q & q' & q-q' \end{pmatrix} Y_2^{q-q'}(\theta,\phi)\right) \tag{2.92}$$

and $Y_l^m(\theta,\phi)$ is a spherical harmonic and the two-row matrix is a Wigner 3-$j$ symbol. Note that when integrating over the entire sphere, we have $\int d\Omega f_{qq'}(\theta,\phi) = \delta_{qq'}$ [90]. This formalism allows one to compute the dipole radiation pattern for any arbitrary state in the excited manifold by taking the expectation value, giving

$$D(\theta,\phi) = \langle\psi_e|\mathcal{D}(\theta,\phi)|\psi_e\rangle \tag{2.93}$$

Note that this result sums over all polarizations of the emitted photon, so applications where only one particular polarization is to be imaged will require a more sophisticated analysis.

We will simplify our analysis of this situation by assuming that the atom is in an energy eigenstate and that this eigenstate is also an eigenstate of angular momentum along some quantization axis $\hat{z}$ (remember that this may not be the case if an atom is in an elliptically polarized trap, see Sec. 2.3.2). Since our excited states of interest (both on the blue and red transition) have $J_e = 1$ with $J_g = 0$, we will also focus only on this situation. Then only the $q = q' = -m_e$ terms are nonzero and the dipole

radiation pattern simplifies to

$$D(\theta,\phi) = \frac{3}{8\pi}\sin^2(\theta) \text{ [if } m_e = 0] \tag{2.94}$$

$$D(\theta,\phi) = \frac{3}{16\pi}\left(1+\cos^2(\theta)\right) \text{ [if } m_e = \pm 1] \tag{2.95}$$

where $\theta$ is the angle from the quantization axis $\hat{z}$.

This result has important implications for imaging, as it is prudent to orient the dipole radiation pattern such that scattering into the imaging objective is maximized. For an $m_e = 0$ state, this happens when the quantization axis is oriented such that the objective is at $\theta = 90°$. For an $m_e = \pm 1$ state on the other hand, $\theta = 0°$ is optimal.

We will now compute the collection efficiency $C$ for several (non-exhaustive) cases and an objective with numerical aperture $NA = \sin\alpha$, where $\alpha$ is the maximal collection angle as measured from the optical axis. We define collection efficiency as the fraction of all photons scattered that end up being collected by the imaging objective. We note that the realization of these scenarios requires excitation to an appropriate $|\psi_e\rangle$ (see Eq. 2.93), which requires an appropriate choice of imaging beam polarization as well as consideration of any degeneracy-breaking fields such as a magnetic field or optical trap.

Case (1): $m_e = 0$, objective at $\theta = 90°$
Here it is most convenient to rotate the coordinate frame by 90° by rotating the $\hat{z}$ axis into the $\hat{y}$ axis, where we now have new spherical coordinates $\tilde{\theta}, \tilde{\phi}$ such that the objective is at $\tilde{\theta} = 0$. One can show that in this new frame, $\sin^2(\theta) = \cos^2(\tilde{\theta}) + \sin^2(\tilde{\theta})\cos^2(\tilde{\phi})$. Then we have

$$C_{(1)}(\alpha) = \frac{3}{8\pi}\int_0^{\alpha}\int_0^{2\pi} \sin(\tilde{\theta})\left(\cos^2(\tilde{\theta}) + \sin^2(\tilde{\theta})\cos^2(\tilde{\phi})\right)d\tilde{\phi}d\tilde{\theta} \tag{2.96}$$

$$= \frac{1}{8}\left(4 - \cos(\alpha)\left(3+\cos^2(\alpha)\right)\right) \tag{2.97}$$

$$= \frac{1}{8}\left(4 + (NA^2-4)\sqrt{1-NA^2}\right) \tag{2.98}$$

For $NA = 0.5$, we have $C_{(1)} = 0.094$.

Case (2): $m_e = \pm 1$, objective at $\theta = 0°$

This is straightforwardly evaluated in the original frame, giving

$$C_{(2)}(\alpha) = \frac{3}{16\pi}\int_0^{\alpha}\int_0^{2\pi} \sin(\theta)\big(1+\cos^2\theta\big)d\phi d\theta \tag{2.99}$$

$$= \frac{1}{8}\Big(4 - \cos(\alpha)\big(3+\cos^2(\alpha)\big)\Big) \tag{2.100}$$

$$= \frac{1}{8}\Big(4 + (NA^2-4)\sqrt{1-NA^2}\Big) \tag{2.101}$$

We see that Case (1) and Case (2) give identical collection efficiencies.

Case (3): $m_e = 0$, objective at $\theta = 0^\circ$
This is the worst possible choice and should be avoided. We compute it here only to demonstrate the worst case scenario.

$$C_{(3)}(\alpha) = \frac{3}{8\pi}\int_0^{\alpha}\int_0^{2\pi} \sin(\theta)\sin^2(\theta)d\phi d\theta \tag{2.102}$$

$$= \big(2+\cos(\alpha)\big)\sin^4\left(\tfrac{\alpha}{2}\right) \tag{2.103}$$

Writing this expression in terms of $NA$ is overly cumbersome. For $NA = 0.5$, we have $C_{(3)} = 0.013$, so this is only about ~14% of the efficiency of Cases (1) and (2).

Case (4): Isotropic emission
This situation is not realizable for an atom that has a well-defined angular momentum, but we will use it as a reference case anyway. Here we evaluate the integral

$$C_{(4)}(\alpha) = \frac{1}{4\pi}\int_0^{\alpha}\int_0^{2\pi} \sin(\theta)d\phi d\theta \tag{2.104}$$

$$= \sin^2\left(\tfrac{\alpha}{2}\right) \tag{2.105}$$

$$= \frac{1}{2}\Big(1 - \sqrt{1-NA^2}\Big) \tag{2.106}$$

For $NA = 0.5$, we have $C_{(4)} = 0.067$.

These various cases are plotted as a function of $NA$ in Fig. 2.17. We note that for a dual-objective setup such that the second objective is on the other side of the first objective, all of these collection efficiencies should simply be multiplied by 2.

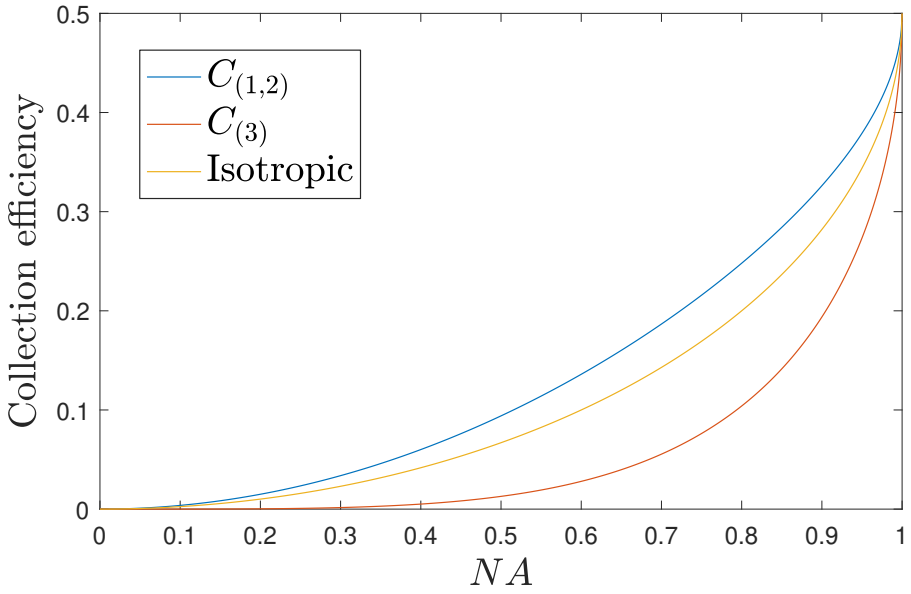


Figure 2.17: Collection efficiencies as a function of numerical aperture for the various cases discussed in Sec. 2.6.3.

### 2.6.4 EMCCD camera

The photons which are collected through the imaging objective are imaged onto the sensor of an electron-multiplying charge-coupled device (EMCCD) camera (Andor iXon Ultra 888). A CCD sensor detects photons by converting them to electrons. The feature that distinguishes an EMCCD from a normal CCD is an electron-multiplying (EM) gain before the readout register, which is important for detecting a small number of photons. The EM gain multiplies each electron into numerous electrons, which functions to overcome intrinsic readout noise in the camera's analog electronics. It is important to understand how this mechanism works and in what situations it is useful. In particular, we will see that the EM gain is only truly beneficial under circumstances of very low background counts, and that it is therefore important to minimize background. We will follow a treatment given in Ref. [130] as well as the technical manual Ref. [131].

We assume that $n$ electrons are produced on a sensor pixel. In realistic imaging conditions, $n$ is a probability distribution, but to begin with, we will assume it is a fixed number. The EM gain, whose strength will be parametrized by a number $g$, will multiply this number of electrons into a larger number $s$ of *signal electrons*, which then will be read out via the camera's electronics. $s$ will be given by a distribution which depends on $n$ [130]:

$$P_n^{\text{sig}}(s) = \frac{s^{n-1}e^{-\frac{s}{g}}}{g^n(n-1)!}\theta(s) \ [n > 0] \tag{2.107}$$

$$P_0^{\text{sig}}(s) = \delta(s) \tag{2.108}$$

where $\theta(s)$ is a Heaviside-theta and $\delta$ is a Dirac-delta. Eq. 2.108 is correct for the gain of zero electrons under the assumption that no spurious electrons are produced during the process of multiplication. If such an electron is produced, then it can be multiplied as well, however it may see an effectively smaller gain as it is already partway through the gain register (see Ref. [131] for details of the multiplication process). We will however ignore such effects for now and assume the given formulas are accurate.

These signal electrons are now counted by the camera's analog electronics and digitized to produce *counts*, which is the ultimate signal reported to the user*. The conversion from signal electrons to counts is not without noise, however. Indeed,

*Up to some overall scaling and offset that is specific to the camera and its settings, see Ref. [131].

the number of counts resulting from a given number of signal electrons is given by a Gaussian distribution parametrized by some standard deviation $\sigma$. The distribution of counts as a function of original electrons $n$ is therefore a convolution of a Gaussian distribution with Eqs. 2.107–2.108. We will call this distribution of counts $P_n^{\mathrm{ct}}(c)$. We point the reader to Ref. [130] for a procedure on calibrating $g$ and $\sigma$.

We will now calculate the overlap between two count distributions, one produced by $n$ initial electrons and the other by $m$ initial electrons. This will tell us how well we can tell the difference between these two possible signals. We will define such an overlap by the integral

$$\mathrm{Overlap}(n, m) = 2 \int \frac{P_n^{\mathrm{ct}}(c) P_m^{\mathrm{ct}}(c)}{P_n^{\mathrm{ct}}(c) + P_m^{\mathrm{ct}}(c)} dc \tag{2.109}$$

This value is zero when the two distributions are completely distinguishable and is one when they are identical.

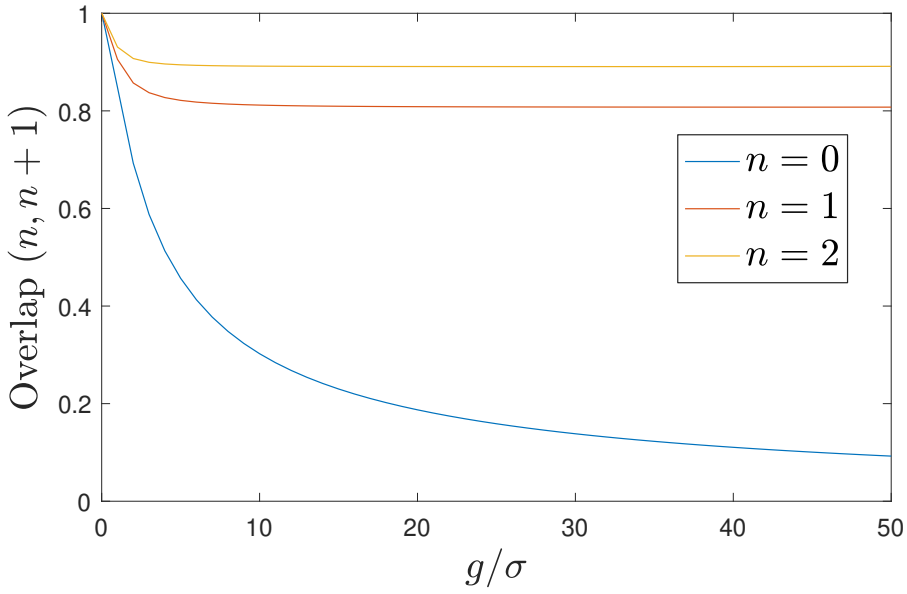


Figure 2.18: Overlap between counts distributions $P_n^{\mathrm{ct}}(c)$ and $P_{n+1}^{\mathrm{ct}}(c)$ as a function of the EM gain to readout noise ratio $g/\sigma$.

We plot this value in Fig. 2.18 as a function of $g/\sigma$ for $n \in \{0, 1, 2\}$ and $m = n+1$. We see that increasing the EM gain $g$ has the most significant effect when distinguishing between 0 and 1 initial electrons, whereas for higher values of $n$, the effect is not as pronounced and furthermore saturates at some value. Intuitively, this can be explained as so: multiplying zero electrons will always (ideally) produce zero signal electrons, whereas multiplying a finite number will always produce some number

that scales with $g$. So there is always a benefit of increasing gain when distinguishing between zero and a finite number, whereas for two finite numbers the benefit is less and eventually vanishes for high enough gain. Thus, to really take advantage of the functionality of an EMCCD, *background light should be minimized as much as possible*. Distinguishing between 0 background photons and 1 atomic photon is much better than distinguishing between, e.g., 10 background photons and 10 background plus 1 atomic photons.

Minimizing background becomes even more important when we also realize that the initial electron number $n$ is itself is a distribution. There are several stochastic processes that enter this: the number of photons scattered into the objective (either by an atom or by background), the number of photons that pass through the collection optics (characterized by some transmission efficiency), and the number of photons striking the sensor that are actually converted to electrons (characterized by the *quantum efficiency* of the camera sensor). All of these distributions are either Poisson distributions or very close, and their convolution — giving $n$ — is also Poissonian. The overlap between two Poissonian distributions of mean $\lambda$ and $\lambda + m$ is also minimized when $\lambda$ is small.

Practically, the way to minimize background is to minimize scatter of the imaging beam off surfaces near the imaging objective, to minimize the intensity of the beam by selecting a detuning that is not too large (see Sec. 2.6.2), and to use narrow optical filters in front of the camera. The filters should be *especially* good at rejecting light at the trap wavelength, and also at the wavelengths used for cooling and repumping such as 689 nm, 679 nm, and 707 nm. It is furthermore also important to minimize background originating from dark counts on the camera, caused by things like thermal excitations or so-called "clock-induced charges" [131]. These can be minimized by cooling of the sensor to a sufficiently low temperature (a common EMCCD feature) and optimizing readout parameters of the camera, such as the readout speed.

Finally, we note that some EMCCD cameras are able to be used in a "photon counting" mode [131] which may help with detecting a small number of photons. The idea here is to take advantage of time resolution: instead of taking one image of many photons, a time-series of many low-exposure images is taken such that it is very unlikely that each pixel on each image is exposed to more than 1 photon. Then each image ideally only records either 0 or 1 charges. If the EM gain is turned up high, then each photon can be detected with very high fidelity. We do not use such

a mode, but note that it may be useful in certain circumstances.

### 2.6.5 Atomic point-spread function

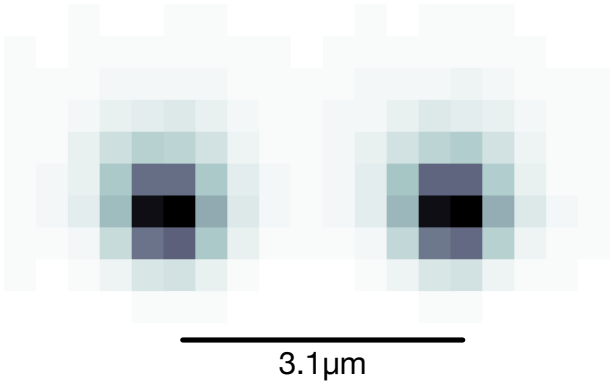


Figure 2.19: Typical measured point-spread functions of two atoms in tweezers spaced by 3.1 $\mu$m. Each pixel corresponds to about 345 nm. The actual pixel size is 13 $\mu$m and the magnification is $\times$37.5. The PSFs are significantly broader than one would expect from a diffraction-limited imaging system, as shown in Fig. 2.20.

Although an atom is essentially a "point-source" in that its characteristic size is much smaller than the wavelength that it emits, its fluorescence image will have some intrinsic spread with a functional form sometimes called the *point-spread function* or PSF. This size of the PSF is important as it gives a length scale beyond which two atoms can be easily distinguished. This is one of the various limits on how tightly spaced an atom array can be, though practically there are usually other limits that become important at longer scales (see Sec. 2.7).

The physics of the PSF is practically identical to the discussion given in Sec. 2.2 regarding the diffraction of light through a finite aperture. Indeed the same procedure can be applied simply by propagating in reverse the fluorescence light which scatters into the solid angle collected by the imaging objective. Approximating the dipole radiation pattern to be isotropic with no polarization gradients*, the result is an Airy disk as given by Eq. 2.7, such that the characteristic size of the ideal PSF scales as $\frac{f}{kR} \propto \lambda/NA$. We see from this result that imaging with shorter wavelengths beneficially allows for a smaller PSF.

*This approximation is usually sufficient, though we point the reader to Ref. [132] for a discussion on how elliptically polarized fluorescence may shift the PSF.

This result assumes ideal, "diffraction-limited" imaging conditions. In practice, a few things may degrade the PSF, such as defocus, optical aberrations, thermal spread of the PSF by atomic motion, and pixelization on the camera sensor.

In our setup, we observe a fluorescence PSF that is significantly larger than what the diffraction limit predicts. We have found that similar broadening is seen on the camera even when imaging a test beam with a high-quality lens, suggesting that much of our aberrations may be due to our camera (potentially from its sensor window). We find that using larger magnification alleviates such broadening. Using larger magnification accounts for the significant increase in resolution seen between Fig. 2.25 and Fig. 2.19 (note length scales in each figure). However, we believe that a further increase in magnification is necessary to fully overcome this broadening.

Fig. 2.19 shows typical PSFs of two atoms separated by 3.1 $\mu$m. Fig. 2.20 compares the PSFs of an ideal, diffraction-limited point-source with our measured PSF. In addition, it shows the expected PSF broadening due to thermal motion at typical tweezer trap frequencies and $T = 50$ $\mu$K. We expect this temperature (which is one-tenth of our typical trap depth) to be a safe upper bound for the temperature of our atoms during imaging as any temperature higher than this would likely cause loss during imaging beyond what we measure (see Sec. 2.6.8). We see that thermal broadening is not enough to explain the broadness of the PSF that we measure.

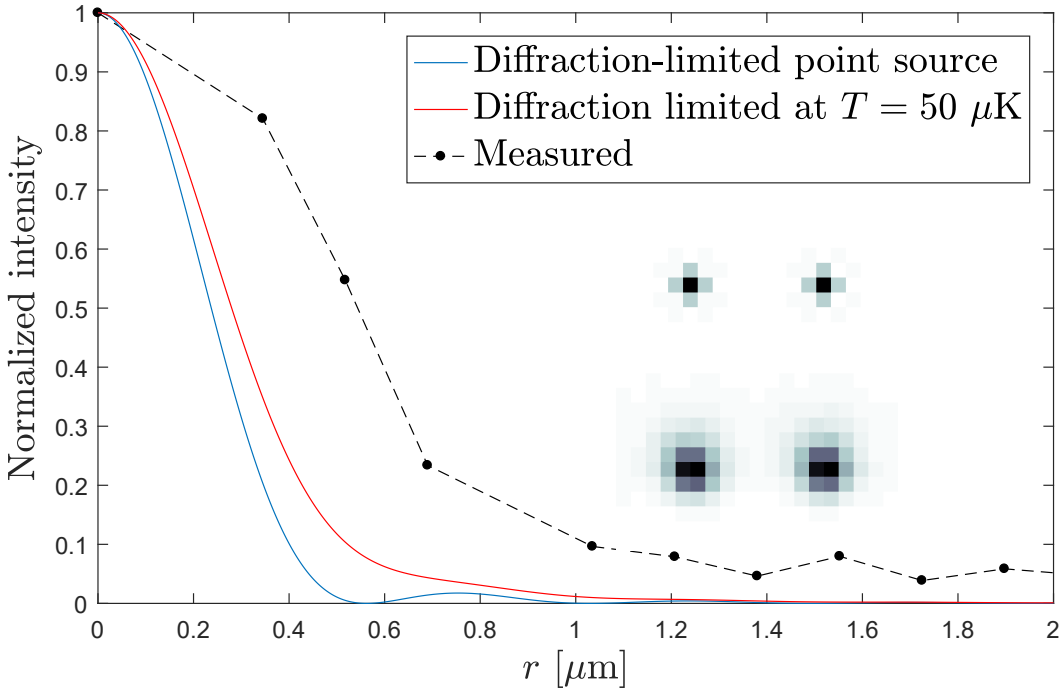


Figure 2.20: Expected and measured point-spread functions when imaging with $\lambda = 461$ nm light and an $NA = 0.5$ objective. **Blue:** Simulated diffraction-limited PSF of a point source. We assume a uniform fluorescence pattern in the scalar and paraxial regime, giving an Airy pattern as computed in Eq. 2.7. Corrections due to breakdown of the aforementioned assumptions are expected to be small for at this NA. **Red:** Simulated average of diffraction-limited PSFs (with the same assumptions as for the blue curve) over an ensemble of point-sources whose positions in 3D space are given by a classical thermal distribution with $T = 50$ $\mu$K in a tweezer with radial trap frequency $\omega_r = 2\pi \times 80$ kHz and axial trap frequency $\omega_a = 2\pi \times 12$ kHz. We reasonably expect this temperature to be an upper bound on the temperature of the atoms during imaging. Computation of each component PSF includes effects of defocus as prescribed by Eq. 2.6. **Black:** Measured point-spread function as given by a radial average over an ensemble of many fluorescence images. Broadening is suspected to arise from aberrations, in part due to the camera. **Inset top:** The simulated diffraction-limited PSF (as in the blue curve) of two atoms separated by 3.1 $\mu$m as would be seen on the pixelized camera sensor. **Inset bottom:** The measured PSF of two atoms separated by 3.1 $\mu$m as seen on the camera sensor. Both insets have each pixel corresponding to 345 nm.

### 2.6.6 Detection and binary thresholding

When we obtain an image, we must ultimately decide whether or not an atom is visible at the position of a particular tweezer. The result of this decision is *binary*: an atom is either detected or it is not, and the actual number of photons that were detected in order to make this conclusion is not important. Note that one does not have to assume that only a *single* atom is occupying the tweezer, and we can still make a binarization between an occupied tweezer and an unoccupied tweezer if more than one atom is present.

The first step in detection is to determine where in the image an atom's PSF actually is. This usually requires taking several images, averaging them, and finding the centroids of the various atomic PSFs in the array. We note that all of the techniques discussed in this section assume that the PSF is *stable* and does not drift around or defocus. For controlling defocus, it is useful to have the imaging objective be on a piezo-controlled translation stage. Another strategy is to use the same objective for both creating the tweezers *and* collecting fluorescence. Then, assuming there are no significant chromatic aberrations, the atom will automatically be in focus.

The next step is to derive some kind of numerical signal from the image. In the simplest case, this signal could be the number of counts on a single pixel. However, since the PSF of an atom is often larger than a single pixel, this would make these adjacent counts go to waste. A second pass attempt may then be to include all counts in a sufficiently large region around the center of the PSF. However, this now runs into the issue that it includes an increasingly large area of the image which is mostly background and which will only add noise to the signal.

The choice of signal which we have found to be ideal is a *weighted* sum over pixels, where we obtain the weights from the pixel values of the averaged PSF. We empirically find this method to give the best imaging fidelity. Other methods that might be used are fitting to an averaged PSF or using principal component analysis, which we find to give roughly equivalent results. In the context of an array of atoms, it is important to only sum over a region around the PSF small enough such that counts from neighboring atoms do not start entering the region. For all data in this work, we will be in a regime of sufficient atomic separation where PSFs do not overlap and this is easy to do. If one must obtain a signal in a regime where adjacent PSFs are not fully resolved, it is recommended to use principal component analysis [51] as a deconvolution technique.

Finally, we choose a *classification threshold* for the signal such that all signals below this threshold correspond to "atom not detected" and all signals at or above this threshold correspond to "atom detected." This threshold can in principle be chosen as anything, but we will see in Sec. 2.6.7 that there is in fact one choice which optimizes imaging fidelity.

### 2.6.7 Figures of merit

Now that we have laid the groundwork for single-atom imaging, we can describe the framework for benchmarking its performance. As stated in the beginning of Sec. 2.6, we are looking to quantify two things: (1) what is the probability that we are correct about the presence or absence of an atom and (2) what is the probability that the atom will remain trapped after imaging. We call item (1) the *fidelity* of imaging, and item (2) the *survival* probability. We will now discuss how to quantify both.

#### *Fidelity*

After each image, we systematically classify (by the procedure described in Sec. 2.6.6) the image as either "atom detected" or "atom not detected." We define the *imaging fidelity F* as the probability of this decision being true. That is, it is the probability that we either decide that an atom is detected when one was present at the start of the imaging process, or that we decide that an atom is not detected when one was not present at the start of the image. This may also be termed the *accuracy* of our binary classification. Note that it is important to specify that this definition applies to the *start* of the image, as atoms may be lost during an image*.

Determining imaging fidelity is a model-dependent process that makes a few assumptions. For example, our prior knowledge about the probability of an atom being present is important for determining imaging fidelity. If we had prior knowledge that, for example, a tweezer contained an atom with probability 1, then we could have unity fidelity by just deciding "atom detected" every time, regardless of what an image says or whether an image was taken at all. Our actual prior knowledge — based on modeling and observations (Sec. 2.4.2) — is that a tweezer contains an

*In some circumstances, such as very tightly spaced arrays, atoms may also in fact *appear* in tweezers where they originally were not by moving from tweezer to tweezer. However, for typical array spacings ($> 3\ \mu$m), we have never observed such an event and we will ignore this possibility.

atom with probability $f = 0.5$. Note that this means that the lowest "reasonable" (without intentionally trying to be wrong) imaging fidelity possible is 0.5 — you can simply guess the result and be correct half the time.

We know that the signal histogram (such as the one in Fig. 2.22) is the sum of a component coming from the absence of an atom and a component coming from the presence of an atom. If we have a model for the functional form of these contributions, we can compute the imaging fidelity by integrating the areas of both contributions that are on the "correct" side of the chosen classification threshold (see Sec. 2.6.6 for a definition of signal and classification threshold). In particular, if $P_{\text{atom}}(x)$ is the model function for the histogram distribution of an atomic signal and $P_{\text{bkd}}(x)$ is that of a no-atom background (with both distributions separately normalized to an area of 1), then the imaging fidelity is

$$F = (1-f)\int_{-\infty}^{x_t} P_{\text{bkd}}(x)dx + f\int_{x_t}^{\infty} P_{\text{atom}}(x)dx \tag{2.110}$$

$$F = \frac{1}{2}\Big(\int_{-\infty}^{x_t} P_{\text{bkd}}(x)dx + \int_{x_t}^{\infty} P_{\text{atom}}(x)dx\Big)\ [f \to \frac{1}{2}] \tag{2.111}$$

where $x_t$ is the classification threshold.

The remaining problem is now to figure out proper functional forms for the two probability distributions and to fit them to the measured histogram. For reasonably good imaging, the histogram often looks like two well defined peaks - one for background and one for an atom. Often, Gaussians are used to model these peaks [37, 89]. However, a more accurate model (especially important when imaging a small number of photons) should include a skew that arises from the camera gain (Sec. 2.6.4) as well as the Poissonian nature of photon scattering and detection. One possible model is a Gaussian convolved with Eqs. 2.107–2.108 and also convolved with a Poisson distribution of the $n$ parameter of these distributions. Such a model takes into account camera readout noise, camera gain, and Poissonian scattering/detection.

In certain circumstances, it might be necessary to add another contribution to $P_{\text{atom}}(x)$. In particular, we find that when imaging at a trap wavelength of 515.2 nm, every photon scattered by the atom entails a small probability of the atom being immediately lost (Sec. 2.6.8). This results in an exponential distribution of the number of photons that an atom scatters before it is lost. To account for this effect in the imaging fidelity, we must add an exponential distribution to $P_{\text{atom}}(x)$. This exponential distribution has a maximum at the signal value corresponding to one scattered photon (counter-intuitively, it is most likely that an atom is lost at the

very first scatter) and decreases exponentially until it reaches the atom signal peak corresponding to atoms that were not lost. In principle, if imaging proceeds for a long enough time, all atoms are lost and the entire atom signal histogram looks entirely exponential (with some convolution of readout/detection distributions). Other loss mechanisms, such as from heating, are generally not exponential but can also contribute to some kind of smearing of the atom signal histogram.

Once a correct model is found and the histograms are properly fit, there should exist a unique choice of classification threshold $x_t$ that maximizes the fidelity $F$.

Finally, we note that in addition to the overall fidelity $F$, we can define values $F_0$ and $F_1$ that are the probability of correctly identifying the absence/presence of an atom, respectively. These are given by

$$F_0 = \int_{-\infty}^{x_t} P_{\text{bkd}}(x)dx \tag{2.112}$$

$$F_1 = \int_{x_t}^{\infty} P_{\text{atom}}(x)dx \tag{2.113}$$

such that $F = (1 - f)F_0 + fF_1$. It is possible to adjust $x_t$ such as to favor one or the other of these. For example, if one wants to avoid false positives as much as possible but does not care about potentially "missing" some atoms (false negatives), then $x_t$ can be increased beyond its optimal value for $F$.

### *Survival*

If we care about the atom still being there after imaging (and in tweezer array platforms we very much do care about this — see Sec. 2.7.3), then imaging fidelity is only half the battle. We also need to optimize for *survival*: the probability that an atom which was present at the start of the imaging process is still there after the end of the imaging process. We will denote survival by $S$.

If we had an imaging scheme that had perfect fidelity ($F = 1$), this would be easy to measure: one just takes two consecutive images and computes the probability that an atom is detected in the second image, conditional on it being detected in the first. We will call the result of such a measurement $S_0$ (even if $F < 1$). If $F = 1$, then $S = S_0$. If $F < 1$, as it realistically always is, then $S_0$ needs to be corrected for imaging errors before being interpreted as the true survival. We note that in our works Ref. [89, 116], the reported value of survival was in fact $S_0$ and

not $S$. However, the fidelity $F$ in both works was high enough for this to be a good approximation.

$S_0$ is given by the probability of positive detection in both images divided by the probability of positive detection in the first image. Under the assumption of a filling fraction $f = 0.5$, this is given by:

$$S_0 = \frac{F_1^2 S + F_1(1-F_0)(1-S) + (1-F_0)^2}{F_1 + (1-F_0)} \tag{2.114}$$

where $F_0$ and $F_1$ are defined in Eqs. 2.112–2.113. Inverting for $S$, we get

$$S = \frac{(F_1 + 1 - F_0)(S_0 + F_0 - 1)}{F_1(F_0 + F_1 - 1)} \tag{2.115}$$

This calculation assumes that both images have the same fidelities, but a similar calculation is possible if that is not the case.

Finally, we note that survival itself may enter into the calculation of $F_1$, as an atom may be lost during imaging *before* it scatters enough photons to be positively detected, which reduces $F_1$. Such a situation requires an independent model for loss (such as the exponential model described in Sec. 2.6.8).

***Model-free calculation of fidelity and survival***

We have so far discussed computing imaging fidelities $F_0, F_1$, and $F$ by fitting signal histograms. These values also enter into our corrected survival $S$. However, this approach can be highly dependent on the functional form of the histogram in its low-probability wings. Here we present an approach to computing fidelities and true survival that does not depend on a model function. Although we have not used this approach in our work, we confirm that it computes fidelities and survivals at least as high as those reported in Ref. [116]. Note that a similar approach is outlined in Appendix B5 of Ref. [97].

Unlike the fitting approach, this approach requires two back to back images and computes all of $F_0, F_1, F$, and $S$ directly and simultaneously. For some choice of classification threshold, let $x_1$ be one if an atom is detected in the first image and zero otherwise, and let $x_2$ be the same for the second image. Then we define $p_{x_1 x_2}$ as the probability of detecting the sequence $x_1 x_2$. Enumerating all

probabilities, we have

$$p_{11} = fF_1^2S + (1-f)(1-F_0)^2 + fF_1(1-S)(1-F_0) \tag{2.116}$$

$$p_{10} = fF_1S(1-F_1) + fF_1(1-S)F_0 + (1-f)(1-F_0)F_0 \tag{2.117}$$

$$p_{01} = f(1-F_1)SF_1 + f(1-F_1)(1-S)(1-F_0) + (1-f)F_0(1-F_0) \tag{2.118}$$

Note that $p_{00} = 1 - \left(p_{11} + p_{10} + p_{01}\right)$ and $f$ is the filling fraction. Here we have assumed that if an atom is not present (note, present is not the same as detected) during the first image, it must also not be present during the second image. I.e., there is no hopping or filling of atoms after the initial filling. Furthermore, we have assumed both images to have the same fidelities. A final subtle point is that we have assumed no correlation between detection and survival in the first image, which may not be entirely true.

One can now solve Eqs. 2.116–2.118 for $F_0, F_1, S$ in terms of $p_{11}, p_{10}, p_{01}$, and $f$. There will generally be two solutions, and typically one can be rejected as it will indicate a fidelity below 0.5. Finally, one can define the overall fidelity by $F = fF_1 + (1-f)F_0$.

$p_{11}, p_{10}, p_{01}$ are directly measurable for a given classification threshold, but $f$ must be assumed (which is the same situation when using the fitting approach). One typically assumes $f = 0.5$ on physical grounds (Sec. 2.4.2), however, the resulting values of $F_0$ and $F_1$ can be highly sensitive to even small fluctuations in $f$, and may even end up being higher than 1, which is unphysical. There is typically a narrow domain of $f$ for which the values of $F_0$ and $F_1$ are both physical, which predicts a narrow range of possible physical values for $f, F_0, F_1, F$, and $S$.

### 2.6.8 Results

We now report on the results of our imaging at two different trap wavelengths: 515.2 nm [89] and 813.4 nm [116]. In both results, we will be imaging photons on the blue (461 nm) transition while cooling on the red transition. However, in Sec. 2.6.8 we will also discuss imaging on the red (689 nm) transition.

***For traps at 515.2 nm***

***Note: This section presents results from our publication Ref. [89].***

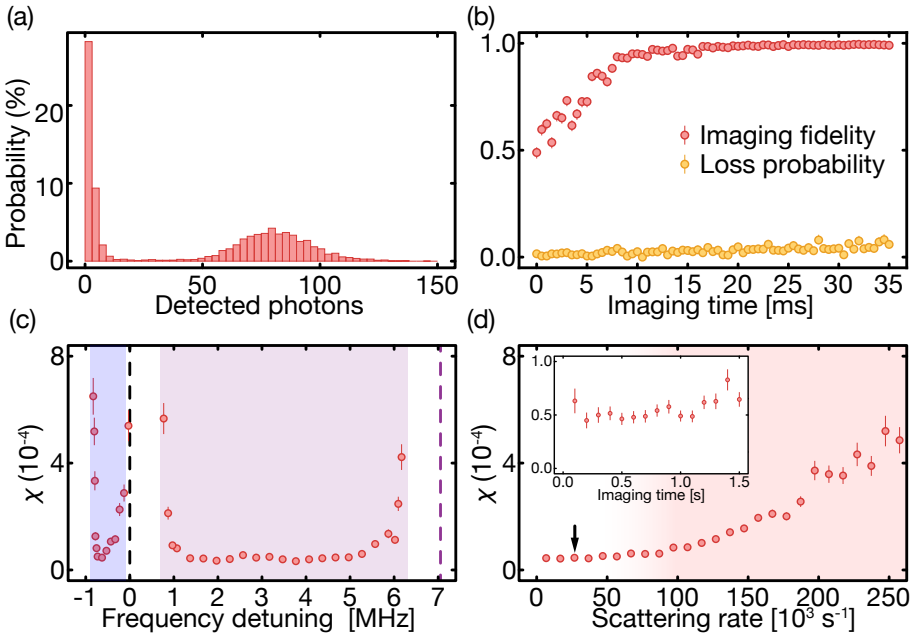


Figure 2.21: Results of imaging on the blue transition while cooling on the red transition in $\lambda = 515.2$ nm tweezers at a trap depth of 1.4 mK. All data is for a single tweezer. **(a)** A histogram of detected photons, showing well-defined zero-atom and single-atom peaks. However, note that there is a small "bridge" of counts between these two peaks, making them not fully resolved. We attribute this bridge to loss, as will be discussed in this section. **(b)** Imaging fidelity and loss probability as a function of imaging time for optimal imaging parameters. **(c)** Loss coefficient $\chi$ (defined in this section) as a function of relative red cooling frequency, where 0 is the free-space resonance. Two regions are optimal, corresponding to magic cooling (blue region) and non-magic cooling (purple region). The horizontal axis is $\Delta/(2\pi)$. **(d)** Loss coefficient as a function of scattering rate. For small enough scattering rates, the loss coefficient saturates to a minimal value. Beyond roughly $60\times10^3$ s$^{-1}$, heating begins to dominate loss (red region). Inset: Loss coefficient as a function of imaging time at the scattering rate indicated by an arrow in the containing figure.

The high available power, large polarizability, and tight waist of 515.2 nm traps allows for deep and tight traps. We are thus able to achieve relatively large trap depths of 1.4 mK in this wavelength while still allowing for large array sizes (Sec 2.7.1). However, note that the results reported in this section were obtained with a single tweezer. Also note that this is the same tweezer as the one probed by sideband spectroscopy in Fig. 2.15.

Fig. 2.21 shows optimized results of imaging in $\lambda = 515.2$ nm tweezers under a magic ellipticity for the red transition [89]. We measure an imaging fidelity of $F = 0.993(9)$ for sufficiently long imaging times (>20 ms). Fluorescence collection of blue photons is done through the tweezer-generating objective, and in addition fluorescence collected through the opposing objective is retro-reflected back to the camera. Cooling is provided during imaging by retro-reflected and piezo-modulated red beams in all three directions. We find there to be two regions of red detuning that give optimal cooling, one in a narrow (∼100 kHz) range of red detunings, and another in a much broader range (∼4 MHz) of blue detunings. We attribute the red-detuned feature to magic sideband cooling to the $|A(\gamma)\rangle$ state of the red transition, while the broad blue-detuned feature is non-magic cooling to the $|B(\gamma)\rangle$ state, which is more weakly trapped than the ground state (see Sec. 2.3.4 for a definition of these states). Thus, on the broad blue detuned cooling feature, we expect a repulsive Sisyphus mechanism to exist (Sec. 2.5.2 & 2.5.2). This prediction is supported by the fact that we observe similar fidelities when cooling with only a single beam instead of the multiple beams which were used for recording of the reported data.

While the imaging fidelity achieved is appreciably high, the survival is unfortunately not as remarkable. At an imaging time of 20 ms, we report an uncorrected survival (Sec. 2.6.7) of $S_0 \sim 0.97$. Fig. 2.21 (b) shows that the loss (defined as $1 - S_0$ in the language of Sec. 2.6.7) increases linearly as a function of time. We find that, below a certain scattering rate, loss per scattered photon does *not* continue decreasing with scattering rate (Fig. 2.21 (d)), suggesting that heating due to scattering is not the limiting factor in this regime.

We ultimately find in this non-heating-dominated and cooling-optimized regime that survival depends solely on the number of photons scattered $N$. In particular, we find that survival is well-modeled by an exponential dependence on $N$ by $S_0 = e^{-\chi N}$, where $\chi$ is an experimentally determined *loss coefficient*. This exponential loss manifests as a "bridge" between the zero-atom and single-atom peak in the histogram of Fig. 2.21 (a) and prevents full resolution of the two peaks. Note that we take this loss model into account in our calculation of the imaging fidelity, as briefly discussed in Sec. 2.6.7. $\chi = -\ln(S_0/N)$ is the value plotted in Fig. 2.21 (c,d) (lower $\chi \rightarrow$ higher survival). This value is computed by measuring $S_0$ as well as an estimate of the number of photons scattered by the atom during imaging obtained via the number of photons detected on the camera and an estimate of the collection efficiency of our imaging system (see Ref. [89] Appendix E2). The inset of Fig. 2.21 (d) shows

that $\chi$ is insensitive to the time that an atom is imaged for.

The observation of an exponential dependence of survival on the number of scattered photons is consistent with a loss mechanism in which every scattered photon carries with it a probability of losing the atom. This is again inconsistent with any kind of heating or motional mechanism, as a single scattered photon should not be able to expel an atom that is cooled to low temperatures. Indeed, for heating-dominated loss, one finds that the loss rate is initially low while the atom is cold and then rapidly increases once the atom's energy becomes comparable to the trap depth. This cannot be modeled by a simple exponential.

Our interpretation of such behavior is instead that each scattering event holds a small probability of putting the atom in some unrecoverable electronic state. For the blue transition in Sr, an immediately suspicious candidate is the small 5s5p $^1$P$_1$ $\rightarrow$ 5s4d $^1$D$_2$ leakage channel. Indeed, one finds that this state has a highly unfortunate transition 5s4d $^1$D$_2$ $\leftrightarrow$ 5s4f $^1$F$_3$ at 515.75 nm. For our trapping wavelength of $\lambda$ = 515.2 nm, this makes this state *highly* anti-trapped (Sec. 2.3.4). Furthermore, the lifetime of 5s4d $^1$D$_2$ is a fairly long ~300 $\mu$s [133], whereas numerical simulation suggests that anti-trapping expels atoms from 5s4d $^1$D$_2$ within a few $\mu$s. Therefore, it is reasonable to expect that practically all atoms that decay to 5s4d $^1$D$_2$ will be lost.

If we assume all decay into 5s4d $^1$D$_2$ results in loss, $\chi^{-1}$ provides a lower bound for the branching ratio $\frac{5s5p\ ^1P_1 \rightarrow 5s^2\ ^1S_0}{5s5p\ ^1P_1 \rightarrow 5s4d\ ^1D_2}$. This is a lower bound as we have not ruled out other loss mechanisms. Under optimized cooling and scattering rate parameters, we measure $\chi^{-1}$ to be in the range of $17(3) \times 10^3$ to $24(4) \times 10^3$. The source of the systematic uncertainty is uncertainty of the collection efficiency of our imaging system stemming from uncertainty in the dipole radiation pattern (see Ref. [89] Appendix E2). *Ab initio* theory performed by our collaborators (Ref. [89] Appendix A4) actually predicts a value for this branching ratio approximately equal to our measured lower bound, which suggests that decay into 5s4d $^1$D$_2$ is the dominant loss mechanism. We note, however, that this branching ratio differs significantly from the widely quoted value of $50 \times 10^3$ measured in Ref. [134]. We do *not* claim a refutation of this previously reported value, and leave a resolution of this disagreement to further study.

We note here the possibility of repumping 5s4d $^1$D$_2$ before it has a chance to expel the atom. We tried such a scheme by applying a beam at 717 nm, targeting the 5s4d $^1$D$_2$ $\rightarrow$ 5s6p $^1$P$_1$ transition which should quickly decay back to the ground

state [133]. However, we saw no appreciable gain with this scheme, and attribute its failure to the very large magnitude of anti-trapping. We also note that the laser which was available to us at 515.2 nm was not tunable, and there is reason to believe that tuning beyond the resonance at 515.75 nm may alleviate losses from 5s4d $^1D_2$. There is indeed no particular reason why 515.2 nm exactly should be used except that high power lasers exist at that wavelength. Note that — very unfortunately — 532 nm suffers from an essentially identical problem (Sec. 2.3.4).

Finally, we note there are additional observed losses of 5s5p $^3P_1$ (the excited state of the red transition) at this trapping wavelength. These losses are most clearly observed when exciting exclusively on the red transition, but are also in principle present when cooling with the red during blue imaging. These losses are *not* alleviated by the 679 nm and 707 nm repump beams. We note that Ref. [97] also observes such losses and hypothesizes a plausible loss channel via 5s5d $^3D_{1,2}$.

***For traps at 813.4 nm***

***Note: This section presents results from our publication Ref. [116].***

We now move to imaging at the clock-magic wavelength $\lambda = 813.4$ nm. Here, 5s4d $^1D_2$ is trapped. Furthermore, the longer wavelength can be reasonably expected to suppress losses on the red transition as it should be much further detuned from any transitions.

Indeed, the results for imaging at this wavelength are highly positive. From a dataset of 10,000 pairs of subsequent images at 50 ms exposure in an array of 25 atoms spaced at 7 $\mu$m, we measure [116] an array-averaged imaging fidelity of $F = 0.99991(1)$ and a survival of $S_0 = 0.99932(8)$ (with $S_0$ as defined in Sec. 2.6.7). The very high survival of this imaging scheme is exemplified in our ability to repeat imaging of atoms more than 2000 times while only losing about half of them, as shown in Fig. 2.22 (b). We note that between all subsequent images, there is a 29 ms dead time of only cooling.

Cooling is provided by a single, non-retroreflected red beam along the radial tweezer direction, as shown in Fig. 2.16 (a). The intensity of this red beam is estimated to be at 1000 $I_{\text{sat}}$. We find a broad range of red-detuned frequencies for the red transition that provide effective cooling during imaging, as shown in Fig. 2.22 (c). We excite on the red transition to the $|m_J^x = \pm 1\rangle$ excited states, which are more trapped than the ground state for 813.4 nm tweezers (Sec. 2.3.4), resulting in an

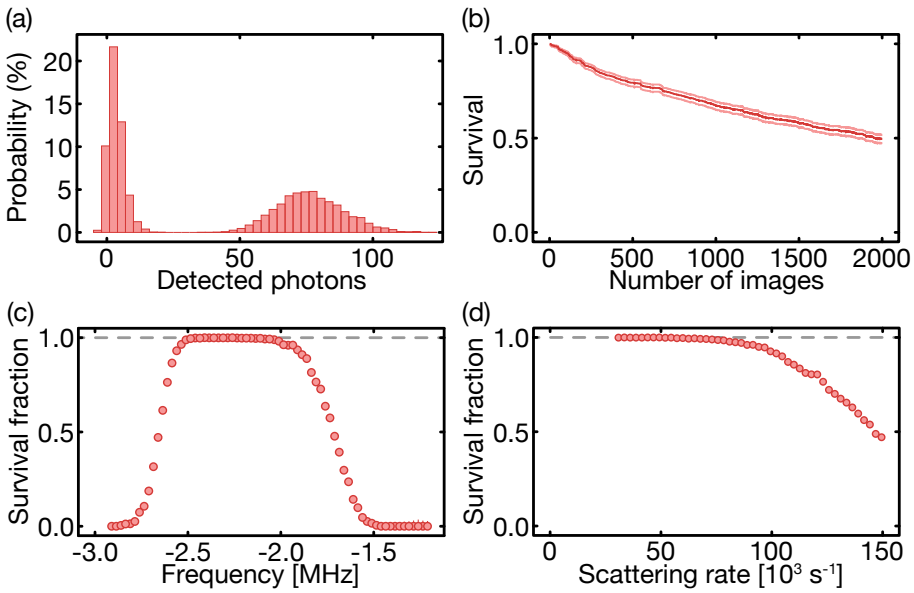


Figure 2.22: Results of imaging on the blue transition while cooling on the red transition in $\lambda = 813.4$ nm tweezers at a trap depth of $k_B \times 0.5$ mK. All data is for a 50 ms exposure time, and all data except that in (a) is averaged over an array of 25 tweezers. **(a)** A histogram of detected photons from a single representative tweezer, showing well-defined zero-atom and single-atom peaks. **(b)** Survival over multiple images versus number of images taken. Light red lines indicate $\pm 1\sigma$ statistical error. There is a 29 ms dead-time between subsequent images. **(c)** Survival during imaging as a function of relative frequency of the red cooling beam. Zero is the free-space resonance of the red transition. The horizontal axis is $\Delta/(2\pi)$. $I \sim 1000 I_{sat}$. **(d)** Survival as a function of estimated scattering rate of blue photons.

energy *attractor* during cooling (Sec. 2.5.2). Finally, excitation on the red transition does not appear to induce any significant loss rate, and indeed continuous cooling on the red transition allows for an observation of $> 7$ min lifetimes of trap occupation (Sec. 2.6.8). Note that 679 nm and 707 nm repump beams are always on during imaging and cooling, as shown in Fig. 2.16.

In conclusion, trapping at 813.4 nm — in addition to its benefit of being magic for the clock transition — allows for significantly increased imaging fidelities and survival over trapping at 515.2 nm, as well as elimination of the losses seen on the red transition when trapping with 515.2 nm. The approximately percent-level gain of fidelity and survival may not seem like much, but in fact it is highly important for repeated imaging, for the preparation of large, defect-free arrays (Sec. 2.7.3), and for minimizing state preparation and measurement errors in all applications such as atomic clocks (Sec. 3.4.6) and quantum operations (Sec. E). *We will therefore from*

*this point forward assume all trapping is done with 813.4 nm.*

A takeaway lesson to be had from the comparison of 515.2 nm and 813.4 nm is to treat all "unproven" trapping wavelengths with suspicion until they are demonstrated to work well, *especially* ones toward shorter wavelengths. Although we now know about the problems with 5s4d $^1D_2$ as well as those on the red transition, we had not even considered them before beginning our explorations at 515.2 nm. One can try one's best to be as careful as possible in selecting a wavelength, but it is advised to have an understanding that numerous unanticipated things can go wrong.

***Lifetimes at 813.4 nm***

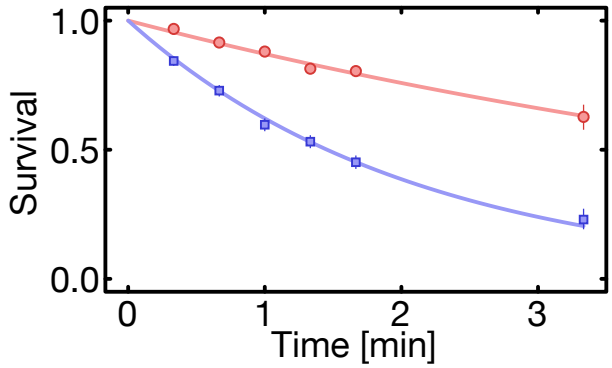


Figure 2.23: Trap occupation lifetimes in $\lambda = 813.4$ nm tweezers. Data is averaged over a stochastically filled array of 25 tweezers. The red data corresponds to a lifetime while cooling on the red transition with a single cooling beam. The blue data corresponds to a lifetime while imaging and cooling under the parameters discussed in Sec. 2.6.8. Curves are fits to exponential decay. For the red data, we find a lifetime of 434(13) s, while for the blue we find 126(3) s.

The very high survival observed in Sec. 2.6.8 is a testament not only to the quality of our imaging procedure, but also suggests that we have minimized all other processes that may kick an atom out of a trap. One of these potential processes is collisions with background gases. For optical traps, the achievable trap depths are typically orders of magnitude smaller than the energy scales of collisions with background gases. This means that any collision "event" expels an atom from the trap with near 100% certainty, and that there is no way to mitigate this large energy transfer with, e.g., cooling or making the trap deeper. This leads to an exponential decay of trap occupation as a function of time, with a timescale we will call the *vacuum lifetime*. For optical traps, the vacuum lifetime is purely a function of the quality of the vacuum in the experimental chamber.

Fig. 2.23 shows (in red) the lifetime for an atom to remain in the trap while being cooled on the red transition (with a single non-retroreflected beam) and also illuminated by 679 nm and 707 nm repump beams. We measure [116] an exponential lifetime of 434(13) s, or about 7.23(22) min. This provides a *lower bound* for our vacuum lifetime, as we have not ruled out any other possible limiting timescales (e.g., it is possible there is a very slow population of some unrecoverable state). This value was re-measured a little over a year after its initial measurement and was found to be reproducible.

The blue curve shows a similar measurement but this time while imaging under the conditions discussed in Sec. 2.6.8. Here we measure an exponential lifetime of 126(3) s, showing that scattering blue photons does lead to a measurable amount of excess loss. We have not determined whether this comes predominantly from heating or from population of unrecoverable states. We note that our typical imaging sequence involves only 50 ms of imaging. The lifetime measured under imaging predicts a loss of $4 \times 10^{-4}$ for a 50 ms pulse, whereas the value we measured with a two-image sequence (uncorrected for imaging fidelity) was $6.8 \times 10^{-4}$ (Sec. 2.6.8). We note that the two-image scheme does have a 29 ms dead-time in between.

Finally, we discuss our measured lifetimes *without* cooling or imaging. That is, the lifetime of just an atom in a trap. The first observation for this lifetime is that it does not follow an exponential decay. Instead, we observe that the loss rate is initially low and gradually becomes larger. This is consistent with loss via heating. The timescale on which this loss reaches 50% is typically ~20 s, but depends strongly on trap parameters such as trap depth and spacing between neighboring tweezers. This latter effect of array spacing matters due to interference between the light of neighboring tweezers, creating intensity fluctuations that can heat an atom (Sec. 2.5.3 and Sec. 2.7.1).

#### *Imaging on the red transition*

All discussion of imaging so far has been by use of a blue imaging beam and the collection of blue (461 nm) photons on a camera. However, we have also observed high-fidelity and high-survival imaging by simply illuminating an atom in a $\lambda = 813.4$ nm trap with a single red beam and collecting *red* (689 nm) photons.

We find that a single beam with a single detuning is sufficient to both scatter photons and keep the atom from heating out of the trap — likely a benefit of having an energy

*attractor* (Sec. 2.5.2) on the non-magic red transition. While we have not done a thorough study on this regime and thus will not quote exact numbers for fidelity and survival, our preliminary data suggests that they are at least comparable with the numbers quoted in Sec. 2.6.8. We note the similarity of this scheme to the one used for imaging single Ytterbium atoms in Ref. [83].

This incredibly simple imaging scheme does have a few drawbacks, however. The first is that the maximal scattering rate of the red transition is only $23.6 \times 10^3$ s$^{-1}$, whereas we have shown that high-fidelity-and-survival imaging on the blue transition can support scattering rates of up to $\sim 75 \times 10^3$ s$^{-1}$ at our trap depths (Fig. 2.22) (with the maximal scattering rate of the blue transition being $94.2 \times 10^6$ s$^{-1}$). This means that red imaging generically requires a longer imaging time than blue imaging to achieve the same fidelity. However, for shallower traps where a very low scattering rate is necessary anyway, red imaging may be a good choice.

Furthermore, the diffraction-limited size of the PSF on the 689 nm red transition is 1.5 times bigger than that on the 461 nm blue transition (Sec. 2.6.5).

Finally, we note that 679 nm and 707 nm repump beams (Fig. 2.6.1) *are* still necessary when imaging (or exciting, in general) on the red transition as Raman scattering can occur via the trap light from 5s5p $^3$P$_1$ to 5s5p $^3$P$_{0,2}$. These repump wavelengths are unfortunately close to 689 nm and therefore may be a source of background photons even when using a relatively narrow optical filter.

## 2.7 Tweezer arrays

We now turn our attention to the creation of multiple copies of a tweezer to create a *tweezer array*. We will discuss techniques for generating arrays, for ensuring that all tweezers in an array are as identical as possible (uniformization), and for moving tweezers around (rearrangement). Rearrangement is a *key* feature of tweezer arrays, particularly in the context of entanglement and many-body physics, as it allows us to overcome the stochastic initial filling of tweezers (Sec. 2.4.2) to create an array with a contiguous block of single atoms and no empty tweezers in between. We call such arrays *defect-free*.

### 2.7.1 Generation via acousto-optic deflectors

Several technologies are available for generating tweezer arrays. The most commonly used are acousto-optic deflectors (AODs) [48, 83, 89, 97] and spatial-light

modulators (SLMs) [45, 46, 135]. While we have been engaged in a parallel effort to implement SLMs (see Ref. [136]), all results in this work were done using AODs and that is what we will focus on in this section.

Figs. 2.24–2.25 show typical averaged atomic fluorescence images of a 1- and 2-dimensional array, respectively.



Figure 2.24: An averaged image of atomic fluorescence in a 1D array of 61 tweezers spaced by 3.1 $\mu$m.

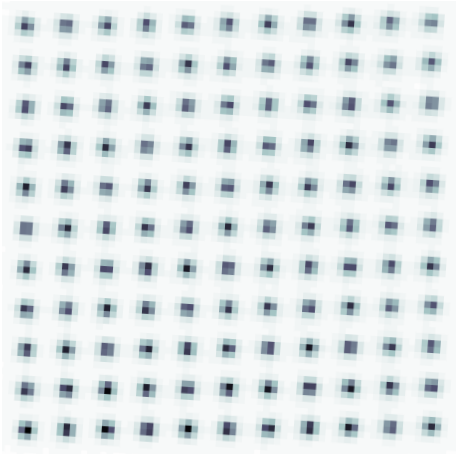

Figure 2.25: An averaged image of atomic fluorescence in a 2D array of 11×11 = 121 tweezers spaced by 9 $\mu$m [89]. Note that the PSF in this image was significantly broadened by aberrations from the camera window. This was later alleviated, as shown in Fig. 2.24.

### *Principle*

An AOD deflects an optical beam by creating a traveling acoustic wave inside a crystal*. The resulting diffraction can be analyzed with classical optics [137], but for intuitive purposes it is easiest to envision the process as an interaction between photons and phonons. Under an appropriate Bragg condition, the light, having an angular frequency and wavevector $\omega_i = c|\vec{k}_i|$, can either absorb or emit a phonon of angular frequency and wavevector $\omega_s = c_s|\vec{k}_s|$, where $c_s$ is the speed of sound in the crystal. In fact, this process can happen multiple times, and we call the net

*AODs are very similar to acousto-optic *modulators* (AOMs), but are more optimized for beam deflection.

number of phonons absorbed the *order* of diffraction. For the purposes of array generation, we will only consider the positive first order (i.e. one absorbed phonon), but it should be kept in mind that other orders do exist.

By conservation of energy and momentum, the diffracted light must have angular frequency $\omega_f = \omega_i + \omega_s$ and wavevector $\vec{k}_f = \vec{k}_i + \vec{k}_s$. Note that the Bragg condition for this is

$$\begin{aligned} \cos(\theta_{\text{Bragg}}) &= \hat{k}_i \cdot \hat{k}_s \\ &= \frac{1}{2}\left(\frac{c_s^2 - c^2}{c c_s}\right)\frac{\omega_s}{\omega_i} + \frac{c_s}{c} \end{aligned} \tag{2.119}$$

For typical optical and acoustic parameters, this is usually very close to 90° and varies very little with changing of $\omega_s$ over the typical dynamic range. For example, with an 813.4 nm light beam, a center acoustic frequency of $\omega_s = 2\pi \times 100$ MHz with a spread of $\Delta\omega_s = \pm 2\pi \times 20$ MHz, and a speed of sound of the $TeO_2$ crystal's shear mode of $c_s = 617$ m/s, the central Bragg angle is $\theta_{\text{Bragg}} = 90.8°$ with a variation over the dynamic range of $\omega_s$ of $\Delta\theta_{\text{Bragg}} = 0.16°$. The finite variation of both $\hat{k}_i$ and $\hat{k}_s$ in the crystal allows for accommodation of this range of Bragg angles.

Of particular interest to us is the deflection of the angle of the incoming wavevector. Since the Bragg angle is nearly 90°, the deflection angle $\theta$ between $\vec{k}_i$ and $\vec{k}_f$ is given very nearly by

$$\tan\theta \approx \frac{c}{c_s}\frac{\omega_s}{\omega} \tag{2.120}$$

For a typical center acoustic frequency of $\omega_s = 2\pi \times 100$ MHz at an optical wavelength of 813.4 nm, this gives a deflection angle of 7.5°. However, what we really care about is small variations $\Delta\omega_s$ around this center frequency and the resulting further deflection $\Delta\theta$ from this central deflection angle. Since all the angles we are working with are sufficiently small, the sine and tangent functions are both approximately linear. Dropping all approximation signs, we find that $\sin(\Delta\theta) = \frac{c}{c_s}\frac{\Delta\omega_s}{\omega}$.

If we put the AOD at the focal plane of a lens of focal length $f$ such that $\Delta\theta = 0$ is the direction along the lens' optical axis, that lens will collimate the light ray deflected at $\Delta\theta$ to a ray which is parallel to the optical axis and which is at a distance of $\Delta x = f\sin(\Delta\theta)$ from the optical axis. Finally, we obtain

$$\Delta x = f\frac{c}{c_s}\frac{\Delta\omega_s}{\omega} \tag{2.121}$$

Thus, if we put the crystal of the AOD (or optically map it) to the input focal point of the objective that creates our tweezer, we can shift the position of the tweezer along a direction orthogonal to the tweezer axis. The distance by which the tweezer is shifted is directly proportional to the frequency of the applied acoustic wave.

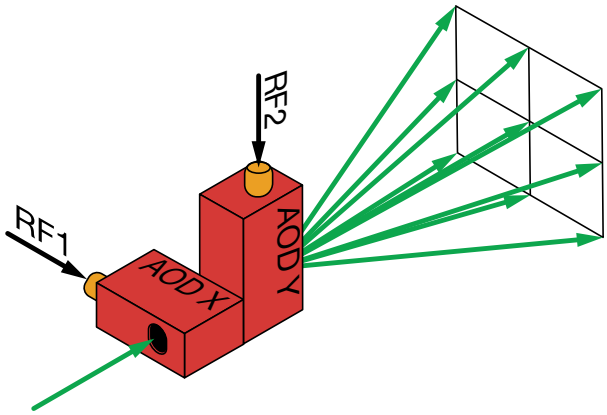


Figure 2.26: Two AODs at an orthogonal angle producing a two-dimensional spread of diffraction angles. RF1 and RF2 label the acoustic signals sent to both devices. While the angle between the AODs here is 90°, different angles can be used, producing tweezer arrays of varying lattice geometries. In practice, it is best to optically map the crystal of one AOD into the crystal of the second AOD, which can be done by a one-to-one optical telescope between the two devices (not shown).

The creation of an array is only a simple extension of this principle. Instead of driving the crystal with a sinusoidal signal of a single frequency, we drive it with a signal that is a sum of several discrete frequencies. Assuming interference effects are negligible (see discussion of phase in Sec. 2.7.1), the result will be an array of tweezers, with each tweezer's position corresponding to one acoustic frequency. This can furthermore be extended to two dimensions by optically mapping the crystal of one AOD into a second AOD that is rotated by some angle. Fig. 2.26 illustrates this concept.

Although we are in principle able to generate at least 100 tweezers in 1D, the maximum workable size we have used is 81 tweezers [138] at a spacing of 2.5 $\mu$m, and even here the small spacing introduces some issues (Sec. 2.7.1). Given the limit on how tightly tweezers can be spaced, the limits to the array size come in part from the bandwidth of our AOD, the field of view of our objective, and the available laser power.

***Acoustic signal and choice of phase***

Let us examine the signal $A(t)$ sent to an AOD to produce a (1D) tweezer array of $N_t$ tweezers:

$$A(t) = \sum_{i=1}^{N_t} A_i \cos\left(\omega_i t + \phi_i\right) \tag{2.122}$$

We define such a signal digitally, and upload it to an arbitrary waveform generator (AWG) for output to the AOD (App. A.5).

We have three degrees of freedom per tweezer (in 1D): the frequency $\omega_i$ which determines the position via Eq. 2.121, the amplitude $A_i$ which determines the intensity of the tweezer (by an ideally quadratic $I_i \propto |A_i|^2$ relation, up to saturation), and the phase $\phi_i$ which at first glance does not seem obviously important.

However, it is found in experiment that $\phi_i$ must be chosen to be roughly uniformly distributed in $[0, 2\pi)$ to avoid severe non-uniformities and cross-talk (dependence of one tweezer's intensity on others) in the array. A plausible explanation for this is that a choice of $\phi_i$ which are mostly similar leads to large instantaneous spikes in $A(t)$. This then creates significant frequency mixing due to non-linearities in the system.

Further optimization of phase choice may be made to explicitly minimize non-linear mixing [48]. The idea here is that non-linearities (in the electronic or acoustic domain) can mix the frequencies $\omega_i, \omega_j$ to both $(\omega_i + \omega_j)$ and $(\omega_i - \omega_j)$. These can then be further mixed back into the original domain. In this way, cross-talk between different tweezers can happen. For example, assume that our signal has components at 100 MHz, 101 MHz, and 102 MHz. One possibility is that the 101 MHz and 100 MHz components mix to produce a signal at 1 MHz. This is then mixed again with the signal at 101 MHz to produce a second-order-mixed signal at 102 MHz, interfering with and altering the amplitude of the original signal at 102 MHz. To mitigate this, it is possible to choose the phases $\phi_i$ to minimize such mixing. It is furthermore possible to do this without a detailed knowledge of the non-linear process by e.g. just assuming that it is approximately quadratic in amplitude. We omit a discussion of a specific algorithm to do this, and point the reader to Ref. [48] for a discussion.

Finally, it is important to ensure that there are no sudden jumps in the phase of the waveform. An AWG realistically generates a finite length waveform that is then repeated indefinitely. The length of this waveform should be chosen such that it is

commensurate with all of the frequencies $\omega_i$ so that the waveform does not have a discontinuous phase jump when it repeats. We find that if this condition is *not* met, heating and loss of atoms results due to deformation of the tweezers during the phase jump.

***Optical interference and overlap***

A side-effect of AODs is that each tweezer's optical frequency is slightly different, as given by $\omega_f = \omega_i + \omega_s$. For tweezer arrays spaced sufficiently far enough such that optical interference is minimal, this shift usually has practically no measurable effect on any relevant physics — with the notable exception of ultra-narrow spectroscopy on the clock transition (Sec. 3.1.2, Fig. 3.6, and Refs. [100, 138]).

However, this does become an overall issue when the spacing between neighboring tweezers becomes sufficiently small. It was shown in Fig. 2.3 that real tweezers have outer rings in their optical profile, which can interfere with the central trapping regions of neighboring tweezers, causing a fluctuation of the trap. Even though these outer rings are fairly small in amplitude, this fluctuation can be significant enough to heat atoms. It is particularly unfortunate that the slow frequency of this fluctuation, which is given by $\omega_{i+1} - \omega_i$, is usually close to twice the trap frequency for spacings where interference becomes significant, which is especially bad for heating (Sec. 2.5.3). Indeed, bringing tweezers close together typically increases heating for two reasons: the optical overlap increases and the frequency difference approaches twice the trap frequency. This can potentially be alleviated by using shallower tweezers, though that of course brings its own problems.

We note that spatial light modulators (SLMs) in principle do not have such an interference issue as they produce an array by imprinting a static phase pattern on light, not by modulating it.

In addition to interference of the outer rings, the trapping regions of neighboring tweezers may start significantly overlapping. This may allow sufficiently hot atoms to leave the tweezer they were originally in and enter a neighboring one. This is undesired. We have found that such events happen (rarely, but observably) when imaging atoms in arrays of trap depth $k_\mathrm{B} \times 0.5$ mK spaced below 3 $\mu$m. Mitigating this could involve using deeper tweezers or using slower scattering rates so as to keep atoms colder while imaging.

Finally, we note that spatial resolution of the imaging system (Sec. 2.6.5) also becomes a limiting factor at particularly small spacings ($< 3\ \mu$m).

### 2.7.2 Uniformization

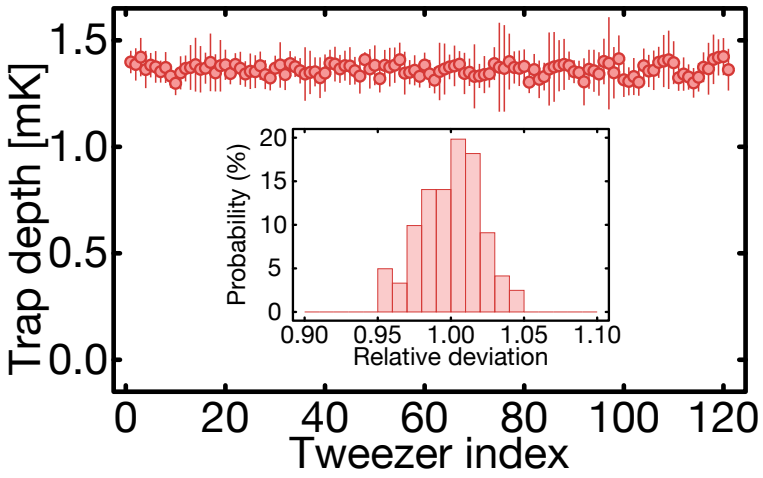


Figure 2.27: Trap depths for tweezers in an $11 \times 11$ 2D array (such as the one in Fig. 2.25), measured by spectroscopy on the narrow red transition under a non-magic condition [89]. Inset: a histogram of the relative deviation from the mean. The standard deviation is 2%.

It is highly beneficial to have each tweezer in an array be as identical as possible. There are three main things that can vary between tweezers in an array: (1) intensity, (2) polarization, and (3) geometry such as the shape or orientation of a tweezer. In this section we will focus on items (1) and (2), and only comment that (3) is a function of the quality of the optical setup generating the tweezers. Inter-tweezer spacing is also something that can potentially vary across an array, but is in principle easily corrected by appropriate choice of AOD signal frequencies. Also notable is that externally applied global fields, such as optical beams or magnetic fields, can have local variation across the array.

Items (1) and (2) are particularly important in Sr, particularly in the context of cooling on the red transition. As the red transition is fairly narrow (7.5 kHz), it can be detuned significantly by even few-percent variations in the differential light shift from the trap. We showed in Sec. 2.3.1 that the differential light shift is proportional to intensity (at least in the case of non-magic traps), and in Sec. 2.3.3 we discussed how tweezer polarization can also significantly affect the light shift. If either of

these factors creates a significantly non-uniform differential light shift across the array, cooling and generically exciting on the red transition will suffer.

We comment here on the potential appeal of choosing a magic-trapping condition on the red transition (Sec. 2.3.4), such that the differential polarizability is zero for all trap intensities. This can easily be done for a single tweezer at both 515.2 nm and 813.4 nm wavelength tweezers by using a magnetic field with an appropriate angle to the tweezer polarization. However, the burden of uniformity is now placed entirely on the tweezer polarization (and to some extent on the field, though it is relatively easy to homogenize on the length scales of an array). Furthermore, note that the differential polarizability at a magic field angle may be more *sensitive* to fluctuations in the tweezer polarization (Sec. 2.3.3). In practice, we find that even with a nominally magic field angle and a careful optical setup, there are still typically measurable light shifts originating from polarization non-uniformities.

The main problem with this is that tweezer polarizations are not individually *tunable*. On the other hand, tweezer intensities *are*, and quite easily so: one simply needs to adjust the $A_i$ in the signal sent to the AOD (Eq. 2.122). This is easily done digitally*. Therefore, it can be argued that having a finite differential light shift is actually *beneficial* to uniformizing an array, as it affords one a knob over which one has a very high degree of control. As a final note on this, we note the existence of wavelengths for which the red transition can in principle be made insensitive to both intensity and polarization; for a discussion on this, see Sec. 2.3.3.

Therefore, we typically work in a regime where the differential light shift is finite and tunable. To be explicit, we typically use a configuration where the tweezer polarizations are orthogonal to a strong externally applied magnetic field, and this field is also orthogonal to the direction of propagation of the tweezers. We then target the Zeeman-insensitive state of the red transition for all cooling and excitation, which has a polarizability equal to that of the states labeled $|m_J^x = \pm 1\rangle$ in Fig. 2.6 — although the appropriate label of the state in this circumstance would be $|m_J = 0\rangle$.

Uniformization of the differential light shift then proceeds as follows:

1. Measure a spectroscopic signal on the red transition that informs on the differential light shift for each tweezer.

*This would appear to work only for 1D arrays created by an AOD, as a 2D array generated by crossed AODs does not provide amplitude control of each individual tweezer — only over rows and columns. However, we experimentally find that an $11 \times 11$ 2D array can be uniformized to within 2% standard deviation using only control over rows and columns (Ref. [89] and Fig. 2.27).

2. Compute *adjustment factors*, which are numbers by which each tweezer's intensity should be multiplied in order to obtain a uniform differential light shift, as well as the desired mean value of this shift.

3. Image the tweezer light (not the *atom* fluorescence) onto an auxiliary camera and record the observed integrated intensity of each tweezer.

4. Adjust $A_i$ (as defined in Eq. 2.122) until the intensities measured on the camera are equal to the product of the originally imaged intensities times the determined *adjustment factors*.

5. Repeat item (1) to verify uniformity. If uniformity is not sufficient, repeat the process.

The "spectroscopic signal" of item (1) may be a number of things. For example, it can be an excitation-and-shelving scheme as described in Sec. 2.5.4. More commonly, since the optimization of cooling is actually the ultimate goal, the spectroscopic feature we use is a cooling feature. We probe these by sweeping the detuning of the red cooling laser and performing some kind of rapid one-point thermometry — such as adiabatic rampdown, release-and-recapture [127, 128], or an adiabatic rapid passage over a red sideband (Sec. 2.5.4) — at each point of the sweep.

The adjustment of $A_i$ in item (4) generically requires some algorithmic approach. A simple formula which calculates how much each $A_i$ needs to change by is not practical, as there is some level of non-linearity and cross-talk between tweezer intensities. The algorithm we commonly use is simultaneously adjusting each $A_i$ using a PI (proportional-integral) feedback algorithm until their corresponding tweezer intensities reach sufficiently close to the desired value. Phases may also be simultaneously optimized as discussed in Sec. 2.7.1.

We routinely apply this procedure to our arrays (usually every few days) to maintain uniformity, and typically achieve uniformities of the differential light shift at or below the 2% level (as measured by standard deviation). Such a result is shown for an $11 \times 11$ 2D array in Fig. 2.27.

### 2.7.3 Rearrangement

One of the primary applications of tweezer arrays is realizing physics which involves entanglement between many atoms (Sec. 5.1.1). This is typically realized via short-range Rydberg interactions (Chap. 4), where the distance between two atoms is

very important. As we want to perform such operations in a controlled manner, the stochastic filling of tweezers described in Sec. 2.4.2 will not work for this purpose.

The development of tweezer rearrangement [46, 48, 52, 53] was crucial to the development of tweezer arrays as a platform for quantum science. With this technique, an initially stochastically loaded array can be rearranged to have atoms at desired positions. Most notably, *defect-free* arrays can be achieved: ones that have an atom at every site with no empty tweezers in between. We also note the development of non-tweezer rearrangement schemes in optical lattices [54].

### *Moving tweezers*

The mechanics of tweezer rearrangement with AODs [48, 53] is a simple extension of the results of Sec. 2.7.1 (see Ref. [46] for a purely SLM-based approach). We know that the position of a tweezer along the axis of the AOD deflection is proportional to the frequency of the acoustic wave applied (Eq. 2.121). Therefore, to obtain a dynamical position $\Delta x(t)$, we simply apply a dynamical frequency.

Note that the definition of frequency for a cosine function is the time derivative of the argument of the cosine. Therefore, the correct generalization of Eq. 2.122 to dynamically moving tweezers is*

$$A(t) = \sum_{i=1}^{N_t} A_i \cos\left(\omega_c t + \phi_i(t)\right) \tag{2.123}$$

where $\omega_c$ is the center frequency of the AOD and

$$\phi_i(t) = \phi_i(0) + \omega \frac{c_s}{c} \frac{1}{f} \int_0^t \Delta x(t) dt \tag{2.124}$$

See Eq. 2.121 for a definition of the remaining variables.

We find that cooling atoms on the red transition while moving them is important to minimizing loss during rearrangement. For $k_\mathrm{B} \times 0.5$ mK deep tweezers under cooling, we find that atoms can be moved as fast as $\frac{d}{dt}\Delta x(t) \sim 1$ cm/s without increased levels of loss.

*A common mistake is to just modify the cosine as $\cos\left(\omega_i t + \phi\right) \rightarrow \cos\left(\omega_i(t) t + \phi\right)$. This will not give the desired result!

***1D rearrangement algorithm***


Figure 2.28: Atomic fluorescence image of an array of 36 atoms **(a)** before and **(b)** after rearrangement. The array spacing is 3.1 $\mu$m.

We now discuss how to actually achieve a 1D array with atoms in the desired position. The first step is to prepare a stochastically loaded array of single atoms (Sec. 2.4.2) and to image this array, determining which tweezers are occupied and which are not. Then, one must compute a signal of the form Eq. 2.123 that moves the occupied tweezers into their desired final positions. This must be done without an occupied tweezer "colliding" with any other tweezers (occupied or not), and can in principle involve discarding excess atoms. Of course, the initial number of atoms must also be at least equal to the final desired number of atoms. We will focus only on cases where the initial and final *tweezer* arrays are identical, such that the initial and final static signals (Eq. 2.122) are identical — though of course atoms may have moved around or been expelled in between.

Computing signals of the form Eq. 2.123 on-the-fly turns out to take a significant amount of time (~100 ms) for a contemporary computer. This is due to both computation time and transfering to the AWG which outputs the signal to the AOD. 100 ms may not seem like a lot, but it is in fact a significant portion of a typical experimental cycle time of a tweezer array experiment (typically <1 s). Furthermore, it is beneficial to minimize waiting time as fixed-timescale lifetimes such as vacuum collisions may limit the rearrangement success probability for large array sizes (Sec. 2.7.3).

Therefore, it is beneficial to have rearrangement signals pre-computed and stored on the memory of the AWG. However, enumerating every single possible rearrangement of identical atoms naïvely requires computation and storage of $\binom{2N_t}{N_t}$ signals*, where $N_t$ is the number of tweezers. This is prohibitive for reasonably sized arrays, even if restrictions are made on what moves can be reasonably expected to occur.

Therefore, we employ an iterative rearrangement algorithm that significantly reduces the signal storage requirements such that all necessary signals can be reasonably

*This assumes no excess atoms are to be expelled from the array. If this restriction is relaxed, the number is even larger.

stored directly on the AWG memory. The idea here is to sequentially move entire subsets of the array either one move to the right or one move to the left. For example, if we would like to create a defect-free array and there is an empty tweezer at position $k$, we simultaneously move tweezers $\{1, ..., k-1\} \rightarrow \{2, ..., k\}$. Concurrently, we extinguish the empty tweezer originally at $k$ and re-illuminate a tweezer at position 1. This procedure is then repeated until there are no longer defects in the array. Such a scheme requires only $O(N_t)$ storage of signals for defect-free final arrays. For arbitrary final arrays, the storage requirement is $O(N_t^2)$ [139]. Note that the exact functional form of the shifting motion and of the extinguishing/relighting can be arbitrary, so long as the tweezer array before the shift is identical to the one after the shift. These functional forms are usually chosen to be some smooth function, with amplitudes interpolated between neighboring tweezers. With these signals stored on the AWG memory, we only need to send a command sequence to the AWG telling it which signals to execute in what order.

Finally, at the end of a rearrangement sequence and before proceeding with the experiment, it is customary to verify that the rearrangement was successful by imaging the rearranged array. Here, unsuccessful rearrangements can be post-selected away. However, this does not guarantee that the array will continue to be correct after the image, as loss may occur during this second image. We discuss such limitations in the following Sec. 2.7.3.

#### *Rearrangement system size limits*

The success of rearrangement depends crucially on the probability that the atom will survive (1) the first image which determines the initial position of the stochastically loaded atoms, (2) the actual rearrangement motion itself, and (3) the second image which verifies the success of the rearrangement. Furthermore, the probability of correctly identifying an atom ($F_1$), as well as that of correctly identifying the *lack* of an atom ($F_0$), play a very important role in both the first and second image. These values are the imaging fidelities discussed in Sec. 2.6.7. However, taking these into account requires a more sophisticated analysis and we will leave this beyond the scope of this work. We will therefore assume that $F_0$ and $F_1$ are large enough such that errors in imaging are negligible. Note that this actually puts very stringent requirements on these values if we insist that no errors are allowed for any atom in the array.

We already defined in Sec. 2.6.7 the imaging survival $S$. Here we will also define the probability of surviving the rearrangement motion as $S_m$. Then the total probability of an atom surviving the entire rearrangement procedure is $S_r \equiv S^2 S_m$ (assuming that the first and second image have the same survival probability). We note that $S_r$ is fundamentally limited to $e^{-t/\tau}$, where $t$ is the time necessary for the entire rearrangement procedure and $\tau$ is the vacuum lifetime (Sec. 2.6.8).

The probability of *all* $N_a$ atoms in an array being successfully rearranged is* $S_r^{N_a}$. Note that for large $N_a$, this function is highly sensitive to even small deviations of $S_r$ from 1.

We will now calculate the the probability of achieving a defect-free array of $N_a$ atoms in an array of $N_t$ tweezers with an initial stochastic filling fraction of $f$, where typically $f = 0.5$. Note again that we are assuming perfect imaging fidelities (Sec. 2.6.7) in both the first and second image. The result is

$$P(N_a) = \left(1 - \sum_{n=0}^{N_a-1} \binom{N_t}{n} f^n (1-f)^{N_t-n}\right) S_r^{N_a} \tag{2.125}$$

Here, we have assumed that if the initially stochastically loaded array has more than $N_a$ atoms, that the excess atoms are expelled with 100% probability from the array. The first factor (in parenthesis) of Eq. 2.125 accounts for the probability of having at least $N_a$ initial atoms in a stochastically loaded array.

Let us assume we have sufficiently large $N_t$ such that the first factor of Eq. 2.125 is effectively 1. Then $P(N_a) \approx S_r^{N_a}$. Under this condition, we can now ask what is the maximum defect-free array size $N_a$ that has a success probability of at least $e^{-1}$. The answer is

$$N_a^{\max} = -\ln(S_r)^{-1} \tag{2.126}$$

$$\approx (1 - S_r)^{-1} \tag{2.127}$$

where Eq. 2.127 is valid for $(1 - S_r) \ll 1$. Thus we see that the largest defect-free array characteristically achievable is much more than a function of the number of tweezers you can generate: it is also very much limited by the probability of a single atom's survival.

*Here, we assume that $S_r$ does not depend on where in the array an atom is or where it is being moved to. One can generalize to a trajectory-dependent $S_r^i$, where $i$ indexes all the rearrangement trajectories. Then the total success probability is $\prod_i S_r^i$. We see that this number is limited by the worst $S_r^i$.

Let us also make the lax assumption that $S_m = 1$, such that all loss occurs only from imaging and $P(N_a) = S^{2N_a}$. Then Eq. 2.126 can be reduced to $N_a^{\max} = -\frac{1}{2}\ln(S)^{-1}$. From this analysis, we see that the imaging survival $S_0 = 0.99932$ reported* for $\lambda = 813.4$ nm tweezers in Sec. 2.6.8 limits our characteristic defect-free array size to $N_a^{\max} = 735$, which is significantly larger than the arrays that we can currently reasonably generate. On the other hand, if we used the markedly worse survival $S_0 \sim 0.97$ reported for $\lambda = 515.2$ nm tweezers in Sec. 2.6.8, we obtain $N_a^{\max} = 16$, a significant decrease. This analysis is the main reason why the loss reported in Sec. 2.6.8 was determined to be such a major detriment for 515.2 nm tweezers. Note once more that the limit we have presented here takes into account only survival, and we do not account for further imperfections due to imperfect imaging fidelities.

*We will make the approximation $S = S_0$, see Sec. 2.6.7.

# Chapter 3

# THE CLOCK STATE

In this chapter, we examine the clock state of Sr: 5s5p $^3P_0$. This state is interesting to us for a few reasons. The first is its role in the clock *transition* of Sr, 5s$^2$ $^1S_0 \leftrightarrow$ 5s5p $^3P_0$. This transition has been exploited to create some of the most stable clocks in the world [11, 12, 15]. We will discuss in this chapter the application of atomic arrays to optical clocks [99, 100, 138]. Additionally, the clock transition is a promising candidate for a long-lived optical qubit in strontium (Sec. 5.1.2).

Another reason the clock state is interesting to us is its use as a "second ground state" from which excitation to Rydberg states can follow. This will be discussed more in depth in Chap. 4.

We will also discuss in the Outlook (Sec. 5.1.3) ideas about using Rydberg interactions to generate spin-squeezed states on the clock transition as a pathway toward entanglement-enhanced metrology.

## 3.1 The clock transition in bosonic strontium

In the bosonic isotopes of Sr (such as the one we work with, $^{88}$Sr), the clock transition 5s$^2$ $^1S_0 \leftrightarrow$ 5s5p $^3P_0$ is *strictly* dipole forbidden by both the $J = 0 \rightarrow J' = 0$ and $\Delta S = 0$ electric dipole selection rules. These selection rules are strict in the case of the clock transition because both the $J$ and $S$ quantum numbers of the clock state are exact. For $J$, this is true of all states due to rotational symmetry. For $S$, spin-orbit mixing with singlet states (as occurs for 5s5p $^3P_1$, see Sec. 2.1.2) is only possible between states of equal $J$. For the clock state, there is no $J = 0$ singlet state that can be mixed with. Indeed, for all experimental purposes the unperturbed clock transition in bosonic Sr can be assumed to have a natural linewidth of zero. The actual value is theoretically predicted to be $\Gamma = 2\pi \times 8.8 \times 10^{-13}$ Hz [140] via an E1M1 decay channel to the ground state.

### 3.1.1 Admixture with magnetic field

In order to drive the clock transition, we thus need to break rotational symmetry and admix the unperturbed clock state with a state that has $J = 1$. We do this with a magnetic field [141]. The perturbing Hamiltonian of a magnetic field $\vec{B}$ is $H_Z = \mu_B \vec{B} \cdot (g_L \vec{L} + g_S \vec{S})$, where $g_L \approx 1$ and $g_S \approx 2$. We will choose our quantization axis to point along $\vec{B}$. This simplifies the Hamiltonian to $H_Z = \mu_B B(g_L m_L + g_S m_S)$ for states in the same $|S, L\rangle$ manifold, and zero otherwise.

$H_Z$ has no first-order shift on the clock state, but it does mix the clock state with 5s5p $^3$P$_1$ $m_J = 0$. Via perturbation theory, it can be shown [141] that the perturbed clock state is

$$|\psi_{\text{clock}}(B)\rangle = |5s5p\ ^3P_0\rangle + \frac{\mu_C B}{\hbar \Delta_{01}} |5s5p\ ^3P_1\rangle \tag{3.1}$$

$$\mu_C \equiv \sqrt{\tfrac{2}{3}}(g_L - g_S)\mu_B \tag{3.2}$$

where $\Delta_{01} = 2\pi \times 5.6$ THz is the splitting between 5s5p $^3$P$_0$ (the clock state) and 5s5p $^3$P$_1$. While Eq. 3.1 is not strictly normalized, we assume that $\frac{\mu_C B}{\hbar \Delta_{01}}$ is small.

This admixture gives the perturbed clock state a finite decay rate to the ground state, given by

$$\Gamma_{\text{clock}}(B) = \Gamma_{^3P_1} \frac{\mu_C^2 B^2}{\hbar^2 \Delta_{01}^2} \tag{3.3}$$

which is proportional to $B^2$. We note that even for a large field of $B = 1000$ G, this results in a very small decay rate of $\Gamma_{\text{clock}} = 2\pi \times 0.3$ mHz ($\tau = 530$ s). We also note for the sake of intuition that the clock transition in the fermionic $^{87}$Sr can be thought of as experiencing a "natural" magnetic field due to its nonzero nuclear spin of $I = 9/2$, giving the clock transition a finite decay even at zero external field. On a more formal level, one can note that the strict restriction of $J = 0 \nrightarrow J' = 0$ and $\Delta S = 0$ are relaxed in the fermion as the exact quantum numbers there are $F = F' = 9/2$ [142].

The admixture of the clock state with 5s5p $^3$P$_1$ allows for a finite dipole coupling to the Sr ground state 5s$^2$ $^1$S$_0$. We can calculate the Rabi frequency on the clock transition to be

$$\Omega_{\text{clock}}(B) = \frac{\mu_C B}{\hbar \Delta_{01}} \sqrt{\frac{3\Gamma_{^3P_1} \lambda^3 I}{4\pi^2 \hbar c}} (\hat{\epsilon} \cdot \hat{B}) \tag{3.4}$$

where $I$ is the optical beam intensity, $\lambda = 698.4$ nm is the wavelength of the clock transition, and $\hat{\epsilon} \cdot \hat{B}$ is the projection of the excitation beam's polarization onto the direction of the magnetic field. This can be derived from Eqs. 2.85–2.86 along with the relation $s = \frac{2\Omega^2}{\Gamma^2}$. Thus we see that Rabi frequency scales linearly with $B$.

### 3.1.2 Systematic energy shifts

The recommended value [143] of the vacuum wavelength and corresponding transition frequency of the unperturbed clock transition in $^{88}$Sr is

$$\lambda_{\text{clock}} = 698.445\ 608\ 419\ 382 \text{ nm} \tag{3.5}$$

$$\nu_{\text{clock}} = \omega_{\text{clock}}/(2\pi) = 429.228\ 066\ 418\ 007 \text{ THz} \tag{3.6}$$

This resonance can however shift due to external factors — these are often referred to as *systematic shifts* in the context of metrology. Systematic shifts are not only important as DC values, but also as sources of frequency noise (Sec. 3.2.3). Here we will discuss magnetic shifts, *probe shifts* due to the light that excites the clock transition, and trapping light shifts. Additional shifts that can be studied but are beyond the scope of this work include blackbody radiation shifts [88, 144, 145], DC electric shifts [88, 145], and background gas shifts [145, 146]. Interaction shifts between trapped atoms are also an important topic for certain platforms, but are ideally absent in a tweezer platform (Sec. 3.4).

#### *Magnetic shift*

We will continue the perturbation theory that gave us Eq. 3.1 to now calculate the energy shift of the perturbed clock state. Since the ground state is unperturbed by a magnetic field, this shift can also be interpreted as the shift of the clock resonance. The result is

$$\Delta\omega_B(B) = -\frac{\mu_C^2 B^2}{\Delta_{01}} \tag{3.7}$$

Thus there is an energy shift that is proportional to $B^2$. Numerically, this is approximately a coefficient of $-2\pi \times 0.23$ Hz/G$^2$.

#### *Probe light shift*

The beam that excites the clock transition (which we will refer to as the *probe* beam) induces a differential light shift on the clock transition. This differential shift results

from both a shift on the ground state and on the clock state. A calculation of this shift would involve a polarizability calculation for both states at $\lambda = 698.4$ nm, in the vein of the analysis presented in Sec. 2.3.4. Note as both ground and excited states are $J = 0$, these polarizabilities are purely scalar and have no dependence on polarization. We forgo a full analysis and restate the result given in Ref. [141]:

$$\Delta\omega_I(I) = \kappa I \tag{3.8}$$

$$\kappa = -2\pi \times 18 \text{ mHz}/(\text{mW}/\text{cm}^2) \tag{3.9}$$

Note that $\Delta\omega_I/\Omega \propto \sqrt{I}$, so the magnitude of the shift relative to the linewidth grows as $\sqrt{I}$.

***Trap light shifts***

Lastly, we discuss light shifts from trapping. In the context of polarizability as discussed in Sec. 2.3, there exists a magic wavelength for the clock transition at $\lambda_{\text{magic}} = 813.427$ nm (vacuum) [28]. Being at this wavelength would normally eliminate light shifts; however, there are two practical issues that arise for the clock transition when used at very narrow linewidths. The first is particular to tweezer arrays generated by an AOD (Sec. 2.7.1). Each tweezer in an AOD-generated array has an optical frequency shift from its neighbor on the order of a few hundred kHz to a few MHz, depending on the array spacing. This means that each tweezer will have a slightly different light shift than the others. These differences are usually far too small to be noticeable in the light shift of any other transition, but can be seen in narrow-line clock operation (Refs. [100, 138] and Fig. 3.6). This issue can be solved by generating the array with an SLM instead.

The second potential issue is that it is possible to observe light shifts arising from beyond-second-order perturbation theory (i.e. beyond the treatment of Sec. 2.3). The next-leading perturbation is fourth order in the dipole Hamiltonian, and produces an additional light shift that is proportional to $I^2$ (Fig. 3.6), known as *hyperpolarizability* [147]. With a nonzero hyperpolarizability, there is in fact no wavelength for which the light shift is zero for *all* intensities, so a magic wavelength is in principle defined only in the limit of zero trap intensity. However, for all trap intensities, one can find a wavelength where the light shift is at a local extremum with respect to intensity. This has been called an *operationally magic* configuration [148], and is favorable as it produces a total light shift that is minimally sensitive to fluctuations

or inhomogeneities in the trap intensities. Hyperpolarizability is, however, sensitive to the trap's polarization ellipticity, even for a $J = 0$ state like the clock state [149]. This may be a source of inhomogeneities in an array optical clock. Ultimately, however, it is anyway favorable to operate high-stability clocks in as shallow a trap as possible [99] where hyperpolarizability effects are small.

A formula for hyperpolarizability light shifts in a tweezer as a function of motional state can be found in Eq. E1 of Ref. [138].

### 3.1.3 State detection

We will describe two ways to perform state detection on the clock transition, which we will refer to as the *destructive* and *non-destructive* methods.

The destructive method is to push ground state atoms out of the trap by applying a high-intensity beam resonant on the blue transition. This is ideally done in traps that are relatively shallow ($\lesssim 50\ \mu$K). The atoms remaining in the clock state are then repumped into the imaging transition and imaged. We find that a push-out pulse as short as 500 $\mu$s is sufficient to eliminate atoms in the ground state with a fidelity of >99.99%. Furthermore, the speed of this scheme is fast compared to the timescale of trap scattering of the clock state into the ground state. Thus, for tweezers less than 50 $\mu$K deep, the fidelity of *not* pushing-out clock state atoms is also similarly high. We forgo a full analysis of the state-detection fidelity, but note that we are able to measure ~99.8% clock state population when optically pumping to the clock state instead of coherently driving (Ref. [150]), which places a lower bound on the clock state detection fidelity of this scheme.

The non-destructive method is to simply image the ground state, leaving excited atoms dark in the clock state. Here, we must leave the 679 nm repump off, however (Fig. 2.16). There are two processes that produce infidelity in this scheme: (1) Raman scattering out of the clock state and (2) leakage from the blue transition into 5s5p $^3$P$_2$. For item (1), note that high-fidelity imaging favors relatively deep traps and therefore higher Raman scattering rates. There is some uncertainty here as to whether it is best to perform such detection with the 707 nm repump on or off. On the one hand, it can put leakage from the imaging transition back into the imaging cycle, but on the other hand it also gives rise to the possibility that Raman scattering from the clock state into 5s5p $^3$P$_2$ will also enter the imaging cycle. We forgo an analysis on this question.

The non-destructive scheme generally has an inferior state detection fidelity to the destructive scheme (see Ref. [116] for a fidelity analysis) but does allow atoms to be reused as no atoms are pushed out of the trap. This is useful for reducing dead-time in clock operation (Sec. 3.4).

## 3.2 Coherent excitation and its limits

This section will explore one general question: "how well can we perform Rabi oscillations on the clock transition?" The answer to this question is important for at least two reasons: (1) preparing the atoms in the clock state with high fidelity for subsequent Rydberg excitation and (2) the use of the clock transition as an optical qubit.

The ideal Rabi Hamiltonian on a two-level system (TLS) is given by

$$H/\hbar = \tfrac{1}{2}\left(\Omega\sigma^x - \Delta\sigma^z\right) \tag{3.10}$$

where $\sigma^\mu$ are Pauli operators*, $\Omega$ is the Rabi frequency, and $\Delta$ is the detuning. If the initial state is the ground state $|g\rangle$, the solution to this ideal Hamiltonian on-resonance ($\Delta = 0$) is $|\psi(t)\rangle = \cos\left(\frac{1}{2}\Omega t\right)|g\rangle + \sin\left(\frac{1}{2}\Omega t\right)|e\rangle$. A $\pi$-pulse at $t = \frac{\pi}{\Omega}$ should thus ideally implement the state-flip unitary $U = \sigma^x$. How well a system actually realizes this operation can be characterized by a *$\pi$-fidelity* given by $\langle e|\rho|e\rangle$, where $\rho$ is the density matrix.

Although any two-level system is in principle described by the same Hamiltonian, in this section we will examine effects that are most pertinent to specifically the clock transition, which is characterized by narrow linewidths and long timescales. In Sec. 4.4, we will answer very similar questions but for Rydberg transitions, which typically have short timescales, broad linewidths, and other systematic considerations. Our analysis in both sections should not be considered as absolutely exhaustive, but will include all effects that we believe to be major contributions.

For completeness, here we list some effects we deem to be negligible. Blackbody radiation coupling of the clock state to the nearby 5s4d $^3D_1$ state is expected to have a total scattering rate of time constant $\tau_{\mathrm{BBR}} \approx 170$ s [99, 124], which is much longer than the relevant timescales we will consider and therefore will be ignored (but can become important for state-of-the-art clock systems). Scattering from the clock (probe) beam is also deemed to be negligible at the typical intensities used.

*$\sigma^z = |e\rangle\langle e| - |g\rangle\langle g|,\ \sigma^x = |g\rangle\langle e| + |e\rangle\langle g|$

Finally, it is assumed that the rate of spontaneous decay is negligible, which is a good approximation for the clock state (especially in the bosonic species).

### 3.2.1 Thermal and motional effects

The clock transition typically has a linewidth much smaller than all trap frequencies. Thus, it is most convenient to discuss atomic motion in the language of the quantum harmonic oscillator, as we did in Sec. 2.5.1. We will assume magic trapping conditions throughout.

We know from Sec. 2.5.1 that motional transitions in the resolved-sideband regime manifest as discrete resonances spaced at the trap frequency $\omega$. The transition which does not change the motional state is known as the *carrier* and the transitions which do are known as *sidebands*. For coherent excitation, we choose to excite on the carrier — not only to preserve the motional state, but because this transition is least sensitive to motional dephasing.

However, it is not completely insensitive to motion. Looking at Fig. 2.11, we see that the matrix element of this transition does depend on the motional state. Quantitatively, we can rewrite Eq. 2.59 specifically for carrier ($n = n'$) transitions:

$$\langle n_i | e^{i\eta(a_i + a_i^\dagger)} | n_i \rangle = e^{-\frac{1}{2}\eta_i^2} L_n(\eta_i^2) \tag{3.11}$$

where $L_n(y)$ is a Laguerre polynomial, $\eta_i = (\vec{k} \cdot \hat{r}_i)\sqrt{\frac{\hbar}{2m\omega_i}}$ where $\hat{r}_i$ is the direction along which the $a_i$ operators are defined (assumed to be a principal axis of the trap), and $\omega_i$ is the trap frequency along this direction. An approximation to this equation is given to second order in $\eta$ by Eq. 2.60.

The frequency of oscillations between $|g\rangle$ and $|e\rangle$ is proportional to this matrix element. For an atom with motional state $|n_x, n_y, n_z\rangle$, the oscillation frequency is given by

$$\Omega_{n_x,n_y,n_z} = \Omega e^{-\frac{1}{2}(\eta_x^2+\eta_y^2+\eta_z^2)} L_{n_x}(\eta_x^2) L_{n_y}(\eta_y^2) L_{n_z}(\eta_z^2) \tag{3.12}$$

where $\Omega$ is the Rabi frequency in the limit of an ideal TLS ($\eta \to 0$). Note that the way we have defined $\eta_i$ takes into account the projection of the wavevector $\vec{k}$ onto each dimension.

Let us now simplify by assuming that $\vec{k}$ points along only one of the trap principal axes, such that only the $\eta$ of one direction is nonzero. Note that $L_n(0) = 1$ for all

$n$, so we can work with a single $\eta$ and $n$ in this 1D case. For a thermal ensemble of thermal occupation $\bar{n}$, the averaged excitation probability for Rabi oscillations on carrier resonance is

$$P_e(t) = \frac{1}{1+\bar{n}} \sum_{n=0}^{\infty} \left(\frac{\bar{n}}{1+\bar{n}}\right)^n \sin^2\left(\tfrac{1}{2}\Omega_n t\right) \tag{3.13}$$

$$= \frac{1}{1-e^{-\frac{\hbar\omega}{k_B T}}} \sum_{n=0}^{\infty} e^{-\frac{\hbar\omega n}{k_B T}} \sin^2\left(\tfrac{1}{2}\Omega_n t\right) \tag{3.14}$$

Note that this formula is only valid in the resolved sideband regime $\omega \gg \Omega$.

Qualitatively, this thermal spread of the oscillation frequency results in an overall slowing down of the Rabi oscillations as well as dephasing at early times, as shown in Fig. 3.1. The rate of this dephasing can be used as a form of thermometry. Our measured data closely reproduces the predicted dephasing at early times, and the temperature extracted from this method agrees well with temperatures extracted from sideband spectroscopy (Sec. 2.5.4). At later times, the oscillations can re-phase, leading to a revival of the excitation probability.

For small $\bar{n}$ and $\eta$, we can estimate the maximum achievable $P_e$ as

$$P_e^{\max} \approx 1 - \frac{\pi^2}{4}\eta^4 \bar{n} \tag{3.15}$$

This occurs at a time slightly later than the $\pi$-time that would be predicted in a non-thermal TLS. Note that this value is *independent of* $\Omega$, so thermal dephasing cannot (at least, in the sideband-resolved regime) be "beaten" with a faster Rabi frequency. Indeed, thermal dephasing in the sideband-resolved regime is invariant in the timescale. This is *not* the case in the regime of $\Omega \gg \omega$, however, where thermal dephasing *can* be beaten with faster Rabi frequency. That regime will be used for Rydberg excitation (Sec. 4.4).

Note that Eq. 3.15 implies that the thermal $\pi$-infidelity scales as $\omega^{-2}$. Therefore, suppressing thermal dephasing calls for the use of tighter traps. This can be done by using deeper (i.e. higher intensity) traps — however, this is at odds with $\pi$-fidelity limits set by trap light scattering (Sec. 3.2.2), so a balance must be struck between the two.

We will now briefly discuss infidelities in the Rabi oscillations due to off-resonant excitation of motional sidebands. In other words, we will make an estimate of the failure of the resolved-sideband regime. A quantitative treatment is best done

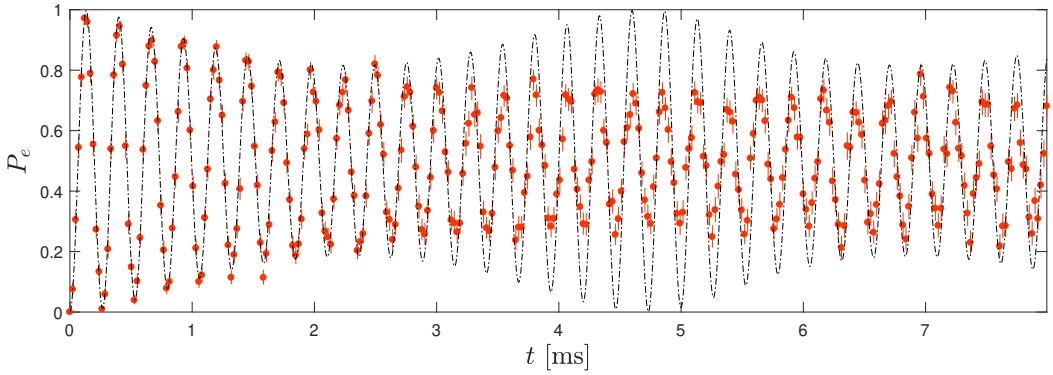


Figure 3.1: Rabi oscillations on the clock transition. Red points are experimental data, while the grey dashed line is the expected thermal dephasing for $\bar{n} = 0.29$, as given by Eq. 3.13. The trap frequency is $\omega = 2\pi \times 82$ kHz while the bare Rabi frequency (without motional corrections) is $\Omega = 2\pi \times 3.9$ kHz. The magnetic field is $|B| \sim 710$ G. Data is averaged over 43 tweezers. No correction or rescaling is performed for the vertical axis. The discrepancy between the data and the grey dashed line at later times can be explained by a breakdown of the assumption that $\vec{k}$ only points along one principal axis of the trap, and in particular if the trap frequencies along the different directions are unequal. In fact, from sideband spectroscopy such as in Fig. 2.14, we know that our clock beam does have components along both radial axes and that they have a frequency splitting of $\sim 2\pi \times 2.5$ kHz. Although this is not plotted here, it can be shown that such a situation leads to pushing out of the revival to later times.

by numerical evolution, but we can make an estimate of the amplitude of off-resonant excitations. The sidebands are detuned by $\omega$ and oscillate at a frequency of approximately $\eta\Omega$. Thus their oscillation amplitude will be approximately $\frac{\hbar k^2 \Omega^2}{2m\omega^3}$. For our typical parameters, this value is in the range of $10^{-4}$, so it is not typically significant. However, it does pose an upper limit on how large $\Omega$ can be chosen in the sideband-resolved regime. We note that such limits are not valid when $\Omega \gg \omega$, where it is again actually beneficial to choose larger $\Omega$.

Finally, we note the possibility of dephasing due to thermal sampling of the clock probe beam profile, which can lead to fluctuations in both the Rabi frequency and in the detuning (Sec. 3.1.2). This becomes an especially important problem for smaller probe beams that one would use to obtain large Rabi frequencies.

### 3.2.2 Trap light scattering

Atoms in either the ground or the clock state can scatter trap photons. The rate of such scattering is directly proportional to the trap intensity $I$, or equivalently

the trap depth* $U_0$. Scattering generically reduces the fidelity of Rabi oscillations. Furthermore, trap scattering continually depopulates the clock state even if it were initially perfectly prepared.

Scattering in the ground state is dominated by the 5s5p $^1$P$_1$ intermediate state, which ultimately leaves the atom still in the ground state. On the other hand, atoms in the clock state can scatter trap photons via a number of intermediate states, the most significant of which are 5s6s $^3$S$_1$, 5p$^2$ $^3$P$_1$, and 5s5d $^3$D$_1$. Scattering via these intermediate states can either leave the atom in the clock state (Rayleigh scattering) or transfer it to 5s5p $^3$P$_{1,2}$ (Raman scattering). We neglect any other potential processes that take the atom completely out of this manifold. If Raman scattering transfers the clock state atom to 5s5p $^3$P$_1$, the atom decays back to the ground state on a relatively fast timescale ($\tau = 21$ $\mu$s).

If Raman scattering transfers the atom to 5s5p $^3$P$_2$, it may stay there for a long time as this state is also metastable. However, it too can scatter trap photons, and can eventually return to either the clock state or 5s5p $^3$P$_1$. We note that here the trap polarization is important. For example, if the atom ends up in the "stretched state" $|$5s5p $^3$P$_2$ $m_J = \pm 2\rangle$ while the trap polarization is purely $\sigma_\pm$ (requiring a circularly polarized trap), then scattering can no longer move the atom to any other state in the 5s5p $^3$P$_J$ manifold. We note that this is a potentially interesting situation for the realization of an excited state that is long-lived even under deep trapping.

A full model of these dynamics can become quite involved and we forgo such an analysis. A simpler question is: "if an atom is prepared in the clock state, for how long does it remain there?" To answer this, we refer to Ref. [124] which computes a Rayleigh scattering rate from the clock state into the other 5s5p $^3$P$_J$ states of $\Gamma_s = 7.82 \times 10^{-4}$ s$^{-1} \cdot (U_0/E_r)$, where $E_r = 2\pi\hbar \times 3.43$ kHz is the recoil energy for a $\lambda = 813.4$ nm trap. For a given trap depth $U_0$, this rate can be used to compute an exponential decay of the clock population. Such a treatment does not, however, take into account scattering from 5s5p $^3$P$_2$ back to the clock state.

### 3.2.3 Technical noise

We briefly discuss various types of technical noise that can detriment clock Rabi oscillations. We also point the reader to Sec. 4.4.3 which contains several elaborations

*Here, there may be a small thermal correction such that hotter atoms see a smaller intensity and therefore do not scatter as quickly, but we ignore this.

that are also relevant here.

***Laser phase/frequency noise***

The first is laser phase (or frequency) noise. This noise is largely set by the cavity to which the clock laser is stabilized, and to some extent the lock electronics. A full model of how laser noise affects excitation is best performed via Monte Carlo numerics (Ref. [117] and Sec. 3.4.6).

A general comment that can be made here is that Rabi dephasing due to laser phase noise can typically be overcome by larger Rabi frequencies. This is because laser frequency noise typically drops off at higher modulation frequencies (see, e.g. Fig. 3.2.3), and it can be shown that Rabi dephasing is most sensitive to frequency noise at a modulation frequency near the Rabi frequency [151]. Note that, although laser frequency noise generally decreases with modulation frequency at low modulation frequencies, there may be a region of increased noise at modulation frequencies near or above the servo bandwidth of the laser lock. However, this is typically at modulation frequencies on the order of a few hundred kHz (i.e. well above typical clock Rabi frequencies).

Since clock Rabi frequencies are well within or below the acoustic range, mechanical and vibrational noise in the optical setup may also produce significant phase noise. For example, we have seen clear sidebands appear in the Rabi signal due to the vibration of piezo mirrors on our optical table. Vibration of any fiber optics in the setup may also produce phase noise. For this purpose, we use a fiber noise cancellation (FNC) system [152].

On top of phase noise, there is usually also a highly linear drift of the cavity resonance frequency with time. It is beneficial to negate this drift with a well-calibrated feedforward mechanism.

***Intensity noise***

Intensity noise on the clock light is another potential problem. This manifests in two ways: (1) noise in the Rabi frequency $\Omega$, but also by (2) noise in the detuning $\Delta$. As for (1), see Sec. 4.4.3 for a relevant discussion. As for (2), note Eq. 3.8, giving $\delta\Delta = -\kappa\delta I$. As this produces noise in the detuning, it can be analyzed in a similar way to laser frequency noise.

We use active power stabilization via photodiode feedback to an AOM to minimize intensity fluctuations.

***Magnetic field noise***

From Eqs. 3.4–3.7, we see that fluctuations in the $B$ field may also be a source of noise in $\Omega$ and $\Delta$. For a fluctuation $\delta B$ around a mean value of $B$, we have $\delta\Delta = \frac{2\mu_C^2}{\Delta_{01}} B\delta B$ and $\delta\Omega/\Omega = \delta B/B$. We use active stabilization of the current in our magnetic coils to minimize noise in the magnetic field (App. A.2). Homogeneity of the field is typically not a problem if the coils are sufficiently large and close to a Helmholtz configuration.

### 3.2.4 Results for $\pi$-fidelity

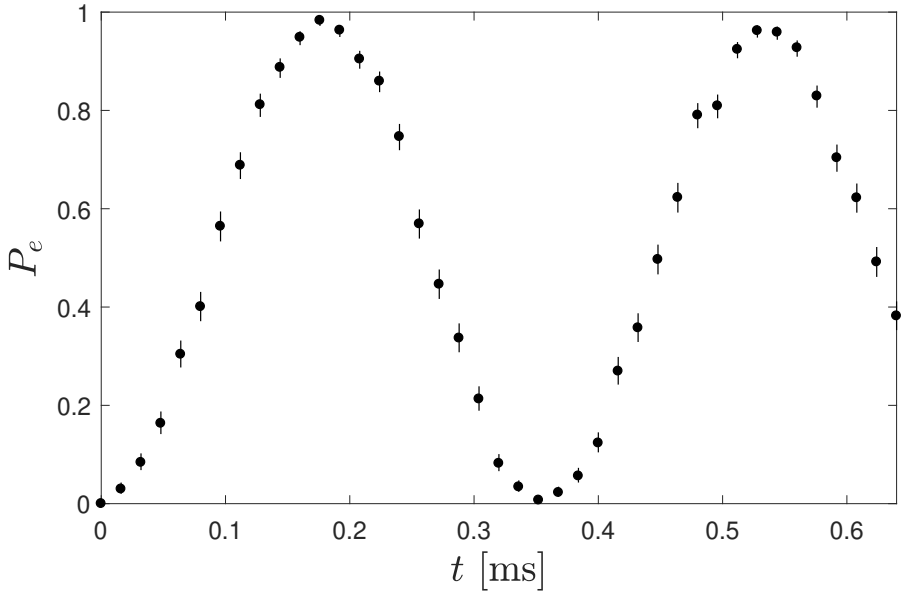


Figure 3.2: Resonant ($\Delta = 0$) Rabi oscillation on the clock transition at $\Omega = 2\pi \times 2.8$ kHz. The magnetic field is $|B| \sim 710$ G. Data is averaged over 61 tweezers with radial trap frequencies of $\omega = 2\pi \times 82$ kHz. No correction or rescaling is performed for the vertical axis.

We typically achieve $\pi$-fidelities on the clock transition of ~98.5%, as shown in Fig. 3.2. These results are obtained for Rabi frequencies of $\Omega \sim 2\pi \times 2 - 4$ kHz with radial trap frequencies of $\omega \sim 2\pi \times 80$ kHz. Although the dephasing timescale of our Rabi oscillations agrees quite well with that predicted by thermal dephasing (Fig. 3.1), the $\pi$-fidelity is significantly lower than what would be predicted from

thermal dephasing alone (which is ~99.7%). We have yet to conclude on a mechanism that accounts for this discrepancy and leave this to future work. This limit is also not set by state detection fidelity (Sec. 3.1.3).

## 3.3 Principles of clock operation

In this section, we shift our focus to a regime of very narrow linewidths for the purposes of operating a precise optical clock. We will no longer be chiefly interested in the fidelity of our Rabi oscillations (although this will still play a role to some extent) and instead try to achieve as precise of a clock as possible.

A *clock* works by counting events and labeling the occurrence of each event as the passage of some unit of time. One could count, e.g., how many times a pendulum has swung or how many times a quartz crystal has vibrated. These devices are called *local oscillators*. In our case, our local oscillator is the electromagnetic oscillation of laser light — namely of the light from our clock laser. The laser's frequency can, however, vary from device to device and can change over time. Here enter atoms, whose identical nature and narrow electronic transitions act as a near ideal universal reference for local oscillators to be calibrated against. By interrogating an atom with a laser, we can measure how far the laser's frequency is from the atom's transition and correct the frequency accordingly. This is the basic principle of an atomic clock.

We will touch only very briefly on some key concepts behind clock operation, and leave a more in-depth exposition beyond the scope of this work as there is already a large body of more specialized literature on this topic. Namely, we point the reader to Ref. [15] for an excellent review and starting point.

### 3.3.1 Atomic feedback, sensitivity, and noise

First, we describe how a laser is referenced to an atomic transition. Atoms are driven by the clock laser such as to produce a narrow spectral peak. This can be done either via a Rabi or Ramsey pulse sequence. By choosing probe detunings $\nu + \Delta\nu$ and $\nu - \Delta\nu$ on two opposing sides of this spectral peak and measuring the excitation probability $P$ on each side, an error signal $e = P(\nu + \Delta\nu) - P(\nu - \Delta\nu)$ can be derived, providing feedback on how to tune the laser frequency $\nu$ such that the spectral feature remains centered around the two probes.

Therefore one converts a measure of an excitation probability into a measure of frequency. The sensitivity of this conversion between excitation to frequency is $\frac{de}{d\nu}$, the slope of the error signal versus frequency (assuming that we probe the peak on its side, where $P(\nu)$ is approximately linear). The greater this slope, the greater the sensitivity of our probe. For a typical Rabi or Ramsey lineshape, this slope

is inversely proportional to the linewidth (we point the reader to Ref. [153] for a discussion of the exact evaluation of $\frac{de}{d\nu}$ in ideal Rabi lineshapes.). Therefore, the narrower our linewidth, the more sensitive our probe of the frequency.

A discussion of sensitivity would be unimportant, however, if the signal $P$ we measure were noise-free. Indeed, with a perfect measurement of $e$, even an extremely broad line would be a perfect clock. However, if there is some noise $\delta e$ in the measurement, this directly translates to a frequency imprecision of $\delta\nu = \delta e / \frac{de}{d\nu}$. Thus, to minimize the frequency uncertainty, it is apparent that we want to maximize the slope $\frac{de}{d\nu}$ (by minimizing the linewidth) as well as minimize $\delta e$.

While there are a number of effects that can enter into the noise of $e$, one is at the most fundamental level: *quantum projection noise*, or QPN. QPN arises from the fundamental fact that reading out the state of an atom can only give you a *binary* answer: either the atom is measured in the ground state or it is measured in the excited state. Its quantum state previous to measurement may have been described by a state-vector with a continuously-variable excitation probability $P \in [0, 1]$, but a single measurement cannot return such a continuous value: it must produce either the value zero or one. If we average $N$ such measurements and we assume that the measurements are *uncorrelated*, then the result will be a random variable whose distribution has a standard deviation proportional to $1/\sqrt{N}$. QPN in a Rabi lineshape is illustrated in Fig. 3.3.

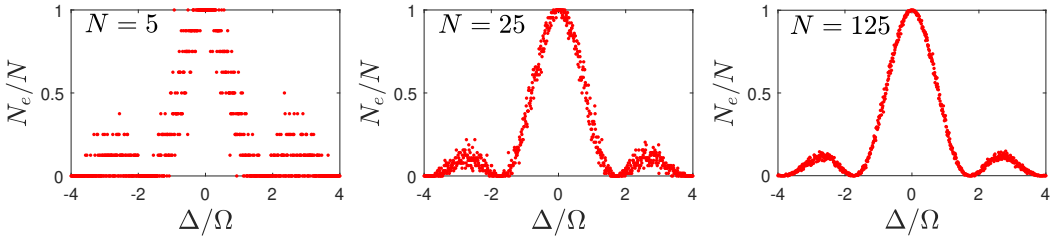


Figure 3.3: Quantum projection noise in a Rabi lineshape. A simulated Rabi oscillation with Rabi frequency $\Omega$ is evolved for a time $t = \pi/\Omega$ as a function of detuning $\Delta$. The initial state is the ground state and the final state has some excitation probability $P$. The vertical axis plots the *measured* excited state population $N_e/N$, where $N_e$ is the number of atoms measured to be in the excited state (simulated by sampling from a binomial distribution with mean $NP$) and $N$ is the total number of atoms. We show this for $N \in \{5, 25, 125\}$.

If we probe multiple atoms simultaneously, we can interpret $N$ as the number of atoms. Thus, we see that the number of atoms available for us to probe sets a fundamental limit to the noise $\delta e$ and therefore to the precision of our frequency

probe. Assuming QPN is the *only* source of noise in $e$, we have $\delta\nu \sim 1/(\sqrt{N}\frac{de}{d\nu})$. If we now also assume that the *only* source of spectral linewidth arises from the finite interrogation time, then we also have $\frac{de}{d\nu} \sim T$, where $T$ is the interrogation time. We thus obtain in this idealized regime the relation $\delta\nu \sim 1/(T\sqrt{N})$.

However, this scaling is only true up to some limit beyond which it is no longer as beneficial to increase $T$ or $N$. For example, if the measurable linewidth of the spectral feature is limited not by the interrogation time but rather by some decoherence mechanism such as spontaneous decay, trap scattering (Sec. 3.2.2), or frequency noise, then increasing $T$ will not produce a narrower feature and in fact will only increase the dead-time between feedback cycles, which is detrimental to clock performance [153–155]. Similarly, increasing $N$ only has significant benefit if QPN is the dominant source of noise in the measurement of $e$ [156], and not instead, e.g. frequency noise. Independent sources of noise add in quadrature, so decreasing one source of noise has diminishing returns if it is already much lower than other sources. We will show in our results in Sec. 3.4 that we reach such a laser-noise-limited regime with as few as 10's of atoms (Fig. 3.7).

We note that frequency noise enters as *both* a limit to the linewidth [120] *and* as a noise source in measuring $e$ (where it is sometimes referred to as Dick noise or the Dick effect) [153–155]. Though it may come from noise in systematic factors such as probe intensity or magnetic field (Sec. 3.1.2), frequency noise is usually attributed to the laser itself. Therefore, the development of laser systems with intrinsically lower noise (which mostly falls on the task of producing lower noise reference cavities [157–159]) is highly important to creating better clocks, as we see that an atomic clock can not only be limited by atomic decoherence, but also by the intrinsic instability of its local oscillator. However, we point the reader to Ref. [99] for a study in which long-lived atom-atom coherence is measured even in the absence of equally long-lived atom-laser coherence.

### 3.3.2 Quantifying performance & Allan deviation

We will now discuss how to quantify the performance of a clock. Two values are relevant here: *systematic uncertainty* (sometimes referred to as accuracy) and *instability*. Systematic uncertainty is a measure of how well one has determined the various systematic shifts of the atomic resonance. Determining systematic uncertainty requires tabulating an error budget of various systematic shifts, such as from a magnetic field, probe shift, blackbody radiation shift, and trap light

shift. However, we leave a further discussion of this (noting that some concepts are somewhat touched upon in Sec. 3.1.2) beyond the scope of this work and again refer the reader to the review of Ref. [15] as well as to certain milestone results in Refs. [12, 14, 29, 160] for more discussion.

*Instability* is a measure of how precisely the frequency of the local oscillator can be determined, either absolutely or differentially to another oscillator. Measuring this requires comparing the local oscillator's frequency to that of another oscillator*. This can be done by, e.g., beating the two oscillators. Interestingly, a local oscillator under feedback can also be compared to itself. For a laser, this is as simple as splitting the light into two AOM paths and feeding frequency corrections to the AOMs instead of the laser itself (which is usually done anyway). Then, instability can be measured by comparing the frequencies of the two AOMs. If there is only one atomic reference, then the two AOMs can be referenced to the atoms *asynchronously*, which means that one AOM is referenced to the atoms and given feedback, then the other, and the cycle repeats. In practice, this can also be done with just one AOM that switches back and forth between two frequency "rails".

What we end up with is a pair of frequency records taken at given times, $\nu_{1,2}(t_k)$. If the two oscillators are of similar stability (or of identical stability in the case of self-comparison of the same laser and atomic system), then the quantity we are interested in is $y(t_k) \equiv \frac{1}{\sqrt{2}} \frac{\nu_2(t_k) - \nu_1(t_k)}{\nu_{\text{clock}}}$, where $\nu_{\text{clock}}$ is given by Eq. 3.6. We will call this quantity the *fractional frequency difference*. Here, the factor of $\frac{1}{\sqrt{2}}$ accounts for the fact that we are comparing two equally noisy systems to each other.

We now define $\bar{y}_i(\tau)$ as the average of $y(t_k)$ averaged over a block of time (indexed by $i$) that has a timespan of $\tau$. We then define the *Allan variance* of $y$ as

$$\sigma_y^2(\tau) = \frac{1}{2} \left\langle \left( \bar{y}_{i+1}(\tau) - \bar{y}_i(\tau) \right)^2 \right\rangle_i \tag{3.16}$$

and the *Allan deviation*† as $\sigma_y(\tau) = \sqrt{\sigma_y^2(\tau)}$.

Intuitively, the Allan deviation tells you what the error on your measurement of $y$ is after averaging for a timespan $\tau$. There is a useful relation between power laws in the power spectral density of $y$, which we will denote by $S_y(f) \sim f^\alpha$, and those in

*There is also the notable "three-cornered hat" method of comparing three oscillators against each other in such a way as to isolate the instability contributions of each oscillator [161].

†We note that there are a number of variants of these formula and evaluating any of them can be practically tricky (especially when doing so with error bars), so it is recommended to use the "industry standard" software Stable32 for this purpose [162].

its Allan deviation, which we will denote by $\sigma_y(\tau) \sim \tau^\beta$, given by [161]

$$\beta = -\tfrac{1}{2}(1+\alpha) \tag{3.17}$$

One generally finds that for sufficiently long averaging, $\bar{y}_i$ follow a Gaussian white noise ($\alpha = 0$) spectrum. Thus, one often observes $\sigma_y(\tau) \sim 1/\sqrt{\tau}$ behavior in the Allan deviation for long enough $\tau$. This makes sense, as the standard error of a Gaussian distribution decreases as the inverse square root of the number of measurements, and here $\tau$ is proportional to the number of measurements. This affirms our intuition that the Allan deviation measures "precision at a given averaging time." The instability of a clock is then often quoted as $\sigma_y(\tau) = x/\sqrt{\tau}$, where $x$ is the instability "at one second of averaging" (even if the $1/\sqrt{\tau}$ trend is not valid at $\tau = 1$ s).

It should be noted, however, that the measured value of $x$ in an AOM comparison scheme (as described above) may not be exactly the correct value for the true Allan deviation of the local oscillator, i.e., if $y$ is defined as the frequency of the local oscillator instead of as the AOM frequency under feedback. This can be the case for both asynchronous and synchronous comparisons. In this case, it is necessary to rely on a model to link the measured Allan deviation with the true Allan deviation of the local oscillator (see, e.g., Refs. [11, 138] or Sec. 3.4.5).

The Allan deviation is also able to capture slow drifts in $y$, which may be caused by drifts in systematic parameters between two clock systems. This will be seen as the Allan deviation reaching a minimum at some late $\tau$ and trending back up. Unfortunately, this detection of long systematic drifts is not possible when doing a self-comparison with a single laser and single atomic system, as long term drifts will be common-mode to both "rails" and thus $y$ cannot drift*. Therefore, a full self-comparison does not give full information as to the long-term instability of the system.

Finally, note that a measurement of $y$ may be useful not only as a measurement of instability, but also as a measurement of systematic shifts. Instead of recording $\nu_1(t_k)$ and $\nu_2(t_k)$ under nominally identical settings, we can intentionally create a systematic shift in one of the rails (of a potentially unknown magnitude) by using different experimental parameters (fields, etc) on that rail. Then, instead of $y$

*_Unless_ there is some systematic offset that oscillates with a period commensurate with the time in between rails, and its differential value between the two rails somehow changes over time. This is, however, a very unusual situation.

averaging to (ideally) zero, it will average to some finite value which is ($\frac{1}{\sqrt{2}}$ times) the fractional systematic shift. The Allan deviation of $y$ (or rather, its inverse) tells us how long we have to average for (in actual experimental time units) in order to "resolve" a fractional systematic shift of a given magnitude.

## 3.4 An atomic-array optical clock with single-atom readout

***Note: This section is a partial reproduction of our publication Ref. [138] with minor editing and certain sections of the publication's Appendix omitted.***

Currently, the most accurate and stable clocks use optical interrogation of either a single ion or an ensemble of neutral atoms confined in an optical lattice. Here, we demonstrate a new optical clock system based on an array of individually trapped neutral atoms with single-atom readout, merging many of the benefits of ion and lattice clocks as well as creating a bridge to recently developed techniques in quantum simulation and computing with neutral atoms. We evaluate single-site resolved frequency shifts and short-term stability via self-comparison. Atom-by-atom feedback control enables direct experimental estimation of laser noise contributions. Results agree well with an *ab initio* Monte Carlo simulation that incorporates finite temperature, projective read-out, laser noise, and feedback dynamics. Our approach, based on a tweezer array, also suppresses interaction shifts while retaining a short dead time, all in a comparatively simple experimental setup suited for transportable operation. These results establish the foundations for a third optical clock platform and provide a novel starting point for entanglement-enhanced metrology, quantum clock networks, and applications in quantum computing and communication with individual neutral atoms that require optical clock state control.

### 3.4.1 Introduction

Optical clocks — based on interrogation of ultra-narrow optical transitions in ions or neutral atoms — have surpassed traditional microwave clocks in both relative frequency stability and accuracy [11, 14, 15, 29]. They enable new experiments for geodesy [14, 163], fundamental physics [164, 165], and quantum many-body physics [166], in addition to a prospective redefinition of the SI second [167]. In parallel, single-atom detection and control techniques have propelled quantum simulation and computing applications based on trapped atomic arrays; in particular, ion traps [168], optical lattices [169], and optical tweezers [74, 76]. Integrating such techniques into an optical clock would provide atom-by-atom error evaluation, feedback, and thermometry [144]; facilitate quantum metrology applications, such as quantum-enhanced clocks [16, 61, 170, 171] and clock networks [172]; and enable novel quantum computation, simulation, and communication architectures that require optical clock state control combined with single atom trapping [81, 173,

174].

As for current optical clock platforms, ion clocks already incorporate single-particle detection and control [175], but they typically operate with only a single ion. Research towards multi-ion clocks is ongoing [176]. Conversely, optical lattice clocks (OLCs) [11, 14, 15] interrogate thousands of atoms to improve short-term stability, but single-atom detection and control remains an outstanding challenge. An ideal clock system, in this context, would thus merge the benefits of ion and lattice clocks; namely, a large array of isolated atoms that can be read out and controlled individually.

Here we present a prototype of a new optical clock platform based on an atomic array which naturally incorporates single-atom readout of currently ∼40 individually trapped neutral atoms. Specifically, we use a magic wavelength 81-site tweezer array stochastically filled with single strontium-88 ($^{88}$Sr) atoms [116]. Employing a repetitive imaging scheme [116] (Sec. 2.6.8), we stabilize a local oscillator to the optical clock transition [106, 141] with a low dead time of ∼100 ms between clock interrogation blocks.

We utilize single-site and single-atom resolution to evaluate the in-loop performance of our clock system in terms of stability, local frequency shifts, selected systematic effects, and statistical properties. To this end, we define an error signal for single tweezers which we use to measure site-resolved frequency shifts at otherwise fixed parameters. We also evaluate statistical properties of the in-loop error signal, specifically, the dependence of its variance on atom number and correlations between even and odd sites.

We further implement a standard interleaved self-comparison technique [160, 177] to evaluate systematic frequency shifts with changing external parameters – specifically trap depth and wavelength – and find an operational magic condition [145, 148, 178] where the dependence on trap depth is minimized. We also demonstrate a proof-of-principle for extending such self-comparison techniques to evaluate *single-site-resolved* systematic frequency shifts as a function of a changing external parameter.

Using self-comparison, we evaluate the fractional short-term instability of our clock system to be $2.5 \times 10^{-15}/\sqrt{\tau}$. To compare our experimental results with theory predictions, we develop an *ab initio* Monte Carlo (MC) clock simulation [179] (Sec. 3.4.6), which directly incorporates laser noise, projective readout, finite temperature, and feedback dynamics, resulting in higher predictive power

compared to traditionally used analytical methods [15]. Our experimental data agree quantitatively with this simulation, indicating that noise processes are well captured and understood at the level of stability we achieve here. Based on the MC model, we predict a fractional instability of (1.9–2.2)$\times 10^{-15}/\sqrt{\tau}$ for single clock operation, which would have shorter dead time than that in self-comparison.

We further demonstrate a direct evaluation of the $1/\sqrt{N_A}$ dependence of clock stability with atom number $N_A$, on top of a laser noise dominated background, through an atom-by-atom system-size-selection technique. This measurement and the MC model strongly indicate that the instability is limited by the frequency noise of our local oscillator. We note that the measured instability is comparable to OLCs using similar transportable laser systems [180].

We note the very recent, complementary results of Ref. [100] that show seconds-long coherence in a tweezer array filled with ~5 $^{88}$Sr atoms using an ultra-low noise laser without feedback operation. In this and our system, a recently developed repetitive interrogation protocol [116] (Sec. 2.6.8), similar to that used in ion clocks, provides a short dead time of ≈100 ms between interrogation blocks, generally suppressing the impact of laser noise on stability stemming from the Dick effect [153]. Utilizing seconds-scale interrogation with such low dead times combined with the feedback operation and realistic upgrade to the system size demonstrated here promises a clock stability that could reach that of state-of-the-art OLCs [11, 13, 14, 181] in the near-term future, as further discussed in the outlook section.

Concerning systematic effects, the demonstrated atomic array clock has intrinsically suppressed interaction and hopping shifts: First, single atom trapping in tweezers provides immunity to on-site collisions present in one-dimensional OLCs [182]. While three-dimensional OLCs [181] also suppress on-site collisions, our approach retains a short dead time as no evaporative cooling is needed. Further, the adjustable and significantly larger interatomic spacing strongly reduces dipolar interactions [183] and hopping effects [184]. We experimentally study effects from tweezer trapping in Sec. 3.4.4, but leave a full study of other systematics, not specific to our platform, and a statement of accuracy to future work. In this context, we note that our tweezer system is well-suited for future investigations of black-body radiation shifts via the use of local thermometry with Rydberg states [144].

The results presented here and in Ref. [100] provide the foundation for establishing a third optical clock platform promising competitive stability, accuracy, and robustness, while incorporating single-atom detection and control techniques in a

natural fashion. We expect this to be a crucial development for applications requiring advanced control and read-out techniques in many-atom quantum systems, as discussed in more detail in the outlook section.

### 3.4.2 Functional principle

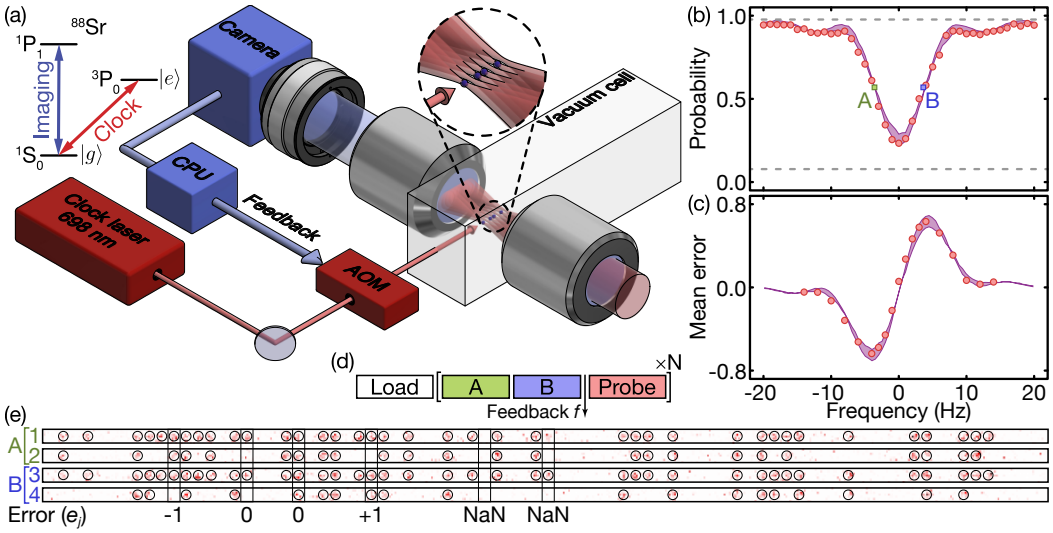


Figure 3.4: Atomic array optical clock. **(a)** We interrogate ~40 $^{88}$Sr atoms, trapped in an 81-site tweezer array, on the ultra-narrow clock transition at 698 nm and use high-resolution fluorescence imaging at 461 nm to detect population changes in the clock states (labeled $|g\rangle$ and $|e\rangle$) with single-atom resolution. This information is processed by a central processing unit (CPU) and a feedback signal is applied to the clock laser frequency using an acousto-optic modulator (AOM). **(b)** Tweezer-averaged probability to remain in $|g\rangle$ as a function of frequency offset measured with an in-loop probe sequence (circles). Dashed horizontal lines indicate state-resolved detection fidelities [116]. To generate an error signal, we interrogate twice: once below ($A$) and once above ($B$) resonance. **(c)** Tweezer-averaged error signal as a function of frequency offset (circles). The shaded areas in (b) and (c) show results from MC simulations. **(d)** Simplified experimental sequence, consisting of tweezer loading and $N$-times-repeated $AB$ feedback blocks followed by an optional probe block, with $N = 10$ throughout. **(e)** To detect the clock state population in block $A$, we take a first image before interrogation to identify which tweezers are occupied and a second image after interrogation to detect which atoms remain in $|g\rangle$ (images 1 and 2). The same procedure is repeated for block $B$ (images 3 and 4). We show fluorescence images with identified atoms (circles) and examples of single tweezer error signals $e_j$.

We generate a tweezer array with linear polarization and 2.5 $\mu$m site-to-site spacing in an ultra-high vacuum glass cell using an acousto-optic deflector (AOD) and a high-

resolution imaging system (Fig. 3.4a)[116]. The tweezer array wavelength is tuned to a magic trapping configuration close to 813.4 nm, as described below. We load the array from a cold atomic cloud and subsequently induce light-assisted collisions to eliminate higher trap occupancies [89, 116]. As a result, ~40 of the tweezers are stochastically filled with a single atom. We use a recently demonstrated narrow-line Sisyphus cooling scheme [116] to cool the atoms to an average transverse motional occupation number of $\bar{n} \approx 0.66$, measured with clock sideband spectroscopy. The atoms are then interrogated twice on the clock transition, once below ($A$) and once above ($B$) resonance, to obtain an error signal quantifying the frequency offset from the resonance center (Fig. 3.4b,c). We use this error signal to feedback to a frequency shifter in order to stabilize the frequency of the interrogation laser — acting as a local oscillator — to the atomic clock transition. Since our imaging scheme has a survival fraction of >0.998 [116] (Sec. 2.6.8), we perform multiple feedback cycles before reloading the array, each composed of a series of cooling, interrogation, and readout blocks (Fig. 3.4d). During clock interrogation, the magnetic field is $|B| \sim 9$ G and the probe intensity is $I \sim 1560$ mW/cm$^2$.

For state-resolved readout with single-shot, single-atom resolution, we use a detection scheme composed of two high-resolution images for each of the $A$ and $B$ interrogation blocks (Fig. 3.4e) [116]. A first image determines if a tweezer is occupied, followed by clock interrogation. A second image, after interrogation, determines if the atom has remained in the ground state $|g\rangle$. This yields an instance of an error signal for all tweezers that are occupied at the beginning of both interrogation blocks, while unoccupied tweezers are discounted. For occupied tweezers, we record the $|g\rangle$ occupation numbers $s_{A,j} = \{0, 1\}$ and $s_{B,j} = \{0, 1\}$ in the images after interrogation with $A$ and $B$, respectively, where $j$ is the tweezer index. The difference $e_j = s_{A,j} - s_{B,j}$ defines a single-tweezer error variable taking on three possible values $e_j = \{-1, 0, +1\}$ indicating interrogation below, on, or above resonance, respectively. Note that the average of $e_j$ over many interrogations, $\langle e_j \rangle$, is simply an estimator for the difference in transition probability between blocks $A$ and $B$.

For feedback to the clock laser, $e_j$ is averaged over all occupied sites in a single $AB$ interrogation cycle, yielding an array-averaged error $\bar{e} = \frac{1}{N_A} \sum_j e_j$, where the sum runs over all occupied tweezers and $N_A$ is the number of present atoms. We add $\bar{e}$ times a multiplicative factor to the frequency shifter, with the magnitude of this factor optimized to minimize in-loop noise.

### 3.4.3 In-loop spectroscopic results

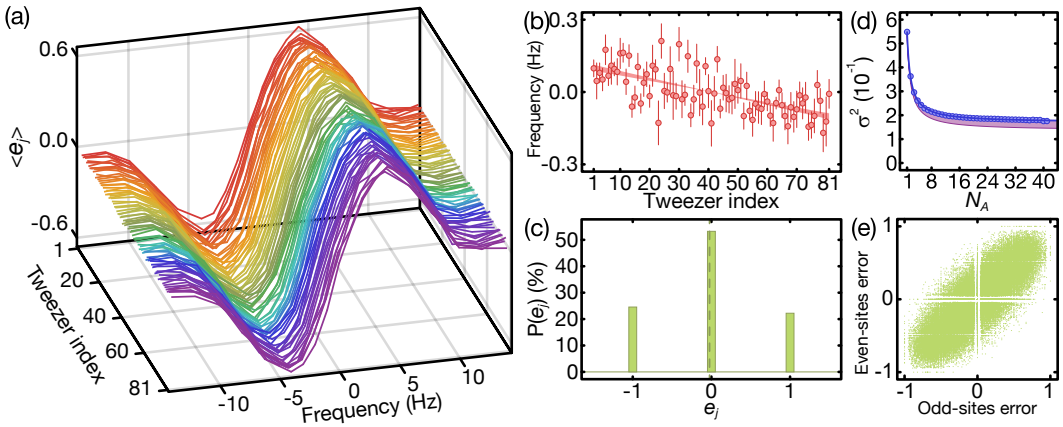


Figure 3.5: Site-resolved error signal. **(a)** Repetition-averaged single-tweezer error signal $\langle e_j \rangle$ as a function of frequency offset measured with an in-loop sequence. **(b)** Fitted zero-crossings as a function of tweezer index for our usual interrogation trap depth of $U_1 = 245(31)E_r$ where $E_r = h \times 3.43$ kHz (circles). Solid lines correspond to theory predictions, with the shaded area resulting from systematic uncertainty in trap depth. **(c)** Ternary probability distribution for $e_j$ for a selected tweezer. The vertical dashed line shows the mean. **(d)** Variance of the error signal as a function of atom number, calculated through post-selection. Solid line is a fit with a $1/N_A$ function plus an offset. Purple region is a MC simulation. **(e)** Plot of correlations between the error signals of even and odd sites.

We begin by describing results for in-loop detection sequences. Here, feedback is applied to the clock laser (as described before) and probe blocks, for which the interrogation frequency is varied, are added after each feedback cycle. Using a single probe block with an interrogation time of 110 ms (corresponding to a $\pi$-pulse on resonance) shows a nearly Fourier-limited line-shape with full-width at half-maximum of ~7 Hz (Fig. 3.4b). We also use these parameters for the feedback interrogation blocks, with the $A$ and $B$ interrogation frequencies spaced by a total of 7.6 Hz. Using the same in-loop detection sequence, we can also directly reveal the shape of the error signal by using two subsequent probe blocks spaced by this frequency difference and scanning a common frequency offset (Fig. 3.4c). The experimental results are in agreement with MC simulations, which have systematic error denoted as a shaded area throughout, stemming from uncertainty in the noise properties of the interrogation laser (Sec. 3.4.6).

Importantly, these data also exist on the level of individual tweezers, both in terms of averages and statistical fluctuations. As a first example, we show a tweezer-resolved

measurement of the repetition-averaged error signal $\langle e_j \rangle$ for all 81 traps (Fig. 3.5a) as a function of frequency offset.

Fitting the zero-crossings of $\langle e_j \rangle$ enables us to detect differences in resonance frequency with sub-Hz resolution (Fig. 3.5b). The results show a small gradient across the array due to the use of an AOD: tweezers are spaced by 500 kHz in optical frequency, resulting in an approximately linear variation of the clock transition frequency. This effect could be avoided by using a spatial light modulator for tweezer array generation [45]. We note that the total frequency variation is smaller than the width of our interrogation signal. Such "sub-bandwidth" gradients can still lead to noise through stochastic occupation of sites with slightly different frequencies; in our case, we predict an effect at the $10^{-17}$ level. It is possible to eliminate this type of noise in future clock iterations with a local feedback correction factor.

Before moving on, we note that $e_j$ is a random variable with a ternary probability distribution (Fig. 3.5c) defined for each tweezer. The results in Fig. 3.5a are the mean of this distribution as a function of frequency offset. In addition to such averages, having a fully site-resolved signal enables valuable statistical analysis. As an example, we extract the variance of $\bar{e}$, $\sigma^2_{\bar{e}}$, for an in-loop probe sequence where the probe blocks are centered around resonance.

Varying the number of atoms taken into account (via post-selection) shows a $1/N_A$ scaling with a pre-factor dominated by quantum projection noise (QPN) [15] on top of an offset stemming mainly from laser noise (Fig. 3.5d). A more detailed analysis reveals that, for our atom number, the relative noise contribution from QPN to $\sigma_{\bar{e}}$ is only ~26%. A similar conclusion can be drawn on a qualitative level by evaluating correlations between tweezer resolved errors from odd and even sites, which show a strong common mode contribution indicative of sizable laser noise (Fig. 3.5e).

### 3.4.4 Self-comparison for evaluation of systematic shifts from tweezer trapping

We now turn to an interleaved self-comparison [160, 177], which we use for stability evaluation and systematic studies. The self-comparison consists of having two feedback loops running in parallel, where feedback is given in an alternating fashion to update two independent AOM frequencies $f_1$ and $f_2$ (Fig. 3.6a). This is used for a lock-in type evaluation of clock frequency changes with varying parameters. As a specific example, we operate the clock with our usual interrogation trap depth $U_1$

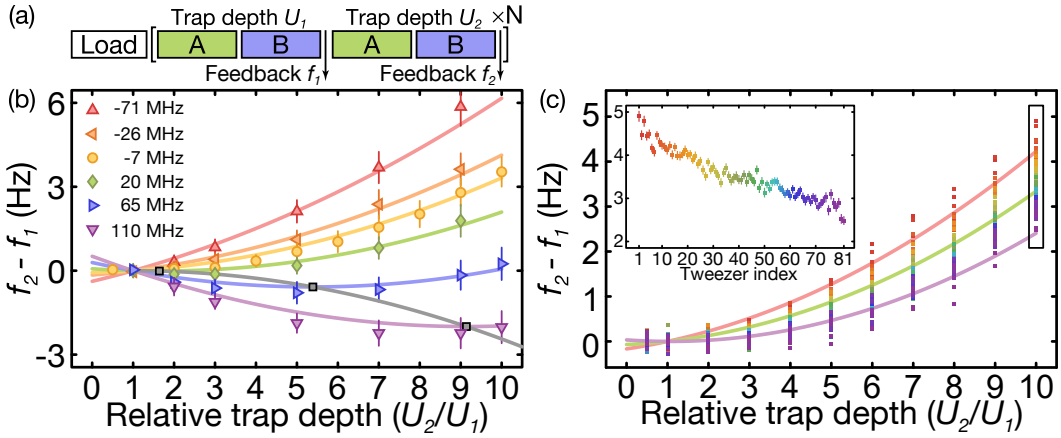


Figure 3.6: Systematic evaluation of clock shifts with tweezer depth and wavelength. **(a)** Illustration of interleaved self-comparison, where two independent AOM frequencies ($f_1$ and $f_2$) are updated in an alternating fashion. Respective interrogation blocks are set to two independent tweezer depths $U_1$ and $U_2$. **(b)** Average frequency difference $f_2 - f_1$ as function of $U_2/U_1$, with $U_1$ fixed to our usual interrogation depth, for multiple frequency offsets of the trapping laser (see legend for color coding). We fit the data with a model for light shifts in optical tweezers (colored lines) with only a single free parameter (for all data simultaneously), accounting for an unknown frequency offset. Operational magic intensities are found at the minima of these curves (gray squares and connecting line), which minimize sensitivity to trap depth fluctuations. The trap laser frequency is tuned such that the minimum coincides with our nominal depth. **(c)** Combining this technique with the single-tweezer resolved error $\langle e_j \rangle$, we can extract a frequency dependence with trap depth for each tweezer (colored squares). Solid lines show the expected dependence for the outermost and central tweezers. The data corresponds to the $-7$ MHz set in (b). Inset: Local frequency shifts for $U_2/U_1 = 10$. The color coding of the inset defines the color coding of its containing sub-figure.

during blocks for feedback to $f_1$ and with a different trap depth $U_2$ during blocks for feedback to $f_2$. The average frequency difference $f_2 - f_1$ now reveals a shift of the clock operation frequency dependent on $U_2$ (Fig. 3.6b). For optimal clock operation, we find an "operationally magic" condition that minimizes sensitivity to trap depth fluctuations [145, 148, 178] by performing two-lock comparisons for different wavelengths (Fig. 3.6b). We note that this type of standard self-comparison can only reveal array-averaged shifts.

In this context, an important question is how such lock-in techniques can be extended to reveal site-resolved systematic errors as a function of a changing external parameter. To this end we combine the tweezer resolved error signal $\langle e_j \rangle$ with interleaved self-comparison (Fig. 3.6c). Converting $\langle e_j \rangle$ to frequencies (using measured

error functions, such as in Fig. 3.5a) yields frequency estimators $\delta f_{1,j}$ and $\delta f_{2,j}$ for each tweezer during $f_1$ and $f_2$ feedback blocks, respectively. These estimators correspond to the relative resonance frequency of each tweezer with respect to the center frequency of the individual locks. Plotting the quantity $\delta f_{2,j} - \delta f_{1,j} + f_2 - f_1$ then shows the absolute frequency change of each tweezer as a function of trap depth (Fig. 3.6c).

### 3.4.5 Self-comparison for stability evaluation

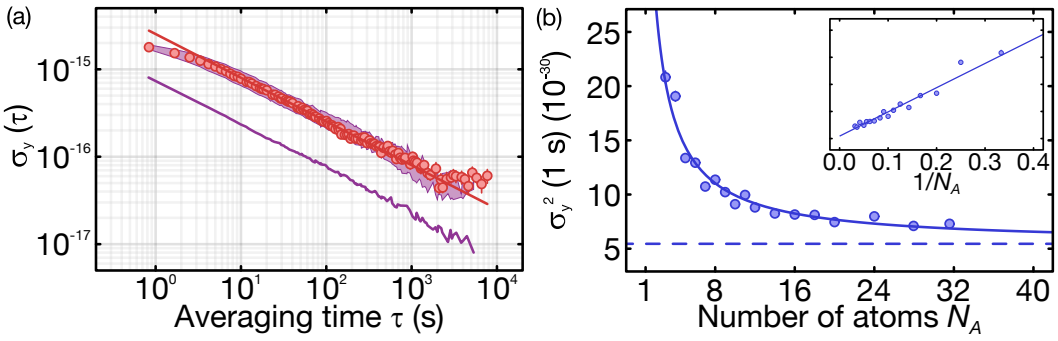


Figure 3.7: Stability results. **(a)** Fractional Allan deviation $\sigma_y$ obtained via self-comparison as a function of integration time $\tau$ (circles). Fitting a $1/\sqrt{\tau}$ behavior past an initial lock onset time (red solid line), we find $2.5 \times 10^{-15}/\sqrt{\tau}$. The shaded area denotes MC results. The purple solid line shows the quantum projection noise limit obtained from MC by switching off all other noise sources. **(b)** Based on atom-by-atom feedback control, we perform a series of self-comparisons with fixed atom number $N_A$. Shown is the Allan variance $\sigma_y^2$ at one second (from a $1/\sqrt{\tau}$ fit) as a function of $N_A$. Inset: Allan variance $\sigma_y^2$ as a function of $1/N_A$. Solid lines show a fit with a functional form $\sigma_y^2 = \sigma_\infty^2 + \sigma_{N_A}^2$, where $\sigma_{N_A}$ scales as $1/\sqrt{N_A}$.

We use the same self-comparison sequence to evaluate the fractional clock instability by operating both locks with identical conditions (Fig. 3.7a). This approach follows previous clock studies, where true comparison to a second, fully independent clock system was not available [160, 177]. We plot the Allan deviation $\sigma_y$ [185] of $y = (f_2 - f_1)/(\nu_0\sqrt{2})$ in Fig. 3.7a, where $\nu_0$ is the clock transition frequency and the $\sqrt{2}$ factor is introduced to take into account the addition of noise from two identical sources. The results show a $1/\sqrt{\tau}$ behavior after a lock onset time, where $\tau$ is the averaging time in seconds. Fitting this behavior yields $\sigma_y = 2.5 \times 10^{-15}/\sqrt{\tau}$, in excellent agreement with MC simulations (Fig. 3.7a).

Self-comparison evaluates how fast averaging can be performed for systematic studies — such as the one shown in Fig. 3.6 — and reveals the impact of various

noise sources on short-term stability; however, by design, this technique suppresses slow drifts that are common to the $f_1$ and $f_2$ interrogation blocks. We performed a separate stability analysis by locking $f_1$ to the left half of the array and $f_2$ to the right half of the array [181], a method which is sensitive to slow drifts of gradients, and found no long-term drift of gradients to within our sensitivity.

Having shown good agreement between our data and MC simulations, we are able to further use the simulation to predict properties of our clock that are not directly experimentally accessible. One of these properties is the true stability of the local oscillator frequency, computed directly by taking the Allan deviation of the simulated laser frequency time traces under feedback. This allows us to simulate the stability of single clock operation, which has shorter dead time than the double clock scheme that we use to evaluate stability in experiment. Following this protocol, our simulations predict (1.9–2.2)$\times 10^{-15}/\sqrt{\tau}$ for the local oscillator stability during single clock operation (Sec. 3.4.6). In this context, we note the results of Ref. [100], where stability is evaluated by converting a spectroscopic signal into a frequency record (without a closed feedback loop). Based on interrogation with an ultra-low noise laser system, they achieve a short-term stability of $4.7\times 10^{-16}/\sqrt{\tau}$ with ∼5 atoms in tweezers.

Generically, clock stability improves with increasing atom number as $1/\sqrt{N_A}$ through a reduction in readout-noise as long as atoms are uncorrelated. However, in the presence of laser noise — which is common mode to all atoms — a limit to stability exists even for an infinite number of atoms [15]. Intriguingly, we can directly extract such contributions by performing a series of self-comparisons where we adjust the atom number one-by-one (Fig. 3.7b). To this end, we restrict the feedback operation to a subset of atoms in the center of the array with desired size, ignoring the remainder. We are able to achieve stable locking conditions for $N_A \geq 3$ with typical feedback parameters. We evaluate the Allan variance at one second as a function of $N_A$ and fit the results with a function $\sigma_y^2 = \sigma_\infty^2 + \sigma_{N_A}^2$, where $\sigma_{N_A}$ scales as $1/\sqrt{N_A}$. We find $\sigma_{N_A} = 6.7\times 10^{-15}/\sqrt{N_A \cdot \tau}$ and $\sigma_\infty = 2.3\times 10^{-15}/\sqrt{\tau}$, the latter being an estimator for the limit of our clock set by laser noise, in agreement with MC simulation.

### 3.4.6 Monte Carlo clock simulations

***Operation***

We compare the performance of our clock to Monte Carlo (MC) simulations. The simulations include the effects of laser frequency noise, dead time during loading and between interrogations, quantum projection noise, finite temperature, stochastic filling of tweezers, and experimental imperfections such as state-detection infidelity and atom loss. The effects of Raman scattering from the trap and of differential trapping due to hyperpolarizability or trap wavelength shifts from the AOD are not included as they are not expected to be significant at our level of stability.

Rabi interrogation is simulated by time evolving an initial state $|g\rangle$ with the time-dependent Hamiltonian $\hat{H}(t) = \hbar\big(\Omega S^x - (\Delta(t) \pm \Delta_o)S^z\big)$, where $\Omega$ is the Rabi frequency, $\Delta_o$ is an interrogation offset, and $\Delta(t)$ is the instantaneous frequency noise defined such that $\Delta(t) = \frac{d\phi(t)}{dt}$, where $\phi(t)$ is the optical phase in the rotating frame. The frequency noise $\Delta(t)$ for each Rabi interrogation is sampled from a pre-generated noise trace (Secs. 3.4.6 & 3.4.6) with a discrete timestep of 10 ms. Dead time between interrogations and between array refilling is simulated by sampling from time-separated intervals of this noise trace. Stochastic filling is implemented by sampling the number of atoms $N_A$ from a binomial distribution on each filling cycle, and atom loss is implemented by probabilistically reducing $N_A$ between interrogations.

To simulate finite temperature, a motional quantum number $n$ is assigned to each of the $N_A$ atoms before each interrogation, where $n$ is sampled from a 1D thermal distribution using our experimentally measured $\bar{n} \sim 0.66$. Here, $n$ represents the motional quantum number along the axis of the interrogating clock beam. For each of the unique values of $n$ that were sampled, a separate Hamiltonian evolution is carried out with a modified Rabi frequency given by $\Omega_n = \Omega e^{-\frac{\eta^2}{2}} L_n(\eta^2)$ [112], where $\eta = \frac{2\pi}{\lambda_{clock}}\sqrt{\frac{\hbar}{2m\omega}}$ is the Lamb-Dicke parameter, $L_n$ is the $n$-th order Laguerre polynomial, and $\Omega$ is the bare Rabi frequency valid in the limit of infinitely tight confinement.

At the end of each interrogation, excitation probabilities $p_e(n) = |\langle e|\psi_n\rangle|^2$ are computed from the final states for each $n$. State-detection infidelity is simulated by defining adjusted excitation probabilities $\tilde{p}_e(n) \equiv f_e p_e(n) + (1 - f_g)(1 - p_e(n))$, where $f_g$ and $f_e$ are the ground and excited state detection fidelities [116], respec-

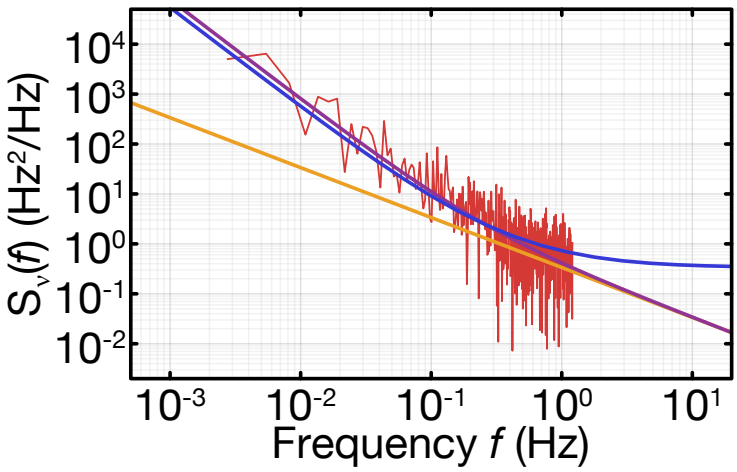


Figure 3.8: Frequency noise spectrum of the clock laser. Power spectral density of the frequency noise of our clock laser measured from a beat signal with a reference laser over a 42-hour period (red trace). Our theoretical estimate of the thermal noise contribution is plotted in yellow. Plotted also are our best- (purple) and worst- (blue) case models for total frequency noise, as used in Monte Carlo simulations.

tively. To simulate readout of the $j$-th atom on the $i$-th interrogation, a Bernoulli trial with probability $\tilde{p}_e(n_j)$ is performed, producing a binary readout value $s_{j,i}$. An error signal $\bar{e} = \frac{1}{N_A}\sum_j (s_{j,i-1} - s_{j,i})$ is produced every two interrogation cycles by alternating the sign of $\delta_o$ on alternating interrogation cycles. This error signal produces a control signal (using the same gain factor as used in experiment) which is summed with the generated noise trace for the next interrogation cycle, closing the feedback loop.

***Generating frequency noise traces***

Using a model of the power spectral density of our clock laser's frequency noise (Sec 3.4.6), we generate random frequency noise traces in the time domain [117] for use in the Monte Carlo simulation. Given the power spectral density of frequency noise $S_\nu(f)$, we generate a complex one-sided amplitude spectrum $A_\nu(f) = e^{i\phi(f)}\sqrt{2S_\nu(f)\Delta f}$, where $\phi(f)$ is sampled from a uniform distribution in $[0, 2\pi)$ for each $f$ and $\Delta f$ is the frequency discretization. This is converted to a two-sided amplitude spectrum by defining $A_\nu(-f) = A^*_\nu(f)$. Finally, a time trace $\nu(t) = \mathcal{F}\{A(f)\}(t) + \nu_l(t)$ is produced by taking a fast Fourier transform (FFT) of $A(f)$ and adding an experimentally calibrated linear drift term $\nu_l(t)$.

***Frequency noise model***

The power spectral density of the frequency noise of our clock laser is modeled by the sum of contributions from random walk frequency modulation (RWFM) noise ($f^{-2}$), flicker frequency modulation (FFM) noise ($f^{-1}$), and white frequency modulation (WFM) noise ($f^{0}$), such that $S_\nu(f) = \alpha f^{-2} + \beta f^{-1} + \gamma f^{0}$. We obtain these parameters through an estimation of the thermal noise of our reference cavity and a fit of a partially specified frequency noise power spectral density obtained via beating our laser with a reference laser (Fig. 3.8). Due to a remaining large uncertainty in the white noise floor of our laser, we define a worst- and best-case noise model. The range between these models is the dominant source of uncertainty in our Monte Carlo simulations.

FFM noise results from thermal mechanical fluctuations of the reference cavity [157, 158]. By estimating the noise contribution from the ultra-low expansion spacer, fused silica mirrors, and their reflective coating, we estimate a fractional frequency instability of $\sigma_y = 1.6 \times 10^{-15}$ at 1 s, which corresponds to a frequency noise power spectral density of $\beta f^{-1} = 0.34\ \mathrm{Hz}^2/\mathrm{Hz}$ at $f = 1$ Hz.

As a worst case noise model, we assume a cross-over frequency from FFM to WFM noise at 1 Hz (Fig. 3.8), such that $\gamma = \beta f^{-1} = 0.34\ \mathrm{Hz}^2/\mathrm{Hz}$, and we estimate a frequency noise power spectral density of $\alpha f^{-2} = 0.05\ \mathrm{Hz}^2/\mathrm{Hz}$ at 1 Hz for RWFM noise. As a best case noise model, assuming no cross-over from FFM to WFM noise (such that $\gamma = 0.00\ \mathrm{Hz}^2/\mathrm{Hz}$), we estimate a frequency noise power spectral density for RWFM noise of $\alpha f^{-2} = 0.08\ \mathrm{Hz}^2/\mathrm{Hz}$ at $f = 1$ Hz. We note that the difference in predicted clock stability between the best and worst case model is relatively minor. This indicates that dominant contributions to clock instability stem from frequencies where we have experimental frequency noise data and where both models exhibit similar frequency noise. This is confirmed by an analytical Dick noise analysis [153] (not shown).

### 3.4.7 Outlook on atomic-array optical clocks

Our results merge single-particle readout and control techniques for neutral atom arrays with optical clocks based on ultra-narrow spectroscopy. Such atomic array optical clocks (AOCs) could approach the sub-$10^{-16}/\sqrt{\tau}$ level of stability achieved with OLCs [11, 13, 14, 181] by increasing interrogation time and atom number. Reaching several hundreds of atoms is realistic with an upgrade to two-dimensional

arrays, while Ref. [100] already demonstrated seconds-long interrogation. A further increase in atom number is possible by using a secondary array for readout, created with a non-magic wavelength for which higher power lasers exist [89, 97]. We also envision a system where tweezers are used to "implant" atoms, in a structured fashion, into an optical lattice for interrogation and are subsequently used to provide confinement for single-atom readout. Further, the lower dead time of AOCs should help to reduce laser noise contributions to clock stability compared to 3d OLCs [181], and even zero dead time operation [13, 181] in a single machine is conceivable by adding local interrogation. Local interrogation could be achieved through addressing with the main objective or an orthogonal high-resolution path by using spatial-light modulators or acoustic-optic devices. For the case of addressing through the main objective, atoms would likely need to be trapped in an additional lattice to increase longitudinal trapping frequencies.

Concerning systematics, AOCs provide a fully site-resolved evaluation combined with an essential mitigation of interaction shifts, while being ready-made for implementing local thermometry using Rydberg states [144] in order to more precisely determine black-body induced shifts [15]. In addition, AOCs offer an advanced toolset for generation and detection of entanglement to reach beyond standard quantum limit operation — either through cavities [61, 186] or Rydberg excitation [16] — and for implementing quantum clock networks [172]. Further, the demonstrated techniques provide a pathway for quantum computing and communication with neutral alkaline-earth-like atoms [81, 166, 174]. Finally, features of atomic array clocks, such as experimental simplicity, short dead time, and three-dimensional confinement, make these systems attractive candidates for robust portable clock systems and space-based missions [145].

# Chapter 4

# ENTANGLEMENT AND RYDBERG PHYSICS

In this chapter we will explore how long-range interactions can be induced between atoms in neighboring tweezers via excitation to Rydberg states. We will find that such interactions can create entanglement between atoms with respect to the qubit defined by the Rydberg transition. These concepts will be the basic building blocks of more complex many-body models that we will explore in Sec. 5.1.1. Rydberg states are particularly good candidates for quantum information tasks [187, 188] not only because of their interactions, but because they can be coherently excited on timescales much faster than their dephasing timescales (Sec. 4.4).

We note the related concept of Rydberg *dressing* [16, 189], where lower-lying states are given a small admixture with Rydberg states and in which case the interacting qubit is defined not on the Rydberg transition but on the lower-lying transition. While such schemes are very much possible in our platform (most notably on the clock transition [16]), we leave such explorations as an outlook (Chap. 5).

We begin with a description of how Rydberg states are excited, read out, and detected (Sec. 4.1). We will then discuss how interactions arise between Rydberg states, the phenomenon of *Rydberg blockade*, and how this leads to entanglement between atoms (Sec. 4.2). We will show results for single- and two-atom excitation and entanglement fidelities (Sec. 4.3), and finally discuss sources of error in these quantities (Sec. 4.4).

## 4.1 Excitation and readout

Rydberg states are generally defined as states of large electronic principal number $n$. These states often have a sufficiently large energy such that direct, single-photon excitation to them from the ground state requires deep ultraviolet lasers that are not very convenient to use. Therefore, one often uses a two-stage or two-

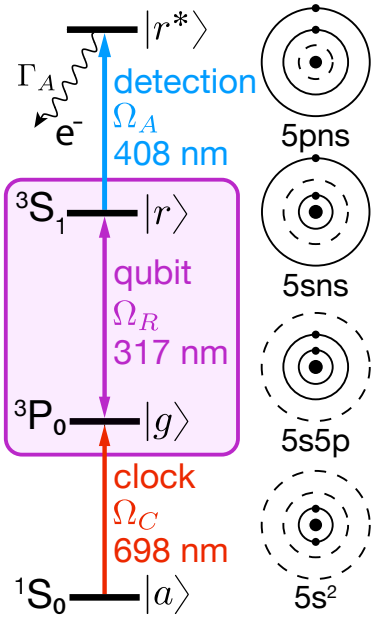


Figure 4.1: Initialization, excitation, and readout of a Rydberg qubit. The qubit itself is highlighted in a purple box. Atoms in the absolute ground state $|a\rangle$ are first transferred to the clock state $|g\rangle$, and subsequently excited to a Rydberg state $|r\rangle$. State detection is performed by exciting atoms in $|r\rangle$ to an auto-ionizing state $|r^*\rangle$ and imaging the remaining atoms.

photon excitation via an intermediate state. There are various such pathways to reaching Rydberg states in Sr, such as excitation via singlet states [190] or via 5s5p $^3P_1$ [191, 192].

Our approach, however, will be via the clock state 5s5p $^3P_0$. Since this state can be quite long-lived, we will not treat it as an "intermediate state" in a two-photon transition, but in fact as a stable "ground state" from which Rydberg states are accessible via a single photon. This fact that our excitation scheme is effectively single-photon results in a few potential benefits over two-photon schemes typical of previous work [119, 193], such as a larger Rabi frequency (which can help overcome sources of dephasing such as laser frequency noise) and the lack of intermediate state decay.

Our procedure will be a two-stage process: a transfer of atoms to the clock state (Sec. 4.1.1) *followed* by single-photon excitation to a Rydberg state (Sec. 4.1.2), *not* a simultaneous two-photon transition. In this context, we will refer to the clock state as $|g\rangle$ — the ground state of the Rydberg qubit — and the Rydberg state as $|r\rangle$. If we would like to refer to the absolute ground state 5s$^2$ $^1S_0$, we will call it

$|a\rangle$. We perform readout of $|r\rangle$ by exciting to an auto-ionizing state we will call $|r^*\rangle$ and imaging remaining atoms (Sec. 4.1.3). These various states and transitions are summarized in Fig. 4.1. We note the existence of other schemes that define a qubit between two different Rydberg states, driven by microwave pulses [194].

### 4.1.1 Clock state initialization

We initialize atoms in the clock state $|g\rangle$ from the absolute ground state $|a\rangle$ via a two-step procedure: (1) a coherent transfer via the clock transition and (2) incoherent transfer via optical pumping.

Transferring as many atoms as possible via coherent operations on the clock transition is desirable in order to ensure that atoms are not heated during the transfer. This is an important consideration for minimizing errors in excitation, readout, and interactions (Sec. 4.4.2). The optical cooling mechanisms we have available to us (Sec. 2.5) ultimately leave cold atoms in the absolute ground state $|a\rangle$, and we currently have no developed scheme for cooling atoms directly in the clock state $|g\rangle$. By working in sideband-resolved and clock-magic ($\lambda = 813.4$ nm) tweezers, we can selectively drive the carrier on the clock transition, thereby transfering atoms from the ground state to the clock state with no change in the motional state. We perform the transfer on the clock transition under a magnetic field of $|B| = 710$ G, which is then reduced to $|B| = 71$ G for Rydberg excitation.

We find that it is beneficial to perform the $\pi$-pulse in initially deep ($U_0 \sim k_B \times 0.5$ mK and $\omega_r \sim 2\pi \times 80$ kHz) tweezers to avoid thermal dephasing (Sec. 3.2.1) and to then immediately adiabatically ramp down the traps to about $1/10^{\text{th}}$ of the initial trap depth. This serves two purposes. The first is to minimize trap scattering (Sec. 3.2.2), which can cause them to leave the clock state. The second is to adiabatically lower the temperature so that the atoms have a high probability of being recaptured after Rydberg excitation (see Sec. 4.4.2), during which we turn our traps off (it is also possible to choose to leave the traps on, in which case it is still beneficial to work with weak traps so as to minimize light shifts and the dephasing that ensues from them [151]). An adiabatic change of the trap depth maintains a constant $\bar{n}$ along all directions (by definition) but changes the temperature as $T_f = \frac{\omega_f}{\omega_i} T_i$ (Sec. 2.5.1).

The time-profile of our ramp follows

$$U_0(t) = \frac{U_0(0)}{(1 + t/\tau)^2} \tag{4.1}$$

where $\tau \gg 1/\omega_i$ is a timescale chosen to be much longer than the inverse of $\omega_i$, the initial trap frequency. Ideally, $\omega_i$ is that of the *weakest* trapping direction, which for tweezers is the axial direction. We confirm via sideband spectroscopy that the mean radial motional quantum number $\bar{n}_r$ is preserved after the end of this ramp, but have not made a similar confirmation for the axial motional quantum number.

As summarized in Sec. 3.2.4, we typically "only" reach ~98.5% transfer fidelity with a $\pi$-pulse*. While this is already fairly good, it can be increased by subsequently optically pumping atoms out of the ground state and into the clock state. This can be done by turning on 689 nm, 688 nm, and 707 nm beams at the same time. The first two of these beams drive atoms along the pathway of $5s^2\ {}^1S_0 \rightarrow 5s5p\ {}^3P_1 \rightarrow 5s6s\ {}^3S_1$. From here, atoms can decay into any of the states of the $5s5p\ {}^3P_J$ manifold, with the clock state ($J = 0$) being our target. The 707 nm beam cycles atoms out of $5s5p\ {}^3P_2$, ultimately making the clock state the only dark state. Under optimized parameters, atoms are typically fully pumped into the clock state in ~10 $\mu$s.

After coherent transfer and optical pumping as described, we measure a state transfer fidelity of 99.8% [150].

The downside of optical pumping is that the atoms which are transferred by this method are expected to be hotter than atoms which were coherently transferred. We have not conclusively measured or modeled this claim, but its truth is very likely given the numerous photons that an atom needs to absorb and emit in order to reach the clock state, as well as the time that it spends in differentially trapped states such as $5s6s\ {}^3S_1$ and $5s5p\ {}^3P_2$. We discuss implications of temperature in Sec. 4.4.2. It is furthermore possible that some atoms are not only heated, but are in fact lost from the trap during pumping. This may be particularly problematic if pumping is done in an already ramped-down trap (as we do). We expect such loss to play a role in the residual 0.2% of our state transfer infidelity.

### 4.1.2 Rydberg excitation

From the clock state $5s5p\ {}^3P_0$, we can excite any Rydberg state with quantum numbers $5sns\ {}^3S_1$ or $5snd\ {}^3D_1$. Practically all of our experimental results will be on s states. There are a number of differences between the two series, such as different matrix elements to the clock state, different systematics (Sec. 4.1.4), and different

*We note the possibility of increasing the fidelity of coherent transfer via a non-trivial pulse sequence on the clock transition such as an adiabatic rapid passage or some other optimized sequence [195].

interaction strengths. Perhaps most notable of all, however, is the difference in the angular pattern of their interaction potentials [196–198], where a pair of atoms in s states typically have a nearly isotropic interaction whereas a pair in d states can have strong angular dependence.

### *Quantum defects*

Rydberg states can often be modeled as "modified" hydrogenic eigenstates. For a Rydberg state of quantum numbers* $5snl\ ^{2S+1}L_J$, we can define a modified quantum number $n^\star$ such that

$$n^\star(n,l,S,J) = n - \delta(n,l,S,J) \tag{4.2}$$

where $\delta$ is the *quantum defect*. One finds that many properties of the Rydberg state match those of a hydrogenic state with effective principal quantum number $n^\star$ [199]. For example, the energy of the Rydberg state (with respect to the ionization threshold) is given by [197]

$$\mathscr{E}(n,l,S,J) = -\frac{2\pi\hbar c R}{n^\star(n,l,S,J)^2} \tag{4.3}$$

where $R = (1 - \frac{m_e}{m})R_\infty$ with $m_e$ the electron mass, $m$ the mass of the neutral atom, and $R_\infty = \frac{m_e e^4}{64\pi^3\hbar^3\varepsilon_0^2 c}$ the Rydberg constant. Note that this is identical to the formula for the energy levels of hydrogen atom, where $n^\star = n$.

So far this may seem like a practically useless reshuffling of variables as $\delta$ still has a dependence on $n$, but typically its dependence on $n$ becomes negligible for large $n$. This can be more formally stated by expanding $\delta$ into the following series:

$$\delta(n,l,S,J) = \sum_{k=0}^{\infty} \frac{\delta_{2k}(l,S,J)}{\big(n - \delta_0(l,S,J)\big)^{2k}} \tag{4.4}$$

The validity of this expansion is a result of *quantum defect theory* [196, 197, 200]. A consequence of this is that $\delta(n,l,S,J) \approx \delta_0(l,S,J)$ for $n \gg \delta_0$. For further precision at small $n$, higher order terms can be included. Finally, note that $\delta$ typically becomes small for $l > 2$ [196, 199].

In Table 4.1, we reproduce from Ref. [196] the leading-order $k = 0$ quantum defect coefficients for the $5sns\ ^3S_1$ and $5snd\ ^3D_1$ Rydberg series of Sr. Ref. [196] can be

*We assume throughout that the non-excited inner electron is in its ground-state orbital 5s (except when discussing auto-ionization, see Sec. 4.1.3). This implies $l = L$. Rydberg states with an excited inner electron are auto-ionizing.

consulted for terms up to $k = 4$ and for the defects of other relevant Sr Rydberg series.

| Series | $\delta_0 \approx \delta$ |
|---|---|
| $5sns\ ^3S_1$ | 3.371(2) |
| $5snd\ ^3D_1$ | 2.658(6) |

Table 4.1: Quantum defects $\delta_0$ for relevant Rydberg states in Sr [196]. For the range of $n$ that we will be interested in ($n \geq 40$), only $\delta_0$ is really significant and we have $\delta \approx \delta_0$.

We note that not all Rydberg series are so well-behaved and well-described by a convergent set of coefficients. In particular, if there is a state in the midst of the Rydberg series that does not belong to that series, it can perturb the series in such a way that its properties no longer scale with $n^\star$ in a hydrogenic way for states in the series near the perturber [201]. However, for the series in Sr and range of $n$ that we are interested in, there are not expected to be any significant perturbers [196].

***Transition wavelengths and frequencies***

Using the known energy of the clock state [87], the quantum defect coefficients given in Table 4.1, and Eq. 4.3, we tabulate the transition wavelengths and frequencies for clock to Rydberg transitions in Table 4.2 for $n \in [40, 80]$, which is the typical range of Rydberg states that we will consider in our work. Experimentally, we find these predicted transition wavelengths to be accurate.

***Transition matrix elements***

To maximize $\pi$-fidelities during Rabi oscillations, it is generally favorable to drive Rydberg transitions with as large a Rabi frequency ($\Omega$) as possible. Doing so helps beat several dephasing timescales: (1) spontaneous decay and blackbody transitions, (2) laser noise, and (3) thermal dephasing. As to thermal dephasing, note that we are assuming we are well into the sideband-*un*resolved regime ($\Omega \gg \omega$), so the analysis of Sec. 3.2.1 which was in the sideband-resolved regime and concluded that thermal dephasing could not be beat with a larger $\Omega$ is *not* valid here. With a large enough $\Omega$, one can beat these mechanisms and eventually enter an intensity-noise-dominated regime that cannot be helped by larger $\Omega$ (in the same way as for the clock transition, see Sec. 3.2.3). Dephasing mechanisms will be discussed further in Sec. 4.4. For

| | $5snS\ ^3S_1$ | | $5snD\ ^3D_1$ | |
|---|---|---|---|---|
| $n$ | $\lambda_{vac}$ [nm] | $f$ [THz] | $\lambda_{vac}$ [nm] | $f$ [THz] |
| 40 | 317.1290 | 945.3327 | 317.0978 | 945.4258 |
| 41 | 317.0859 | 945.4613 | 317.0571 | 945.5472 |
| 42 | 317.0461 | 945.5800 | 317.0195 | 945.6595 |
| 43 | 317.0093 | 945.6899 | 316.9846 | 945.7635 |
| 44 | 316.9751 | 945.7918 | 316.9522 | 945.8601 |
| 45 | 316.9434 | 945.8864 | 316.9221 | 945.9499 |
| 46 | 316.9139 | 945.9744 | 316.8941 | 946.0336 |
| 47 | 316.8864 | 946.0564 | 316.8680 | 946.1116 |
| 48 | 316.8608 | 946.1330 | 316.8435 | 946.1846 |
| 49 | 316.8368 | 946.2046 | 316.8206 | 946.2529 |
| 50 | 316.8144 | 946.2717 | 316.7992 | 946.3169 |
| 51 | 316.7933 | 946.3345 | 316.7791 | 946.3770 |
| 52 | 316.7736 | 946.3936 | 316.7602 | 946.4335 |
| 53 | 316.7550 | 946.4491 | 316.7424 | 946.4867 |
| 54 | 316.7375 | 946.5013 | 316.7256 | 946.5367 |
| 55 | 316.7210 | 946.5506 | 316.7098 | 946.5840 |
| 56 | 316.7055 | 946.5970 | 316.6949 | 946.6286 |
| 57 | 316.6908 | 946.6409 | 316.6808 | 946.6707 |
| 58 | 316.6769 | 946.6824 | 316.6675 | 946.7106 |
| 59 | 316.6638 | 946.7217 | 316.6548 | 946.7484 |
| 60 | 316.6513 | 946.7589 | 316.6428 | 946.7842 |
| 61 | 316.6395 | 946.7942 | 316.6315 | 946.8182 |
| 62 | 316.6283 | 946.8277 | 316.6207 | 946.8505 |
| 63 | 316.6177 | 946.8595 | 316.6104 | 946.8812 |
| 64 | 316.6076 | 946.8898 | 316.6006 | 946.9105 |
| 65 | 316.5979 | 946.9186 | 316.5913 | 946.9383 |
| 66 | 316.5887 | 946.9460 | 316.5825 | 946.9648 |
| 67 | 316.5800 | 946.9722 | 316.5740 | 946.9901 |
| 68 | 316.5717 | 946.9971 | 316.5659 | 947.0142 |
| 69 | 316.5637 | 947.0210 | 316.5582 | 947.0373 |
| 70 | 316.5561 | 947.0437 | 316.5509 | 947.0593 |
| 71 | 316.5488 | 947.0655 | 316.5438 | 947.0804 |
| 72 | 316.5419 | 947.0863 | 316.5371 | 947.1006 |
| 73 | 316.5352 | 947.1062 | 316.5306 | 947.1199 |
| 74 | 316.5288 | 947.1253 | 316.5245 | 947.1384 |
| 75 | 316.5227 | 947.1436 | 316.5185 | 947.1561 |
| 76 | 316.5169 | 947.1611 | 316.5128 | 947.1732 |
| 77 | 316.5112 | 947.1779 | 316.5074 | 947.1895 |
| 78 | 316.5058 | 947.1941 | 316.5021 | 947.2052 |
| 79 | 316.5007 | 947.2096 | 316.4971 | 947.2203 |
| 80 | 316.4957 | 947.2245 | 316.4922 | 947.2348 |

Table 4.2: Transition wavelengths (in vacuum) and frequencies for clock to Rydberg transitions, derived from quantum defect coefficients from Ref. [196] summarized in Table. 4.1.

now, we will focus on answering the question of what Rabi frequencies we can expect on the Rydberg transition.

The Rabi frequency at intensity $I$ and complex polarization $\hat{\epsilon}$ of a dipole-allowed transition from $|g\ m_{J_g}\rangle$ to $|r\ m_{J_r}\rangle$ is given by

$$\Omega(I,\hat{\epsilon}) = \frac{1}{\hbar}\sqrt{\frac{2I}{c\varepsilon_0}}\langle r\ m_{J_r}|\hat{\epsilon}\cdot\vec{d}|g\ m_{J_g}\rangle \tag{4.5}$$

$$= \frac{1}{\hbar}\sqrt{\frac{2I}{(2J_r+1)c\varepsilon_0}}\langle r||d||g\rangle \sum_{q=-1}^{1}\epsilon_q\langle J_r\ m_{J_r}|J_g\ m_{J_g};\ 1\ q\rangle \tag{4.6}$$

where $\vec{d} = -e\vec{r}$ is the dipole operator, $\epsilon_q$ is the $q^{\text{th}}$ spherical component* of $\hat{\epsilon}$, and we decomposed the dipole operator via the Wigner-Eckart theorem (Eq. 2.22) into an angular part given by Clebsch-Gordan coefficients and a reduced dipole matrix operator (RDME) $\langle r||d||g\rangle$. Note that we have defined our RDMEs via Eq. 2.22 to be symmetric under $g \leftrightarrow r$ (see also Sec. 2.3.2 for further relation of RDMEs to other physical quantities).

Since we are looking at a $J_g = 0 \leftrightarrow J_r = 1$ transition, all the Clebsch-Gordan coefficients are $\langle 1\ m_{J_r}|0\ m_{J_g};\ 1\ q\rangle = \delta_{q,(m_{J_r}-m_{J_g})}$. Furthermore, let us assume that the polarization $\hat{\epsilon}$ is purely along the component that we want to drive and that our driving beam is Gaussian with total power $P$ and waist radius at the atoms of $w$ (see Eq. 2.18 for the central intensity of a Gaussian beam and Eq. 2.8 for the definition of $w$). Then we can simplify to

$$\Omega = \frac{1}{\hbar}\frac{2}{w}\sqrt{\frac{P}{3\pi c\varepsilon_0}}\langle r||d||g\rangle \tag{4.7}$$

$$[J_g = 0 \leftrightarrow J_r = 1,\ \text{polarization aligned},\ \text{Gaussian beam}]$$

We now need to determine the value of the RDME $\langle r||d||g\rangle$. Before we cite a specific value for this, we first quote a highly useful approximate trend of ground-to-Rydberg RDMEs [199, 201]:

$$\langle r||d||g\rangle \propto (n^\star)^{-3/2} \tag{4.8}$$

where $n^\star$ is the modified principal quantum number (defined in Eq. 4.2) of the Rydberg state $|r\rangle$. This result essentially follows from the scaling of the Rydberg wavefunction at the origin with $n^\star$ under the assumption that the ground state

*We decompose $\hat{\epsilon}$ into spherical components $\epsilon_q$ such that $\epsilon_0 = \epsilon_z$ and $\epsilon_{\pm1} = \mp(\epsilon_x \pm i\epsilon_y)/\sqrt{2}$.

wavefunction is almost entirely localized at the origin when compared to the Rydberg wavefunction [199, 201].

So in principle, the determination of the RDME for one Rydberg transition lets us determine (or at least, closely estimate) the RDMEs of all the ground-to-Rydberg transitions in that series (assuming the series is "well-behaved" and there are no significant perturbers).

We directly determine the value of the RDME for the clock* to $5s61s\ ^3S_1$ transition of Sr by measuring $P$ and $w$ of a well-aligned and polarization-optimized Gaussian beam and the resulting resonant Rabi frequency $\Omega$. For a beam waist radius of $w = 20\ \mu$m and a power of $P = 120$ mW, we measure a Rabi frequency of $\Omega = 2\pi\times 13$ MHz, implying an RDME of $\langle 5s61s\ ^3S_1||d||5s5p\ ^3P_0\rangle = 4.6\times10^{-3} ea_0$, where $e$ is the elementary charge and $a_0$ is the Bohr radius.

Applying Eq. 4.8, this implies†

$$\langle 5sns\ ^3S_1||d||5s5p\ ^3P_1\rangle = 2.0\times\left(n^\star\right)^{-3/2} ea_0 \tag{4.9}$$

We finally discuss matrix elements to the d series $5snd\ ^3D_1$, as this is the other series accessible from the clock state. Ground p to Rydberg d transitions in Rubidium have matrix elements approximately two times as large as those to s states (see Ref. [199] Table B.5), and it is expected that a similar situation occurs in Sr. Although we have not made precise measurements of Rabi frequencies at these transitions, we have successfully driven them and observed that the Rabi linewidth is indeed about a factor of two larger than that of s states. Therefore, if maximizing Rabi frequency is desired, these states may be an option, though this does come at the cost of a shorter radiative lifetime (Sec. 4.4.1). However, we will exclusively use s states for our experimental results.

### 4.1.3 Auto-ionization detection

For a qubit to be useful, one must be able to read out its state in addition to simply driving it. Since our ultimate array readout is fluorescence imaging, we would like

*As a reminder, we are treating the clock state here as a "ground" state.

†One may wonder if this treatment runs into trouble with the validity of the dipole approximation $2\pi r/\lambda \ll 1$. Indeed, Rydberg wavefunctions have a large characteristic radius $r \sim$100's nm, and the excitation light is a short wavelength of $\lambda = 317$ nm. However, the ground/clock state wavefunction is still much smaller than $\lambda$ and effectively bounds any overlap integral to a very small region in which the dipole approximation should still be very much valid.

to be able to map either the ground (i.e., clock) or the Rydberg state to some kind of state that is dark to fluorescence imaging, while mapping the other state into a state that is bright during imaging. The dark "state" may also be an expulsion of atoms from the trap.

Whatever process one chooses to achieve this mapping must be significantly faster than the timescale on which a Rydberg atom decays into any bright state (or any state that gets mapped onto a bright state). Rydberg atoms typically have a decay timescale of a few tens to hundreds of $\mu$s (see Sec. 4.4.1). This means that simply pumping the clock state back into the imaging cycle and hoping Rydberg atoms will remain dark is not an option, as reasonably achievable imaging times are at least in the ms timescales. Rydberg atoms therefore must be either rapidly expelled from the trap or shelved in some long-lived dark state.

Previous work with alkali Rydberg atoms has relied on anti-trapping [74, 202] or trap photoionization [66, 203] to make Rydberg atoms dark. The timescales of these processes is typically a few $\mu$s, resulting in typical state detection infidelities of a few percent.

### *Auto-ionization mechanism and rates*

Two-electron atoms offer a different mechanism: auto-ionization [204–207]. Auto-ionization is a process that can occur when two electrons are excited to bound states that have a combined energy greater than the ionization threshold of a single electron. Then, bound-to-continuum coupling can drive one of the electrons out of its bound state and into the continuum, thus ionizing the atom. This is to be distinguished from photoionization, where the absorption of a photon directly drives an electron into a continuum state. The appeal of auto-ionization processes is that they can be very fast — much faster than the detection processes previously used for alkali.

The auto-ionizing transitions that we will use are the $5sns\ {}^3S_1 \leftrightarrow 5p_{3/2}ns_{1/2}$ transitions, where $n$ is the principal quantum number of the Rydberg electron. As discussed in Sec. 2.1.2, the notation for the auto-ionizing excited state uses quantum numbers $j_i$ for each of electron independently, and there are two practically degenerate options for the total angular momentum, which are $J \in \{1, 2\}$. However, the $J = 1$ states have a significantly faster auto-ionization rate than the $J = 2$ states [206, 208], which has important implications for the polarization of the beam used to drive the auto-ionizing transition. In particular, one must keep in mind

that the Clebsch-Gordan coefficient $\langle 1\ m_J + q | 1\ m_J; 1\ q\rangle$ is *zero* for $m_J = q$ (most notably, even for $m_J = q = 0$). More specifically, when using a $5snS\ ^3S_1\ m_J = 0$ Rydberg sub-level, one must minimize the $q = 0$ polarization component (i.e. the component parallel to the quantization axis) of the auto-ionization beam in order to maximize driving to the $J = 1$ auto-ionizing state.

The wavelength of these transitions is $\lambda = 407.9$ nm, and is nearly independent of $n$ for large enough $n$. Indeed, this is also the wavelength for the $5s_{1/2} \leftrightarrow 5p_{3/2}$ transition in the $Sr^+$ ion.

Auto-ionization rates scale with the square of the Rydberg electron wavefunction's value at the origin. By similar arguments as those cited for Eq. 4.8, one expects an $(n^\star)^{-3}$ scaling of the auto-ionization rate with effective principal quantum number [204]. Furthermore, auto-ionization rates drop rapidly with $l$ for $l > 3$ [204], where $l$ is the Rydberg electron orbital angular momentum quantum number.

Ref. [205] provides experimental measurements of the linewidths of the $5p_{3/2}ns_{1/2}\ J = 1$ states. Since auto-ionization is the dominant line-broadening mechanism of such states, one can directly convert these linewidths to auto-ionization rates. Ref. [209] fits these values and extracts a trend of:

$$\Gamma_A(5p_{3/2}ns_{1/2}\ J = 1) = \frac{2\pi \times 9.0 \times 10^{14}}{(n^\star)^3}\ \mathrm{s}^{-1} \tag{4.10}$$

For our $n = 61$ state, this predicts $\Gamma_A = 2\pi \times 4.7$ GHz.

This rate must be literally interpreted as the rate of auto-ionization when the atom is *fully* in the auto-ionizing state. However, this is not the case when one is actually driving the auto-ionizing transition. To obtain the experimentally realized rate of auto-ionization, we consider three atomic states: the Rydberg state $|r\rangle$, the auto-ionizing state $|r^*\rangle$, and the ionic dark state $|\mathrm{ion}\rangle$. Let $\Gamma_i$ be the rate of exponential decay of $|r^*\rangle \rightarrow |r\rangle$. From Ref. [210], we have $\Gamma_i = 2\pi \times 22.4$ MHz. $\Gamma_\mathrm{A}$ (Eq. 4.10) is the rate of exponential decay $|r^*\rangle \rightarrow |\mathrm{ion}\rangle$. We define a Rabi frequency of the $|r\rangle \leftrightarrow |r^*\rangle$ transition as $\Omega = \Gamma_i\sqrt{\frac{I}{2I_s}}$, where $I$ is the auto-ionization beam intensity and $I_s = 43.2\ \mathrm{mW/cm^2}$ is the saturation intensity of this transition.

We assume that the auto-ionization beam has appropriately chosen polarization (see discussion above) and that $\Gamma_i \ll \Gamma_A, \Omega$. Then $|\mathrm{ion}\rangle$ will be populated on a timescale of approximately

$$\tau_\mathrm{ion} \approx \left(\frac{\Gamma_A}{2}\frac{s_A}{1+s_A}\right)^{-1} \tag{4.11}$$

where $s_A = 2\Omega^2/\Gamma_A$. This result is verified by numerical evolution and is consistent with the known result of the "continuous Quantum Zeno mechanism" [211, 212] when $\Gamma_A \gg \Omega$. We use a 2.8 mW auto-ionization beam with a measured waist of w = 16(1) $\mu$m at the position of the atoms [150], giving $\Omega = 2\pi \times 3$ GHz and an *expected* $\tau_{\text{ion,th}} \sim 0.2$ ns for n = 61.

### *Experimental results*

Fig. 4.2 shows the results of auto-ionization. Atoms are prepared in the Rydberg state via a $\pi$-pulse, then the auto-ionization beam is turned on for a variable amount of time, and finally remaining atoms are returned to the clock state via a second $\pi$-pulse on the Rydberg transition. We measure the population of remaining atoms after this sequence and use it to determine the fraction of atoms that were auto-ionized. We measure a $1/e$ auto-ionization timescale of $\tau_{\text{ion,meas}} = 35(1)$ ns [150]. This timescale is at least an order of magnitude faster than that of previously used alkali Rydberg detection schemes [52, 74, 203] and is thus a significant advancement in Rydberg state detection fidelity, which we will quantify shortly.

Nonetheless, our measured value of $\tau_{\text{ion,meas}}$ is still about two orders of magnitude *slower* than our predicted value of ~0.2 ns. We hypothesize that this is attributable to the finite rise time of the AOM that switches the auto-ionization beam on, which we measure to be 250 ns. If the AOM rise time is indeed the limiting factor, then the $\tau_{\text{ion}}$ could conceivably be even further decreased by higher laser intensity and faster beam switching, or by using a pulsed laser [207]. However, we also cannot rule out some unforeseen intrinsic mechanism that limits $\tau_{\text{ion}}$.

### *State detection fidelity*

If the decay of the Rydberg state into a bright (or bright-equivalent) state is given by an exponential process of timescale $\tau_B$, we can quantify the state-detection fidelity $D$ of a particular detection scheme by the formula

$$D = \frac{1}{\tau_B} \int_0^\infty e^{-t/\tau_B} P_d(t) dt \tag{4.12}$$

where $P_d(t)$ is the probability that the Rydberg atom has has been mapped to a permanent dark state by time $t$. For illustration, if $P_d(t) = (1 - e^{-t/\tau_{\text{ion}}})$, then $D = \frac{1}{1+\tau_{\text{ion}}/\tau_B} \approx 1 - \frac{\tau_{\text{ion}}}{\tau_B}$, where the approximation is valid for $\tau_{\text{ion}} \ll \tau_B$.

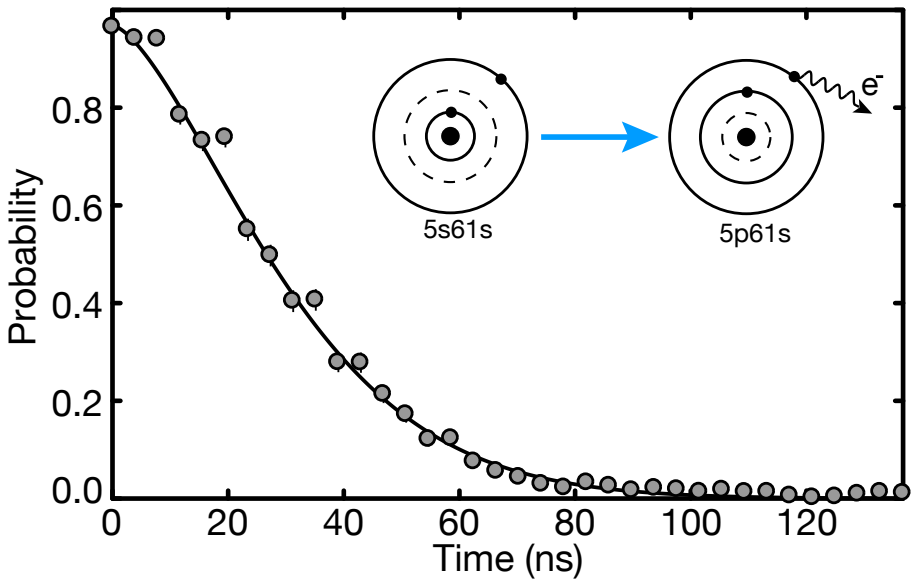


Figure 4.2: The measured effect of auto-ionization for variable pulse time. Atoms are prepared in the Rydberg state via a $\pi$-pulse, then the auto-ionization beam is turned on for a variable amount of time, and finally remaining atoms are returned to the clock state via a second $\pi$-pulse on the Rydberg transition. The probability of measuring a remaining atom after this sequence is plotted on the vertical axis, with the solid black line a fit (described in the text). $t = 0$ is calibrated to be such that no measurable auto-ionization is seen before this time. The inset illustrates the auto-ionization process.

We fit the data in Fig. 4.2 to a function of the form $c\left(1 - e^{-(t/\tau_{\text{ion}})^a}\right)$ where $c$ accounts for a scaling factor on the y-axis and $a$ is a generalized exponent that allows us to phenomenologically model the rise time of the AOM. We identify $P_d(t) = 1 - e^{-(t/\tau_{\text{ion}})^a}$ with fitted coefficients $\tau_{\text{ion}} = 35(1)$ ns and $a = 1.5(1)$.

In Ref. [150], we assumed for $n = 61$ a decay timescale into bright states of $\tau_B = 80(20)$ $\mu$s. Using Eq. 4.12 and the measured $P_d(t)$ in Fig. 4.2, this produces a state-detection fidelity of $D = 0.9996(1)$. The dominant uncertainty in this value comes from the uncertainty of $\tau_B$.

***Experimental measurement of bright state decay***

We now believe that 80 $\mu$s is actually an underestimate for $\tau_B$, implying that the true value of $D$ is even higher than originally quoted. Namely, our estimation of $\tau_B = 80$ $\mu$s was based on a fit to the *total* depopulation rate of the *singlet* 5s$n$s $^1S_0$ states given in Ref. [209]. However, this rate included both spontaneous decay

*and* blackbody radiation. Blackbody radiation induces transitions to other Rydberg states — which are still dark to our detection scheme — and thus it should not be accounted for in $\tau_B$. Furthermore, the spontaneous decay rate of the *triplet* Rydberg series (which we work with) may be different than that of the singlet series.

We directly measure the timescale of decay of the 5s61s $^3S_1$ state into bright states to be $\tau_B = 168(14)$ $\mu$s. The procedure for this measurement was to prepare atoms in the Rydberg state, wait a variable amount of time, apply an auto-ionization pulse, and measure the fraction of atoms that were then bright. The initial rate of increase of this fraction gives us $\tau_B$. Our new measured value produces a state-detection fidelity* of $D = 0.99981(2)$.

### 4.1.4 Systematic shifts

We now explore several systematic effects that may shift the transition frequency of the clock to Rydberg transition. While a constant shift in the Rydberg transition frequency is on its own of little importance, variations in this shift can cause noise, drifts, and infidelity in Rydberg Rabi oscillations (similarly to how systematic shifts on the clock transition described in Sec. 3.1.2 are a potential cause of Rabi $\pi$-infidelity, as discussed in Sec. 3.2.3). We will come back to the effect of systematic effects on interactions in Sec. 4.2.2.

We will discuss the effects that we deem are most important. We will ignore blackbody radiation shifts as they are very small [144]. We also point the reader to Refs. [213, 214], which discusses shifts of Rydberg states and their interactions due to RF fields, which we will not discuss here.

#### *DC electric field*

Here we describe how a DC electric field can shift the energy of a Rydberg state. This is also known as a DC Stark shift. The treatment here essentially applies to any atomic state, but as we will soon argue, such shifts are really only significant for states of large principal quantum number $n$, with the effect scaling very sharply with $n$. We will thus assume that the ground (clock) state does not shift significantly, so

*While it is generally positive that $D$ is larger than initially estimated, it implies slightly less favorable SPAM correction (App. E). However, we have verified that this new $D$ produces SPAM corrected values identical to those published in Ref. [150] up to rounding.

we may identically talk about the shift of the Rydberg state's energy as we do about the shift of the transition frequency.

We will show in Sec. 4.2.2 how a DC field can not only shift transition frequencies, but also interaction strengths.

We will begin with a perturbative treatment. However, it is important to note that *electric fields achievable in a lab can cause shifts in Rydberg states that go far beyond perturbation theory*. After we describe the perturbative approach, we will give a brief discussion on non-perturbative regimes.

The dipole Hamiltonian of an electric field $\vec{E}$ is

$$H_d = -\vec{d} \cdot \vec{E} \tag{4.13}$$

with $\vec{d} = -|e|\vec{r}$ the dipole operator. We note, as we did in Sec. 2.3, that this Hamiltonian only has nonzero matrix elements between states of different spatial parity, so there are no first order energy shifts of bare atomic eigenstates and we must go directly to second order perturbation theory. Note that the spatial parity of a bare atomic eigenstate is given by $P = (-1)^{\sum_i l_i}$, where $l_i$ are the various electronic orbital quantum numbers. For us, the inner electrons will always have even total parity, so we have $P = (-1)^l$ where $l$ is the Rydberg electron orbital quantum number.

Our perturbative treatment will in fact be nearly identical to that given for AC electric fields in Sec. 2.3, and we again follow Ref. [90]. One may be tempted to simply take the $\omega \to 0$ limit of all the results in Sec. 2.3, and in fact this largely works — with some small caveats. One is that it is no longer reasonable to work with an "intensity" $I$, as in, e.g., Eqs. 2.21 & 2.27. To remedy this, note that all results in Sec. 2.3 are valid under the substitution $\frac{I}{2c\varepsilon_0} \to \frac{1}{2}E_{\text{rms}}^2$, where $E_{\text{rms}}$ is the time-domain *root mean square* of the electric field. For a DC field* $\vec{E}$, we simply have $E_{\text{rms}} = |\vec{E}|$.

We thus simply restate the relevant results of Sec. 2.3 here in the $\omega \to 0$ limit and with the prescription above. Furthermore, note that complex polarization is not possible for a DC field, which simplifies certain formulas. In particular, there is no vector polarizability term.

The Cartesian tensor polarizability operator for a degenerate manifold of states $|i\rangle$ is:

$$\alpha_{\mu\nu} = \sum_j \frac{2}{\hbar\omega_{ji}} d_\mu |j\rangle\langle j| d_\nu \tag{4.14}$$

*Whereas for a monochromatic AC field, the root mean square is $\frac{1}{\sqrt{2}}$ of the absolute value of the complex amplitude.

where $\mu, \nu$ are Cartesian coordinate indices, $d_\mu$ is the $\mu$ component of the vector dipole operator $\vec{d}$, and $\omega_{ji} = \frac{1}{\hbar}(\mathscr{E}_j - \mathscr{E}_i)$ where $\mathscr{E}_i$ is the unperturbed atomic energy of the degenerate manifold to which $|i\rangle$ belongs.

Then the effective second-order perturbative Hamiltonian is

$$H_d^{\text{eff}} = -\frac{1}{2}|\vec{E}|^2 \sum_{\mu,\nu} \alpha_{\mu\nu}\epsilon_\mu\epsilon_\nu \tag{4.15}$$

where $\epsilon_\mu$ is the $\mu$ component of the unit polarization vector $\hat{\epsilon}$, which is defined by $\vec{E} = |\vec{E}|\hat{\epsilon}$.

Performing a spherical tensor decomposition (Sec. 2.3.2), we have

$$H_d^{\text{eff}} = -\frac{1}{2}|\vec{E}|^2\left(\alpha_{\text{s}} + \frac{\alpha_{\text{t}}}{J(2J-1)}\left(3(\hat{\epsilon}\cdot\vec{J})^2 - J(J+1)\right)\right) \tag{4.16}$$

Here, $\vec{J}$ is the unitless spin-$J$ vector operator and

$$\alpha_{\text{s}} = \frac{2}{3(2J+1)}\sum_{\beta'}\frac{|\langle\beta||d||\beta'\rangle|^2}{\hbar\omega_{\beta'\beta}} \tag{4.17}$$

$$\alpha_{\text{t}} = \sqrt{\frac{40J(2J-1)}{3(J+1)(2J+1)(2J+3)}}\sum_{\beta'}(-1)^{J+J'}\begin{Bmatrix}1 & 1 & 2\\ J & J & J'\end{Bmatrix}\frac{|\langle\beta||d||\beta'\rangle|^2}{\hbar\omega_{\beta'\beta}} \tag{4.18}$$

where $\begin{Bmatrix}\dots\end{Bmatrix}$ is a Wigner 6-$j$ symbol and we again use Greek letters $\beta$ and $\beta'$ to indicate entire degenerate manifolds without specifying a particular sub-level. The quantities $\alpha_{\text{s}}$ and $\alpha_{\text{t}}$ are the DC scalar and tensor polarizabilities, respectively. They are specific to each degenerate atomic manifold $|\beta\rangle$. Importantly, they do not depend on the direction of the $\vec{E}$ field. Note that they are literally the $\omega \to 0$ limit of Eqs. 2.24 & 2.26.

The task remaining is to once again determine the RDMEs $\langle\beta||d||\beta'\rangle$, however this time the most relevant ones are those *between* Rydberg states, particularly those closest in $n$. For an s Rydberg state, only those to p states are nonzero. Unlike the RDMEs of common optical transitions, RDMEs between Rydberg states are not often conveniently tabulated in a database. However, they are also relatively easy to compute *ab initio*, owing that to their hydrogen-like property. We discuss calculation of Rydberg-Rydberg RDMEs in App. D.

It is useful to discover how the polarizabilities scale with $n$. We begin with the scaling of $\langle r\rangle$, where $r$ is the radial electronic coordinate. This is a widely known

result for hydrogenic wavefunctions, and a derivation can be found in Ref. [201]:

$$\langle r \rangle \propto (n^\star)^2 \tag{4.19}$$

As the dipole operator is proportional to $r$, we infer that the RDME between nearby Rydberg states also has a scaling exponent of 2, and thus its square (as it enters in the polarizabilities) has an exponent of 4. Finally, note that for neighboring Rydberg states we have

$$\omega_{\beta'\beta} \propto (n^\star)^{-3} \ [\beta, \beta' \text{ neighboring}] \tag{4.20}$$

which can be inferred by differentiating Eq. 4.3 with respect to $n^\star$. This argument is not very rigorous as often a major contribution in the polarizability is from states of the same $n$ but different $l$. Nevertheless, Eq. 4.3 gives us a picture of how level spacings in general scale with $n^\star$ and the end result turns out to be valid.

Taking all exponents into account, we ultimately have

$$\alpha_{s,t} \propto (n^\star)^7 \tag{4.21}$$

which is confirmed in Refs. [199, 201]. This is quite a severe scaling with principal quantum number and justifies ignoring any DC electric shifts of the ground state.

We compute $\alpha_{s,t}$ via Eqs. 4.17–4.18 for 5s$n$s $^3\mathrm{S}_1$ states with $n \in [50, 70]$ in Fig. 4.3. We also plot $(n^\star)^7$ trend lines with an overall scaling factor fixed at the value at $n = 61$. We find

$$\alpha_\mathrm{s}(n) = 2\pi\hbar \times 6.0 \times 10^{-11} \times (n^\star)^7 \ \mathrm{MHz/(V/cm)^2} \tag{4.22}$$

$$\alpha_\mathrm{t}(n) = 2\pi\hbar \times 4.2 \times 10^{-13} \times (n^\star)^7 \ \mathrm{MHz/(V/cm)^2} \tag{4.23}$$

We see that for the $^3\mathrm{S}_1$ series, $\alpha_\mathrm{t}$ is much smaller than $\alpha_\mathrm{s}$, which means that the electric shift is approximately isotropic and well-approximated by $\Delta\mathscr{E} \approx -\frac{1}{2}\alpha_\mathrm{s}|\vec{E}|^2$. For higher $l$ states, this is usually no longer the case.

We now briefly touch on regimes beyond perturbation theory. For this, a full diagonalization [197, 198, 215] of a subset of states is necessary. We perform such a diagonalization, with the result shown near 5s61s $^3\mathrm{S}_1$ in Fig. 4.4. Note that this calculation is mostly done for illustrative purposes and may be quantitatively inaccurate at larger fields due to our truncation of summation only up to f states.

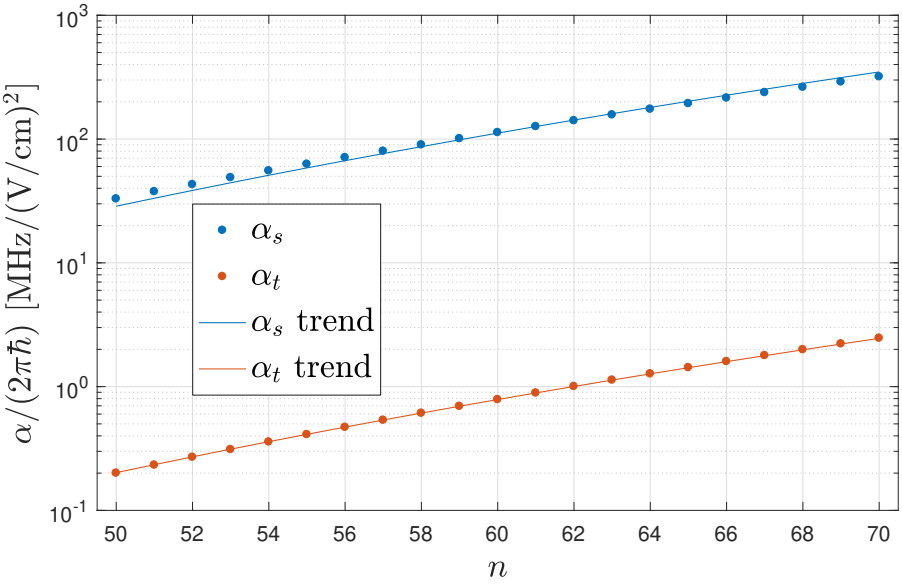


Figure 4.3: Scalar and tensor DC polarizabilities of the $5sns\ ^3S_1$ series. Trend lines are $\alpha(n = 61) \times (n^\star)^7$ (Eqs. 4.22–4.23). While the vertical axis is on a logarithmic scale, both polarizabilities are indeed positive. Note that by convention, Eq. 4.16 has a factor of $-\frac{1}{2}$ in front of $|\vec{E}|^2$.

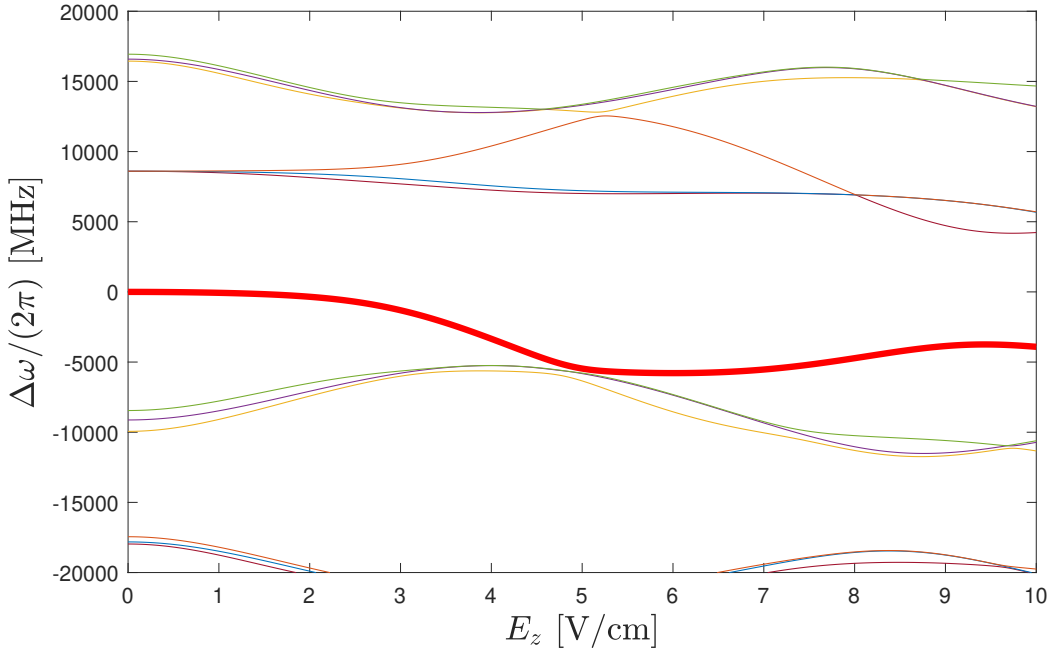


Figure 4.4: Non-perturbative diagonalization of DC electric shifts near $n = 61$. The energy of the state that is adiabatically connected to the 5s61s $^3S_1$ $m_J = 0$ state at zero field is plotted in bold red. Energies are plotted as a shift with respect to the unperturbed energy of this state. The electric field is oriented along the quantization axis, and only $m_J = 0$ states are plotted as other states do not couple. The calculation includes states with $n \in [54, 63]$ and $l \in \{\mathrm{s}, \mathrm{p}, \mathrm{d}, \mathrm{f}\}$. This truncation in $l$ may produce inaccuracies toward larger fields.

Finally, we discuss the practical element of controlling DC electric fields in the lab. As we see that even modest fields of $\lesssim 1$ V/cm can create relative large shifts on the order of tens of MHz, such control can be very valuable. Ideally, this would be done via dedicated electrodes that can create a tunable uniform field at the atoms in all directions [216, 217]. However, we do not currently have such electrodes installed in our apparatus. A less versatile but easier to implement option for controlling stray fields (which, however, we have also yet to implement) is to illuminate any glass near the atoms (of, e.g. the science cell) with ultraviolet light (see supplements of Refs. [119, 217]).

***Magnetic field: Zeeman and diamagnetic effects***

A magnetic field $\vec{B}$ produces the following Hamiltonian:

$$H_B = \underbrace{\mu_{\mathrm{B}}\vec{B}\cdot(g_L\vec{L}+g_S\vec{S})}_{H_{\mathrm{Z}}} + \underbrace{\tfrac{1}{8m_e}|\vec{d}\times\vec{B}|^2}_{H_{\mathrm{dm}}} \tag{4.24}$$

where $\mu_{\mathrm{B}}$ is the Bohr magneton, $g_L \approx 1$, $g_S \approx 2$, $m_e$ is the electron mass, and $\vec{d}$ is the vector dipole operator.

The first term, $H_{\mathrm{Z}}$, of Eq. 4.24 is the well-known Zeeman shift. For a regime in which $J$ and $m_J$ are good quantum numbers (which is always true for manifolds without fine structure such as $^3\mathrm{S}_1$, and approximately true in low-field for manifolds with fine structure), the Zeeman shift can also be written as $H_{\mathrm{Z}} = \mu_{\mathrm{B}} g_J \vec{B}\cdot\vec{J}$, where $g_J$ is the Landé $g$-factor of the state (see footnote after Eq. 2.28). For $^3\mathrm{S}_1$, we have $g_J \approx 2$.

The second term, $H_{\mathrm{dm}}$, of Eq. 4.24 is the less-well-known diamagnetic shift [197]. Usually, such a term is completely ignored for low-lying states, but as we will soon see it is yet another term which scales rapidly with principal quantum number, making it important for Rydberg states. It is important to stress that while the diamagnetic shift scales with $|\vec{B}|^2$, it is *distinct* from the *quadratic Zeeman effect*, which is just an effect of $H_{\mathrm{Z}}$ mixing different $J$ levels, does not depend on dipole matrix elements, and is only found in manifolds with fine structure. On the other hand, $H_{\mathrm{dm}}$ *does* depend on dipole matrix elements and *is* present even without fine structure. Also note that the diamagnetic effect always results in positive energy shifts.

The first useful thing to note about this term is that its leading order perturbation is first order. As it is proportional to $|\vec{d}|^2$, it has nonzero matrix elements between states of the same parity, and more importantly it has nonzero diagonal matrix elements. Knowing this and using Eq. 4.19, we can deduce that the diamagnetic shift has a scaling of $(n^\star)^4$.

It will be once again insightful to perform perturbation theory and a spherical tensor decomposition to isolate the radial and angular parts of the perturbative diamagnetic effect. We will not provide a full derivation, but give the following useful facts. First, note that we can rewrite the diamagnetic Hamiltonian as $H_{\text{dm}} = \frac{1}{8m_e}\left(|\vec{d}|^2 - (\vec{d}\cdot\hat{B})^2\right)|\vec{B}|^2$. Second, we can relate quadratic dipole matrix elements (which may also be called *quadrupole* matrix elements) to dipole matrix elements by

$$\langle a|d_\mu d_\nu|b\rangle = \sum_k \langle a|d_\mu|k\rangle\langle k|d_\nu|b\rangle \tag{4.25}$$

Finally, we just follow the procedure for tensor decomposition outlined in Ref. [90] (which was also used for the results in Secs. 2.3.2 & 4.1.4). The effective perturbative Hamiltonian is

$$H_{\text{dm}}^{\text{eff}} = -\frac{1}{2}|\vec{B}|^2\left(b_{\text{s}} + \frac{b_{\text{t}}}{J(2J-1)}\left(3(\hat{B}\cdot\vec{J})^2 - J(J+1)\right)\right) \tag{4.26}$$

$$b_{\text{s}} = -\frac{1}{m_e}\frac{1}{6(2J+1)}\sum_{\beta'}|\langle\beta||d||\beta'\rangle|^2 \tag{4.27}$$

$$b_{\text{t}} = \frac{1}{m_e}\sqrt{\frac{5J(2J-1)}{24(J+1)(2J+1)(2J+3)}}\sum_{\beta'}(-1)^{J+J'}\begin{Bmatrix}1 & 1 & 2\\ J & J & J'\end{Bmatrix}|\langle\beta||d||\beta'\rangle|^2 \tag{4.28}$$

Here, $b_{\text{s}}$ and $b_{\text{t}}$ are scalar and tensor coefficients, respectively. We have chosen their overall scaling such as to have the form of Eq. 4.26 similar to that of Eq. 4.16. See App. D for computing Rydberg-Rydberg RDMEs.

For the $^3\text{S}_1$ series, the tensor component $b_{\text{t}}$ is extremely small, so for this series the diamagnetic interaction is to very good approximation purely scalar. Using our computed value of $b_{\text{s}}(n=61) = -2\pi\hbar\times 5.5\ \text{kHz/G}^2$ (note the factor of $-\frac{1}{2}$ in front of $|\vec{B}|^2$ in Eq. 4.26) at $n = 61$ and the expected trend with $n^\star$, we have for the $^3\text{S}_1$ series:

$$b_{\text{s}}(n) = -2\pi\hbar\times 5.0\times 10^{-7}\times(n^\star)^4\ \text{kHz/G}^2 \tag{4.29}$$

where G is the Gauss unit, being equal to $10^{-4}$ T. As mentioned previously, the $^3S_1$ series has no fine structure and therefore no quadratic Zeeman shift. Therefore, this scalar diamagnetic shift will be the only magnetic shift that an $m_J = 0$ state in this series sees. However, for an $m_J = 0$ Rydberg state in a series with fine structure (such as $^3D_1$), the quadratic Zeeman shift usually produces a quadratic shift on the same order as that of the diamagnetic shift and must be accounted for as well.

A large magnetic field is often desirable when driving ground to Rydberg transitions in order to minimize excitation to undesired sub-levels. One then often chooses an $m_J = 0$ state to be insensitive to the linear Zeeman shift. However, as the diamagnetic shift is still present and as it is quadratic, the higher the chosen field, the more sensitive the detuning of the transition becomes to fluctuations in the field. We note, however, the interesting possibility of using an $m_J = -1$ state at a field where the opposite-signed Zeeman and diamagnetic effects create a local extremum in the detuning as a function of magnetic field. For $|n = 61\ ^3S_1\ m_J = -1\rangle$, this occurs at $|B| = 504$ G. This situation would then both provide a large magnetic field while also having minimal sensitivity to magnetic fluctuations. However, we do not currently use this scheme and instead use an $m_J = 0$ state with an approximately $|B| \approx 71$ G field.

***(Anti)-trapping light shifts***

Here we discuss light shifts on Rydberg states arising from the trap. Trap light shifts are important in their own right simply as systematic effects (and therefore as a potential source of noise and dephasing), but are also important for the question of whether or not a Rydberg atom remains trapped.

The treatment of light shifts and polarizabilities of Rydberg states requires the consideration of a few subtleties not discussed in Sec. 2.3. To start with, since Rydberg states are close to the ionization threshold, a large contribution to the polarizability at optical wavelengths comes from coupling to continuum states. Therefore, a discrete sum-over-states approach is no longer fully appropriate.

A widely used model for Rydberg polarizabilities is to separate the contributions of the inner ion and of the Rydberg electron, and to assume that the contribution of the Rydberg electron is described by the purely scalar *ponderomotive* polarizabil-

ity [217–219]:

$$\alpha_p(\omega) = -\frac{e^2}{m_e\omega^2} \tag{4.30}$$

As for the contribution from the inner ion, we can apply all the same results from Sec. 2.3. For our Rydberg states, the inner electron is in the 5s $^2S_{1/2}$ (or more briefly just $5s_{1/2}$) state of the $Sr^+$ ion core. This state has nonzero scalar and vector polarizabilities, but we will assume a linearly polarized trap such that only the scalar polarizability enters.

Fig. 4.5 plots the predicted total polarizability at linear polarization for Sr Rydberg states with the inner electron in $5s_{1/2}$, including both the ionic [210] and ponderomotive contribution. We see that at $\lambda = 813.4$ nm, Rydberg states see an anti-trapping polarizability of $\alpha = -203.5$ au. Meanwhile, the clock and absolute ground state have a trapping polarizability of $\alpha = 286.0$ au [88]. Rydberg states are predicted to be anti-trapped for all wavelengths $\lambda > 590$ nm, but trapped for 422 nm $< \lambda <$ 590 nm.

Of particular interest may be the predicted trapping polarizabilities at $\lambda = 515$ nm ($\alpha = 112$ au) and at $\lambda = 532$ nm ($\alpha = 79$ au).

We experimentally measure [150] the differential light shift between the clock state and the 5s61s $^3S_1$ Rydberg state at $\lambda = 813.4$ nm and linear polarization parallel to a dominant magnetic field, with the results shown in Fig. 4.6. We find a linear trend with trap depth/intensity of $\Delta\nu(U) = 18.8(9)\ \text{MHz} \times (U/U_0)$, where $U_0 \sim k_B \times 0.5$ mK is our typical maximal clock state trap depth (measured via light shifts on the red transition). We can thus calculate an experimentally measured total polarizability of this Rydberg state at this wavelength and at linear polarization of $\alpha_{\text{meas}} = (1 - \frac{2\pi\hbar\Delta\nu}{U_0})\alpha_{\text{clock}} = -230$ au. The discrepancy between this measured value and the predicted value discussed above can be explained by a roughly 5% underestimation of our clock state trap depth, which is within what we estimate our systematic error on this quantity to be. If we assume the theoretical value of $\alpha$ to be correct, then we would have $U_0 = 0.53$ mK.

However, this is not necessarily the end of the Rydberg trap light shift story. All results discussed so far assume that the atom sees a uniform trap intensity across its electronic wavefunction. However, the Rydberg electron wavefunction is typically quite large ($r$ on the order of 100's of nm) with $r$ scaling as $n^2$. It is therefore entirely possible to excite to a Rydberg state which has a Rydberg electron wavefunction

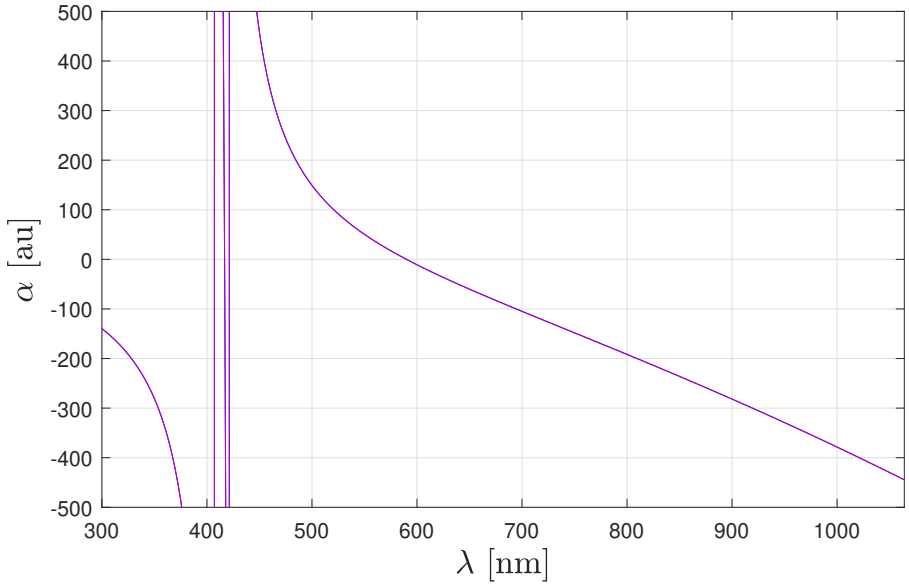


Figure 4.5: Predicted total polarizability at linear polarization versus wavelength $\lambda$ for Sr Rydberg states with inner electron in $5s_{1/2}$. Values are computed by summing contributions from the inner ion and from the Rydberg electron's ponderomotive polarizability. The predicted value at $\lambda = 813.4$ nm is $\alpha = -203.5$ au. Data for RDMEs and energy levels is from Ref. [210]. The small contributions of the core [220] and valence-core [88] polarizabilities are included, as discussed in App. B.

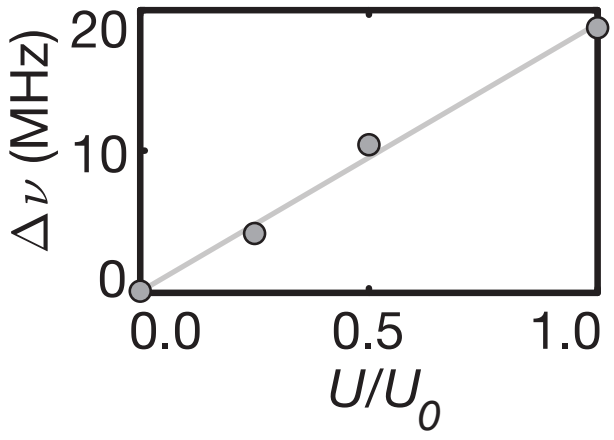


Figure 4.6: Measured differential light shift between the clock state and the $5s61s\,{}^3S_1$ Rydberg state at $\lambda = 813.4$ nm and linear polarization parallel to a dominant magnetic field. $U$ represents the variable trap depth and $U_0 \sim 0.5$ mK is our typical maximal clock state trap depth. The grey line is a linear fit, producing $\Delta\nu(U) = 18.8(9)\ \text{MHz} \times (U/U_0)$.

that extends far beyond the center of the trap [217, 221], thus reducing the effective ponderomotive contribution. Ref. [217] shows that, with a $w = 650$ nm waist tweezer at $\lambda = 532$ nm, the Ytterbium $^3S_1$ Rydberg series is anti-trapped for $n \lesssim 60$, but becomes trapped as $n$ increases beyond that, with the polarizability tending toward that of just the trapped inner ion. Furthermore, it is shown that the anisotropic geometry of a tweezer produces a tensor ponderomotive component.

We omit a full discussion of such a regime in our situation, noting that our tweezer waist is larger at $w \sim 800$ nm, so it is likely that such effects can only be observed at commensurately larger $n$. Furthermore, we note that Sr Rydberg states are expected to be trapped at 532 nm and 515 nm even at low $n$, as shown in Fig. 4.5.

Ultimately, we will choose to operate Rydberg excitation with the traps turned off, as this minimizes dephasing due to light shifts. We can do this as Rydberg Rabi oscillations are typically significantly faster than the timescale on which an atom leaves the trapping region, though turning traps off does ultimately place some limit on the length of the interrogation (Sec. 4.4.2). A configuration that traps both the lower and Rydberg states could enable one to go beyond this limit [217].

***Probe light shift***

Here we discuss light shifts due to the beam which excites the Rydberg transition, which we refer to as the probe beam.

It is important to understand why such a shift might even matter. Typically, beams that are used to excite transitions (and not to act as traps) are not of a sufficiently high intensity to produce light shifts that are significant compared to the linewidth (unless one is probing an ultra-narrow transition like the clock transition, see Sec. 3.1.2). Furthermore, even if there was a significant shift, one could typically expect to compensate for it by appropriately detuning the beam, as is done during clock interrogation.

However, it is possible that Rydberg excitation violates both of these assumptions for high enough Rabi frequencies. As argued in Sec. 3.1.2, the ratio of the probe differential light shift to the power-broadened linewidth goes as $\Delta\omega/\Omega \propto \sqrt{I} \propto \Omega$.

This scaling would, again, not be a problem if we assume we can just compensate for this shift by appropriate detuning. However, for the large Rabi frequencies that we hope to achieve ($\Omega > 2\pi \times 5$ MHz), we run into the potential problem that the

typical switching rise-times achievable by AOMs are limited to tens of nanoseconds (a timescale set by the size of the beam in the AOM and on the speed of sound in the crystal, typically 6 km/s). Let us refer to such an AOM rise time as $\tau_{\mathrm{AOM}}$.

The potential problem occurs when the light shift is both significant compared to the Rabi linewidth *and* the Rabi frequency is fast as compared to the AOM rise time. Then, the atom can experience a significant light shift that also varies with time — *while* it is already well into executing Rabi oscillations. The dynamics of such a process are non-trivial and require detailed modeling of the AOM rise profile to fully capture. For attempted resonant oscillations, it can generally be expected that the atomic state vector will end up precessing on the Bloch sphere with a "tilt," which will be measured as reduced contrast oscillations in the qubit basis. We note that such undesired dynamics can also be expected to occur at the *end* of the pulse, when the AOM switches the beam off. We do not rule out the possibility of using some kind of time-dependent detuning in the AOM signal to compensate for these effects, but this is of course an undesired complication.

Such dynamics can be avoided if one works in the regime

$$\Omega \ll \sqrt{\frac{1}{\kappa \tau_{\mathrm{AOM}}}} \tag{4.31}$$

where $\kappa$ is a coefficient of the probe differential light shift $\Delta\omega$ such that $\Delta\omega = \kappa\Omega^2$.

We measure $\kappa$ for the clock to 5s61s $^3\mathrm{S}_1$ transition under the conditions of linear probe polarization parallel to a strong magnetic field (i.e. with the probe beam completely aligned to drive a $\pi$ transition) [150]. We measured this shift using a relatively low Rabi frequency, such as to ensure that no non-trivial dynamics due to the AOM rise time enter our measurement. However, this also means that any measurable light shift would be very small. Therefore, we chose to use a two-rail lock self-comparison technique, described in the context of clock systematics in Sec. 3.4.4, to efficiently measure this small signal. Here, we follow the frequencies of two independent locks to the Rabi lineshape of the Rydberg transition, with one lock set to a variable probe intensity. This method ideally isolates only the probe shift and cancels any drifts that are common mode to both locks, thus allowing us to average for a sufficiently long time to resolve even small shifts. The results are shown in Fig. 4.7. We obtain a result of $\kappa = 5.1(7)/(2\pi)$ kHz/MHz$^2$. To be clear, this means that for a probe intensity that produces a resonant Rabi frequency of $\Omega = 2\pi \times 1$ MHz with the probe polarization parallel to the magnetic field, one gets a light shift of $\Delta\omega = 2\pi \times 5.1(7)$ kHz.

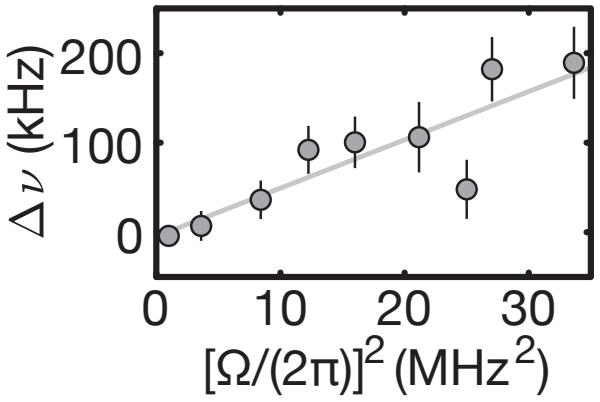


Figure 4.7: Measured probe light shift for the clock to 5s61s $^3S_1$ transition under the conditions of linear probe polarization parallel to a strong magnetic field. The shift is plotted as a function of Rabi frequency squared, which is proportional to probe intensity. The grey line is a linear fit, giving $\kappa = 5.1(7)/(2\pi)$ kHz/MHz$^2$.

Having measured a typical AOM rise time of $\tau_{\mathrm{AOM}} \sim 35$ ns, we can thus expect the condition of Eq. 4.31 to hold so long as $\Omega \ll 2\pi \times 30$ MHz. While we will maintain such a condition throughout this work, it is possible with future upgrades in laser power that this limit will be approached.

A further potential problem with the probe light shift is that probe intensity noise (which can come either from beam fluctuations or from thermal sampling of a small probe beam, see Sec. 4.4.3) can produce noise in the detuning.

***AOM-induced alignment-detuning correlation***

In addition to the probe light shift and AOM rise time effects discussed in Sec. 4.1.4, we discuss here another AOM-induced effect that can produce systematic shifts of the laser detuning during the switch-on and switch-off of the excitation beam. In particular, like the effect discussed in Sec. 4.1.4, the effect we will shortly discuss is particularly significant for Rydberg excitation as the switch-on and switch-off timescales of the AOM are commensurate with the timescale of the excitation dynamics (i.e., the Rabi frequency).

An AOM diffracts a beam by an angle proportional to the frequency of the sound wave in its crystal (see Sec. 2.7.1). The frequency of the sound wave is also equal to the frequency shift that is imparted onto the diffracted light. However, at the early stages of a pulse — when the sound wave is only beginning to traverse the

optical beam (or at the end of pulse when the acoustic wave leaves the optical beam) — the "frequency" of the sound wave as seen by the optical beam is not very well-defined. To be more precise, in taking the Fourier transform of only the first leading (or trailing) cycles of an acoustic wave, one does not obtain a sharp peak in frequency space but rather a broad span of frequencies. This means that at the times when only a few cycles of the acoustic wave cross the optical beam, the optical beam is diffracted into a broad span of angles with a corresponding broad span of optical frequencies (such that the angle is proportional to the frequency). At later times, as the acoustic wave fully traverses the optical beam and the AOM frequency becomes more well-defined, the angular spread of optical diffraction converges to one well-defined angle with a well-defined frequency.

The implications this has on the experiment are the following: if the Rydberg excitation beam is slightly misaligned along the plane of diffraction, then at the beginning (and end) of the Rydberg pulse, the atoms will see a detuning that is proportional to the misalignment. This detuning will then change as the AOM frequency becomes well-defined in the "bulk" of the pulse, and finally change again as the pulse is extinguished. This leads to undesired time-dependent detunings in the excitation dynamics similar to those discussed in Sec. 4.1.4. Therefore, precise alignment of the excitation beam becomes important not only for maximizing Rabi frequency and minimizing intensity fluctuations, but also for eliminating such systematic time-dependent detuning.

We observe such effects directly in our experiment. We use a 100 MHz AOM with a beam waist radius of 200 $\mu$m at the position of the crystal, which is then focused to an approximately 20 $\mu$m waist radius beam at the position of the atoms. Using a piezo mirror, we can tune the beampath such that different AOM diffraction angles are aligned to the atoms. Using a peak Rabi frequency of $\Omega \sim 2\pi \times 6$ MHz (at optimal alignment), we observe alignment-dependent detunings at short pulse times ($t \sim \pi/\Omega$) spanning more than $2\pi \times 10$ MHz as the piezo mirror is tuned along the plane of AOM diffraction. No such detunings are observed when the mirror is moved orthogonally to the diffraction plane.

We further support our theory of this effect by imaging the excitation beam at short pulse times and observing that it has an elongated cross-sectional profile along the diffraction plane. After a sufficiently long pulse time, the cross-section collapses to a radially symmetric one.

We overcome this effect by aligning precisely with piezo mirrors. We expect that

this effect can be made less significant by using a higher frequency AOM.

## 4.2 Interactions, blockade, and entanglement

In this section, we discuss the long-range interactions between atoms in Rydberg states. We will also look at how Rydberg interactions can be used to produce entangled Bell states via Rydberg blockade.

### 4.2.1 Pair dipole interaction

While neutral atoms have no overall electric charge, they do have multipole moments (e.g. dipole, quadrupole, etc.) that can interact at long-range. We point the reader to Refs. [196–198, 222, 223] for derivation and discussion of the generic multipolar expansion of the interaction potential between a pair of neutral atoms.

The multipolar expansion is valid so long as the electron wavefunctions of the atom pair have negligible overlap. The minimum length-scale for this criterion to hold is known as the Le Roy radius [224], given by $R_{\mathrm{LR}} = 2\big(\langle r_1^2\rangle^{1/2} + \langle r_2^2\rangle^{1/2}\big)$, where $r_i$ is the radial coordinate of the outer electron of the $i^{\mathrm{th}}$ atom. For the 5s61s $^3\mathrm{S}_1$ state of Sr, we compute $R_{\mathrm{LR}} = 1.1\ \mu$m. We note that the Le Roy radius scales as $(n^\star)^2$ (Eq. 4.19).

For us, the most relevant term will be the lowest order interaction of the multipole expansion, the *dipole-dipole* pair interaction:

$$H_{dd} = \frac{1}{4\pi\varepsilon_0}\frac{1}{R^3}\Big(\vec{d}^{(1)}\cdot\vec{d}^{(2)} - 3(\vec{d}^{(1)}\cdot\hat{R})(\vec{d}^{(2)}\cdot\hat{R})\Big) \tag{4.32}$$

where $\vec{d}^{(i)}$ is the vector dipole operator of atom $i$ and $\vec{R}$ is the *interatomic axis* vector, extending from the center of one atom to that of the other. $\hat{R} = \vec{R}/R$ is a unit vector, with $R = |\vec{R}|$.

An important observation is that $\langle H_{dd}\rangle = 0$ for any pair states that are tensor products of atomic eigenstates. This can be seen via parity arguments with the dipole operator. Therefore, nonzero interactions between atoms in unperturbed atomic states only appear in second order under perturbation theory. We mention, but will not dive further into, the possibility of engineering first order dipolar interactions by mixing opposite parity states with an external electric field [225].

We will choose not to present a detailed discussion of the second-order perturbation theory of $H_{dd}$ here, and instead point the reader to Refs. [196, 223] for more

discussion on this topic. The reason for this decision is that we find it more useful and generic to treat $H_{dd}$ via non-perturbative diagonalization numerics [197, 198, 215]. A non-perturbative approach not only allows one to study experimentally realizable regimes of strong, non-perturbative interactions, but it also allows for straightforward integration of external magnetic and electric fields, which are often present and affect eigenstates and their interactions in ways that may not be fully transparent under perturbation theory (see, e.g., Sec. 4.2.2).

We will, however, note some commonly-cited results of perturbation theory regarding pair state interactions. Let us call $V$ the interaction shift of a particular pair state. First we discuss the scaling with interatomic separation $R$. Since we have argued that the interaction arises in second order, we can conclude that $V$ should perturbatively scale as the square of $H_{dd}$, and thus we have $V = \frac{C_6}{R^6}$ in the perturbative limit, where $C_6$ is an interaction coefficient. The $C_6$ coefficient is state- and sub-state-dependent, and can also be interpreted as having a dependence on the angle between the interatomic axis and the quantization axis [196, 197] as defined by a dominant external field.

We can infer the scaling of $C_6$ with $n^\star$ by noting that $H_{dd}$ is proportional to the product of two dipole operators, each of which scales with an exponent of 2 (Eq. 4.19). Factoring in both of them and noting that the perturbation is second order, we have an exponent of 8 from the dipole operators. In addition to this, we have a further exponent of 3 from the level spacing (Eq. 4.20), giving a total scaling of

$$C_6 \propto (n^\star)^{11} \tag{4.33}$$

such that

$$V \propto \frac{(n^\star)^{11}}{R^6} \tag{4.34}$$

in the perturbative limit. This is a *very* rapid scaling with $n^\star$, and makes it obvious why these interactions can be entirely ignored for low-lying states, but can become very large for Rydberg states.

Ref. [196] predicts the $C_6$ coefficients for several series in Sr, most notably for the $5s5s\ ^3S_1\ m_J = 1$ series under the assumption that the quantization axis is parallel to the interatomic axis. The value they give for this configuration for $n = 61$ is

$$C_6 = 2\pi \times 275\ \text{GHz}\ \mu\text{m}^6 \tag{4.35}$$

The configuration we use for our experiments is slightly different, however. Specifically, we use $m_J = 0$ with the interatomic axis *perpendicular* to the quantization axis (set by a 71 G magnetic field). We will nevertheless use Eq. 4.35 to estimate the interaction strength $V$ in our configuration. This approximation will be acceptable for us because the s state interaction is nearly isotropic [196] and because the exact value of $V$ will not be incredibly important for the blockade experiments we will show in Sec. 4.3.1.

Before moving on, we briefly mention higher-order pair interaction terms, with the most notable being the quadrupole-quadrupole interaction. For a generic $k_1$-pole-$k_2$-pole interaction (1 for dipole, 2 for quadrupole, etc.), the interaction Hamiltonian scales as $R^{-(k_1+k_2+1)}$. Unlike the dipole-dipole interaction, the quadrupole-quadrupole interaction has a first-order energy shift, making its scaling $\frac{C_5}{R^5}$, with $C_5 \propto (n^\star)^8$. At the typical distances where pair interactions are large, this term is significantly smaller than the dipole-dipole interaction, but can become the leading term for particularly large interatomic spacings [196, 223]. Other multipolar interactions (dipole-quadrupole, dipole-octupole, etc) are typically small in the regime where the multipolar expansion is valid [223], though Ref. [197] contains some interesting further discussion on these terms.

### 4.2.2 Systematic shifts of the interaction

We will now show that even a modest external electric field may drastically change the pair interaction shift. We will do this by employing our numerical diagonalization framework [197, 198, 215] and looking at the interaction shift of a particular pair eigenstate as a function of external electric field.

In particular, we will look at the pair state adiabatically equivalent to the unperturbed 5s61s $^3S_1$ $m_J = 0$ pair state, and we will define its interaction shift $V$ as the shift between an interatomic separation of $R = 3.6$ $\mu$m (our typical interatomic spacing) and that at $R \to \infty$. We will look at this interaction shift as a function of electric field magnitude, with the electric field oriented along the quantization axis. We will also include a $B = 71$ G field along the quantization axis and we will orient the interatomic axis *perpendicular* to the quantization axis, as we have in our experiment.

The results are shown in Fig. 4.8. We see that the interaction shift drops significantly for fields on the order of $E \sim 1$ V/cm. Two effects are taking place here: the energy

splittings between neighboring states coupled by the dipole operator are changing, and the eigenstates themselves are being mixed. Two take-away messages are to be had from this exercise: (1) uncontrolled electric fields — even on an ambient level — can pose major problems and (2) the results of perturbation theory alone (i.e. the oft-cited $C_6$ coefficients) are only valid in particular circumstances, reaffirming our recommendation that full numerical diagonalization is the more worthwhile approach to computing pair interactions.

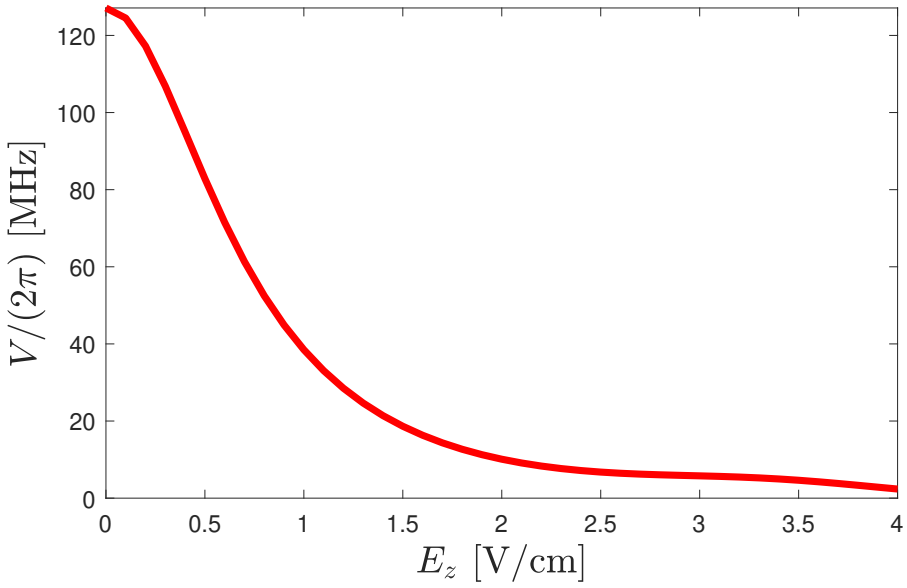


Figure 4.8: Interaction shift $V$ of the pair state (adiabatically equivalent to) 5s61s $^3$S$_1$ $m_J = 0$ as a function of electric field magnitude. The interatomic spacing is $R = 3.6$ $\mu$m. The electric field is oriented along the quantization axis while the interatomic axis is perpendicular to both. A magnetic field of $B = 71$ G is included along the quantization axis. $V$ is defined as the shift between $R = 3.6$ $\mu$m and $R \to \infty$. Our basis of states for diagonalization includes $n \in [60, 62]$ and $l \in \{\mathrm{s}, \mathrm{p}, \mathrm{d}\}$.

We point the reader to Ref. [187] Sec. IID for further exploration of systematic effects on the interaction, as well as Refs. [213, 214] for an in-depth discussion of the effect of RF fields on interactions.

### 4.2.3 Rydberg array Hamiltonian

We will now remove our interest from the origin and computation of Rydberg interactions and simply assume that there exists a certain two-body interaction shift $V_{ij}$ between two Rydberg atoms at positions $i$ and $j$ in an array of potentially many atoms*. It is typically the case with perturbative Rydberg interactions that $V_{ij} = C_6 R_{ij}^{-6}$, but it is not necessary to make such an assumption (e.g., interactions may be made first-order dipolar, giving a scaling of $R^{-3}$, by the application of external electric fields [225] or by going into a non-perturbative regime of very close interatomic spacing). The only things we will assume about $V_{ij}$ is that it is symmetric in exchange of $i \leftrightarrow j$ and that $V_{ii} = 0$.

We will now write down the Hamiltonian of a driven array of Rydberg qubits. The basis will be $\{|g_i\rangle, |r_i\rangle\}$, where for us $|g\rangle$ is the ground state of the Rydberg qubit, $|r\rangle$ is the Rydberg state (see Fig. 4.1), and $i$ indexes the atom at position $i$. Note that an interaction exists only between two atoms that are both in $|r\rangle$; interactions between ground state pairs and between ground-Rydberg pairs are assumed to be zero. There are two convenient ways to write the Hamiltonian. The first is more in the style of "atomic physics":

$$H/\hbar = \tfrac{1}{2}\sum_i \left(\Omega\sigma_i^x - \Delta\sigma_i^z\right) + \tfrac{1}{2}\sum_{\substack{i,j \\ i\neq j}} V_{ij}|r_i r_j\rangle\langle r_i r_j| \tag{4.36}$$

where $\Omega$ is the Rabi frequency, $\Delta$ is the detuning, and $\sigma^\mu$ is the Pauli operator in the $\mu$ direction†. We can also rewrite $H$ (up to constant offset) in a more "quantum simulation" style as

$$H/\hbar = \tfrac{1}{2}\sum_i \left(\Omega\sigma_i^x - (\Delta + \Delta_i^o)\sigma_i^z\right) + \tfrac{1}{8}\sum_{\substack{i,j \\ i\neq j}} V_{ij}\sigma_i^z\sigma_j^z \tag{4.37}$$

$$\Delta_i^o = -\tfrac{1}{2}\sum_{\substack{j \\ j\neq i}} V_{ij} \tag{4.38}$$

Here, $\Delta_i^o$ is an effective on-site detuning that arises from the rewriting of the interaction term into an Ising-type $\sigma_i^z\sigma_j^z$ term. $\Delta_i^o$ is mostly constant in the bulk of a regular array and only has large variation near or at the edge sites. Therefore, this

*And we will further *assume* that there are no three- or generally multi-body interactions.

†$\sigma^z = |r\rangle\langle r| - |g\rangle\langle g|$, $\sigma^x = |g\rangle\langle r| + |r\rangle\langle g|$. There is a subtlety here that we are writing $\sigma^x$ in the "laser frame," i.e., we have rotated away any laser phase between atoms at different sites. This rotation can always be done without consequence when atoms are assumed pinned in place, but ends up producing Doppler terms if motional degrees of freedom are included, see Sec. 4.4.2.

term can be interpreted as an "edge effect" and can sometimes be absorbed into a site-independent $\Delta$ if only bulk physics is of interest. For some periodic systems without an edge — or for systems of only two atoms — $\Delta_i^o$ is site-independent and can be absorbed into $\Delta$.

Note that we have also assumed that $\Omega$ and $\Delta$ have no site-dependent variation. However, this may of course not be true — either intentionally or unintentionally. For example, variations in the beam intensity across the array will produce inhomogeneities in $\Omega$, and field gradients or site-addressing beams can produce inhomogeneities in $\Delta$.

For a 1D array of $N$ regularly-spaced atoms with no externally-applied gradients, $H$ has reflection symmetry under $i \to N - (i - 1)$ (assuming indexing starts from $i = 1$). If the array is regularly spaced *and* periodic (i.e. having a circular geometry), $H$ also has $N$-fold discrete rotational symmetry; i.e., $i \to \big((i + k - 1) \mod N\big) + 1$ for integer $k$. Such symmetries can be useful to effectively reduce the size of the Hilbert space when classically simulating $H$.

### 4.2.4 Rydberg blockade & Bell state generation

Consider two Rydberg qubits both initially in $|g\rangle$ and driven with some Rabi frequency $\Omega$ and with $\Delta = 0$. In the absence of Rydberg interactions, both qubits would independently execute resonant Rabi oscillations between $|g\rangle$ and $|r\rangle$.

However, now let us assume that there are strong interactions between them, such that $V \gg \Omega$. In this case, excitation to the pair state $|rr\rangle$ becomes off-resonant and is suppressed. This phenomenon where only one atom is "allowed" to occupy the Rydberg state is known as *Rydberg blockade* [64–66].

An estimate of how well excitation to $|rr\rangle$ is suppressed can be given by adiabatic elimination [187], with the result being that the maximum probability of double excitation is (for $V \gg \Omega$):

$$\max_t P_{rr} \approx \frac{1}{2}\frac{\Omega^2}{V_{ij}^2} \tag{4.39}$$

If $V = C_k R^{-k}$, we can define a *blockade radius*

$$R_B = \left(\frac{C_k}{\Omega}\right)^{1/k} \tag{4.40}$$

which gives an estimate on the interatomic separation necessary for a Rydberg blockade. If we take $k = 6$ and assume a scaling of $\Omega \propto (n^\star)^{-3/2}$ (Eq. 4.8), then we get the scaling $R_B \propto (n^\star)^{25/12}$.

We now define two orthogonal Bell states

$$|W\rangle = \tfrac{1}{\sqrt{2}}(|gr\rangle + |rg\rangle) \tag{4.41}$$

$$|D\rangle = \tfrac{1}{\sqrt{2}}(|gr\rangle - |rg\rangle) \tag{4.42}$$

and we note that

$$\langle gg|H|D\rangle = 0 \tag{4.43}$$

$$\langle gg|H|W\rangle = \tfrac{1}{2}(\sqrt{2}\Omega) \tag{4.44}$$

Therefore, the dynamics of a resonantly driven qubit pair starting from $|gg\rangle$ in the limit of Rydberg blockade are effectively those of a two-level system executing Rabi oscillations between $|gg\rangle \leftrightarrow |W\rangle$ with an effective Rabi frequency of

$$\Omega_2 = \sqrt{2}\Omega \tag{4.45}$$

as the matrix element in Eq. 4.44 is $\sqrt{2}$ larger than it is for a normal two-level system with Rabi frequency $\Omega$.

Thus we have shown that Rydberg interactions can be exploited to create an entangled Bell state $|W\rangle$ between two atoms. The fidelity limit of this procedure imposed by blockade violation is slightly different than that suggested by Eq. 4.39. In particular, for $V \gg \Omega$:

$$\max_t P_W \approx 1 - \frac{5}{8}\frac{\Omega^2}{V^2} \tag{4.46}$$

which is a result that follows from perturbation theory [195] and is verified by numerical diagonalization.

These results can be extended for $N$ atoms that are mutually blockaded [74, 187]. We will not explore this in depth, but note that the result is a Rabi oscillation between

$$|g\rangle^{\otimes N} \leftrightarrow \frac{1}{\sqrt{N}}\sum_{i=1}^{N}|g_1 g_2 ... r_i ... g_{N-1} g_N\rangle \tag{4.47}$$

with an effective Rabi frequency of

$$\Omega_N = \sqrt{N}\Omega \tag{4.48}$$

## 4.3 Experimental results

***Note: This section presents results from our publication Ref. [150].***

We now present the results of our Rydberg excitation scheme. In Sec. 4.3.1, we show single-atom and two-atom blockaded oscillations. In Sec. 4.3.2, we present a novel argument for estimating the Bell state fidelity of our blockaded oscillations via a lower bound.

### 4.3.1 Single-atom & two-atom blockade oscillations

We excite our Rydberg qubits (Fig. 4.1) with two different array configurations: (a) an effectively non-interacting configuration where single atoms are spaced by $R_1 = 10.8\ \mu$m, and (b) a strongly-interacting blockaded configuration where interacting atoms are separated by $R_2 = 3.6\ \mu$m and the separation between adjacent pairs is at least $10.8\ \mu$m. These configurations are illustrated in Fig. 4.9.

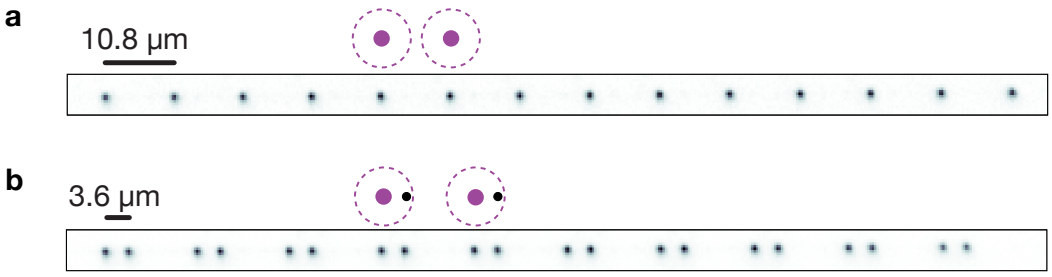


Figure 4.9: Averaged fluorescence images of two array configurations. **(a)** Non-interacting array of 14 occupied tweezers spaced by $10.8\ \mu$m. A pictorial representation of two non-interacting atoms outside of each others' blockade radii (not to scale) is shown. **(b)** Array of strongly-interacting (blockaded) pairs of atoms. Atoms within a pair are separated by $3.6\ \mu$m, while there is at least $10.8\ \mu$m between atoms in adjacent pairs. 10 pairs of tweezers are pictured in the average image, though not all of them are necessarily occupied in a given trial. A pictorial representation of two blockaded pairs is shown, with the purple dot representing an atom in $|r\rangle$ while the black dot represents an atom in $|g\rangle$. The Rydberg excitation beam propagates along the array.

We use 5s61s $^3S_1$ as our Rydberg state $|r\rangle$. By Eq. 4.35, we expect an interaction shift of $V_2 \approx 2\pi \times 130$ MHz for strongly-interacting pairs at $R_2 = 3.6\ \mu$m and only $V_1 \approx 2\pi \times 170$ kHz for "non-interacting" atoms at $R_1 = 10.8\ \mu$m. We will use a Rabi frequency of $\Omega \gtrsim 2\pi \times 6$ MHz throughout, which is safely in the blockaded regime with respect to $V_2$ as well as large enough to effectively make $V_1$ negligible.

As a point of reference, the blockade radius at $\Omega = 2\pi \times 6.0$ MHz and the $C_6$ given in Eq. 4.35 is $R_B = 6.0\ \mu$m (Eq. 4.40).

After verifying the presence of an atom and performing Rydberg excitation, we measure either the absence (denoted by 0) or presence (denoted by 1) of an atom at the end of the experiment (Sec. 2.6.6). For single atoms, we define $P_x$ as the probability of measuring $x$, where $x \in \{0, 1\}$. For blockaded pairs, there are 2 bits of binary information and thus four possible measurement outcomes. We define $P_{x_1x_2}$ as the probability of measuring the bitstring $x_1x_2$ in the atom pair. We also define the symmetrized probability $P_{\{10\}} = P_{10} + P_{01}$ of measuring *one but not both* of the atoms as 1 (which will be most useful in observing blockade oscillations), as well as the anti-symmetrized $P_{[10]} = P_{10} - P_{01}$.

Due to our auto-ionization state-detection scheme (Sec. 4.1.3), our measurements of 0 or 1 infer the atomic state via the mapping $0 \rightarrow |r\rangle$ and $1 \rightarrow |g\rangle$. This mapping of course assumes perfect state-preparation and measurement (SPAM), and we discuss in App. E how to perform so-called SPAM correction to infer what the measured populations of $|g\rangle$ and $|r\rangle$ would be without SPAM errors.

Fig. 4.10a shows $P_1$ for a typical single-atom (array configuration (a)) Rabi oscillation at early times for $\Omega = 2\pi \times 6.8$ MHz, while Fig. 4.10b shows $1 - P_{\{10\}}$ for a typical two-atom blockaded (array configuration (b)) oscillation under approximately the same $\Omega$. For the blockaded oscillations, we measure an oscillation frequency of $\Omega_2 = 2\pi \times 9.8$ MHz, which is close to $\sqrt{2}\Omega$ as anticipated by Eq. 4.45.

Table 4.3 lists measured values at the $\pi$ and $2\pi$ times (as reported in Ref. [150] Extended Data Table I). Note that $\sum P_{x_1x_2} = 1$. We also list SPAM corrected values (App. E).

Fig. 4.11 plots both single-atom and two-atom blockaded oscillations for long times and allows us to measure coherence times for both oscillations. We find that both oscillations dephase with an approximately Gaussian envelope. We believe this dephasing is dominantly caused by a combination of intensity noise (see Sec. 4.4.3) and residual interaction between neighboring atoms/pairs. For the single atom oscillations, we measure a Rabi frequency of $\Omega = 2\pi \times 6.0$ MHz and a $1/e$ dephasing time of ~42 cycles. For the two-atom blockaded oscillations, approximately the same $\Omega$ is used and we measure an effective two-atom Rabi frequency of $\Omega_2 = 2\pi \times 8.5$ MHz with a $1/e$ dephasing time of ~60 cycles. Again, $\Omega_2$ is approximately $\sqrt{2}$ times larger than $\Omega$, as anticipated by Eq. 4.45.

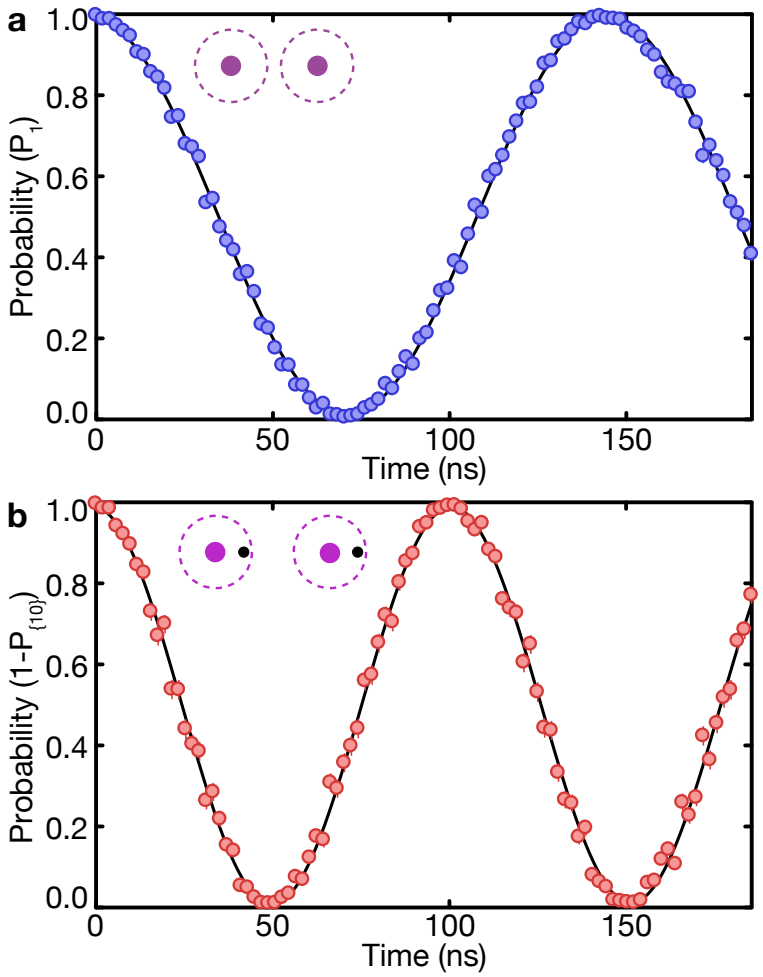


Figure 4.10: Short-time single- and two-atom oscillations on the Rydberg transition. **(a)** Single-atom Rabi oscillations on our Rydberg qubit (Fig. 4.1), measuring $P_1$. We measure a Rabi frequency of $\Omega = 2\pi \times 6.80$ MHz. **(b)** Two-atom blockaded oscillations, measuring $1 - P_{\{10\}} = 1 - (P_{10} + P_{01})$. We measure an effective Rabi frequency of $\Omega_2 = 2\pi \times 9.8$ MHz. Auto-ionization state-readout is used in both (a) and (b), with an auto-ionization pulse length of 5 $\mu$s. Data is averaged over all atoms/pairs in the array. The vertical axis is *not* SPAM corrected in either (a) or (b). Inset illustrations correspond to the array configuration used (see Fig. 4.9).

| Variable | Measured value | SPAM corrected | Notes |
|---|---|---|---|
| $P_0(T_\pi)$ | 0.9951(9) | 0.9967(9) | Single-atom $\pi$-fidelity |
| $P_1(T_{2\pi})$ | 0.9951(9) | 0.998(1) | Single-atom $2\pi$-return |
| $P_{\{10\}}(T_\pi)$ | 0.992(2) | 0.996(2) | Blockaded $\pi$-fidelity |
| $P_{[10]}(T_\pi)$ | 0.01(1) | 0.01(1) | Imbalance at $\pi$ |
| $P_{00}(T_\pi)$ | 0.0032(7) | 0.0014(9) | Blockade violation at $\pi$ |
| $P_{11}(T_{2\pi})$ | 0.989(2) | 0.996(3) | Blockaded $2\pi$-return |
| $P_{[10]}(T_{2\pi})$ | 0.004(2) | 0.004(2) | Imbalance at $2\pi$ |
| $P_{00}(T_{2\pi})$ | 0.0036(7) | 0.002(1) | Blockade violation at $2\pi$ |

Table 4.3: Measured and SPAM corrected values for single-atom as well as two-atom blockaded oscillations at $\pi$ and $2\pi$ times [150]. $P_{\{10\}} = P_{10} + P_{01}$ and $P_{[10]} = P_{10} - P_{01}$. $T_\pi$ and $T_{2\pi}$ signify the $\pi$ and $2\pi$ times, respectively. See App. E for the SPAM correction procedure.

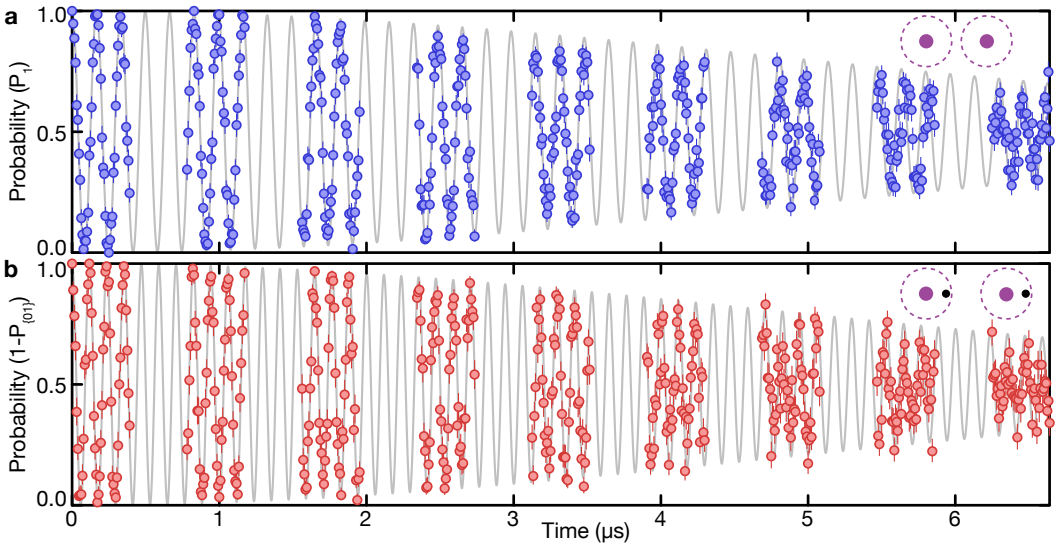


Figure 4.11: Long-time single- and two-atom oscillations on the Rydberg transition. **(a)** Single atom Rabi oscillations on our Rydberg qubit (Fig. 4.1), measuring $P_1$. We measure a Rabi frequency of $\Omega = 2\pi \times 6.0$ MHz and a $1/e$ dephasing time of ~42 cycles. **(b)** Two-atom blockaded oscillations, measuring $1 - P_{\{10\}} = 1 - (P_{10} + P_{01})$. We measure an effective Rabi frequency of $\Omega_2 = 2\pi \times 8.5$ MHz and a $1/e$ dephasing time of ~60 cycles. Auto-ionization state-readout is used in both (a) and (b), with an auto-ionization pulse length of 5 $\mu$s. Data is averaged over all atoms/pairs in the array. The vertical axis is *not* SPAM corrected in either (a) or (b). Inset illustrations correspond to the array configuration used (see Fig. 4.9).

### 4.3.2 Bell-state fidelity bound

We would now like to be able to determine how well our blockaded oscillations prepare an entangled two-atom Bell state, as predicted in Sec. 4.2.4. Although

observing a value of $P_{\{10\}}$ (see Sec. 4.3.1) close to 1 is highly *suggestive* of an entangled Bell state, such a measurement is also fully compatible with a non-entangled statistical mixture $\rho = \frac{1}{2}\big(|rg\rangle\langle rg| + |gr\rangle\langle gr|\big)$.

Specifically, we must assume that the quantum state of our atoms at a given time is described by a generically non-pure density matrix $\rho$. We can label the entries of $\rho$ as $\rho_{i,j}$, where $i, j \in \{gg, gr, rg, rr\}$. We would then like to know the value of the fidelity $\mathcal{F}$ defined as

$$\mathcal{F} = \max_{\phi} \langle W_\phi|\rho|W_\phi\rangle \tag{4.49}$$

$$= \frac{1}{2}\Big(\rho_{gr,gr} + \rho_{rg,rg} + 2|\rho_{gr,rg}|\Big) \tag{4.50}$$

where

$$|W_\phi\rangle = \tfrac{1}{\sqrt{2}}\big(|gr\rangle + e^{i\phi}|rg\rangle\big) \tag{4.51}$$

Here, we generically allow our Bell state to have any given phase $\phi$ and we are content with defining the fidelity as the overlap of $\rho$ with the $|W_\phi\rangle$ that produces the *maximal* overlap. This is justified as $\phi$ can always be rotated via a frame rotation (see footnote after Eq. 4.36).

We are mainly interested in the value of $\mathcal{F}$ at a blockaded $\pi$-pulse, where ideally $\mathcal{F}$ should be close to 1. We can immediately identify the quantity $\rho_{gr,gr}+\rho_{rg,rg} = P_{\{10\}}$, which we directly measure. However, we have no direct access to the off-diagonal quantity $|\rho_{gr,rg}|$ in our measurement basis, so an ideal measurement of $P_{\{10\}} = 1$ alone can at most give a lower-bound of $\mathcal{F} \geq \frac{1}{2}$.

In previous work, $\mathcal{F}$ was measured via parity oscillations [119, 226]. The idea here would be to perform the blockaded $\pi$-pulse, locally rotate the phase of one of the qubits in the pair by a variable angle $\phi$ (i.e., applying the unitary operator $U = e^{i\frac{1}{2}\phi\sigma_1^z}$), and then perform another $\pi$-pulse (applying $U = e^{i\frac{1}{2}\pi(\sigma_1^x+\sigma_2^x)}$). If the initial state was an ideal $|W\rangle$ state, a rotation of $\phi = \pi$ would produce a $|D\rangle$ state (Eq. 4.42) that would then *not* rotate back to $|gg\rangle$ after the applied $\pi$-pulse along $\sigma^x$. Generically, an oscillating signal is expected as a function of $\phi$, and the *contrast* of these oscillations measures $\mathcal{F}$.

However, such a scheme requires the ability to perform locally-addressed $\sigma^z$ rotations. While we can potentially achieve this by using the light shift of the traps with local addressing provided by the AOD, we chose to instead estimate $\mathcal{F}$ via a novel

lower-bound argument* that makes certain assumptions on the time evolution of the purity of $\rho$.

We begin with a simple mathematical proof bounding a particular off-diagonal element $|\rho_{a,b}|$ from below as a function of diagonal elements of $\rho$ and the *purity* of $\rho$ (defined as $\mathrm{Tr}\left\{\rho^2\right\}$). The proof is as follows:

$$\begin{aligned}
\mathrm{Tr}\left\{\rho^2\right\} &= \sum_{ij} |\rho_{i,j}|^2 && (4.52)\\
&= \sum_{i} \rho_{i,i}^2 + \sum_{i\neq j} |\rho_{i,j}|^2 && (4.53)\\
&= \sum_{i} \rho_{i,i}^2 + \sum_{\substack{i\neq j\\(i,j)\neq(a,b)\\(i,j)\neq(b,a)}} |\rho_{i,j}|^2 + 2|\rho_{a,b}|^2 && (4.54)\\
&\leq \sum_{i} \rho_{i,i}^2 + \sum_{\substack{i\neq j\\(i,j)\neq(a,b)\\(i,j)\neq(b,a)}} \rho_{i,i}\rho_{j,j} + 2|\rho_{a,b}|^2 \text{ [Cauchy's inequality]} && (4.55)\\
&= \sum_{i} \rho_{i,i}^2 + \sum_{i\neq j} \rho_{i,i}\rho_{j,j} - 2\rho_{a,a}\rho_{b,b} + 2|\rho_{a,b}|^2 && (4.56)\\
&= \underbrace{\sum_{ij} \rho_{i,i}\rho_{j,j}}_{1} - 2\rho_{a,a}\rho_{b,b} + 2|\rho_{a,b}|^2 && (4.57)\\
&= 1 - 2\rho_{a,a}\rho_{b,b} + 2|\rho_{a,b}|^2 && (4.58)
\end{aligned}$$

This implies that

$$|\rho_{a,b}|^2 \geq \tfrac{1}{2}(\mathrm{Tr}\left\{\rho^2\right\} - 1) + \rho_{a,a}\rho_{b,b} \tag{4.59}$$

This expression allows us to bound the off-diagonal $|\rho_{gr,rg}|$ with the purity of $\rho$ as well as the measurable $\rho_{gr,gr}$ and $\rho_{rg,rg}$.

The purity of $\rho$ is still, nevertheless, not a directly measurable quantity. However, it can *also* be bounded from below by

$$\mathrm{Tr}\left\{\rho^2\right\} \geq \sum_{i} \rho_{i,i}^2 \tag{4.60}$$

where each term in the sum *is* a measurable quantity.

We now pause to see if these arguments have actually improved our bound on $\mathcal{F}$, under the assumption that we have made *ideal* measurements of $\rho_{gr,gr} = \rho_{rg,rg} = \frac{1}{2}$

*We credit this argument to Hannes Pichler.

and $\rho_{gg,gg} = \rho_{rr,rr} = 0$ at a particular time. Our bound on the purity from Eq. 4.60 is $\mathrm{Tr}\left\{\rho^2\right\} \geq \frac{1}{2}$. This unfortunately leaves our lower bound on $|\rho_{gr,rg}|$ at exactly zero, so it appears that we have made no progress on our bound of $\mathcal{F} \geq \frac{1}{2}$.

If we were to instead make a measurement at a point in time where $\rho$ has a diagonal element close to 1, Eq. 4.60 would allow us to bound the purity at this time to a value also very close to 1. Such a situation ideally occurs at the $2\pi$ time of a blockade oscillation, where ideally we have $\rho_{gg,gg} = 1$ and all other entries zero. However, this is also of course not anywhere close to an entangled Bell state.

The question now is this: Is there a way we can use the purity bound at the $2\pi$ time to also bound the purity at the $\pi$ time? Indeed, this is precisely the reason why we chose to re-formulate the argument in terms of the purity: *it is reasonable to assume that the purity of $\rho$ does not increase with time**. If this assumption is made, then we can bound from below the purity at the $\pi$ time by the purity at the $2\pi$ time†, which in turn can be *tightly* bounded by measurable quantities. To be precise, we have:

$$\mathrm{Tr}\left\{\rho^2\right\}(T_\pi) \geq \mathrm{Tr}\left\{\rho^2\right\}(T_{2\pi}) \geq \sum_i \rho_{i,i}^2(T_{2\pi}) \tag{4.61}$$

where $T_\pi$ and $T_{2\pi}$ are the $\pi$ and $2\pi$ times, respectively.

Combining all our results, we end up with a lower bound on $\mathcal{F}(T_\pi)$ of

$$\mathcal{F}(T_\pi) \geq \frac{1}{2}\Bigg(\rho_{gr,gr}(T_\pi) + \rho_{rg,rg}(T_\pi) + 2\sqrt{\max\left(0, \left(\textstyle\sum_i \rho_{i,i}(T_{2\pi})^2 - 1\right)/2 + \rho_{gr,gr}(T_\pi)\rho_{rg,rg}(T_\pi)\right)}\Bigg) \tag{4.62}$$

This procedure can potentially be interpreted as a parity oscillation with only a single point at $\phi = 0$, where we bound the contrast of the would-be parity oscillation using only its first point and an assumption of non-increasing purity.

Using our measured values in Table 4.3 with the mappings $P_{00} \to \rho_{rr,rr}$, $P_{10} \to \rho_{gr,gr}$, $P_{01} \to \rho_{rg,rg}$, and $P_{11} \to \rho_{rr,rr}$, we get

*However, there are certain situations where, e.g., coupling to the environment can actually *increase* the purity. The easiest example is a single atom in a mixed state of ground and excited state decaying to the ground state. We have considered such scenarios and present further arguments in Ref. [150] Supplement D2 that show that a purity increase from spontaneous decay would — in the worst case — negligibly affect our bound on $\mathcal{F}$.

†It is actually unimportant that this later time be chosen at exactly $2\pi$. More generally, it can be any point at a time later than the $\pi$ time at which the purity bound is maximized.

| Variable | Measured value | SPAM corrected |
|---|---|---|
| $\mathcal{F}(T_\pi)$ | $\geq$0.980(3) | $\geq$0.991(4) |

Table 4.4: Measured and SPAM corrected lower bounds for the Bell state fidelity $\mathcal{F}(T_\pi)$ at the $\pi$-time $T_\pi$ [150].

## 4.4 Sources of error in dynamics

We now discuss effects that produce undesired dynamics not captured by the ideal Hamiltonian of Eqs. 4.36–4.38. We will generically refer to such effects as errors. These will include decay and blackbody radiation (Sec. 4.4.1), thermal and motional effects (Sec. 4.4.2), and technical noise (most notably that of laser intensity and frequency noise) (Sec. 4.4.3).

Some effects that we will neglect to analyze include far off-resonant scattering of photons (including potential photo/auto-ionization) by beams such as the trapping beam (if it is left on during Rydberg excitation, which for us it is typically not) or even by the excitation beam. We point the reader to Refs. [209, 217, 227] for further discussion on these topics.

Note that this section will be specifically dedicated to effects that produce errors in *dynamics* instead of errors in state preparation and measurement, which are separately discussed in App. E.

### 4.4.1 Decay and blackbody radiation

One of the key features making Rydberg states a viable platform for coherent quantum simulation is their relatively long radiative lifetimes. Compared to lower-lying excited states, which have typical lifetimes of a few to tens of nanoseconds, Rydberg states typically have lifetimes of tens to hundreds of microseconds. Of course, the true figure of merit is not just the lifetime but the number of achievable coherent cycles, which is approximately limited by the ratio $\Omega/\Gamma$ of the achievable Rabi frequency $\Omega$ over the total depopulation rate $\Gamma$.

For a Rydberg state, two radiative depopulation rates are important: the spontaneous decay rate $\Gamma_s$ as a result of coupling to the electromagnetic vacuum, and the blackbody radiation (BBR) transition rate $\Gamma_{\mathrm{BBR}}(T)$ as a result of coupling to the finite photon occupation of certain modes at finite temperature $T$. Unlike for lower-lying states, BBR is significant for Rydberg states as room-temperature produces non-negligible mode occupation at frequencies near the level separation between

neighboring Rydberg states (typically tens of GHz). Furthermore, dipole matrix elements between neighboring Rydberg states (App. D) are typically much larger than those between low-lying states, owing to the scaling of Eq. 4.19.

***Spontaneous decay***

The scaling of the spontaneous decay rate $\Gamma_s$ of Rydberg states with $n^\star$ can be approximately deduced from Eq. 4.8 by noting that $\Gamma_s$ is proportional to the square of a dipole matrix element, as given by Eq. 2.29 (there is additionally a contribution proportional to $\omega^3$ where $\omega$ is the transition frequency, but the variation of this between Rydberg states is fractionally small and negligible). We thus approximately have

$$\Gamma_s \propto (n^\star)^{-3} \tag{4.63}$$

An absolutely fundamental limit to the number of achievable coherent cycles is thus given by $\Omega/\Gamma_s$ (assuming no other sources of error and zero temperature for BBR). At a fixed laser intensity, this quantity scales as

$$\Omega/\Gamma_s \propto (n^\star)^{3/2} \tag{4.64}$$

While this trend may suggest that it is beneficial to work with larger $n$ Rydberg states, there are other effects that scale unfavorably with increasing $n$ (Sec. 4.5) which compel a compromise at a lower $n$.

It may be useful to determine not just the total spontaneous decay rate of a Rydberg state, but also its branching ratio into various lower-lying states. We will attempt to do this for the 5s61s $^3S_1$ Rydberg state. We begin by combining Eq. 2.29 and Eq. D.1 to get

$$\Gamma_{\beta'\to\beta} = \frac{\omega_{\beta'\beta}^3}{3\pi\varepsilon_0\hbar c^3}\frac{|\langle\beta||d||\beta'\rangle|^2}{2J'+1} \tag{4.65}$$

$$\begin{aligned} &= \frac{\omega_{\beta'\beta}^3}{3\pi\varepsilon_0\hbar c^3}\left(e\int_0^\infty dr r^3 R_{nl}^*(r)R_{n'l'}(r)\right)^2 \dots \\ &\quad \dots\times(2L+1)(2L'+1)\begin{pmatrix} L & L' & 1 \\ 0 & 0 & 0\end{pmatrix}^2 \dots \\ &\quad \dots\times\delta_{SS'}(2J+1)\begin{Bmatrix} J & J' & 1 \\ L' & L & S\end{Bmatrix}^2 \end{aligned} \tag{4.66}$$

where $\beta$ is shorthand for the $n, l, S, J$ quantum numbers. Our excited state has $l' = 0, S' = 1, J' = 1$ and it will be able to decay into states with $l = 1, S = 1, J \in \{0, 1, 2\}$. When considering only such pathways, it can be shown that

$$\Gamma_{\beta' \to \beta}(l' = 0, S' = 1, J' = 1) \propto \omega^3_{\beta'\beta} f(n, n')(2J + 1) \tag{4.67}$$

where $f(n, n')$ is some function of $n, n'$ that is proportional to the square of the radial wavefunction overlap between the two states. We have already argued that $f(n, n') \propto (n'^{\star})^3$ in Eq. 4.63. However, determining how $f(n, n')$ scales with $n$ (the principal quantum number of the *lower* state) is not so easy. Universal scaling arguments such as quantum defect theory are at best dubious for lower-lying states, and results are generally species-dependent.

Although data is available that allows one to deduce $f(n, n')$ for Rb [228], we have not been able to find equivalent data for Sr. We therefore will not be able to compute branching ratios to states of different $n$, although if the situation is similar to that in Rb, we can estimate that approximately half of Rydberg atoms decay directly to the 5s5p $^3\mathrm{P}_J$ manifold (although $f(n, n')$ is expected to increase with $n$, the decreasing factor of $\omega^3_{\beta'\beta}$ dominates and makes decay to the lowest manifold the dominant pathway).

We can nonetheless compute the branching ratio to the various states of the 5s5p $^3\mathrm{P}_J$ manifold. Using Eq. 4.67, we get a branching ratio of 1.00 : 2.95 : 4.73 for $J = 0, 1, 2$, respectively. Using our measured value of the RDME between the clock state and 5s61s $^3\mathrm{S}_1$ (Sec. 4.1.2), we compute (Eq. 4.65) decay rates of

$$\Gamma_{5s61s\ ^3\mathrm{S}_1 \to 5s5p\ ^3\mathrm{P}_0} = 2\pi \times 72 \text{ Hz} \tag{4.68}$$

$$\Gamma_{5s61s\ ^3\mathrm{S}_1 \to 5s5p\ ^3\mathrm{P}_1} = 2\pi \times 210 \text{ Hz} \tag{4.69}$$

$$\Gamma_{5s61s\ ^3\mathrm{S}_1 \to 5s5p\ ^3\mathrm{P}_2} = 2\pi \times 340 \text{ Hz} \tag{4.70}$$

The sum of these rates gives a timescale of 260 $\mu$s for direct decay into the 5s5p $^3\mathrm{P}_J$ manifold. We can compare this with our measurement of the decay timescale into bright states of $\tau_B = 168(14)$ $\mu$s as reported at the end of Sec. 4.1.3. These two numbers suggest that approximately 65% of the spontaneous decay into bright states goes directly into the 5s5p $^3\mathrm{P}_J$ manifold, while the rest goes into other lower-lying states that subsequently decay into 5s5p $^3\mathrm{P}_J$ (with the timescale of this subsequent decay expected to be relatively rapid, i.e. $\ll 1$ $\mu$s).

Thus we see that in our excitation scheme, the dominant spontaneous decay pathway of the Rydberg state is *not* in fact to its original ground state (the clock state), but

that it is more likely to decay to states that are outside of the originally considered Hilbert space. The implication of this is that the effects of decay in our scheme is not well-captured by a simple two-level model. Qualitatively, a Rabi oscillation between the clock and Rydberg state would show a damped oscillation whose mean value tends toward zero excited state population instead of 1/2.

There is a further complication from decay into 5s5p $^3P_{1,2}$ in that the Rydberg excitation beam resonantly drives these states to continuum states just above the ionization threshold, where photoionization rates are expected to be rapid. In fact, we have measured this rate for 5s5p $^3P_2$ to be $\Omega^2 \times 8 \times 10^{-11}$ s, where $\Omega$ is the Rabi frequency (in angular frequency units, as defined in Eq. 4.38) on the 5s5p $^3P_0 \leftrightarrow$ 5s61s $^3S_1$ clock to Rydberg transition assuming optimal polarization alignment. The implication of this effect is that atoms that decay from the Rydberg state into nominally bright states may subsequently become dark to our detection scheme if the Rydberg drive remains on subsequent to their decay.

***BBR transitions***

The rate of BBR transitions from a manifold $|\beta'\rangle$ to another manifold $|\beta\rangle$ is given by [229]

$$\Gamma_{\mathrm{BBR},\,\beta'\to\beta}(T) = \frac{1}{\exp\left(\frac{\hbar|\omega_{\beta'\beta}|}{k_B T}\right) - 1} \frac{|\omega_{\beta'\beta}|^3}{3\pi\varepsilon_0\hbar c^3} \frac{|\langle\beta||d||\beta'\rangle|^2}{2J'+1} \tag{4.71}$$

We note that this formula assumes an ideal and uniform BBR background. Using the RDMEs computed in App. D, we plot the BBR transition rates for $|\beta'\rangle$ = 5s61s $^3S_1$ at $T$ = 300 K in Fig. 4.12. Summing over all available BBR transitions in $n \in [45, 75]$, we get a total BBR transition rate at $T$ = 300 K of $\Gamma_{\mathrm{BBR}}(300\ \mathrm{K}) = 2\pi \times 840$ Hz.

Eq. 8 of Ref. [229] gives a scaling of

$$\Gamma_{\mathrm{BBR}} \propto (n^\star)^{-2} \tag{4.72}$$

for the total BBR transition rate.

## 4.4.2 Motional and thermal effects

The Hamiltonian of Eqs. 4.36–4.38 assumes that each atom is at a fixed point in space and neglects motional degrees of freedom. Here we will explore several

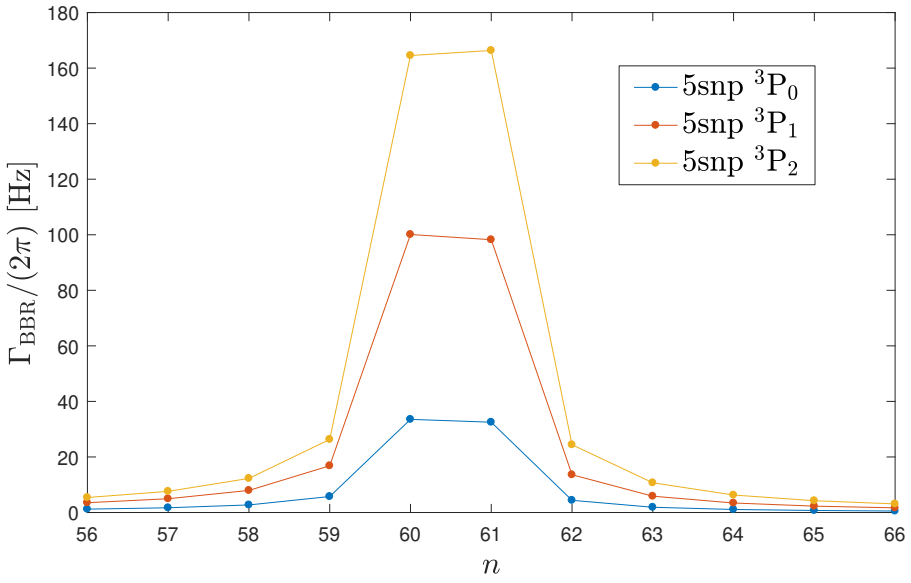


Figure 4.12: Blackbody radiation transition rates of the 5s61s $^3$S$_1$ state to various adjacent Rydberg states at $T = 300$ K.

approaches to capturing errors due to motional degrees of freedom at generically finite temperature. For simplicity (and since it is how we usually perform Rydberg excitation), we will assume that the trap is extinguished during Rydberg excitation (for further exploration with the trap left on, see Ref. [151]).

### *Initial state*

The first question to answer is: what is the initial motional state of the atom immediately after the trap is extinguished? We will assume that the trap is extinguished on a timescale much faster than the initial trap frequency (i.e. diabatically). Then the initial motional state is identical to the state immediately before extinguishing the trap. We will assume that the atom was well inside the harmonic regime of the trap and that immediately before the trap was extinguished, it had a set of trap frequencies $\omega_r, \omega_z$ (radial and axial, respectively). We will furthermore assume a temperature $T$ (for conversion to or from other thermal quantities, see Sec. 2.5.1). Then the initial motional state of the atom is a product of thermal states along each direction, each of which is given by a density matrix

$$\rho_0 = \frac{1}{1 - \exp\left(-\frac{\hbar\omega}{k_B T}\right)} \sum_{n=0}^{\infty} e^{-\frac{\hbar\omega n}{k_B T}} |n\rangle\langle n| \tag{4.73}$$

This density matrix can be evolved directly or used for Monte Carlo sampling of pure initial states.

In the position basis, $\rho_0$ can be rewritten as [230]

$$\rho_0 = \frac{1}{\sqrt{\frac{\pi\hbar}{m\omega}\coth\left(\frac{\hbar\omega}{2k_\mathrm{B}T}\right)}} \times \ldots$$
$$\cdots \times \iint dx dx' \exp\left(\frac{m\omega}{\hbar}\left(\operatorname{csch}\left(\tfrac{\hbar\omega}{k_\mathrm{B}T}\right)xx' - \tfrac{1}{2}\cosh\left(\tfrac{\hbar\omega}{k_\mathrm{B}T}\right)(x^2+x'^2)\right)\right)|x\rangle\langle x'| \quad (4.74)$$

Taking the diagonal elements of $\rho_0$ in the position basis gives us the thermal probability distribution of the position $x$, which ends up being a Gaussian:

$$P(x) = \frac{1}{\sigma_x\sqrt{2\pi}}\exp\left(-\frac{x^2}{2\sigma_x^2}\right) \quad (4.75)$$

$$\sigma_x = \sqrt{\frac{\hbar}{2m\omega}\coth\left(\frac{\hbar\omega}{2k_\mathrm{B}T}\right)} \quad (4.76)$$

A similar analysis can be done in momentum space, resulting in

$$P(p) = \frac{1}{\sigma_p\sqrt{2\pi}}\exp\left(-\frac{p^2}{2\sigma_p^2}\right) \quad (4.77)$$

$$\sigma_p = \sqrt{\frac{\hbar m\omega}{2}\coth\left(\frac{\hbar\omega}{2k_\mathrm{B}T}\right)} \quad (4.78)$$

***Motional effects on internal qubit dynamics***

Next we ask: how does the ensuing motional dynamics affect internal Rydberg qubit dynamics in an ensemble of atoms? Answering this question thoroughly requires evolving the full (motional + internal) quantum state by the full Rydberg Hamiltonian including motion given by

$$H/\hbar = \tfrac{1}{2}\sum_i\left(\frac{|\vec{p}_i|^2}{m} + \Omega\sigma_i^x - \left(\Delta + \Delta^o(\vec{r}_i) + \tfrac{1}{m}\vec{k}\cdot\vec{p}_i\right)\sigma_i^z\right) + \tfrac{1}{8}\sum_{\substack{i,j\\ i\neq j}} V(\vec{r}_{ij})\sigma_i^z\sigma_j^z \quad (4.79)$$

$$\Delta^o(\vec{r}_i) = -\tfrac{1}{2}\sum_{\substack{j\\ j\neq i}} V(\vec{r}_{ij}) \quad (4.80)$$

where $m$ is the atomic mass, $\vec{k}$ is the $k$-vector of the drive beam, and $\vec{r}_{ij} = \vec{r}_i - \vec{r}_j$. Note that here we are in the "laser frame", which gauges away the spacial phase variation of the driving beam and results in a Doppler detuning term. Such a frame transformation is made from the lab frame to the laser frame by taking $\vec{p}_{\text{laser}} = \vec{p}_{\text{lab}} - \frac{\hbar}{2}\vec{k}\sigma^z$ and $\sigma^{\pm}_{\text{laser}} = e^{\pm i\vec{k}\cdot\vec{r}}\sigma^{\pm}_{\text{lab}}$ (for each atom). One can verify that these transformations leave all commutation relations intact.

This is generically a highly complex quantum problem for which a numerical approach is likely not feasible for more than a few atoms (although we have had preliminary success with the two-atom case when working in the center-of-mass frame). We will therefore discuss two simplifying approaches that can make this problem more tractable while still retaining much of the essential physics.

The first approach is to treat $\vec{r}_i$ and $\vec{p}_i$ semi-classically. Here, we replace these quantum operators with their expectation values, which are then evolved via classical dynamics. We point the reader to Ref. [122] for some ideas on this method.

The second, simpler, approach is to treat $\vec{r}_i$ and $\vec{p}_i$ as completely static quantities that are Monte Carlo sampled from Eqs. 4.75 & 4.77. While this approach neglects the dynamical evolution of these variables, it does still capture fluctuations of the Doppler shift and of the interaction strength due to the fluctuations of atomic motion (including zero-point fluctuations at zero temperature).

We give a brief analysis of interaction fluctuations predicted by this "static" model. We assume that a pair of atoms begin interacting after being initialized from two traps spaced by a separation $R$, each having radial/axial trap frequencies $\omega_r, \omega_z$ and a temperature $T$. We will assume that the interaction is isotropic and follows a power law $V = C_k R^{-k}$. We will also assume that the tweezers are separated along $\hat{x}$ and that this is one of the principal axes of the traps. Then we have

$$V(\vec{r}_1, \vec{r}_2) = C_k\left((x_1 - x_2 + R)^2 + (y_1 - y_2)^2 + (z_1 - z_2)^2\right)^{-k/2} \tag{4.81}$$

We can now sample $x_i, y_i, z_i$ from Eq. 4.75. We assume $k = 6$, $\omega_r = 2\pi \times 25$ kHz, $\omega_z = 2\pi \times 4$ kHz, $T = 730$ nK ($\bar{n}_r = 0.24$) (which are realistic parameters after adiabatic lowering of the trap) and plot $\delta V/\bar{V}$ versus trap spacing $R$ in Fig. 4.13. We also compare this typical finite temperature case to an ideal zero temperature case, where there are still residual interaction fluctuations due to the finite extent of the atomic wavefunctions.

We see that at the spacing of $R = 3.6$ $\mu$K we used in Sec. 4.3, we estimate a fractional fluctuation of the interaction strength of about 0.15. From the point of

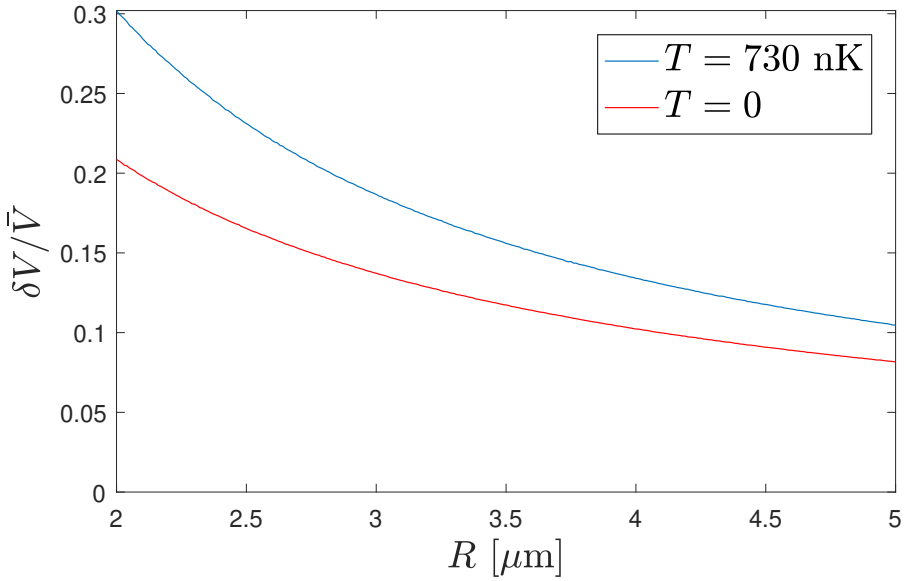


Figure 4.13: Fractional fluctuation of the interaction strength between a pair of atoms initialized in traps separated by $R$ and having radial/axial trap frequencies of $\omega_r = 2\pi \times 25$ kHz and $\omega_z = 2\pi \times 4$ kHz. The traps are separated along a radial axis. The interaction is assumed isotropic with a scaling $V = C_6 R^{-6}$. Atomic positions are sampled independently along three directions from Eq. 4.75. $\delta V$ is the standard deviation of the sampled interaction strengths, while $\bar{V}$ is their mean.

view of interaction fluctuations, it is actually beneficial to use tighter traps before Rydberg excitation so as to localize the atoms better. However, this conflicts with the benefits of using weaker traps in reducing Doppler dephasing, reducing Raman scattering out of the clock state (Sec. 3.2.2), and increasing the available free-flight time when releasing an atom from the trap (Sec. 4.4.2). Finding an optimal trap frequency to use before Rydberg excitation would require a model that takes all of these effects into account, which we leave to future work.

In addition to fluctuations $\delta V$, atomic motion can also cause systematic shifts in the mean interaction strength $\bar{V}$. Depending on trap frequencies and temperature, this shift can be either positive or negative. As an example, for the trap frequencies quoted above, a temperature of $T = 730$ nK, and a trap separation of $R = 3.6$ $\mu$m, we predict $\bar{V} = 0.96 \times V$, where $V$ would be the interaction strength if the atoms were pinned to the trap center. As this systematic shift is also dependent on $R$, it can effectively cause a slight deviation from $V \sim R^{-6}$ scaling.

***Recapture***

In addition to affecting excitation dynamics, motion can prevent recapture of the atom once the trap is re-established at the end of the excitation sequence. In a detection scheme such as ours that maps lack of atomic fluorescence to a Rydberg state, situations where ground state atoms are unsuccessfully recaptured can lead to detection errors*.

Modeling this phenomenon is fairly straightforward in a non-interacting and non-driven regime. For example, one can evolve $\rho_0$ of Eq. 4.73 with the free-space Hamiltonian

$$H = \frac{p^2}{2m} \tag{4.82}$$

$$= \tfrac{1}{4}\hbar\omega(2a^\dagger a - a^2 - a^{\dagger 2}) \tag{4.83}$$

We note that this Hamiltonian only has matrix elements between harmonic oscillator eigenstates of equal parity $P = (-1)^n$.

In the position basis, one can use the free-space propagator to obtain

$$\psi(x,t) = \sqrt{\frac{m}{2\pi i\hbar t}} \int \psi(x',0) e^{-\frac{m(x-x')^2}{2i\hbar t}} dx' \tag{4.84}$$

After simulating the quantum dynamics, the recapture probability can then be calculated by projecting the final state onto the subspace of bound states of the trap (which can be modeled by, e.g., Eq. 2.15).

Classical evolution combined with Monte Carlo sampling of the initial state (using, e.g., Eqs. 4.75 & 4.77) is also a viable approach [36, 125, 126, 128].

The probability of successfully recapturing an atom typically is very close to 1 for short release times and then begins to more rapidly drop beyond some time and with some rate that depend on the temperature $T$ (so an exponential decay is *not* a proper model). Performing adiabatic cooling by slowly lowering the trap depth (Eq. 4.1) before fully extinguishing the trap is beneficial to increasing the recapture timescale. Note also that, for a tweezer geometry, the recapture timescale is mostly sensitive to motion along the radial directions and is only weakly sensitive to axial motion [36].

*Although this phenomenon is technically a SPAM error, we separate its discussion from that of App. E since this is not an error that simply occurs during measurement, but one that depends on the dynamics during excitation.

In Fig. 4.14, we plot a numerically simulated release and recapture curve for a 2D isotropic Gaussian tweezer with trap depth $U_0 = k_B \times 50\ \mu$K, trap frequency $\omega = 2\pi \times 25$ kHz, and temperature $T = 730$ nK ($\bar{n} = 0.24$), which are the typical parameters we have along the radial directions in our traps after adiabatic lowering and immediately before release. We see that in this case, it should be possible to have practically 100% recapture probability for release periods of up to 20 $\mu$s. We also compare this to an ideal $T = 0$ case.

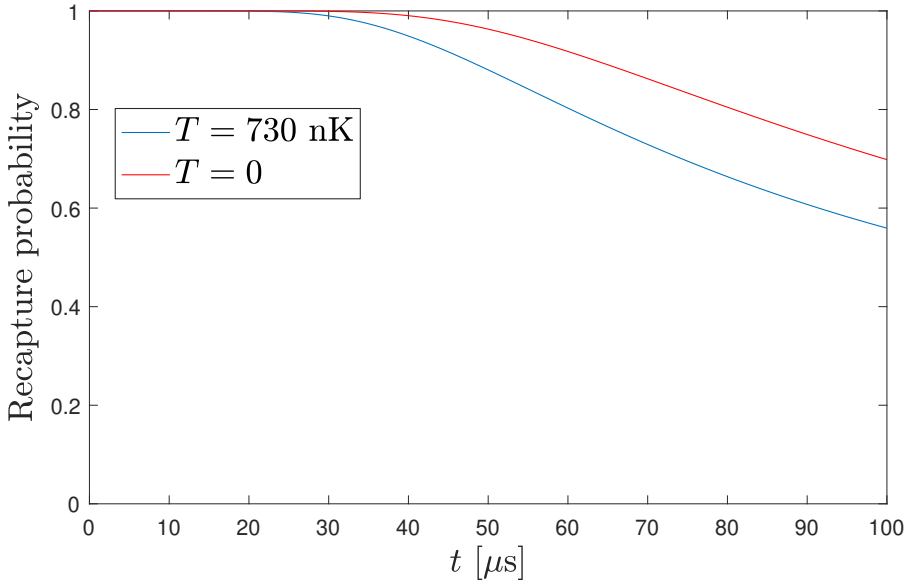


Figure 4.14: Simulated recapture probability as a function of free-flight time for a 2D isotropic Gaussian tweezer with trap depth $U_0 = k_B \times 50\ \mu$K and trap frequency $\omega = 2\pi \times 25$ kHz. The simulation is performed by evolving an initial thermal density matrix in the harmonic oscillator basis (Eq. 4.73) by the Hamiltonian of Eq. 4.83. The final state is projected onto the subspace of bound states of the Gaussian trap to obtain the recapture probability. It suffices to perform the simulation in 1D, and then to weigh each 1D bound state (indexed by $n \in \{0, 1, 2, \dots\}$) by the 2D density of states factor $n + 1$.

We leave a discussion of driven and interacting regimes to future work.

### 4.4.3 Technical noise

We finally discuss errors arising due to non-intrinsic factors — specifically, from technical noise such as intensity and frequency noise. How noise affects dynamics depends both on the magnitude and the spectrum of the noise, where spectrum refers to how the noise is spread in the frequency domain. For example, certain dynamical processes may have resonances at certain frequencies, or may be sensitive to noise in certain frequency bands more than others. For this reason, it is often necessary to not only specify a level of noise, but also to measure its power spectral density $S_x(f)$, where $x$ represents the noise variable.

Sometimes, it is also useful to roughly distinguish between shot-to-shot (slow) and fast noise, where the shot-to-shot noise is effectively static during an excitation period, but fluctuates significantly between excitation periods, while fast noise fluctuates significantly within an excitation period.

Technical noise is often common-mode across an atomic array. Common-mode noise that is also shot-to-shot may produce Rabi/Ramsey oscillations that appear dephased when multiple experimental shots are averaged, even though individual shots may show high contrast signals. Such a situation suggests that the apparent dephasing is not due to intrinsic mechanisms, but is an artifact of averaging many experimental shots with different experimental parameters. It is possible to analyze how much of the observed dephasing comes from common-mode correlated noise and how much is due to intrinsic uncorrelated errors by quantifying interatomic correlations in the measured signal (similarly to what is done in Fig. 3.5e). However, we will not delve into this topic further and instead point the reader to Ref. [99] for one possible approach.

We point the reader to Ref. [151] for further discussion on technical noise during Rydberg excitation.

#### *Intensity noise*

Intensity ($I$) noise enters into the Hamiltonian via noise on the Rabi frequency $\Omega$. Since $\Omega \propto \sqrt{I}$, we have

$$\frac{\delta\Omega}{\Omega} = \frac{1}{2}\frac{\delta I}{I} \tag{4.85}$$

The analysis of intensity noise in single-atom Rabi oscillations becomes significantly simplified if we assume that we work with zero detuning, i.e. $\Delta = 0$. In this case,

each excitation pulse can be fully described by a Rabi pulse area $\mathcal{A}$ given by

$$\mathcal{A} = \int_0^t \Omega(t')dt' \tag{4.86}$$

where $t$ is the length of the pulse and $\Omega(t')$ is the time profile of the Rabi frequency including its noise. Note that we assume $\Omega(t')$ to be real and non-negative at all times, i.e. there is no phase noise associated with $\Omega$.

We will now assume that at each pulse length $t$, the pulse area is given by $\mathcal{A}(t) = \Omega_0 t(1+x)$ where $x$ is normally distributed around zero with a standard deviation of $\sigma_x(t)$. We choose to define a standard deviation that is a function of pulse length as the same noise process can produce different fractional deviations of $\mathcal{A}(t)$ at different pulse lengths.

The average excited state population $P_e(t)$ over an ensemble of resonant Rabi drives starting from the ground state will be

$$P_e(t) = \frac{1}{\sigma_x(t)\sqrt{2\pi}} \int_{-\infty}^{\infty} e^{-\frac{x}{2\sigma_x(t)^2}} \sin^2\left(\tfrac{1}{2}\Omega_0 t(1+x)\right)dx \tag{4.87}$$

$$= \frac{1}{2}\left(1 - e^{-\frac{1}{2}\sigma_x(t)^2\Omega_0^2 t^2}\cos(\Omega_0 t)\right) \tag{4.88}$$

If we assume that we have only shot-to-shot intensity noise, then $\sigma_x$ is a constant and not a function of pulse length $t$. Then, Eq. 4.88 predicts a Gaussian decay of the shot-averaged Rabi signal as a function of pulse length $t$. This decay reaches its $1/e$ value after $\mathcal{N} = \frac{\sqrt{2}}{2\pi\sigma_x}$ full oscillation cycles*. We therefore see that shot-to-shot intensity noise producing dephasing that is *scale invariant* with the Rabi frequency. I.e., one cannot get more coherent cycles by using a faster Rabi frequency.

If instead we assume a white noise profile for $\Omega(t')$, then we have $\sigma_x(t) \propto t^{-1/2}$, and Eq. 4.88 predicts decay with a standard exponential profile as a function of $t$.

Unlike for clock excitation, it is difficult to stabilize a Rydberg pulse over the timescale of excitation via an AOM. This is primarily due to the slow sound propagation in the AOM crystal compared to the fast timescales of Rydberg excitation. The situation can be helped by using a small beam that passes as close as possible to the AOM actuator, but it is still difficult to obtain feedback bandwidths greater than a few hundred kHz. We therefore use a sample-and-hold technique that stabilizes the intensity of the beam via a monitor photodiode while the beam is blocked from

*For emphasis, note that $\sigma_x$ is the fractional standard deviation of the *Rabi* pulse area. A similar result is stated for the fractional standard deviation of *intensity* in Ref. [150]

the atoms by a shutter, after which the beam is turned off, the shutter is opened, and the beam is pulsed at the same feedback voltage that was used immediately before turning the beam off. A future setup could benefit from intensity control via an EOM (elctro-optic modulator).

There are also sources of intensity fluctuations that are more difficult to stabilize than overall power fluctuations. These include fluctuations in pointing and beam shape (polarization fluctuations can also create noise in $\Omega$ despite not affecting the intensity). Since our Rydberg beam is also relatively small ($\sim$15–20 $\mu$m waist radius), effective intensity fluctuations can also arise from thermal fluctuations in the atomic position (Sec. 4.4.2), especially along the axial trapping direction.

We finally note that intensity noise also leads to a small amount of noise on $\Delta$ via the probe light shift (Sec. 4.1.4).

#### *Laser phase/frequency noise*

Laser phase/frequency noise has been studied as a significant factor in Rydberg decoherence in recent experiments [117, 119, 151]. Ref. [151] shows that Rabi dephasing is particularly sensitive to phase noise which has a spectral frequency close to the Rabi frequency. Typically, lasers that are actively stabilized have a spectral region of increased phase noise (called a "servo bump") at frequencies just beyond the bandwidth of the lock, usually at a few hundred kHz to $\sim$1 MHz. Therefore, it is important to choose Rabi frequencies significantly far away from the servo bump or to otherwise minimize its magnitude. For example, Ref. [119] uses a cavity filtering scheme to minimize high-frequency phase noise.

#### *Field noise*

Field noise from electric or magnetic field fluctuations produces noise in the detuning $\Delta$ and therefore can be treated similarly to laser frequency noise. We refer to Secs. 4.1.4 & 4.1.4 for a treatment of how these fields produce shifts. For interacting regimes, fluctuations in the electric field can also cause significant fluctuations in the interaction strength (Sec. 4.2.2).

## 4.5 Summary of $n$ scaling

We summarize several important scaling laws of Rydberg state properties in Table. 4.5. Similar tables are given in Refs. [199, 228].

| Quantity | Symbol | $n^\star$ scaling exponent |
|---|---|---|
| Energy | $\mathscr{E}$ | -2 |
| Energy spacing | $\mathscr{E}_{n+1} - \mathscr{E}_n$ | -3 |
| Mean radial coordinate | $\langle r \rangle$ | 2 |
| Rydberg-Rydberg RDME | $\langle n(l \pm 1)\|\|d\|\|nl \rangle$ | 2 |
| Ground-Rydberg RDME | $\langle n\|\|d\|\|g \rangle$ | -3/2 |
| Spontaneous decay rate | $\Gamma_s$ | -3 |
| BBR transition rate | $\Gamma_{\mathrm{BBR}}$ | -2 |
| Auto-ionization rate of 5p$n$s | $\Gamma_A$ | -3 |
| DC electric shift | $\alpha$ | 7 |
| Diamagnetic shift | $b$ | 4 |
| Short-range interaction | $C_6$ | 11 |
| Long-range interaction | $C_5$ | 8 |
| Blockade radius (for $C_6$) | $R_B$ | 25/12 |

Table 4.5: Scaling of various properties of Rydberg states with effective principal quantum number $n^\star$ (Eq. 4.2).

# Chapter 5

# OUTLOOKS

We thus conclude the presentation of our new experimental platform, having described its key conceptual principles and its performance in single-atom physics, metrology, and Rydberg entanglement. We now turn to future applications and improvements of this platform.

We divide potential future work into three fronts: (1) novelty, which is the implementation or exploration of new concepts, (2) quantity, which means increasing the number of atoms that we can work with and/or the dimensionality of our system, and (3) quality, which broadly refers to both quantifying and reducing the errors in coherent operations as well as in state preparation and measurement.

## 5.1 Novelty

### 5.1.1 Quantum simulation

The dimension of the Hilbert space that the Hamiltonian of Eq. 4.38 acts on is $2^N$, where $N$ is the number of atoms. The exact diagonalization of such Hamiltonians via classical computation thus requires time and memory scaling exponentially with $N$, and is already highly computationally demanding for as low as $N \sim 15$. Therefore, having access to a real quantum system that can execute the Hamiltonian of Eq. 4.38 could allow for the exploration of its otherwise inaccessible physics*. This is the general idea of *quantum simulation* with Rydberg atom arrays [73, 74, 76–78, 188, 231].

*Here we assume standard numerical diagonalization and that no "tricks" are played, such as exploiting symmetries, eliminating energetically inaccessible subspaces, or using ansatz approximations. More broadly, the existence of classical algorithms for the efficient simulation of quantum systems is a deep question far beyond the scope of this work.

One of the more convenient aspects of atom arrays as platforms for quantum science is the ease with which their system sizes and geometries can be reconfigured [46, 48, 53, 74]. In Sec. 4.3, we observed interactions and entanglement between pairs of atoms. However, with only a change in the programming of the AWG rearrangement waveforms, we can easily begin to observe quantum dynamics in systems of three atoms, four atoms, etc., up to as many atoms as we can trap.

Here, we will show preliminary data on such few-to-many-body simulation performed by our experiment. As a slow start, we simply go from two to three atoms in a regime where only nearest-neighbors are blockaded. The 3-atom case is instructive to look at as it is large enough to have rich dynamics but small enough to be easily classically simulated and small enough such that the probability of observing each individual bitstring can be meaningfully tracked as a function of time.

We begin such an experiment by preparing atoms in the ground state of our Rydberg qubit (Fig. 4.1) and applying a global drive that quenches the system to a particular point in the parameter space of the Rydberg array Hamiltonian (Eq. 4.38). At the end of the evolution, we perform auto-ionization and fluorescence imaging for state detection, which gives us a particular bitstring as an output. The probability of observing each bitstring in the 3-atom case is shown as a function of quench time in Fig. 5.1, with the Hamiltonian parameters described in the figure caption.

We can just as easily expand to 5-atom systems. Here, there are already $2^5 = 32$ possible bitstrings (although some of them are almost never accessed due to the blockade restriction), so we instead look at the average magnetization $\langle \sigma^z \rangle$. We look at this both averaged over the entire system and on an atom-resolved basis in Fig. 5.2.

This class of Hamiltonians — where nearest neighbors are deeply blockaded — realizes a 1D hard-boson model described in Ref. [232], sometimes called the Fendley-Sengupta-Sachdev model. This model has a rich quantum phase diagram (over the parameter space of $V/\Omega$ and $\Delta/\Omega$) containing several phases, critical points, and first- and second-order phase transitions.

A particularly interesting region of this phase diagram is an integrable line, where quench dynamics can be mapped onto the dynamics of free fermions. When quenching to this line from an initial $\sigma^z = -1$ state, one expects to see light-cone spreading of correlations throughout the entire system. For large systems, such correlation spreading is an important test of the many-body coherence of the system. We show

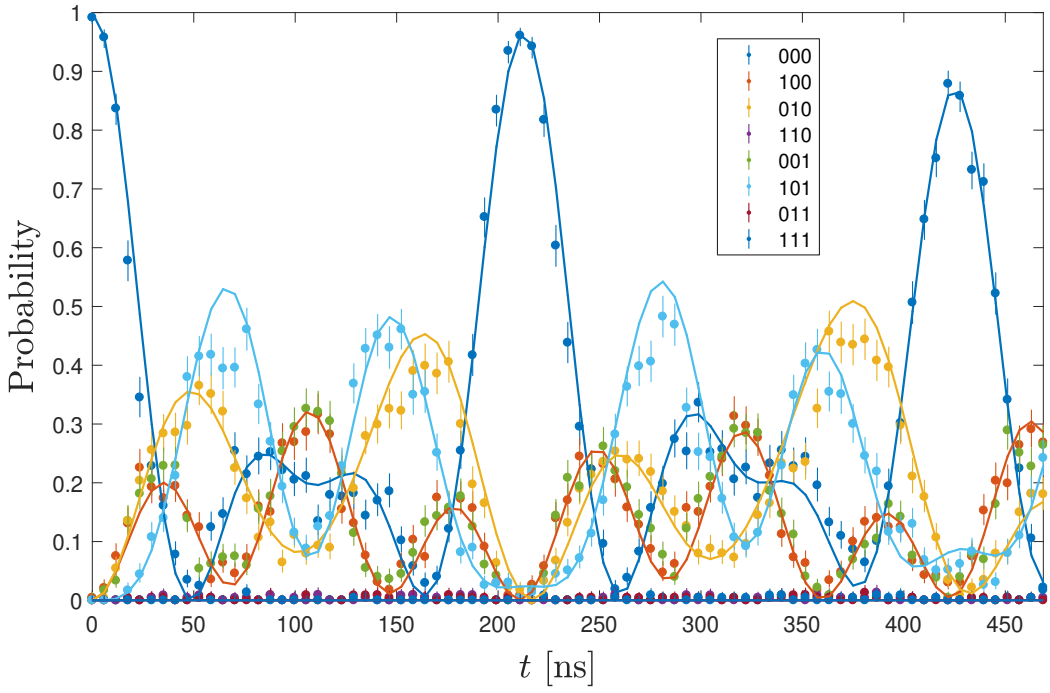


Figure 5.1: Evolution of bitstring probabilities in a 1D equally-spaced 3-atom system. The Hamiltonian is given in Eq. 4.38, having parameters $\Omega = 2\pi \times 6.4$ MHz and $\Delta = 0$. Nearest-neighbors are deeply blockaded, while next-nearest-neighbors have an interaction strength of $V_{nnn} = 2\pi \times 2.3$ MHz. Solid lines are comparison to classical simulation. Data is averaged over several independent 3-atom systems and over many experimental shots.

a preliminary measurement of such correlation spreading in a system of 17 atoms in Fig. 5.3. Here, the experimental procedure is nearly identical to that described for the 3- and 5-atom cases, except we quench to different Hamiltonian parameters (described in the caption of Fig. 5.3).

Some other related outlooks that we will only mention in passing here include topics such as quantum simulation in 2D [234], lattice gauge theories [235, 236], conformal field theories [237, 238], confinement [233, 239], and thermalization [240].

### 5.1.2 Quantum gates

The physical principles and technical challenges of quantum computation are similar to those of quantum simulation in that one attempts to exploit the exponential scaling of a Hilbert space in order to solve classically inaccessible problems. However, quantum computing refers to a broader paradigm where one attempts to implement

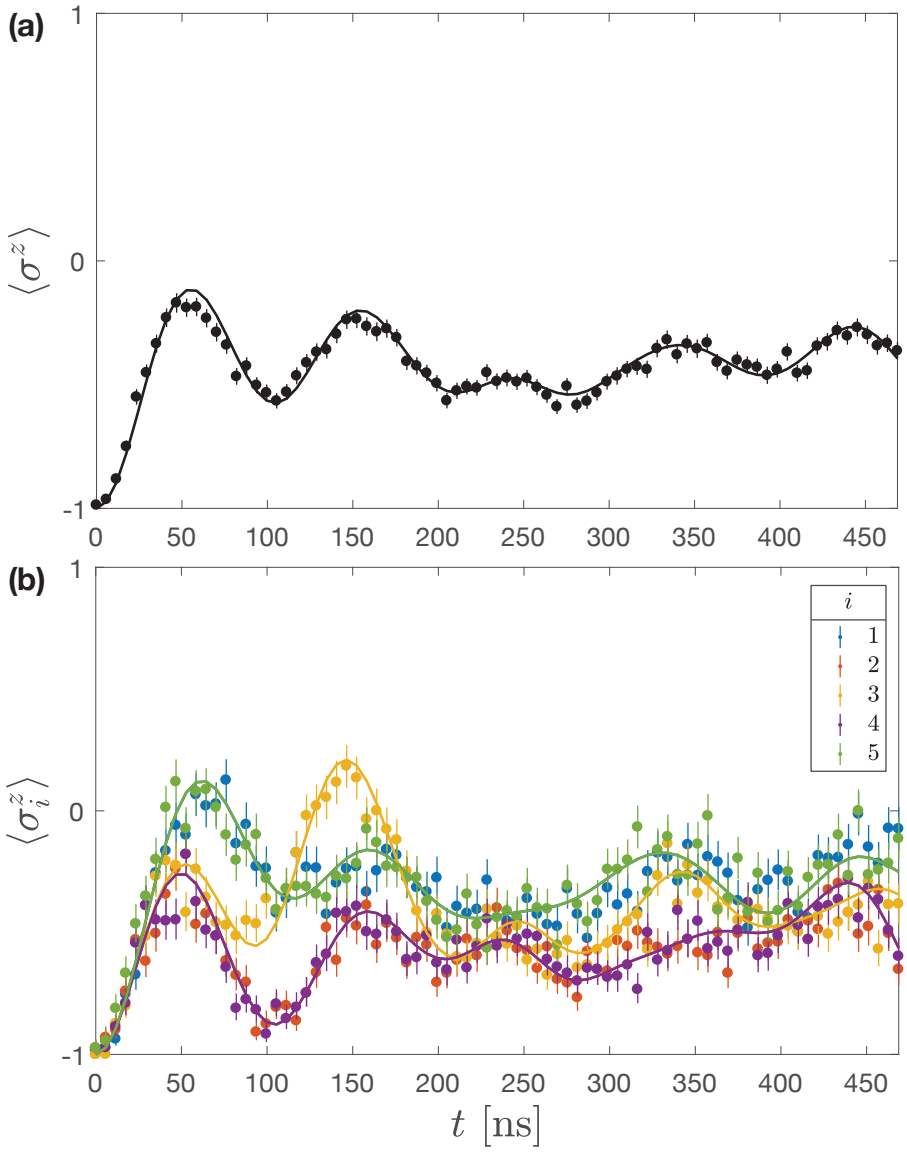


Figure 5.2: Evolution of average magnetization $\langle\sigma^z\rangle$ in a 1D equally-spaced 5-atom system. **(a)** is averaged over the whole system, while **(b)** is atom-resolved. The Hamiltonian is given in Eq. 4.38, having parameters $\Omega = 2\pi \times 6.4$ MHz and $\Delta = 0$. Nearest-neighbors are deeply blockaded, while next-nearest-neighbors have an interaction strength of $V_{nnn} = 2\pi \times 2.3$ MHz. Solid lines are comparison to classical simulation. Data is averaged over several independent 5-atom systems and over many experimental shots.

a generic unitary over a set of qubits, with no regard as to whether such a unitary simulates any particular physical model. The implementation of such unitaries in quantum computation is typically done via operations (also known as gates) on particular qubits or sets of qubits, instead of with a global drive as is common in

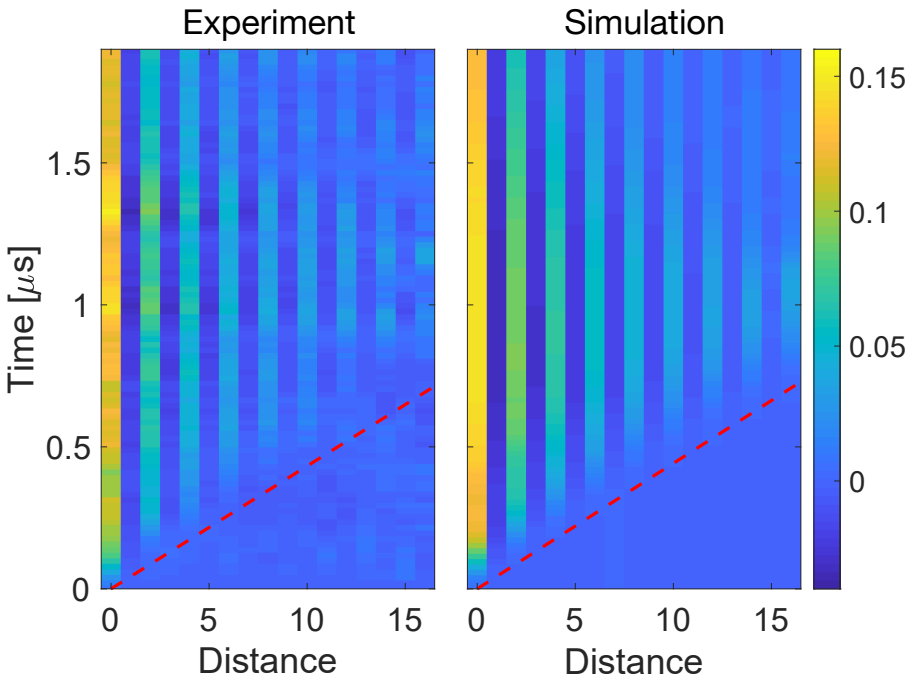


Figure 5.3: Averaged correlator $\frac{1}{4}\left(\langle\sigma_i^z\sigma_{i+d}^z\rangle - \langle\sigma_i^z\rangle\langle\sigma_{i+d}^z\rangle\right)$ as a function of distance $d$ and averaged over all 17 atoms $i$. The Hamiltonian is given in Eq. 4.38, having parameters $\Omega = 2\pi\times 0.9$ MHz and $\Delta = 2\pi\times 2.2$ MHz. Nearest-neighbors are deeply blockaded, while next-nearest-neighbors have an interaction strength of $V_{nnn} = 2\pi\times 2.3$ MHz. We compare experimental results on the left with simulated results on the right. The red dashed line is $d = 4\Omega t$, which is the expected speed of correlation spreading [233] in the nearest-neighbor blockaded regime.

quantum simulation.

It can be shown that any many-qubit unitary can be decomposed into a product of two-qubit gates [5]. It can furthermore be shown that any two-qubit unitary can be arbitrarily approximated by a finite set of single- and two-qubit gates [5]. Such a set of gates that can be used to approximate any two-qubit unitary is known as a *universal* quantum gate set.

In the context of Rydberg atom arrays, the ground to Rydberg qubit that we used in Chap. 4 is not amenable to being used as a qubit for quantum computation. The main reason for this is that interactions between atoms in the Rydberg state are always present (though it is possible that interactions can be at least globally attenuated, see Sec. 4.2.2) which interferes with the ability to perform single-qubit gates. For quantum computing, one would therefore like to define a qubit between two non-interacting states and to use Rydberg states only as auxiliary states for implementing

two-qubit gates. Such schemes have been demonstrated between hyperfine ground states in alkali Rydberg arrays [193, 241].

In strontium, there is no hyperfine structure in the absolute ground state, so a different choice of qubit would be necessary. Our explorations of coherent operations on the clock transition $5s^2\ {}^1S_0 \leftrightarrow 5s5p\ {}^3P_0$ in Sec. 3.2 foreshadow our intentions to use this transition as a qubit, with Rydberg excitation from the clock state allowing for two-qubit gates. Different qubit schemes may also be possible, such as between the two metastable states $5s5p\ {}^3P_{0,2}$, and in the fermionic species between hyperfine levels of $5s5p\ {}^3P_2$ or between nuclear magnetic sub-levels of the absolute ground state [81].

### 5.1.3 Spin-squeezed clock

As discussed in Sec. 3.3.1, quantum projection noise (QPN) is a fundamental source of noise in atomic clocks and scales as $1/\sqrt{N}$ for uncorrelated atoms, with $N$ the number of atoms. However, this scaling may no longer be valid when there are correlations between atoms. In particular, there exist entangled many-atom quantum states known as *spin-squeezed states* for which QPN can scale more favorably with $N$, up to as fast as the so-called Heisenberg limit of $1/N$. Spin-squeezed states have been demonstrated in numerous systems (including the particularly relevant case of ytterbium [61]), a summary of which is given in Ref. [17]. For clocks where QPN is a significant source of noise (and it is important to note that this may *not* be the case for various systems, see discussion in Ref. [156]), using spin-squeezed states can produce gains in precision.

Our platform is in a very natural position to attempt a spin-squeezed clock as we have shown both clock operation (Sec. 3.4) and Rydberg entanglement from the clock state (Sec. 4.3). Proposals for producing spin-squeezed states with Rydberg-dressed interactions are given in Refs. [16, 170]. Generally, one uses an off-resonant Rydberg beam to create a Rydberg state admixture in the clock state in order to generate long-range interactions for clock state atoms.

One technical challenge that will have to be overcome is controlling the light shift of the Rydberg beam on the clock transition, which is likely to fluctuate and thus cause dephasing. A possible solution is to choose the detuning of the Rydberg beam to be at a magic wavelength for the ground and clock state, such that the light shift vanishes. However, this puts a constraint on what Rydberg detuning can be used,

and therefore also puts a constraint on the strength of the dressed interactions that can be achieved. For the magic wavelengths that we have predicted, it is not clear whether the achievable interaction strengths will be sufficiently large for effective spin squeezing. We leave further exploration to future work.

## 5.2 Quantity

Future work on our experiment will benefit greatly from an increase in system size (i.e., the number of atoms). For example, larger system sizes allow for many-body quantum evolution that is increasingly outside of the reach of classical computation.

A major limit to the number of atoms that we can work with is the available laser power of our trapping laser. This problem is exacerbated by the relatively weak polarizability of our trapping wavelength 813.4 nm (Sec. 2.3.4). In particular, traps of several hundred $\mu$K are currently needed for cooling and imaging (and potentially for suppressing thermal dephasing on the clock transition, see Sec. 3.2.1). Barring any loosening of these requirements (such as by imaging with a lower scattering rate, even potentially on the red transition, see Sec. 2.6.8), the available power from our trapping laser (App. A.4.5) currently limits us to ~100 traps, half of which are typically filled with an atom (Sec. 2.4.2). We will discuss several possible approaches for increasing this limit.

The first approach is a technical upgrade to our microscope objectives to increase both their NA and their transmission at our trapping wavelength. This project is already underway and is described further in App. A.3.1.

Another approach is to augment the trap geometry to add additional confinement. One possibility here is to add an auxiliary lattice on top of the tweezers as is done in Ref. [99]. Another possibility is to retro-reflect the tweezers back through the second objective to create a lattice in the axial direction [242], which should increase its confinement significantly.

It is also possible to use entirely different wavelengths where either the polarizability is higher, more power is available, or both. Ref. [99] shows that atoms may be cooled and imaged in 515 nm and then transferred to an 813 nm traps for clock interrogation. However, loss during cooling and imaging at 515 nm is still a problem here (Sec. 2.6.8). 1064 nm is a potentially interesting wavelength due to the very large power available, despite its even lower polarizability and larger diffraction-limited waist than 813 nm (see Sec. 2.3.4).

The enhanced loading schemes discussed in Sec. 2.4.3 constitute another interesting approach, in this case to increase the number of single-atoms that fill the traps instead of increasing the number of traps.

Finally, there is the possibility of combining light from multiple lasers. An exploration of this possibility is detailed in Ref. [151].

Going to higher dimensions (2D or 3D) is eventually also necessary, as there is a limit to the number of atoms in a line that can be fit into the field-of-view of a microscope objective. Higher dimensionality would also allow for greater qubit connectivity and for quantum simulation of a wider array of phenomena [234]. While we have already demonstrated $11 \times 11$ arrays at 515 nm using crossed AODs (Sec. 2.7.1), a more robust approach to higher dimensions would be to use spatial light modulators (SLMs) [46, 53, 243]. The benefit of SLMs is in their ability to produce arbitrary geometries with a high degree of intensity uniformity [135]. See Ref. [136] for further discussion of SLM-related efforts for our experiment.

## 5.3 Quality

Increasing system size begins to have diminishing returns if one is unable to maintain a high degree of control or fidelity over the entire system. As a concrete example, we showed in Sec. 2.7.3 how the probability of successfully rearranging an array decays exponentially with system size. For experiments on many-body quantum states or for quantum computation, a similar trend applies because an error on a single qubit can ruin the entire many-body state. This is the general difficulty of quantum systems: their computational power increases exponentially with system size, but so does their error rate (at least, without some kind of error correction, though this also has stringent requirements on fidelities [5]). Therefore, the future of this experiment (and of all quantum platforms) cannot be only a dash towards novelty and quantity, but must include an effort on the front of quality as well.

In the context of many-body quantum physics, a major challenge is quantifying how close the experimental quantum state is to the state which one would have assuming no errors (i.e. the desired state). Mathematically, this is expressed as the state overlap $\langle\psi|\rho|\psi\rangle$, where $\rho$ is the experimentally realized many-body density matrix and $\psi$ is the desired pure many-body quantum state. However, actually measuring this overlap requires full state tomography which is generally not feasible for many-body states. Instead, we are working toward the estimation of many-body state overlap

via *cross-entropy benchmarking* [10]. This involves comparing a histogram of the experimentally measured bitstrings with the histogram of the desired quantum state's bitstrings. Such histograms are expected to exhibit a *speckle pattern* for coherent quantum states that are sufficiently scrambled in the computational basis. The degree to which the speckle patterns of the experimental and desired quantum states agree can be used to quantify the state overlap.

In addition to quantifying the overlap between our measured and desired quantum states, we are working on a fully integrated numerical model that simulates the effect of all expected noise and error effects (such models were already partially utilized in Refs. [138, 150]). Such a model is crucial to understanding which effects are actually limiting, quantifying their individual error contributions, and predicting how much can be gained by improving them. To this end, we will now summarize the major potential sources of error and infidelity that we have discussed in this work (for both clock and Rydberg excitation), which can be generally divided into errors of preparation, dynamics, and measurement. Preparation and measurement errors are also discussed in the context of Rydberg excitation in App. E.

Possible sources of preparation error include:

- Imaging infidelity (Sec. 2.6.7)
- Imaging loss (Sec. 2.6.7)
- State transfer infidelity (Sec. 4.1.1)

Possible sources of dynamics error include:

- Decay and blackbody radiation (Sec. 4.4.1)
- Thermal and motional effects (Sec. 3.2.1, Sec. 4.4.2)
- Trap scattering (Sec. 3.2.2)
- Laser phase/frequency noise (Sec. 3.2.3, Sec. 4.4.3)
- Laser intensity noise (Sec. 3.2.3, Sec. 4.4.3)
- Field noise (Sec. 3.2.3, Sec. 4.4.3)
- Vacuum collisions (Sec. 2.6.8)

Possible sources of measurement error include:

- State-shelving infidelity (Sec. 3.1.3, Sec. 4.1.3)
- Imaging infidelity (Sec. 2.6.7)

Although this work has demonstrated various state-of-the-art results with regards to, e.g., imaging fidelities, Rydberg detection fidelities, and entanglement fidelities, future work in understanding and taming the various effects listed above is still crucial if our platform is to realize its full potential.

# Appendix A

# THE APPARATUS

In this appendix, we describe the physical aspects of the experimental apparatus that was used to obtain the data presented in this work. A more concise summary of the key elements was already given in Sec. 1.3. We also point the reader to Ref. [79] for more information on this topic from the earlier stages of the experiment's build.

## A.1 Experimental chamber

Our experimental chamber is composed of three ultra-high vacuum sections: an atom source, a glass cell where all "science" is done, and an intermediate pumping section that joins them. Rendered representations of the chamber are shown in Figs. A.1 & A.2.

One highly useful feature of this experiment is that the entire chamber rests on top of a linear translation stage (LinTech 251242). This allows us to move the glass cell out of its operational position for, e.g., beam alignment, access to the objectives, and other maintenance procedures. The chamber can then be reproducibly moved back in for experimental operation.

### A.1.1 Atom source

The atom source section of our chamber (everything from left to right up to and including the gate valve in Fig. A.2) is an AOSense Beam II strontium atomic beam source. This package includes an oven, Zeeman slower, two 2D MOTs, a small ion pump (Gamma TiTan 3S), two non-evaporable getters (NEGs) (SAES), an angle valve, and a gate valve. This entire package was delivered to us already baked and under ultra-high vacuum.

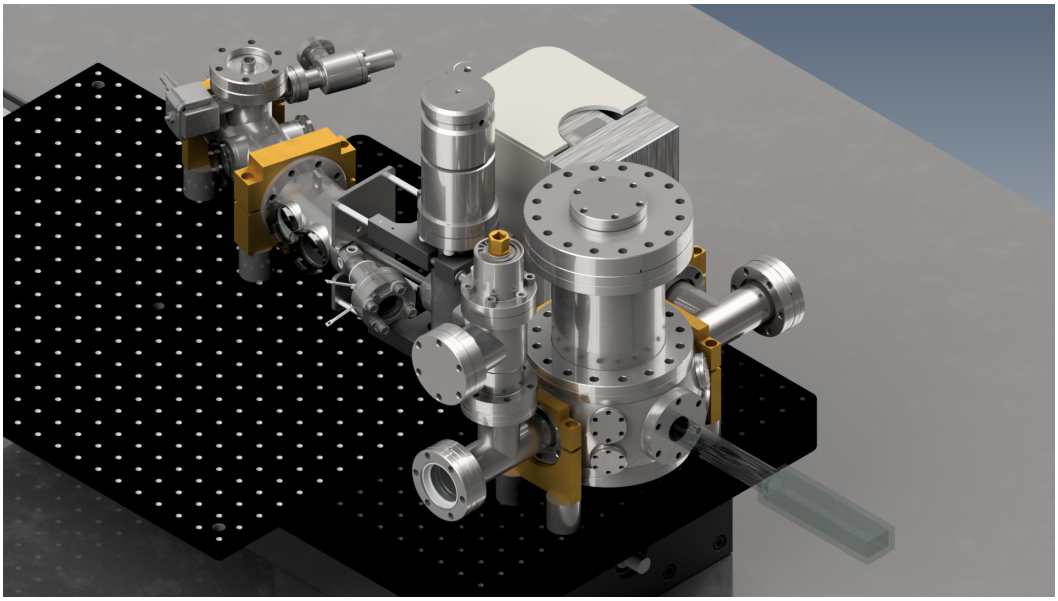

Figure A.1: Rendered representation of our experimental chamber. An atom source (rear) generates an atomic beam that passes through the pumping section (middle) and eventually reaches the glass cell (front). These stages are in turn mounted onto a monolithic 1.5 in thick vertical aluminum breadboard. The entire chamber rests on a 2-inch thick aluminum breadboard which is in turn secured to a large linear translation stage that allows us to move the chamber back from its operational position. A 1/2-inch aluminum breadboard also rests on top of the 2-inch breadboard, allowing for sufficient space for the optics necessary for the atom source.

Atoms originate from a sample of solid strontium in the oven, which can have a mass up to 3.5 g. Upon heating, atoms vaporize and are collimated into an atomic beam via a capillary array. We typically run our oven at a modest temperature of 420 °C, for which AOSense quotes an atomic flux of $3.3 \times 10^{12}$ atoms/s. For an atomic sample of 3.5 g under this temperature, we estimate that the sample will not run out for 230 years. The oven temperature can be pushed to at least as high as 520 °C, where the flux is quoted to rise to $6.9 \times 10^{13}$ atoms/s. However, note that only about $1/100^{\text{th}}$ of the atomic flux out of the oven actually ends up as a useful cold atomic beam (see below).

The atomic beam then passes through a Zeeman slower (see Ref. [21] Sec. 6.2.2). This reduces the velocity of a fraction of the atomic beam to speeds that can be more easily captured by a magneto-optical trap (MOT). All of the necessary magnetic gradients for this slower are internally generated by permanent magnets, which are surrounded by magnetic shielding. An anti-reflection coated window along the atomic beam axis (Fig. A.2) allows for illumination by a blue slowing beam. This

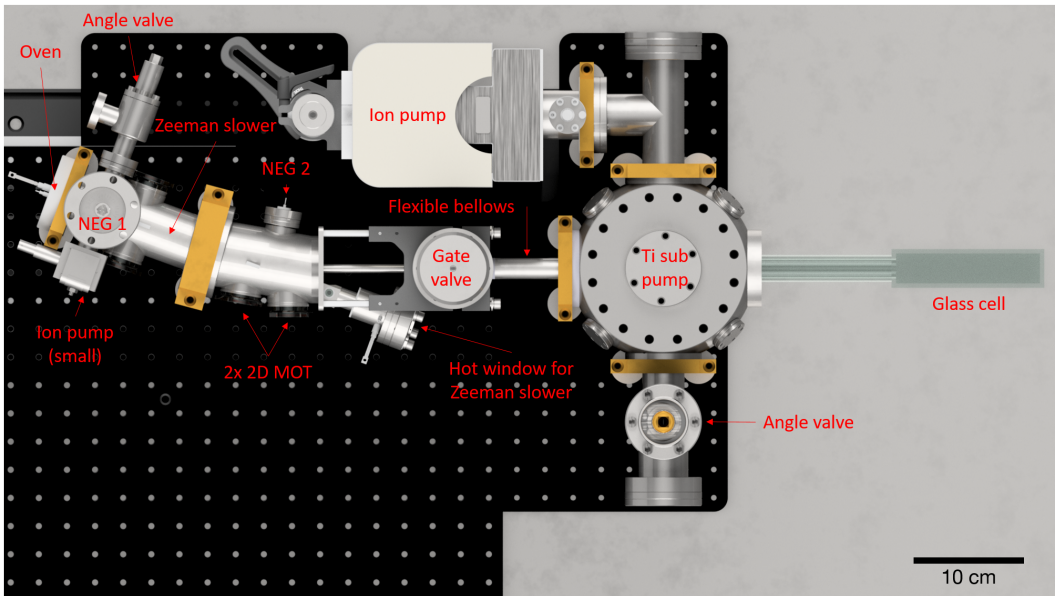


Figure A.2: Top view rendered representation of our chamber with labels of key components.

window also has in-vacuum heating such as to prevent a film of strontium of forming on it. We typically keep this window at 380 °C.

After the Zeeman slower, the atomic beam enters two back-to-back 2D MOTs. These not only cool the atomic beam in the transverse direction, but also serve the very useful function of *angling* the cold atomic beam away from its initial direction of propagation. This effectively separates colder strontium atoms from hotter ones (in particular, ones that were not sufficiently decelerated by the Zeeman slower) as well as from any hot background gas beam (of, e.g., $H_2$) produced by the oven. Therefore, only colder strontium atoms are sent toward the science section of our chamber (i.e. the glass cell) and flux from hot atoms or hot background gases is suppressed. This is likely to play a positive role in achieving good vacuum in the glass cell. Furthermore, since there is no direct line-of-sight from the glass cell to the oven, blackbody radiation from the oven is likely suppressed. Finally, the 2D MOTs act as a convenient and fast optical switch for turning the atomic flux to our glass cell on and off, requiring no mechanical shutters.

All retro-reflection/polarization optics necessary for the 2D MOTs are internally contained — we only provide two elliptical beams as input. All necessary magnetic fields are internally generated by permanent magnets. Since in our chamber design we place a large ion pump (containing its own large permanent magnet) close to the

location of the 2D MOTs, we wrap the 2D MOT section of the atom source with a few layers of magnetic shielding material.

Finally, the cold atomic beam that is angled toward the glass cell passes through a differential pumping channel of length 101.6 mm (4 in) and inner diameter 6.2 mm, which restricts the vacuum conductance between the atom source and the rest of the chamber.

The atom source can be completely sealed away from the rest of the chamber by closing a gate valve after the differential pumping channel.

### A.1.2 Glass cell and surrounding assembly

At the end of the path of the cold atomic beam is our glass cell. This is where we perform practically all experimentation, including 3D MOTs (blue and red), tweezer trapping, single-atom imaging, clock and Rydberg excitation, etc.

Figure. A.3 shows a rendering of the glass cell and some key surrounding components. Two microscope objectives (App. A.3), used for single-atom imaging and tweezer generation, are mounted above and below the cell. An assembly of four pairs of magnetic coils (App. A.2) surround the cell and the objectives. An actual picture of this assembly (minus the objectives) is shown in Fig. A.6.

The cell itself is made of optically contacted quartz and is manufactured by Japan Cell. It is AR coated only on the outside bottom surface for 461 nm–915 nm. A glass-to-metal transition of approximate length 13 cm and inner diameter 1.8 cm joins the science section of the cell to a 2-3/4" fixed CF flange. The dimensions of the glass cell (without the transition section) are summarized in Fig. A.4.

The assembly around the glass cell is designed to allow for a large amount of optical access. For example, the coil shapes are chosen to be in either an elliptical or diamond shape and their mounts have strategically placed cuts to maximize accessible angles. In the horizontal plane, the assembly is designed to allow for at least a 60° beam angle from normal incidence (this is quoted as an angle at the position of the atoms, i.e., taking into account refraction due to the glass). In the vertical plane (containing the objective axis and the direction normal to the atom beam propagation), the possible angle ranges up to 33.7° from normal (again taking into account refraction), which is limited by the dimensions of the glass cell. While we do not currently use the full extent of such angles, they allow for future flexibility in, e.g., creating optical lattices.

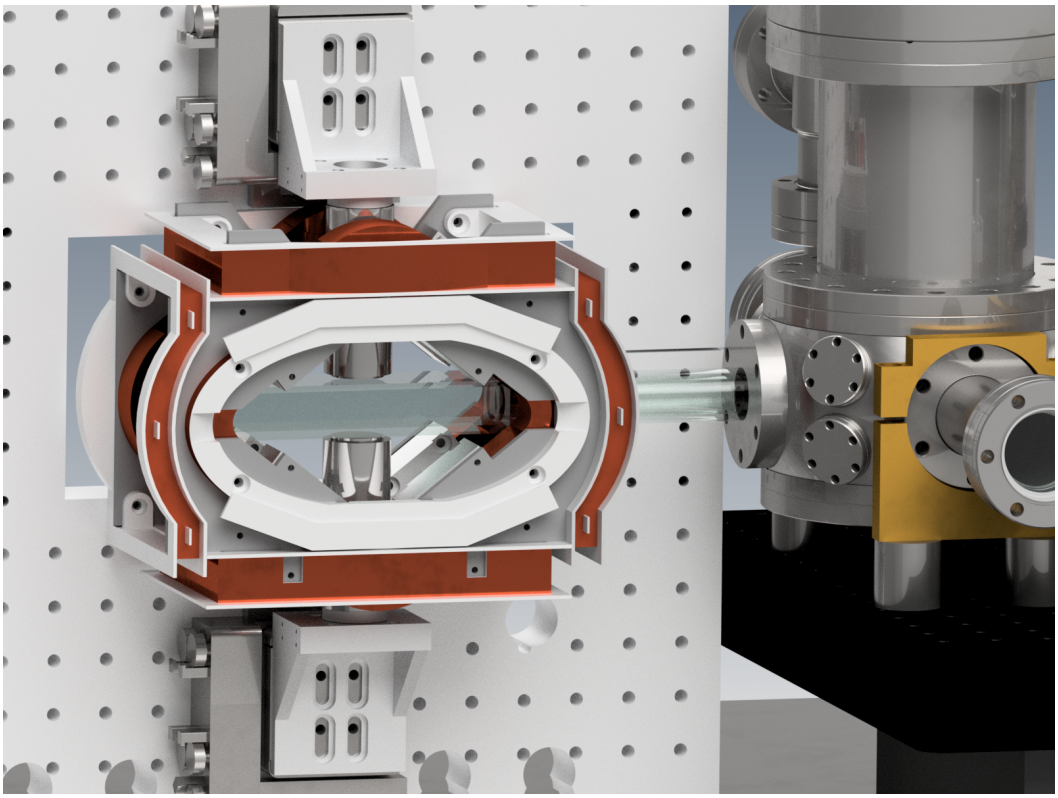

Figure A.3: Rendered representation of our glass cell with surrounding components. Two objectives (App. A.3) are mounted above and below the cell, both on independent 5-axis picomotor stages. Four pairs of magnetic coils, one high-field pair (App. A.2.2) and three low-field pairs (App. A.2.4) surround the glass cell. The low-field coils are held in place by 3D-printed plastic spools, and are represented in this rendition as copper textures on the surfaces of the white plastic spools. However, in reality these coils have finite thickness (See Fig. A.6).

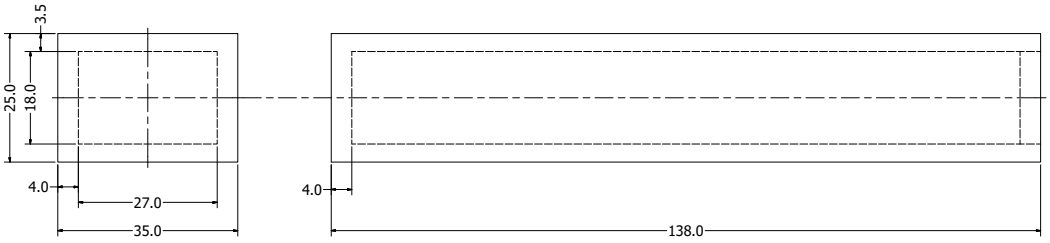


Figure A.4: Dimensions of the glass cell (excluding the glass-to-metal transition and the CF flange). All dimensions in mm. The 3.5 mm thickness windows are the windows through which the microscope objectives are aimed. Not shown: the glass-to-metal transition cylinder that connects the cell to its flange. The approximate dimensions of this cylinder are an inner diameter of 1.8 cm and a length of 13 cm.

### A.1.3 Vacuum

Here we describe how we attain ultra-high vacuum (UHV) in our experimental chamber.

#### *Pumps and gauge measurements*

Our chamber has a total of two ion pumps, two non-evaporable getters (NEGs), and one titanium sublimation (Ti sub) pump. The two ion pumps also act as vacuum gauges and are the only gauges we have installed. In general, ion pumps are expected to perform better at removing inert gases such as $N_2$, while passive pumps such as NEGs and Ti subs are expected to perform better at removing $H_2$ gas. We note that strontium itself is expected to be an effective getter material.

We first describe the pumps in the atom source section of the chamber. One small 3 L/S ion pump (Gamma TiTan 3S) is located very close to the atomic oven (Fig. A.2). Right next to it is a 50 L/s SAES NEG. A bit further down the atom path at the position of the 2D MOT there is another 5 L/s NEG. Both NEGs were delivered to us pre-activated by AOSense.

After the differential pumping channel of the atom source and the flexible bellows connecting it to the rest of the chamber, we have a home-built section of our chamber in between the glass cell and the atom source dedicated to vacuum pumping. This section features a cylindrical section containing Ti sub filaments (Gamma 360819) that can sputter titanium over a surface area of approximately 550 $cm^2$. Connected to this cylindrical section via a right angle is a 75 L/s ion pump (Gamma TiTan 75S CVX). The right angle ensures that titanium will not be sputtered directly into the ion pump, which may damage the ion pump.

We routinely measure pressures of no greater than $1.0 \times 10^{-11}$ Torr with the small ion pump near the atomic oven — which is in fact as low as the pump can measure — even at oven temperatures of 420 °C. With the large ion pump, we routinely measure pressures of $1–3\times10^{-11}$ Torr.

#### *Assembly and bake*

We now describe the procedure by which the chamber was assembled, baked, and pumped down. We performed two bakes: one “pre-bake” of just the stainless steel

parts of our chamber at ~400–450 °C for ~9 days, and a final bake of the fully assembled chamber at ~300 °C for about 20 days.

We first assembled all parts of the intermediate pumping section that were purely stainless steel and blanked off their open ports. Note that we use silver-coated copper gaskets in the vacuum joints to prevent gaskets from becoming stuck to the flanges when components are removed. This intermediate stainless steel assembly was then pumped down with a combination roughing/turbo pump (Pfeiffer HiCube 80 Eco). After pumping down, the assembly (including sections leading up to the turbo pump) was wrapped in a layer of UHV-compatible aluminum foil (for thermal conductivity) and covered with resistive fiberglass insulated heat tape*. Thermocouples were also placed at points of interest along the assembly to monitor the temperature. One more layer of UHV foil was placed on top of the heat tape for conductivity, followed by a layer of fiberglass insulation (meant for car exhausts) and a final layer of UHV foil. After 9 days of this pre-bake at ~400–450 °C, this assembly was brought down to room temperature.

About a month and a half later, all chamber components including the atom source (which came to us already under vacuum and baked), the pre-baked stainless steel sections, the large ion pump, the Ti sub filaments, a couple of monitor viewports, and the glass cell were assembled. Metallic elements were wrapped in a similar way as during the pre-bake, except for the atom source which was already baked and was valved-off from the rest of the setup. Special care was taken for the glass cell, which could not be directly wrapped and furthermore needed a highly uniform temperature profile. We built a custom "bake garage" for the cell that allowed us to wrap heat tape around the cell with about a 1-inch air gap. Three thermocouples were placed inside this garage at different locations to ensure homogeneity of the temperature.

For this final bake, the chamber was pumped down with the turbo pump and the temperature was slowly ramped (ensuring no more than 3 °C/min changes) to about 300 °C, which is a limit imposed by the glass cell†. Before the end of the bake, the large ion pump was turned on to 7 kV in order to degas it while the bake is still on. After the pressure settled again, the ion pump was turned off and each of the three

*As a health precaution, it is advised to use respiratory protection when working with such fiberglass tape to prevent from breathing in fiberglass dust.

†Certain other components had lower limits that we also accommodated locally, such as the ion pump at 250 °C (to avoid demagnetization of its permanent magnets) and 120 °C at the closed gate valve to the atom source.

filaments of the Ti sub were degassed in turn, once at 25 A for 60 s and once at 50 A for 60 s. The ion pump was turned on again, and in a few days this Ti sub degassing procedure was repeated.

After about 20 days of baking, the chamber was slowly brought back down to room temperature. While still pumping with the turbo, one of the Ti sub filaments (the one that was the last to be previously fired) was fired twice at 50 A for 120 s (with the ion pump off) to provide the final layer of titanium for our vacuum, followed by turning the ion pump back on. We have not needed to re-fire the TSP (or make any other adjustments to the vacuum) in over three years of operation.

At this point the valve to the turbo pump was closed, leaving the chamber under its own vacuum. The ion pump was then briefly run at a higher-than-usual voltage of 11.5 kV to remove "whiskers" (metallic deposits on its electrodes that can cause spurious discharges), and then brought back down to 7 kV. Finally, the gate valve to the atom source was opened, completing the vacuum assembly.

At all stages where a turbo pump was used, a residual gas analyzer (SRS RGA100) was also used to analyze the composition of the gases inside the vacuum and to track their individual pressures over time. Such an analysis is useful for detecting certain contaminants such as oils. We also used the RGA multiple times to check for leaks by spraying the outside of the chamber with helium and looking for spikes in helium detection. At the end of the bake, no measurable contaminants or leaks were found by the RGA.

## A.2 Magnetic coils

### A.2.1 Overview

Magnetic fields are important to this experiment for several aspects such as exciting to the clock state, tuning polarizabilities, and tuning the position of the red MOT. We produce magnetic fields by running current through loops of wire (which we will call magnetic coils) placed near our atoms.

The following criteria enter into the design of our magnetic coil system:

1. The ability to produce magnetic fields of $> 500$ G in one direction for obtaining large Rabi frequencies on the clock transition (Sec. 3.1.1).

2. The ability to produce magnetic fields of at least a few Gauss in *all three* directions for, e.g., tuning the position of the red MOT (Sec. 2.4.1), tuning the polarizability of 5s5p $^3P_1$ (Sec. 2.3.4), tuning quantization axes, or compensating for background fields.

3. An acceptable level of uniformity of such fields across typical tweezer array length scales (a few hundred $\mu$m).

4. The ability to produce magnetic quadrupole *gradients* of a few 10's of G/cm for generating MOTs.

5. The ability to stabilize all such fields via feedback.

6. Sufficient thermal stability for all coils.

7. A large degree of optical access around the glass cell.

In this Appendix, we present the coil system which we have designed and built to meet these criteria.

We divide our system into two sets of coils. The first is a pair of water-cooled high-field coils (App. A.2.2) that can produce large fields along one direction and can be switched via an H-bridge (App. A.2.3) to produce gradients. The second is a set of three pairs of smaller, non-cooled low-field coils (App. A.2.4) that can produce small independent fields in all three directions. The mounting and assembly of these coils is pictured in Figs. A.5–A.6.

It will be useful to define three orthogonal axes: the *objective axis* along the axis of the objectives (see Fig. A.3), the *chamber axis* which points along the long dimension of the glass cell toward the vacuum chamber, and the *diamond axis* which is orthogonal to the first two (we call it the diamond axis because the high-field coils are shaped like a diamond, and this is the axis along which they create a large magnetic field).

### A.2.2 High-field coils

Our high-field coils were manufactured by Custom Coils, Inc. Each coil is made of a 4x6 winding of insulated hollow-core copper wire. The cross-section of the conducting part of the wire is a square of side length 0.183 in with a circular hollow core of 0.1 in diameter for water cooling. Including the insulation, the cross-section

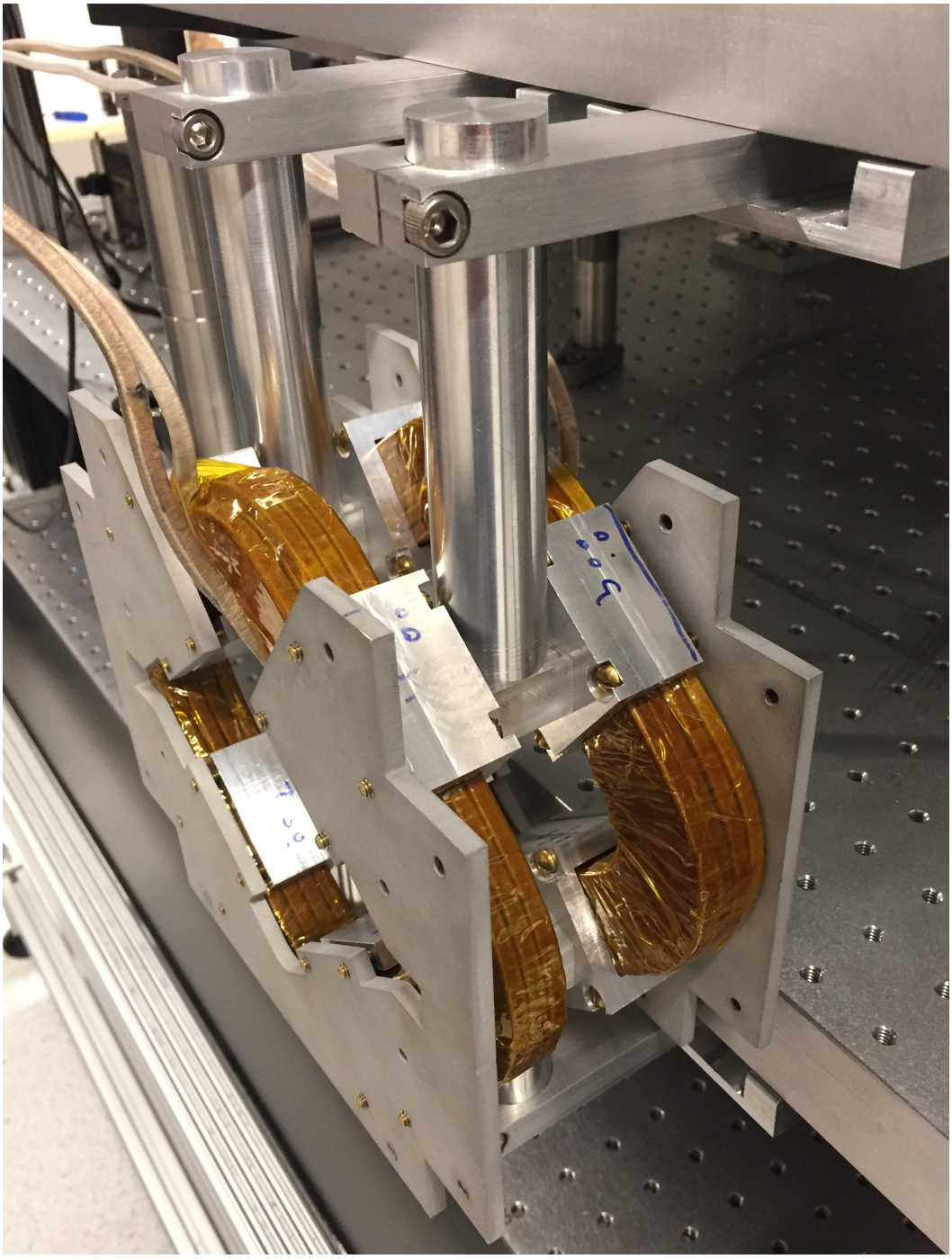

Figure A.5: A picture of our high-field coils and their mount. The mount allows for translation in all three directions as well as for rotation along one axis. Great care is taken that conductive loops near the coil are minimized: note the acrylic spacers bridging the two coils (also note the horizontal cut in the vertical breadboard in Fig. A.3). Furthermore, non-magnetic materials such as aluminum or brass are used for all elements of the mount, including screws.

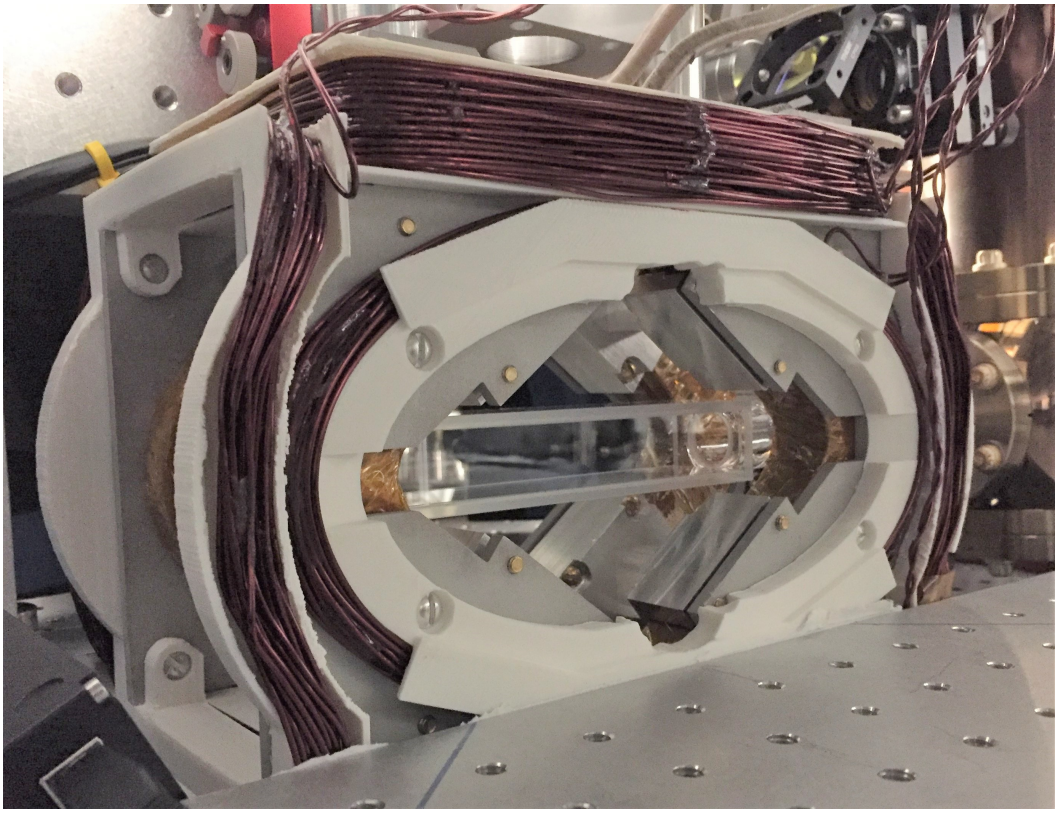

Figure A.6: A picture of our full coil assembly around the glass cell. The high-field coil mount shown in Fig. A.5 also mounts several 3D-printed plastic spools (white) that hold our low-field coils (thin copper wires).

of the wire increases to about 0.2 in square length. We find that we are able to achieve a water flow rate of 8 gallons/hour through each coil (with the water cooling hooked up in parallel) using a differential pressure of about 45 psi.

We chose a rhombus (a.k.a. diamond) shape for the high-field coils as we predicted such a geometry to produce a particularly good combination of high field and optical access. Fig. A.7 shows a drawing of their approximate dimensions. The separation between the nearest opposing faces of the two coils is about 40 mm, allowing for about 2.5 mm of an air gap between the coils and the glass cell on either side (see Fig. A.4).

We drive current through these coils using a Keysight N8732A power supply capable of producing up to 10 V and up to 330 A. We run current through the two coils in series to ensure an equal current in both. At room temperature, we measure a total resistance through both coils of $R = 30$ mOhm and an inductance of $L = 155$ $\mu$H, giving a time constant of $\tau = L/R = 5.2$ ms. Note that the measured $R$ is almost

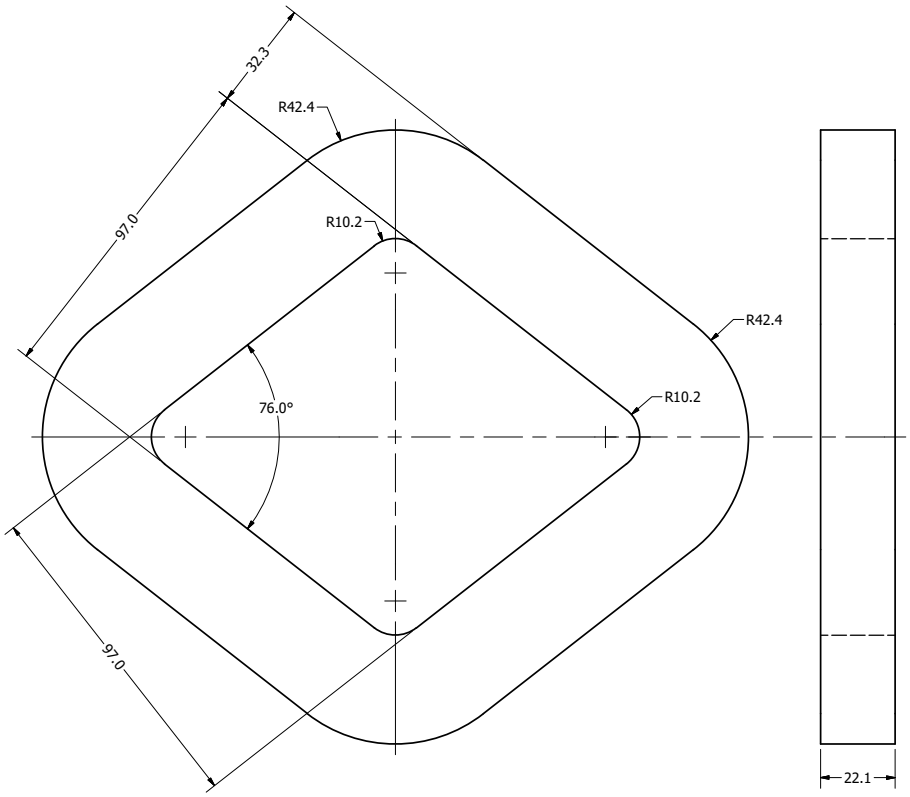


Figure A.7: Approximate dimensions of one of the high-field coils, in mm. The separation between the nearest opposing faces of the pair of coils is about 40 mm (not shown).

exactly equal to the ratio of the max voltage to the max current achievable by the power supply.

When the coils are configured to produce magnetic fields of the same direction/sign (which we will refer to as a Helmholtz configuration), we measure at the center of the coil pair a linear relationship between the current and the field magnitude of 3.2 G/A. With our power supply, this allows us to in principle achieve fields exceeding 1000 G — however, this number will be reduced to about 750 G when we include transistors in series with the coils (App. A.2.3).

When the coils are configured to produce magnetic fields of the opposite direction/sign (which we will refer to as an anti-Helmholtz configuration), the coils produce a quadrupole gradient at their center. Such a quadrupole generically has three principal axes, which in our case are the objective, chamber, and diamond axes (defined at the end of App. A.2.1). The values of the gradients along the three major axes must sum to zero in order to satisfy Gauss's law for magnetism. We summarize

the measured linear scaling of these gradients along with other important values for the high-field coils in Table. A.1.

| Property | Value |
|---|---|
| Resistance ($R$) | 30 mOhm |
| Inductance ($L$) | 155 $\mu$H |
| $\tau = L/R$ | 5.2 ms |
| Number of turns (per coil) | $4 \times 6 = 24$ |
| Wire gauge | 0.183 in SQ, 0.1 in Ø bore |
| Nearest separation | 40 mm |
| Helmholtz field (diamond) | 3.2 G/A |
| Anti-Helmholtz gradient (objective) | 0.28 (G/cm)/A |
| Anti-Helmholtz gradient (chamber) | 0.21 (G/cm)/A |
| Anti-Helmholtz gradient (diamond) | -0.49 (G/cm)/A |

Table A.1: Measured properties of the high-field coil pair (at room temperature). The axis nomenclature (objective, chamber, diamond) is defined at the end of App. A.2.1.

### A.2.3 H-bridge and current stabilization circuit

We now describe an analog electronic system designed to control the current through the high-field coils. This system performs two main functions: (1) electronically switching the polarity of the high-field coils between a Helmholtz and anti-Helmholtz configuration and (2) stabilizing the current through the high-field coils via feedback.

The implementation of such a system involves several elements:

1. Four insulated-gate bipolar transistors (IGBTs) in an H-bridge configuration with the high-field coils.
2. A driver circuit that controls the gate voltage of the four IGBTs.
3. A Hall sensor that measures the current through the coils.
4. A servo that produces an error signal and feedback voltage based on our desired current and the current measured by Hall sensor.

We begin by describing the IGBT H-bridge setup. The setup is shown as an electrical schematic in Fig. A.8. Four N-channel IGBTs (Semikron SKM900GA12E4), each

water-cooled and supporting a current of up to 900 A, are connected around one of the coils in an H-bridge configuration. We label the IGBTs as HHI, HLO, AHHI, and AHLO, where H stands for Helmholtz, AH stands for anti-Helmholtz, HI means higher voltage, and LO means lower voltage. If the two H IGBTs are turned on (i.e. given a large gate voltage) while the two AH IGBTs are turned off (i.e. given 0 gate voltage), then current is sent through the second coil such that it produces a field in the same direction as the first coil. If instead the H IGBTs are off while the AH IGBTs are on, the current through the second coil is reversed and the coil pair now produces a magnetic quadrupole gradient.

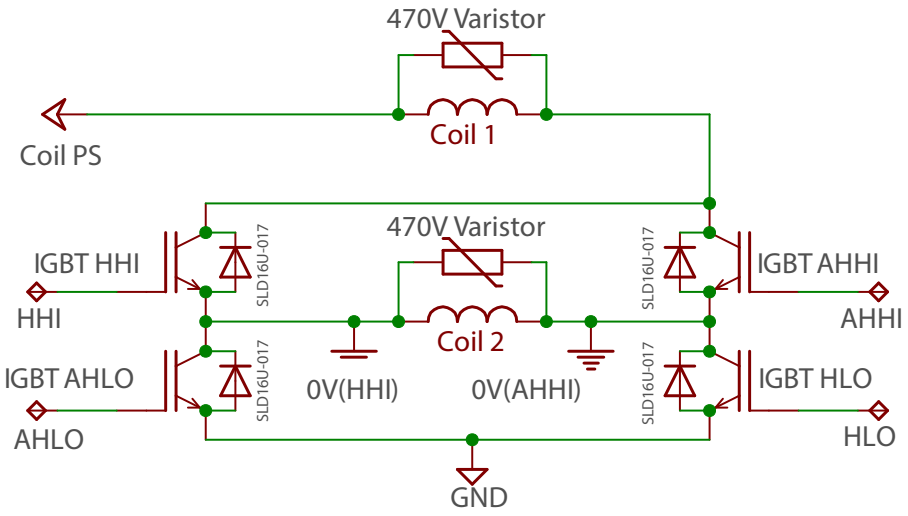


Figure A.8: Electrical schematic of the high-field coil pair and the four-IGBT H-bridge. HHI, AHHI, AHLO, HLO, GND, 0V(HHI), and 0V(HHI) are to be connected with their corresponding lines in Fig. A.9. Varistors are placed across the coils and diodes are placed across the IGBTs for dissipating transient voltage spikes.

In addition to controlling the polarity of the coil pair via an essentially digital on/off voltage applied to the IGBT gates, we can also control the current flowing through the coils by making analog adjustments to the IGBT gate voltage. We do this specifically by adjusting the LO-side gate voltages, while leaving the HI-side gates either completely on or completely off. Therefore, the HI-side gates can be either off (0 V) or on (15 V), while the LO-side gates can be either off (0 V) or on (variable voltage).

We therefore need an electrical circuit that outputs an appropriate gate voltage to each of the four IGBTs when given a digital input (0 or 5V) determining the polarity of the coil pair as well as an analog feedback input determining the gate voltage of

the LO-side gates. We furthermore would like this circuit to ensure total electrical isolation of the coils from the rest of our electronics, including the electronics that produce the digital polarity input and the analog feedback input. In addition to isolating the coils from our other electronics, we also *need* to independently drive each of the HI-side IGBT gates with their own floating power supplies, as it turns out to be impossible to drive all the gates using a common ground. Such a scheme could be possible if the HI-side IGBTs were both P-channel IGBTs (while the LO-side were still N-channel); however, we have not been able to find P-channel IGBTs of similar capabilities to the N-channel ones we use.

The driver circuit that we use to achieve this is partially shown as an electrical schematic in Fig. A.9. The digital input to our circuit is first split off into two, one path for H and one path for AH, with one path going through a logical inverter (CD40106B). Both paths are then passed through 150 mA power buffers (LT1010). Each of the H and AH paths are then further individually split into two again, one for HI and one for LO.

Both HI paths are then sent into an ILQ2 optocoupler, and both LO paths are sent into another ILQ2. These ICs convert an electrical current on their inputs into an optical signal that switches on or off a transistor at the output, therefore allowing for electrically isolated switching of a signal on the output side. They are furthermore able to perform such switching in only a few microseconds, despite being optically actuated.

The HI-side ILQ2 switches on and off fixed 15 V voltages provided by two separately floating external power supplies. These voltages, appropriately switched, are then sent as an output to the HI-side IGBTs.

The LO-side ILQ2 switches on and off a single variable voltage that is sent, appropriately switched, as an output to the LO-side IGBTs. This variable voltage comes from the analog feedback input (whose isolation we will discuss shortly), although some convenient modifications to this voltage are first made by our circuit. In particular, we first pass the analog feedback through an op-amp (LF412) with a trimpot-tunable gain in case amplification is desired. We then add a trimpot-tunable voltage to the amplified analog feedback via a variable voltage regulator (LM317) and another fixed gain op-amp (LF412). The reason for this is that the IGBT gates have a "dead zone" from about 0 to 5 V where they are essentially completely closed and no tunability is available. In order to not have this dynamic range be wasted, we simply add an offset voltage to the amplified analog feedback that already puts it

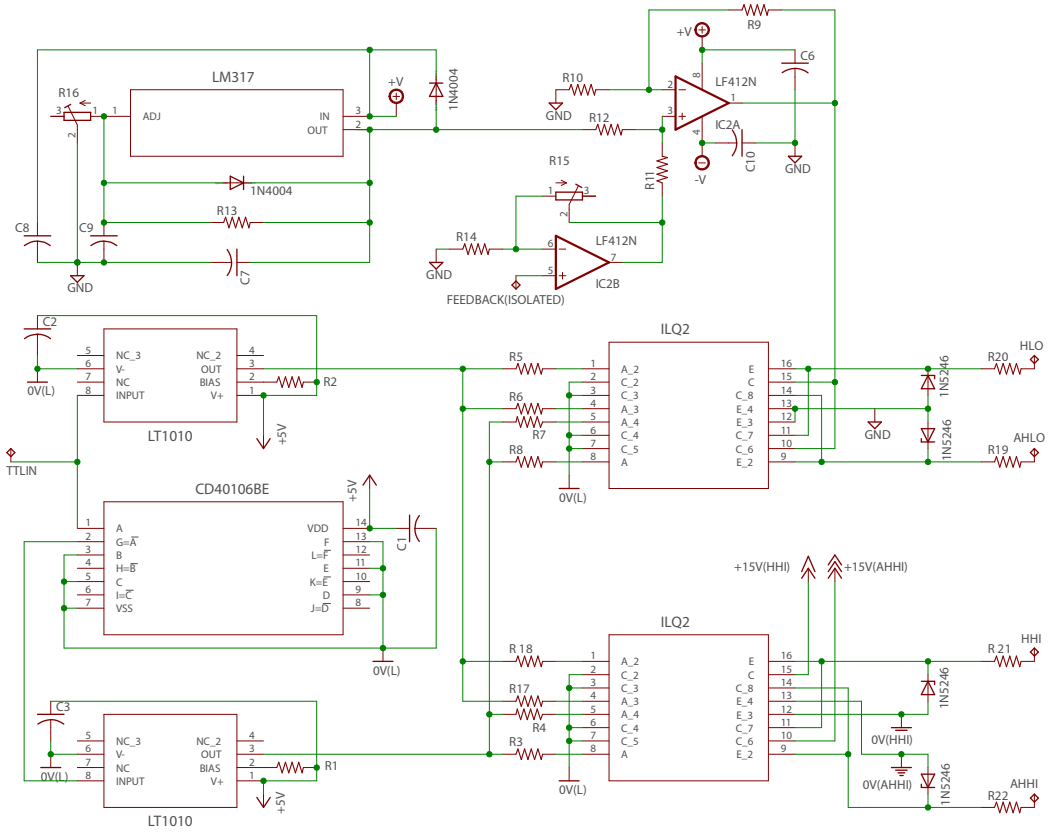


Figure A.9: Electrical schematic of the driver circuit for the four IGBT gates. TTLIN is the digital polarity input while FEEDBACK(ISOLATED) is the post-isolation analog feedback input. 0V(L) represents the reference voltage for the 5 V logic power supply. Resistors at the gate outputs (R19-22) are 1 Ohm. 16 V Zener diodes at the gate outputs protect against over-voltage. Not shown: AD215 isolation amplifier for the analog feedback input, 5 V voltage regulator for logic IC supply.

close to the end of the dead zone (although note that if an IGBTs is digitally closed, its gate voltage is set to exactly 0 V).

Electrical isolation of the analog feedback input is achieved with an AD215 isolation amplifier, which is not shown in Fig. A.9.

This entire setup ultimately requires at least *five* different power supplies. The first is the power supply that actually runs current through the coils. The second, which shares a common ground with the coil power supply (labeled as GND in Figs. A.8 & A.9), powers the output side of the AD215 isolation amplifier as well as the LM317 and 2xLF412s in the driver circuit. This supply needs to have a bipolar dual output as both the AD215 and the LF412 require negative supply voltages (despite no negative signal being used). The third and fourth power supplies provide

independent floating 15 V voltages for the HI-side gates. The fifth power supply powers the input side of the AD215 isolation amplifier and also supplies the ICs that deal with the digital input (CD40106B and LT1010). This fifth supply also needs to have a bipolar dual output for the AD215, and should have its positive output passed through a 5 V voltage regulator before being sent to the digital ICs (such a voltage regulator is not shown in Fig. A.9).

We now discuss how we stabilize the current through the coils and how the analog feedback input is actually produced. We begin with the measurement of the current. The current through the coils is measured by a DaniSense DS400IDSA Hall probe that is placed around the current-carrying cable leading into the coils. This Hall probe produces a current at its output that is proportional to the current passing through its measurement loop. We read this output current by passing it through a Vishay VPR221SZ 50 Ohm precision resistor and reading out the resulting voltage on an INA103 instrumentation amplifier.

This measured voltage is then sent to a Newport LB1005 servo. The servo compares the measured voltage to a given setpoint voltage, and produces an error signal that is output as out analog feedback signal. This is subsequently sent through the AD215 isolation amplifier and into the rest of our driver circuit, as previously outlined.

We run our coil power supply (Keysight N8732A) in constant voltage mode and rely on our IGBTs and feedback circuit for current stabilization. However, different current setpoints require different power supply voltages in order to achieve stability. This is due to the nonlinear response of an IGBT's effective resistance to both the gate voltage and the collector-emitter voltage. In practice, we find that setting the power supply's voltage to slightly higher than the minimum necessary for a certain current produces the best stability.

### A.2.4 Low-field coils

Our low-field coils consist of three pairs of home-made coils wound around 3D-printed plastic spools that are attached to the outside of the high-field coil mounting cage (Fig. A.6). Each coil is made of 16 AWG insulated round copper wire. We drive and control current through the coils with three separate Thorlabs LDC240C 4 A 5 V laser diode drivers*. No explicit cooling is provided for these coils.

The key properties of the three pairs of coils are summarized in Table. A.2.

| Property | Objective axis | Chamber axis | Diamond axis |
|---|---|---|---|
| Resistance ($R$) | 918 mOhm | 436 mOhm | 610 mOhm |
| Inductance ($L$) | 588 $\mu$H | 266 $\mu$H | 289 $\mu$H |
| $\tau = L/R$ | 641 $\mu$s | 610 $\mu$s | 474 $\mu$s |
| Number of turns (per coil) | 36 | 23 | 24 |
| Wire gauge | 16 AWG | 16 AWG | 16 AWG |
| Nearest separation | 123 mm | 180 mm | 94 mm |
| Helmholtz field | 2.3 G/A | 0.82 G/A | 2.3 G/A |

Table A.2: Measured properties of the three low-field coil pairs (at room temperature). The axis nomenclature (objective, chamber, diamond) is defined at the end of App. A.2.1.

The objective axis coils have a rectangular shape with inner side lengths 162 mm and 100 mm. The nearest separation between the two coils is 123 mm. A slight curvature is present on the long side of the rectangle to allow an exit route for the high-field coil leads (See Figs. A.3 & A.6).

The chamber axis coils have a rectangular shape (with a bow, see Fig. A.6) with inner side lengths 125 mm and 99 mm. The nearest separation between the two coils is 180 mm. The furthest separation, at the outer apex of the bow, is 239 mm.

The diamond axis coils have an elliptical shape with an inner full major axis of 194 mm and inner full minor axis of 103 mm. The nearest separation between the two coils is 94 mm.

*In hindsight, these drivers are not the best choice for coils as they have an internal protection that shuts the unit off if it detects an open circuit. This is easily tripped by rapidly switching an inductive load such as a coil. We get around this problem by placing 4.7 V Zener diodes across the output of these supplies.

## A.3 Microscope objectives

Our microscope objectives are a pair of Mitutoyo G Plan Apo 50X objectives. These are placed above and below our glass cell and are used for focusing of the tweezer arrays, imaging the tweezers themselves for diagnostic purposes, and collecting atomic fluorescence.

These objectives have a numerical aperture (NA) of $NA = 0.5$ with an effective focal length of $f = 4$ mm. The working distance (distance between the objective and atoms) is 15.08 mm and assumes 3.5mm glass thickness, for which the objectives are aberration-corrected.

A downside of these objectives for our purposes is their poor transmission (quoted at 58%) at our trapping wavelength 813.4 nm. Our experiment was initially designed for a trapping wavelength of 515.2 nm, for which these objectives have a quoted transmission of 88%. For our fluorescence wavelength of 461 nm, these objectives have a quoted transmission of 83%.

### A.3.1 Future objective upgrade

We have obtained a new pair of custom-made objectives from Special Optics that we hope will be an all-around improvement on our current objectives for future work. These new objectives are designed to have similar physical dimensions and working distance to our current objectives such as to be interchangeable with minimal extra work.

The several ways the new objectives improve on our current ones include increased transmission at 813.4 nm (quoted at and measured to be 92%), an increased NA of $NA = 0.55$ (at the same effective focal length of $f = 4$ mm), and a no-metal Ultem plastic construction. Our tests of these new objectives have shown them capable of generating tweezers through 3.5 mm glass with a very low level of aberration and nearly diffraction-limited waist.

## A.4 Laser systems

### A.4.1 Blue laser

We use a Toptica TA-SHG pro laser system to generate our 461 nm (blue) light. An external cavity diode laser (ECDL) produces a fundamental tone at 922 nm which

is then amplified through a tapered amplifier (TA) and then frequency doubled to 461 nm in a second harmonic generation (SHG) bow tie cavity with a nonlinear crystal. The doubling cavity is maintained in resonance with the light by feedback to a piezo that controls the cavity's length. Sidebands are imprinted on the light before the cavity in order to generate a Pound-Drever-Hall (PDH) signal [244] from which the feedback error signal is derived.

We reference this laser's frequency to the blue transition of strontium via a home-built strontium vapor cell (initially designed for locking the red laser, see Ref. [23] App. B). The vapor cell produces a spectral absorption feature, and an error signal is generated from this feature by phase modulating the light going into the cell with an EOM. A Toptica PDD 110/F module generates the modulation signal and also demodulates the measured signal into a DC error signal. We use Toptica's DLC pro Lock software to lock the laser's frequency to this error signal.

The typical power obtained from the output of this laser is about 600 mW at 461 nm.

### A.4.2 Red laser

We use a Toptica DL pro ECDL to generate our 689 nm (red) light. This laser was purchased as part of a larger narrow-linewidth stabilization system from Stable Laser Systems.

Part of the output of the laser is picked off and sent through a high-finesse cavity for stabilization. Before going through the cavity, this light is passed through a phase-modulating fiber EOM. This EOM creates two sets of sidebands on the light. The first set of sidebands are at several hundred MHz and are used to tune the lock frequency (instead of, e.g., tuning the cavity length). The second set of sidebands are at 5 MHz and are used to generate a PDH from the cavity reflection. A Toptica Fast Analog Linewidth Control (FALC 110) box generates an error signal from the PDH signal and feeds back to the laser current and grating piezo (via a Toptica DLC ext module) using a PID servo.

The cavity has a length of 10 cm, a linewidth (FWHM) of 32 kHz, and a finesse of $47,000$ (measured via cavity ringdown spectroscopy [245]). It is housed inside of a thermally insulated vacuum chamber at $1 \times 10^{-7}$ Torr. The cavity is thermally stabilized at 25.0 °C, which is the temperature measured by Stable Laser Systems at which the cavity frequency is minimally sensitive to temperature (i.e. it is a zero-crossing of the thermal expansion coefficient).

Fig. A.10 provides an Allan deviation measurement (see Sec. 3.3.2) of our red laser's frequency after stabilization, as measured by Stable Laser Systems.

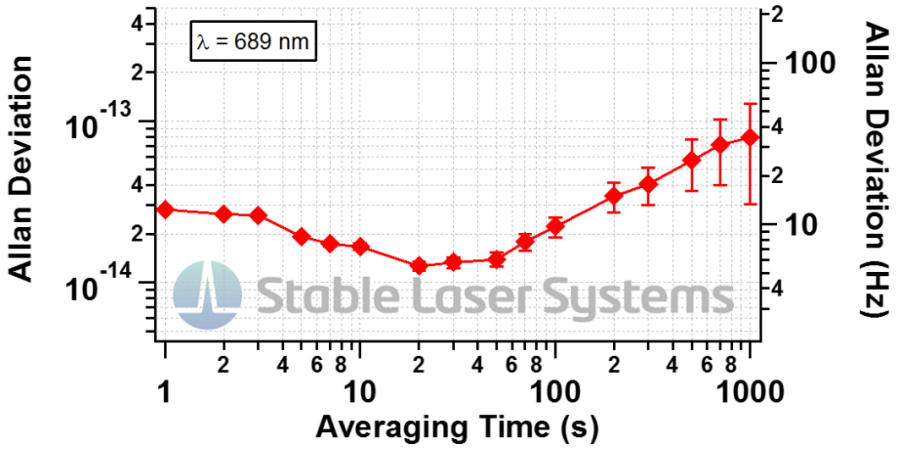


Figure A.10: Allan deviation of our red laser's frequency after stabilization, as measured by Stable Laser Systems.

The cavity stabilization provides a sufficiently narrow linewidth for our laser in order to effectively drive the red transition (however, see Sec. 2.5.3 for further discussion of laser noise not fully captured by the linewidth). However, the cavity also has a highly linear drift of about 3.5 kHz per day. We compensate for this drift by calibrating the lock frequency to our atoms once every day. We do this by generating a red MOT (which is fairly insensitive to the exact frequency), turning off the MOT beams and magnetic gradients, applying a magnetic field of a few Gauss, exciting the atomic cloud with a single red beam in the horizontal direction, quickly pumping the excited atoms to the metastable 5s5p $^3P_{0,2}$ states, and imaging the remaining atoms. When done as a function of red frequency, this procedure produces a depletion spectral feature of about 50 kHz FWHM (limited in part by Doppler broadening). The signal-to-noise on this feature is typically sufficient to calibrate the lock frequency to within 1 kHz.

As discussed in Sec. 2.5.3, a future upgrade to this laser system could include injection locking another laser diode with the transmission of the cavity [119] in order to generate red light with suppressed fast frequency noise.

The typical power obtained from the output of this laser is about 15 mW. This is then sent through a home-built TA (based on a design from the David Weld group at UCSB) that outputs powers of a few hundred mW.

### A.4.3 Clock laser

We restate some specifications given in Ref. [138] App. B2:

Our clock laser is based on a modified portable clock laser system (Stable Laser Systems) composed of an ECDL (Moglabs) stabilized to an isolated, high-finesse optical cavity using the PDH scheme and electronic feedback to the laser diode current and piezoelectric transducer. The optical cavity is a 50 mm cubic cavity [246] made of ultra-low expansion glass, with its mirror substrates made of fused silica. The cavity is maintained at its zero-crossing temperature of 40.53 °C inside a thermally insulated vacuum chamber at a pressure of $5 \times 10^{-9}$ Torr. It has a finesse of $F > 300,000$ at 698 nm.

The clock laser light passes through a first AOM in double-pass configuration, injects an anti-reflection coated laser diode (Sacher Lasertechnik GmbH, SAL-0705-020), passes through a second AOM, and goes through a 10 m long fiber to the main experiment with a maximum output optical power of 20 mW. The first AOM is used for shifting and stabilizing the frequency of the clock laser, whereas the second AOM is used for intensity-noise and fiber-noise cancellation.

Fig. A.11 provides an Allan deviation measurement (see Sec. 3.3.2) of our clock laser's frequency after stabilization, as measured by Stable Laser Systems via beating with another similar leaser. The power spectral density of this beat signal is shown in Fig. 3.8.

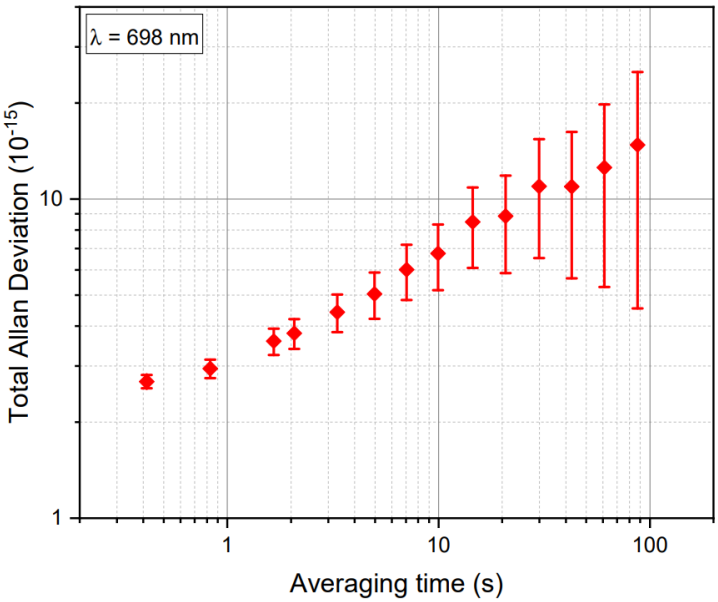


Figure A.11: Allan deviation of our clock laser's frequency after stabilization, as measured by Stable Laser Systems via beating with another similar laser. The vertical axis is the Allan deviation of the quantity $\frac{1}{f}\big(f_1(t) - f_2(t)\big)/\sqrt{2}$, where $f_i$ is the frequency of laser $i$ and $f = 429.228$ THz. The factor of $1/\sqrt{2}$ accounts for the frequency noise of the similarly noisy reference laser. A linear drift is removed.

### A.4.4 Rydberg laser

We use a Toptica TA-FHG pro laser system to generate our Rydberg excitation light. An ECDL produces a fundamental tone at about 1266 nm which is then amplified through a TA. This light is then frequency doubled to about 633 nm in an SHG bow tie cavity with a nonlinear crystal. This is then once again doubled to about 316.5 nm by a fourth harmonic generation (FHG) cavity that is very similar to the SHG cavity.

The SHG and FHG cavities are maintained in resonance with the light by feedback to piezos that control their lengths. Sidebands are imprinted on the light before the cavities in order to generate a PDH signal from which the feedback error signals are derived. For this laser, we generate these sidebands via EOMs placed before each cavity. The modulation frequencies for these sidebands are 20 MHz and 25 MHz before the SHG and FHG, respectively. We estimate that the cavities have linewidths of 7 MHz (with finesse of 150).

We find that the output power of the FHG tends to degrade over time. We also find that moving the nonlinear crystal in the cavity such that the light hits it at a different spot tends to regain some of the output power. These observations suggest that the light gradually degrades the crystal, but only in the localized spot around the beam. The crystal is made of beta barium borate (BBO), and similar observations have been made about BBO in previous work; e.g., in Ref. [247] p.104–107. This reference also reports that flowing oxygen over the crystal helps to prevent such damage. However, we use no such flow (of oxygen or any other gas) in our system.

We lock the Rydberg laser to a high-finesse cavity purchased from Stable Laser Systems (very similar to the cavity described in App. A.4.2). The light sent to the cavity is of the fundamental tone at 1266 nm. Before going through the cavity, this light is passed through a phase-modulating fiber EOM. This EOM creates two sets of sidebands on the light. The first set of sidebands are at several hundred MHz and are used to tune the lock frequency. The second set of sidebands are at 20 MHz and are used to generate a PDH from the cavity reflection. A Toptica Fast Analog Linewidth Control (FALC 110) box generates an error signal from the PDH signal and feeds back to the laser current and grating piezo (via a Toptica DLC ext module) using a PID servo.

The cavity has a length of 10 cm, a linewidth (FWHM) of 110 kHz, and a finesse of $13,600$ (measured via cavity ringdown spectroscopy [245]). It is housed inside

of a thermally insulated vacuum chamber at $2 \times 10^{-7}$ Torr. The cavity is thermally stabilized at 30.5 °C, which is its zero-crossing temperature.

We use picked-off 633 nm light from after the SHG to monitor the laser wavelength with our wavelength meter (App. A.4.8).

Under optimal conditions, the power obtained from the output of this laser reaches about 400 mW at 316.6 nm.

We note that we have operated this laser at output wavelengths of as high as 318.5 nm, which is in the range of wavelengths for the transitions 5s5p $^3P_1 \leftrightarrow$ 5s*n*s $^3S_1$. However, we do not currently work with these transitions.

### A.4.5 Trapping laser

The majority of the results in this work are done at a trapping wavelength of $\lambda = 813.4$ nm, which is a magic wavelength for the clock transition. We use an M Squared SolsTiS PSX-F titanium-sapphire (Ti:sapph) laser to produce this light. This laser produces light at the desired wavelength by pumping a Ti:sapph crystal inside a bow tie cavity with 532 nm light produced by an auxiliary pump laser (Sprout G18). At 813.4 nm, this laser can produce up to about 6 W of optical power.

This laser can produce a large range of wavelengths (at least 725 nm to 975 nm), which can be tuned by three mechanisms offering varying degrees of dynamic range. The most coarse tunability comes from the rotation of an intracavity birefringent filter. The next finer level of tunability is provided by tuning the spacing of an intracavity etalon, which also ensures single cavity mode operation. The finest level of tunability is provided by piezo modulation of the cavity length. We lock the laser's wavelength by modulating this piezo with a feedback signal produced by our wavelength meter (App. A.4.8).

Some of our earlier work (e.g., in Sec. 2.6.8) was done at a trapping wavelength of $\lambda = 515.2$ nm. For this wavelength, we used an AzurLight ALS-515 laser. This laser produces 515 nm light (of up to 10 W) by doubling a 1030 nm fundamental stage. However, it offers no wavelength tunability.

### A.4.6 Auto-ionization laser

For our auto-ionization light at 408 nm, we use a Moglabs LDL ECDL with an output power of around 20 mW. Since the auto-ionization feature is very broad (Sec. 4.1.3),

we either leave this laser unlocked or very coarsely reference it to a Moglabs MWM wavemeter (which is separate from our higher resolution wavemeter described in App. A.4.8).

### A.4.7 Repump lasers

We have three repump lasers at 679 nm, 688 nm, and 707 nm. The 679 nm and 707 nm lasers are Toptica DL 100 ECDLs while the 688 nm laser is a Moglabs CEL Cateye ECDL. All of them output powers near 10–20 mW. We lock all of these lasers using a feedback signal generated from our wavemeter (App. A.4.8) and sent to their piezos.

### A.4.8 Wavelength meter stabilization

We use a HighFinesse WS7 wavelength meter (or wavemeter) along with an 8-channel switch to monitor and stabilize the wavelengths of several of our lasers. This wavemeter has a quoted resolution of 2 MHz. Using an add-on option, this wavemeter can produce feedback voltages for stabilizing laser wavelengths to a desired value. We use this feature to stabilize the wavelength of our 813 nm trapping laser as well as our 679 nm, 688 nm, and 707 nm repump lasers. In terms of accuracy, we periodically calibrate this wavemeter by referencing it to our 689 nm laser, whose wavelength can itself be calibrated to an atomic signal to within 1 kHz (App. A.4.2).

In addition to this high-resolution wavemeter, we use a lower-resolution Moglabs MWM wavemeter for monitoring and stabilizing the auto-ionization laser's wavelength.

## A.5 Arbitrary waveform generator (AWG) and acousto-optic deflector (AOD)

We use a Spectrum M4i.6622-x8 arbitrary waveform generator to produce the polychromatic RF tones that generate and rearrange our tweezer arrays (Eqs. 2.123). This card offers a 4-channel output with a bandwidth of 212 MHz, sampling rate of 625 MS/s, 16-bit resolution, and 2 giga-sample on-board memory. It plugs directly into a x8 PCIe slot of a computer motherboard and is controlled via a MATLAB SDK.

The center frequency of our array signal is near 100 MHz and spans up to about 20 MHz in each direction. We pass the output of the AWG through a voltage-variable attenuator for analog control of the signal amplitude, useful when doing overall ramps of the trap depth. We then pass the signal through a 50 MHz high-pass filter and a 150 MHz low-pass filter to remove harmonics. Finally, the signal is amplified with a Mini Circuits ZHL-03-5WF+ 5 W RF amplifier.

This amplified signal is ultimately sent into our acousto-optic deflector (AOD), an AA Opto-Electronic DTSX-400 coated for 800-850 nm wavelengths. This AOD has a central frequency of about 100 MHz and a bandwidth of 36 MHz. It has a relatively large aperture of 7.5 mm diameter. Its crystal is made of $TeO_2$. The acoustic wave excites the *shear* mode of this crystal, and has a speed of sound of 617 m/s.

# Appendix B

# SOURCES OF POLARIZABILITY DATA

The formulas we have described for calculating polarizabilities (Sec. 2.3.1) in principle require one to sum over all atomic states. However, RDMEs are generally only known for a limited subset of states, with their values varying widely in the literature and with large error. While a truncated sum-over-states approach using approximate RDMEs can decently approximate most polarizabilities, it is often not sufficiently accurate for determining or reproducing fine-tuned features such as magic wavelengths. Other, more advanced polarizability calculation methods [88, 89, 248, 249] can produce more accurate results with an *ab initio* treatment, but are beyond the scope of this work. We will, however, do our best to accurately reproduce certain known results for polarizabilities in Sr with a sum-over-states approach.

For the states involved in the red transition ($5s^2\ {}^1S_0$ and $5s5p\ {}^3P_1$) near 515 nm, we will attempt to reproduce the results from Ref. [89], which contains experimental data from our group and is supplemented by *ab initio* polarizability calculations by theory collaborators Marianna S. Safronova and Sergey G. Porsev.

Three experimental results regarding polarizabilities are notable from this work, which used a trapping wavelength of 515.2 nm: (1) there is a magic ellipticity parameter $\gamma_{\text{magic}} = \pm 24^\circ$ for the red transition, (2) the absolute ratio of vector to tensor polarizability for $5s5p\ {}^3P_1$ was measured as $|\alpha_v|/|\alpha_t| = 0.10(4)$, and (3) the $Q$-value was measured as $Q_{\text{exp}} = -5.1(3)$, where its definition is:

$$Q = \frac{\alpha_s({}^1S_0) - (\alpha_s({}^3P_1) + \alpha_t({}^3P_1))}{\alpha_s({}^1S_0) - (\alpha_s({}^3P_1) - 2\alpha_t({}^3P_1))} \tag{B.1}$$

These three values are particularly amenable to experimental measurement as they do not require knowledge of the exact beam intensity or magnitudes of polarizabilities: they all only depend on ratios of polarizabilities.

The theory calculations in Ref. [89] give a recommended value (where "recommended" means taking into account both *ab initio* theory results and previously ascertained experimental results) of $Q_{\mathrm{th}} = -5.8^{+1.8}_{-4.2}$, where relatively large fractional uncertainty in $Q$ arises from only 2% uncertainty in polarizabilities. Thus, the theoretical model and experimental results are consistent even with tight bounds on theoretically determined polarizability contributions. We will therefore use the theoretically determined RDMEs in Appendix Table I of Ref. [89].

A hindrance here is that RDMEs are given only up to certain low-lying states, leaving significant polarizability contributions unattributed to any particular state (this is not because the enumeration is incomplete, but because it becomes difficult to attribute polarizability contributions to specific higher-lying states using the *ab initio* model [250]). Accounting for these "other" contributions is easy at the particular wavelength for which they are given, but it is unclear how to extend their contribution to other wavelengths. Our approach will be to just add these "other" polarizability contributions as wavelength-independent contributions within a particular window of wavelengths. This is an admittedly crude approximation, but since the "other" contributions come from higher-lying states, it is reasonable to assume that their contributions vary slowly at wavelengths significantly longer than their resonance wavelength.

Furthermore, vector polarizability values are not given for "other" states. We will remedy this for 5s5p $^3\mathrm{P}_1$ near 515 nm by adding a wavelength-independent vector polarizability such that $|\alpha_{\mathrm{v}}|/|\alpha_{\mathrm{t}}|$ agrees with our experimentally measured value (the sign of $\alpha_{\mathrm{v}}$ will not be important to our discussions). After all of these modifications, our model will predict a magic ellipticity parameter for 515.2 nm of 22.6° — reasonably close to the experimentally measured 24°.

A similar treatment will be done for the ground and clock states near 813 nm, this time using data from Ref. [88]. As for 5s5p $^3\mathrm{P}_1$ near 813 nm, we will continue to use data from Ref. [89], however the "other" contributions will be adjusted slightly to match the known magic wavelength with $5\mathrm{s}^2\ ^1\mathrm{S}_0$ at 914 nm [98]. Namely, we will decrease the "other" contribution to $\alpha_{\mathrm{s}}$ (which makes sense, as this contribution should get smaller at longer wavelengths). The "other" contributions to $\alpha_{\mathrm{v}}$ and $\alpha_{\mathrm{t}}$ — which are already small at 515 nm — will be neglected near 813 nm.

One more minor modification we add for all wavelengths is a "core polarizability", which is to good approximation purely scalar, wavelength-independent, and state-independent [220]. A further, smaller correction is the "valence-core polariz-

ability" [88] which is also approximately scalar and wavelength-independent, but is state-dependent.

All sources of data and modifications made are summarized in Table. B.1. The atomic unit of polarizability is au = $\frac{e^2 a_0^2}{E_\mathrm{h}}$, where $a_0$ is the Bohr radius and $E_\mathrm{h}$ is the Hartree unit of energy.

| Values for... | Sources | Notes |
|---|---|---|
| **495 nm – 535 nm** | | |
| $5s^2\ {}^1S_0$ | [89] | $\alpha_\mathrm{s}^\mathrm{other}$ = 7.3 au included |
| $5s5p\ {}^3P_1$ | [89] | $\alpha_\mathrm{s}^\mathrm{other}$ = 66.9 au, $\alpha_\mathrm{t}^\mathrm{other}$ = 0.2 au included, $\lvert\alpha_\mathrm{v}\rvert$ corrected |
| Other states | [89], [88], [87] | |
| **800 nm – 1070 nm** | | |
| $5s^2\ {}^1S_0$ | [88] | $\alpha_\mathrm{s}^\mathrm{other}$ = 2.4 au included |
| $5s5p\ {}^3P_0$ | [88] | $\alpha_\mathrm{s}^\mathrm{other}$ = 34.1 au included |
| $5s5p\ {}^3P_1$ | [89] | $\alpha_\mathrm{s}$ corrected for $\lambda_\mathrm{magic}$ = 914 nm [98] |
| Other states | [89], [88], [87] | |
| **All wavelengths** | | |
| Core polarizability | [220] | 5.4 au |
| Valence-core polarizability | [88] | -0.11 au ($5s^2$)<br>0.15 au (All 5s5p states) |

Table B.1: Summary of RDME and energy data used to calculate polarizabilities presented in the following sections. For multiple sources, order determines precedence in case of contradicting values (highest precedence → lowest precedence). The atomic unit of polarizability is au = $\frac{e^2 a_0^2}{E_\mathrm{h}}$, where $a_0$ is the Bohr radius and $E_\mathrm{h}$ is the Hartree unit of energy.

# Appendix C

# NON-PARAXIAL EFFECTS

The assumption that the polarization of a beam is the same at all points in space is a good approximation for *paraxial* systems, which are optical systems whose $\vec{k}$-vectors only form small angles to a common optical axis. In other words, this is valid for small numerical aperture (NA) lenses. However, forming tight and deep tweezers calls for high NA, so the paraxial approximation comes under question here. In this section we will show how to compute aparaxial effects for high NA systems and that such effects lead to distortions of the electric field profile as well as polarization gradients near the focal plane. Our conclusion will be that for the $NA \sim 0.5$ used for this work, these effects can usually be ignored. However, higher NA systems may require further consideration.

Non-paraxial fields near the focal plane of a lens are computed in Ref. [251], and we restate the central result here. Two key factors differentiate this treatment from the paraxial one: (1) converging wavefronts after the lens are treated as spherical (instead of parabolic as in the paraxial approximation) and (2) polarization after the lens is not assumed constant but instead everywhere tangent to the spherical wavefronts, which introduces polarization in all components.

We assume an input Gaussian with central complex amplitude $\mathcal{E}_{0,i}$, waist $w_i$, and polarization $\hat{\epsilon}(\gamma) = \cos\gamma + i\sin\gamma$. We will use the notation of Sec. 2.2, and further define the cylindrical angle coordinate $\phi$ as the angle from $\hat{x}$. We let $\alpha$ be the angle between the optical axis and a line from the edge of the aperture to the focus, such

that $NA = \sin(\alpha)$. Now we define some integrals:

$$\mathcal{I}_0(r,z) = \int_0^\alpha e^{-\frac{f^2\sin^2(\theta)}{w_i^2}} e^{ikz\cos(\theta)} \cos^{1/2}(\theta)\sin(\theta)\big(1+\cos(\theta)\big)J_0\big(kr\sin(\theta)\big)d\theta \tag{C.1}$$

$$\mathcal{I}_1(r,z) = \int_0^\alpha e^{-\frac{f^2\sin^2(\theta)}{w_i^2}} e^{ikz\cos(\theta)} \cos^{1/2}(\theta)\sin^2(\theta)J_1\big(kr\sin(\theta)\big)d\theta \tag{C.2}$$

$$\mathcal{I}_2(r,z) = \int_0^\alpha e^{-\frac{f^2\sin^2(\theta)}{w_i^2}} e^{ikz\cos(\theta)} \cos^{1/2}(\theta)\sin(\theta)\big(1-\cos(\theta)\big)J_2\big(kr\sin(\theta)\big)d\theta \tag{C.3}$$

Using these, the complex electric field near the focal plane is given (up to overall phase) by [251]

$$\begin{aligned}\vec{\mathcal{E}}_{\mathrm{f}}(r,\phi,z;\gamma) = \Bigg(&\Big(\cos(\gamma)\big(\mathcal{I}_0+\mathcal{I}_2\cos(2\phi)\big)+i\sin(\gamma)\mathcal{I}_2\sin(2\phi)\Big)\hat{x}\\ &+\Big(\cos(\gamma)\mathcal{I}_2\sin(2\phi)+i\sin(\gamma)\big(\mathcal{I}_0-\mathcal{I}_2\cos(2\phi)\big)\Big)\hat{y}\\ &-2i\mathcal{I}_1\big(\cos(\gamma)\cos(\phi)+i\sin(\gamma)\sin(\phi)\big)\hat{z}\Bigg)\tfrac{kf}{2}\mathcal{E}_{0,i}\end{aligned} \tag{C.4}$$

We see that the electric field now has polarization components in all directions despite the input having purely $\hat{x}$ polarization. Note that $\vec{\mathcal{E}}_f$ satisfies the full, non-paraxial Helmholtz equation $(\nabla^2+k^2)\mathcal{E}=0$ for all of its components. In the paraxial $NA \ll 1$ limit, $\mathcal{I}_1$ and $\mathcal{I}_2$ are negligible and $\mathcal{I}_0$ is the only contribution, returning the focal field to purely $\hat{\epsilon}$ polarization everywhere. Furthermore, one can show that in this limit, the field amplitude reduces to that given by Eq. 2.6.

It is also interesting to calculate the intensity* $I_f = \frac{1}{2}c\varepsilon_0|\vec{\mathcal{E}}_f|^2$, which would be the only quantity of interest for trapping in the absence of vector and tensor polarizabilities:

$$\begin{aligned}I_f(r,\phi,z;\gamma) = \Big(&|\mathcal{I}_0|^2+|\mathcal{I}_2|^2+2\cos(2\gamma)\cos(2\phi)\mathrm{Re}(\mathcal{I}_0^*\mathcal{I}_2)\\ &+4|\mathcal{I}_1|^2\big(\cos^2(\gamma)\cos^2(\phi)+\sin^2(\gamma)\sin^2(\phi)\big)\Big)\tfrac{c\varepsilon_0k^2f^2}{8}|\mathcal{E}_{0,i}|^2\end{aligned} \tag{C.5}$$

We note that this quantity is generically not axially symmetric — except for circular input polarization ($\gamma = \pm\frac{\pi}{4}$). This leads to an ellipticity in the trap shape that will cause trap frequencies in two orthogonal radial directions to be slightly different.

*Here, we maintain our definition of intensity as defined only by the electric field. However, other conventions may define it as the total power density of the beam. In the non-paraxial regime, these quantities are not exactly the same, see the coming discussion.

However, the *total power density* of the focal beam including contributions from the magnetic field (not shown) is always axially symmetric [251].

The implications for trapping are mainly relevant for states with finite vector and/or tensor polarizabilities, where changes in polarization across the trap can lead to spatially varying polarizabilities, leading to trap light shifts that are effectively nonlinear in the intensity. Given that these light shifts are also sub-state-dependent, further complication arises if two states are otherwise degenerate and the polarization gradients are the only source of degeneracy-lifting. Both of these concerns, if troublesome, can be alleviated by adding a large external field that dominates over such gradients, as was done in Ref. [36]. Ultimately, we have not found such considerations to be important to this work, and a large magnetic field is often desirable for other reasons anyway (Sec. 2.3.3).

As a final quantitative analysis, we plot $\mathcal{I}_1/\mathcal{I}_0$ and $\mathcal{I}_2/\mathcal{I}_0$ as a function of $r$ at the focal plane ($z = 0$), where non-paraxial effects are most significant. We do this for $NA = 0.5$ and $w_i$ equal to the aperture radius, which are the parameters most commonly used for trapping in this work. The results are shown in Fig. C.1. We see that, within regions where the atomic wavefunction is usually found ($r$ much less than a waist), these quantities are small.

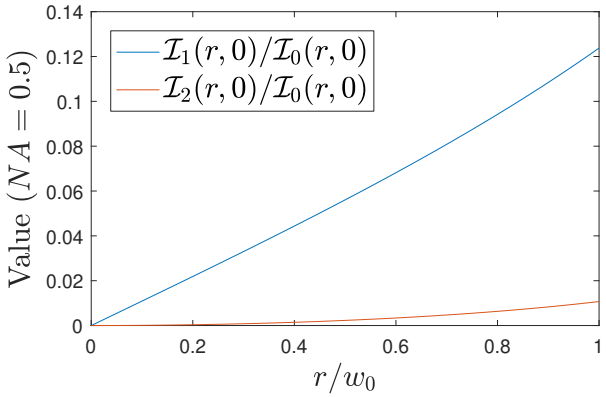


Figure C.1: Non-paraxial factors at the focal plane $z = 0$ as a function of $r/w_0$, where $w_0 = 2f/(kw_i) = 2/(k\,NA)$ is the waist of the approximately Gaussian focal field with $w_i$ equal to the aperture radius, and $NA = 0.5$. The plot is independent of choice of $k$.

# Appendix D

# RYDBERG DIPOLE MATRIX ELEMENTS

Here we compute the dipole matrix elements between Rydberg states.

We begin with a general formula for *reduced* dipole matrix elements (RDMEs):

$$\begin{aligned}\langle n, l, S, J||d||n', l', S', J'\rangle = \Big( - |e| \int_0^\infty dr r^3 R^*_{nl}(r) R_{n'l'}(r) \Big) \dots \\ \cdots \times \sqrt{(2L+1)(2L+1)} \begin{pmatrix} L & L' & 1 \\ 0 & 0 & 0 \end{pmatrix} \dots \\ \cdots \times (-1)^{1+S'+J'} \delta_{SS'} \sqrt{(2J+1)(2J'+1)} \begin{Bmatrix} J & J' & 1 \\ L' & L & S \end{Bmatrix}\end{aligned} \tag{D.1}$$

where $e$ is an elementary charge and $R_{nl}(r)$ is a radial wavefunction such that the full wavefunction of an electron orbital is given by

$$\Psi_{nlm_l}(r, \theta, \phi) = R_{nl}(r) Y_l^{m_l}(\theta, \phi) \tag{D.2}$$

with $Y_l^{m_l}$ a spherical harmonic.

$R_{nl}(r)$ is difficult to compute for low-lying states, but there are several well-known approaches for Rydberg states [196, 197, 199, 252]. We follow the approach of

Ref. [252], which computes the integral directly:

$$\int_0^\infty dr r^3 R^*_{nl}(r) R_{n'l'}(r) = \tfrac{3}{2} a_0 \phi n_c^2 \sqrt{1 - l_c^2/n_c^2} \tag{D.3}$$

$$n_c = \frac{2n^\star n'^\star}{n^\star + n'^\star} \tag{D.4}$$

$$l_c = \tfrac{1}{2}(l + l' + 1) \tag{D.5}$$

$$\phi = g_0(s)\Big(1 + \gamma^2\big(1 + \tfrac{s}{2}\big)\Big) + g_1(s)\gamma(1 + \gamma^2) - \frac{\sin(\pi s)}{\pi s}\gamma^2 \tag{D.6}$$

$$\gamma = (l' - l)(l_c/n_c) \tag{D.7}$$

$$s = n^\star - n'^\star \tag{D.8}$$

$$g_0(s) = \frac{1}{3s}\Big(A_{s-1}(-s) - A_{s+1}(-s)\Big) \tag{D.9}$$

$$g_1(s) = -\frac{1}{3s}\Big(A_{s-1}(-s) + A_{s+1}(-s)\Big) \tag{D.10}$$

$$A_\alpha(x) = \frac{1}{\pi}\int_0^\pi \cos(\alpha\theta - x\sin\theta) d\theta \tag{D.11}$$

where $a_0$ is the Bohr radius and $n^\star$ is the effective principal quantum number (Eq. 4.2).

Having computed the RDME, we can apply Eq. 2.22 to get the spherical components of the full dipole vector operator:

$$\begin{aligned}\langle n, l, S, J, m_J | d_q | n', l', S', J', m_{J'} \rangle \\ = \frac{1}{\sqrt{2J+1}} \langle n, l, S, J || d || n', l', S', J' \rangle \langle J\ m_J | J'\ m'_J; 1\ q \rangle\end{aligned} \tag{D.12}$$

where $\langle J\ m_J | J'\ m'_J; 1\ q\rangle$ is a Clebsch-Gordan coefficient and $q \in \{-1, 0, 1\}$.

If desired, this vector operator can be transformed from spherical to Cartesian components via

$$d_z = d_0 \tag{D.13}$$

$$d_x = \tfrac{1}{\sqrt{2}}(d_{-1} - d_1) \tag{D.14}$$

$$d_y = -\tfrac{1}{i\sqrt{2}}(d_{-1} + d_1) \tag{D.15}$$

# Appendix E

# STATE PREPARATION AND MEASUREMENT (SPAM) ERRORS & CORRECTIONS

***Note: This appendix is an edited reproduction of Supplement C of our publication Ref. [150].***

At the end of a Rydberg excitation and auto-ionization sequence, we perform state readout by imaging the absence (0) or presence (1) of atoms. We infer the final state of the atom by mapping this binary detection value to the atomic state as $0 \rightarrow |r\rangle$ and $1 \rightarrow |g\rangle$. However, imperfections in state preparation, imaging fidelity, and state-selective readout produce errors in this mapping. State preparation and measurement (SPAM) correction attempts to isolate quantities of the pertinent physics (in this case, Rydberg excitation) from such errors. In particular, we attempt to answer the following question: Assuming an atom is perfectly initialized in the ground state $|g\rangle$, what is the probability that it is in $|r\rangle$ after a certain Rydberg excitation pulse?

## E.1 Preparation, excitation, and measurement processes

We begin by assuming that an atom/pair has been registered as present via imaging at the start of the experiment and that it has no detected neighbors within a two-tweezer spacing. If an atom/pair does not fulfill this criterion, it is omitted from our data. For the sake of simplicity, we will assume that there are no errors in this initial detection stage. In particular, the combination of high imaging fidelity and high array rearrangement fidelity make errors in this stage exceptionally unlikely.

Imaging an atom involves a small probability that the atom will be lost, even if it scatters enough photons to be detected. We denote by $S$ the probability that a detected atom survives the first image. After this image, surviving atoms are transferred from the absolute ground state $|a\rangle$ to the clock state $|g\rangle$ (the ground state

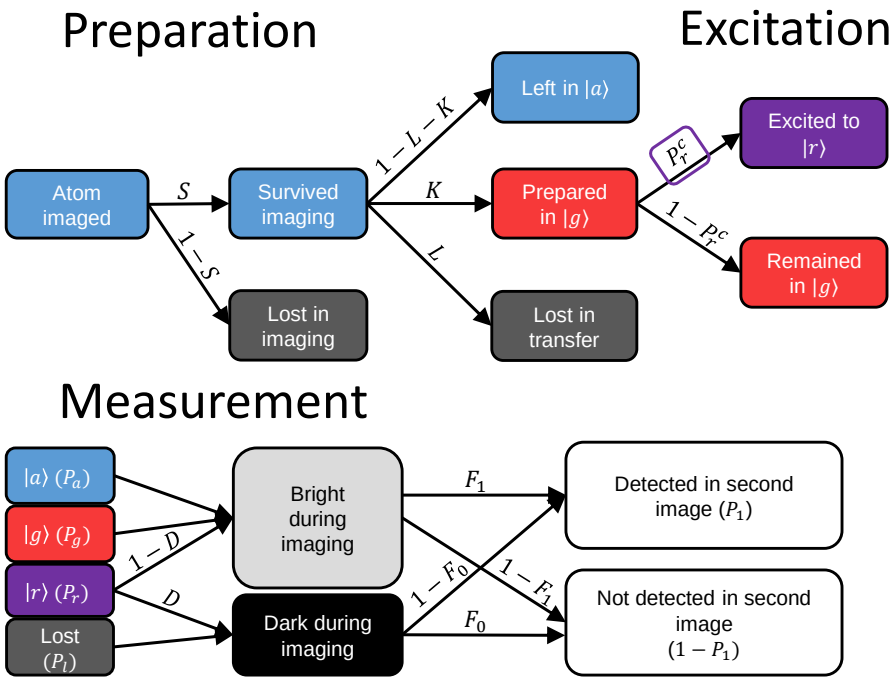


Figure E.1: Probability tree for single-atom SPAM correction. Atomic states are color-coded as blue for $|a\rangle$ (absolute ground state), red for $|g\rangle$ (clock state), purple for $|r\rangle$ (Rydberg state), and dark-gray for lost. Quantities above arrows indicate probabilities. The SPAM corrected quantity of interest, $P_r^c$, is highlighted in a purple box.

of our Rydberg qubit) with a probability of successful transfer denoted by $K$. There is a small probability $L$ that during this transfer, atoms are lost. The rest, which are not lost but not successfully transferred, remain in $|a\rangle$ with a probability $1 - L - K$. The possibilities enumerated up to this point are represented graphically in Fig. E.1 under "Preparation."

At this point, atoms that have been successfully prepared in $|g\rangle$ undergo Rydberg excitation. In the single atom case, they end up in the Rydberg state $|r\rangle$ with a probability $P_r^c$. For the two-atom case, assuming that both atoms have been successfully prepared, there are four possible states in the two-qubit space, with probabilities given by $P_{rr}^c, P_{rg}^c, P_{gr}^c, P_{gg}^c$. Our ultimate goal will be to solve for these values, which we call "SPAM-corrected," indicated here with a superscript $c$.

In the two-atom case, there is the possibility that one atom is successfully prepared while the other is not. In this case, we expect the successfully prepared atom to execute single-atom dynamics. In the case of Rabi oscillations, the Rabi frequency will be reduced by a factor of $\sqrt{2}$. We can thus estimate the Rydberg excitation

probability of the prepared atom as $P^c_{r*} \equiv P^c_r|_{\Omega t=\pi} \cos^2(\Omega t/2)$, where $\Omega$ is the single-atom Rabi frequency and $t$ is the pulse length. Of particular interest are the cases $\Omega t = \pi/\sqrt{2}$ and $\Omega t = 2\pi/\sqrt{2}$, corresponding to the two-atom $\pi$ and $2\pi$ pulses, respectively.

After excitation follows measurement, which involves making Rydberg atoms dark to imaging (i.e., either putting them in a state that scatters no photons or expelling them from the trap) and imaging the remaining bright atoms. In our case, we make Rydberg atoms dark via auto-ionization. We denote by $D$ the probability that a Rydberg atom is successfully made dark to imaging. Furthermore, we denote by $F_0$ the probability of correctly imaging the *absence* of a bright atom (true negative) and by $F_1$ the probability of correctly imaging the *presence* of a bright atom (true positive). $1 - F_0$ gives the probability of a false positive, and $1 - F_1$ gives the probability of a false negative.

Let $P_1$ be the probability of an atom being detected as present (bright) at the end of the experiment, and similarly let $P_{00}, P_{01}, P_{10}, P_{11}$ be the corresponding probabilities for atom pairs (with the sum of these being 1). These are the raw, measured values referred to as "uncorrected" hereafter.

## E.2 Determining SPAM probabilities

We now discuss the determination of the various probabilities discussed. While some of these quantities are directly measurable, some must be estimated from measurements that themselves need SPAM correction. All probabilities entering into SPAM correction calculations are summarized in Table E.1.

| Probability | Symbol | Value |
|---|---|---|
| Imaging true negative | $F_0$ | 0.99997(5) |
| Imaging true positive | $F_1$ | 0.9988(7) |
| Uncorrected survival | $S_0$ | 0.9979(3) |
| Corrected survival | $S$ | 0.9991(7) |
| Uncorrected $\|g\rangle$ transfer | $K_0$ | 0.997(1) |
| Raman scattering to $\|a\rangle$ | $R$ | 0.00104(1) |
| Corrected $\|g\rangle$ transfer | $K$ | 0.998(1) |
| Loss during $\|g\rangle$ transfer | $L$ | 0.0008(8) |
| Rydberg state detection | $D$ | 0.9996(1) |

Table E.1: SPAM probabilities entering our calculations.

We determine $F_0$ and $F_1$ by analyzing the histogram of detected photons from a typical set of images, similarly to the method described in Ref. [89]. The histograms have a zero- and one-atom peak, and we determine false positives and false negatives by the area of these peaks that extends beyond the binary detection threshold. Loss during imaging that leads to false negatives is also taken into account in $F_1$ [89]. Error bars are given by the standard deviation across the array.

We determine $S$ by taking two consecutive images. We measure the value $S_0$, defined as the probability of detecting an atom in the second image conditional on its detection in the first. Obtaining the true value of $S$ from $S_0$ requires correcting for false positives and false negatives in the second image (where we assume that false positives in the first image are negligible). One can write $S_0$ as the sum of atoms that survived and were correctly positively identified and that did not survive and were incorrectly positively identified. Solving for $S$ gives:

$$S = \frac{S_0 + F_0 - 1}{F_0 + F_1 - 1} \tag{E.1}$$

Note again that here we assume a 100% probability of an atom being present in the first image due to rearrangement (instead of the 50% probability assumed in Eq. 2.115).

By a similar procedure, we determine $K$ from a value $K_0$ measured by performing state transfer, using a ground-state push-out pulse as described in Sec. 3.1.3, repumping to the ground state, and measuring the probability of detecting an atom in a subsequent image. To obtain the true $K$, we correct $K_0$ for imaging errors as well as survival probability after imaging. We furthermore modify $K$ with the probability $R$ that a successfully transferred atom goes back to $|a\rangle$ due to trap Raman scattering in the time delay between state transfer and Rydberg excitation. We estimate $R = 0.00104(1)$ by a measure of the lifetime in the clock state at our tweezer depth [116]. We obtain:

$$K = \frac{K_0 + F_0 - 1}{S_0 + F_0 - 1}(1 - R). \tag{E.2}$$

We note that the total clock state preparation fidelity, an important quantity on its own, can be expressed as $\mathcal{F}^{\mathrm{SP}} = SK = 0.997(1)$. To measure the transfer loss probability $L$, we perform state transfer without a push-out pulse, then repump atoms to the ground state, and measure how many were lost (again correcting for imaging loss and imaging errors).

Finally, we determine $D$ by comparing the measured auto-ionization timescale to an estimate of the Rydberg lifetime, as described in Sec. 4.1.3.

## E.3 Correcting the single-atom excitation probabilities

We are now ready to solve for $P_r^c$ in terms of the uncorrected value $P_1$ and the various SPAM probabilities. For clarity, it will be convenient to define variables for the populations of the four possible single-atom states that an atom can be in at the end of Rydberg excitation: lost, $|a\rangle$, $|g\rangle$, and $|r\rangle$. We will call these populations $p_l$, $p_a$, $p_g$, and $p_r$, respectively, with their values determined by the probability tree in Fig. E.1 and summarized in Table E.2.

We can write $P_1$ as a sum of true positive identifications of bright states plus false positive identification of dark states (see "Measurement" in Fig. E.1). In terms of the values defined so far, we have:

$$P_1 = (p_a + p_g + p_r(1 - D))F_1 + (p_l + p_r D)(1 - F_0). \tag{E.3}$$

Substituting in the full expression for the populations from Table E.2 and solving for $P_r^c$, we obtain:

$$P_r^c = \frac{SF_1 + (1 - S)(1 - F_0) - LS(F_0 + F_1 - 1) - P_1}{KSD(F_0 + F_1 - 1)}. \tag{E.4}$$

For the single-atom short-time Rabi oscillations reported in Table 4.3, we observe the bare values of $P_1(\pi) = 0.0049(9)$ and $P_1(2\pi) = 0.9951(9)$, yielding SPAM-corrected pulse fidelities of $\mathcal{F}^{\text{SPAM}}(\pi) = P_r^c(\pi) = 0.9967(9)$ and $\mathcal{F}^{\text{SPAM}}(2\pi) = 1 - P_r^c(2\pi) = 0.998(1)$, respectively.

## E.4 Correcting the two-atom excitation probabilities

For the two-atom case, there are 16 possible states for an atom pair. Similarly to Table E.2, we can write the populations of each of these states in terms of the survival and transfer fidelities in Table E.1, as shown in Table E.3.

| State | Symbol | Value |
|---|---|---|
| Lost | $p_l$ | $(1 - S) + SL$ |
| $\|a\rangle$ (absolute ground state) | $p_a$ | $S(1 - L - K)$ |
| $\|g\rangle$ (clock state) | $p_g$ | $SK(1 - P_r^c)$ |
| $\|r\rangle$ (Rydberg state) | $p_r$ | $SKP_r^c$ |

Table E.2: Possible states for a single atom. Note that the sum of these populations equals unity.

We now write the experimentally measured quantities $P_{10}$, $P_{00}$, and $P_{11}$ in terms of the values in Tables E.1 and E.3. For notational simplicity, we define $\bar{F}_0 \equiv (1 - F_0)$,

| States | Symbol | Value |
|---|---|---|
| Lost, Lost | $p_{ll}$ | $\big((1-S)+SL\big)^2$ |
| {Lost, $\|a\rangle$} | $p_{la}$ | $\big((1-S)+SL\big)S(1-L-K)$ |
| {Lost, $\|g\rangle$} | $p_{lg}$ | $\big((1-S)+SL\big)SK(1-P^c_{r*})$ |
| {Lost, $\|r\rangle$} | $p_{lr}$ | $\big((1-S)+SL\big)SKP^c_{r*}$ |
| $\|aa\rangle$ | $p_{aa}$ | $S^2(1-L-K)^2$ |
| $\{\|ag\rangle\}$ | $p_{ag}$ | $S(1-L-K)SK(1-P^c_{r*})$ |
| $\{\|ar\rangle\}$ | $p_{ar}$ | $S(1-L-K)SKP^c_{r*}$ |
| $\|gg\rangle$ | $p_{gg}$ | $S^2K^2(1-P^c_{rg}-P^c_{gr}-P^c_{rr})$ |
| $\|gr\rangle$ | $p_{gr}$ | $S^2K^2P^c_{gr}$ |
| $\|rg\rangle$ | $p_{rg}$ | $S^2K^2P^c_{rg}$ |
| $\|rr\rangle$ | $p_{rr}$ | $S^2K^2P^c_{rr}$ |

Table E.3: Possible states for two atoms. Note that the sum of these populations equals unity. Terms inside {} have an implied symmetric partner, e.g. $p_{al} \equiv p_{la}$.

and similarly for $F_1$ and $D$:

$$\begin{aligned}
P_{10} =& p_{ll}(\bar{F}_0 F_0) \\
&+ p_{la}(\bar{F}_0 \bar{F}_1) \\
&+ p_{al}(F_1 F_0) \\
&+ p_{lg}(\bar{F}_0 \bar{F}_1) \\
&+ p_{gl}(F_1 F_0) \\
&+ p_{lr}(\bar{F}_0 F_0 D + \bar{F}_0 \bar{D} \bar{F}_1) \\
&+ p_{rl}(\bar{F}_0 D F_0 + F_1 \bar{D} F_0) \\
&+ p_{aa}(F_1 \bar{F}_1) \\
&+ p_{ag}(F_1 \bar{F}_1) \\
&+ p_{ga}(F_1 \bar{F}_1) \\
&+ p_{ar}(F_1 D F_0 + F_1 \bar{D} \bar{F}_1) \\
&+ p_{ra}(F_1 \bar{D} \bar{F}_1 + \bar{F}_0 D \bar{F}_1) \\
&+ p_{gg}(F_1 \bar{F}_1) \\
&+ p_{gr}(F_1 D F_0 + F_1 \bar{D} \bar{F}_1) \\
&+ p_{rg}(F_1 \bar{D} \bar{F}_1 + \bar{F}_0 D \bar{F}_1) \\
&+ p_{rr}(F_1 \bar{D} F_0 D + \bar{F}_0 D \bar{F}_1 \bar{D} + \bar{F}_0 F_0 D^2 + F_1 \bar{F}_1 \bar{D}^2),
\end{aligned} \tag{E.5}$$

$$
\begin{aligned}
P_{00} = & p_{ll}(F_0^2) \\
& + p_{la}(F_0\bar{F}_1) \\
& + p_{al}(\bar{F}_1 F_0) \\
& + p_{lg}(F_0\bar{F}_1) \\
& + p_{gl}(\bar{F}_1 F_0) \\
& + p_{lr}(F_0^2 D + F_0\bar{F}_1\bar{D}) \\
& + p_{rl}(F_0^2 D + \bar{F}_1\bar{D}F_0) \\
& + p_{aa}(\bar{F}_1{}^2) \\
& + p_{ag}(\bar{F}_1{}^2) \\
& + p_{ga}(\bar{F}_1{}^2) \\
& + p_{ar}(\bar{F}_1 F_0 D + \bar{F}_1{}^2\bar{D}) \\
& + p_{ra}(\bar{F}_1{}^2\bar{D} + F_0 D\bar{F}_1) \\
& + p_{gg}(\bar{F}_1{}^2) \\
& + p_{gr}(\bar{F}_1 F_0 D + \bar{F}_1{}^2\bar{D}) \\
& + p_{rg}(\bar{F}_1{}^2\bar{D} + F_0 D\bar{F}_1) \\
& + p_{rr}(\bar{F}_1{}^2\bar{D}^2 + F_0 D\bar{F}_1\bar{D} + F_0^2 D^2 + \bar{F}_1\bar{D}F_0 D),
\end{aligned}
\tag{E.6}
$$

$$
\begin{aligned}
P_{11} =& p_{ll}(\bar{F}_0{}^2) \\
&+p_{la}(\bar{F}_0 F_1) \\
&+p_{al}(F_1 \bar{F}_0) \\
&+p_{lg}(\bar{F}_0 F_1) \\
&+p_{gl}(F_1 \bar{F}_0) \\
&+p_{lr}(\bar{F}_0{}^2 D + \bar{F}_0 F_1 \bar{D}) \\
&+p_{rl}(\bar{F}_0{}^2 D + F_1 \bar{D} \bar{F}_0) \\
&+p_{aa}(F_1^2) \\
&+p_{ag}(F_1^2) \\
&+p_{ga}(F_1^2) \\
&+p_{ar}(F_1 \bar{F}_0 D + F_1^2 \bar{D}) \\
&+p_{ra}(F_1^2 \bar{D} + \bar{F}_0 D F_1) \\
&+p_{gg}(F_1^2) \\
&+p_{gr}(F_1 \bar{F}_0 D + F_1^2 \bar{D}) \\
&+p_{rg}(F_1^2 \bar{D} + \bar{F}_0 D F_1) \\
&+p_{rr}(F_1^2 \bar{D} + \bar{F}_0 D F_1 \bar{D} + \bar{F}_0{}^2 D^2 \bar{D} + F_1 \bar{D} \bar{F}_0 D).
\end{aligned}
\tag{E.7}
$$

Note that $P_{01} = 1 - P_{10} - P_{00} - P_{11}$. Thus, with the three above equations, we can solve for $P^c_{gg}$, $P^c_{rg}$, $P^c_{gr}$, and $P^c_{rr}$ in terms of the experimentally measured values $P_{00}$, $P_{\{10\}}$, $P_{[10]}$, and $P_{11}$ (reported in Table 4.3). The full analytic expressions for these solutions are cumbersome and not shown.

# BIBLIOGRAPHY


[1] Gerlach, W. and Stern, O. *Der experimentelle Nachweis der Richtungsquantelung im Magnetfeld*. Zeitschrift für Physik **9**, 349–352 (1922).

[2] Sakurai, J.J. and Napolitano, J. *Modern Quantum Mechanics*. Addison-Wesley, 2nd ed. (1994).

[3] Bell, J.S. *On the Einstein Podolsky Rosen paradox*. Physics Physique Fizika **1**, 195–200 (1964).

[4] Hensen, B., Bernien, H., Dréau, A.E. et al. *Loophole-free Bell inequality violation using electron spins separated by 1.3 kilometres*. Nature **526**, 682–686 (2015).

[5] Nielsen, M.A. and Chuang, I.L. *Quantum Computation and Quantum Information*. Cambridge University Press, 10th ed. (2010). ISBN 978-1-107-00217-3.

[6] Cirac, J.I. and Zoller, P. *A scalable quantum computer with ions in an array of microtraps*. Nature **404**, 579–581 (2000).

[7] Monz, T., Schindler, P., Barreiro, J.T. et al. *14-Qubit Entanglement: Creation and Coherence*. Physical Review Letters **106**, 130506 (2011).

[8] Zhang, J., Pagano, G., Hess, P.W. et al. *Observation of a many-body dynamical phase transition with a 53-qubit quantum simulator*. Nature **551**, 601–604 (2017).

[9] Song, C., Xu, K., Li, H. et al. *Generation of multicomponent atomic Schrödinger cat states of up to 20 qubits*. Science **365**, 574–577 (2019).

[10] Arute, F., Arya, K., Babbush, R. et al. *Quantum supremacy using a programmable superconducting processor*. Nature **574**, 505–510 (2019).

[11] Oelker, E., Hutson, R.B., Kennedy, C.J. et al. *Demonstration of* $4.8 \times 10^{-17}$ *stability at 1 s for two independent optical clocks*. Nature Photonics **13**, 714–719 (2019).

[12] Bothwell, T., Kedar, D., Oelker, E. et al. *JILA SrI optical lattice clock with uncertainty of* $2.0 \times 10^{-18}$. Metrologia **56**, 065004 (2019).

[13] Schioppo, M., Brown, R.C., McGrew, W.F. et al. *Ultrastable optical clock with two cold-atom ensembles*. Nature Photonics **11**, 48–52 (2017).

[14] McGrew, W.F., Zhang, X., Fasano, R.J. et al. *Atomic clock performance enabling geodesy below the centimetre level*. Nature **564**, 87–90 (2018).

[15] Ludlow, A.D., Boyd, M.M., Ye, J., Peik, E. and Schmidt, P.O. *Optical atomic clocks*. Reviews of Modern Physics **87**, 637–701 (2015).

[16] Gil, L.I.R., Mukherjee, R., Bridge, E.M., Jones, M.P.A. and Pohl, T. *Spin Squeezing in a Rydberg Lattice Clock*. Physical Review Letters **112**, 103601 (2014).

[17] Pezzè, L., Smerzi, A., Oberthaler, M.K., Schmied, R. and Treutlein, P. *Quantum metrology with nonclassical states of atomic ensembles*. Reviews of Modern Physics **90**, 035005 (2018).

[18] Kurosu, T. and Shimizu, F. *Laser Cooling and Trapping of Calcium and Strontium*. Japanese Journal of Applied Physics **29**, L2127–L2129 (1990).

[19] Raab, E.L., Prentiss, M., Cable, A., Chu, S. and Pritchard, D.E. *Trapping of Neutral Sodium Atoms with Radiation Pressure*. Physical Review Letters **59**, 2631–2634 (1987).

[20] Katori, H., Ido, T., Isoya, Y. and Kuwata-Gonokami, M. *Magneto-Optical Trapping and Cooling of Strontium Atoms down to the Photon Recoil Temperature*. Physical Review Letters **82**, 1116–1119 (1999).

[21] Metcalf, H.J. and van der Straten, P. *Laser Cooling and Trapping*. Springer New York (1999). ISBN 978-0-387-98728-6.

[22] Dalibard, J. and Cohen-Tannoudji, C. *Laser cooling below the Doppler limit by polarization gradients: simple theoretical models*. Journal of the Optical Society of America B **6**, 2023 (1989).

[23] Stellmer, S. *Degenerate quantum gases of strontium*. PhD thesis, University of Innsbruck (2013).

[24] Takamoto, M., Hong, F.L., Higashi, R. and Katori, H. *An optical lattice clock*. Nature **435**, 321–324 (2005).

[25] Boyd, M.M., Ludlow, A.D., Blatt, S. et al. *$^{87}$Sr Lattice Clock with Inaccuracy below* $10^{-15}$. Physical Review Letters **98**, 083002 (2007).

[26] Ludlow, A.D., Boyd, M.M., Zelevinsky, T. et al. *Systematic Study of the $^{87}$Sr Clock Transition in an Optical Lattice*. Physical Review Letters **96**, 033003 (2006).

[27] Oskay, W.H., Diddams, S.A., Donley, E.A. et al. *Single-Atom Optical Clock with High Accuracy*. Physical Review Letters **97**, 020801 (2006).

[28] Ludlow, A.D., Zelevinsky, T., Campbell, G.K. et al. *Sr Lattice Clock at $1 \times 10^{-16}$ Fractional Uncertainty by Remote Optical Evaluation with a Ca Clock*. Science **319**, 1805–1808 (2008).

[29] Brewer, S.M., Chen, J.S., Hankin, A.M. et al. *$^{27}Al^{+}$ Quantum-Logic Clock with a Systematic Uncertainty below $10^{-18}$*. Physical Review Letters **123**, 033201 (2019).

[30] Miranda, M., Inoue, R., Okuyama, Y., Nakamoto, A. and Kozuma, M. *Site-resolved imaging of ytterbium atoms in a two-dimensional optical lattice*. Physical Review A **91**, 063414 (2015).

[31] Yamamoto, R., Kobayashi, J., Kuno, T., Kato, K. and Takahashi, Y. *An ytterbium quantum gas microscope with narrow-line laser cooling*. New Journal of Physics **18**, 023016 (2016).

[32] Hu, Z. and Kimble, H.J. *Observation of a single atom in a magneto-optical trap*. Optics Letters **19**, 1888 (1994).

[33] Schlosser, N., Reymond, G., Protsenko, I. and Grangier, P. *Sub-poissonian loading of single atoms in a microscopic dipole trap*. Nature **411**, 1024–1027 (2001).

[34] Kuhr, S., Alt, W., Schrader, D. et al. *Deterministic Delivery of a Single Atom*. Science **293**, 278–280 (2001).

[35] Kaufman, A.M., Lester, B.J. and Regal, C.A. *Cooling a Single Atom in an Optical Tweezer to Its Quantum Ground State*. Physical Review X **2**, 041014 (2012).

[36] Thompson, J.D., Tiecke, T.G., Zibrov, A.S., Vuletić, V. and Lukin, M.D. *Coherence and Raman sideband cooling of a single atom in an optical tweezer*. Physical Review Letters **110**, 133001 (2013).

[37] Nelson, K.D., Li, X. and Weiss, D.S. *Imaging single atoms in a three-dimensional array*. Nature Physics **3**, 556–560 (2007).

[38] Bakr, W.S., Gillen, J.I., Peng, A., Fölling, S. and Greiner, M. *A quantum gas microscope for detecting single atoms in a Hubbard-regime optical lattice*. Nature **462**, 74–77 (2009).

[39] Sherson, J.F., Weitenberg, C., Endres, M. et al. *Single-atom-resolved fluorescence imaging of an atomic Mott insulator*. Nature **467**, 68–72 (2010).

[40] Cheuk, L.W., Nichols, M.A., Okan, M. et al. *Quantum-Gas Microscope for Fermionic Atoms*. Physical Review Letters **114**, 193001 (2015).

[41] Parsons, M.F., Huber, F., Mazurenko, A. et al. *Site-Resolved Imaging of Fermionic $^6$Li in an Optical Lattice*. Physical Review Letters **114**, 213002 (2015).

[42] Haller, E., Hudson, J., Kelly, A. et al. *Single-atom imaging of fermions in a quantum-gas microscope*. Nature Physics **11**, 738–742 (2015).

[43] Edge, G.J.A., Anderson, R., Jervis, D. et al. *Imaging and addressing of individual fermionic atoms in an optical lattice*. Physical Review A **92**, 063406 (2015).

[44] Bergamini, S., Darquié, B., Jones, M. et al. *Holographic generation of microtrap arrays for single atoms by use of a programmable phase modulator*. Journal of the Optical Society of America B **21**, 1889 (2004).

[45] Nogrette, F., Labuhn, H., Ravets, S. et al. *Single-Atom Trapping in Holographic 2D Arrays of Microtraps with Arbitrary Geometries*. Physical Review X **4**, 021034 (2014).

[46] Kim, H., Lee, W., Lee, H.g. et al. *In situ single-atom array synthesis using dynamic holographic optical tweezers*. Nature Communications **7**, 13317 (2016).

[47] Kaufman, A.M., Lester, B.J., Reynolds, C.M. et al. *Two-particle quantum interference in tunnel-coupled optical tweezers*. Science **345**, 306–309 (2014).

[48] Endres, M., Bernien, H., Keesling, A. et al. *Atom-by-atom assembly of defect-free one-dimensional cold atom arrays*. Science **354**, 1024–1027 (2016).

[49] Dumke, R., Volk, M., Müther, T. et al. *Micro-optical Realization of Arrays of Selectively Addressable Dipole Traps: A Scalable Configuration for Quantum Computation with Atomic Qubits*. Physical Review Letters **89**, 097903 (2002).

[50] Piotrowicz, M.J., Lichtman, M., Maller, K. et al. *Two-dimensional lattice of blue-detuned atom traps using a projected Gaussian beam array*. Physical Review A **88**, 013420 (2013).

[51] Lichtman, M.T. *Coherent operations, entanglement, and progress toward quantum search in a large 2D array of neutral atom qubits*. PhD thesis, University of Wisconsin (2015).

[52] Miroshnychenko, Y., Alt, W., Dotsenko, I. et al. *Quantum engineering: An atom-sorting machine*. Nature **442**, 151–151 (2006).

[53] Barredo, D., de Leseleuc, S., Lienhard, V., Lahaye, T. and Browaeys, A. *An atom-by-atom assembler of defect-free arbitrary two-dimensional atomic arrays*. Science **354**, 1021–1023 (2016).

[54] Kumar, A., Wu, T.Y., Giraldo, F. and Weiss, D.S. *Sorting ultracold atoms in a three-dimensional optical lattice in a realization of Maxwell's demon*. Nature **561**, 83–87 (2018).

[55] Kaufman, A.M., Lester, B.J., Foss-Feig, M. et al. *Entangling two transportable neutral atoms via local spin exchange*. Nature **527**, 208–211 (2015).

[56] Greiner, M., Mandel, O., Esslinger, T., Hänsch, T.W. and Bloch, I. *Quantum phase transition from a superfluid to a Mott insulator in a gas of ultracold atoms*. Nature **415**, 39–44 (2002).

[57] Greif, D., Parsons, M.F., Mazurenko, A. et al. *Site-resolved imaging of a fermionic Mott insulator*. Science **351**, 953–957 (2016).

[58] Brown, P.T., Mitra, D., Guardado-Sanchez, E. et al. *Spin-imbalance in a 2D Fermi-Hubbard system*. Science **357**, 1385–1388 (2017).

[59] Raimond, J.M., Brune, M. and Haroche, S. *Manipulating quantum entanglement with atoms and photons in a cavity*. Reviews of Modern Physics **73**, 565–582 (2001).

[60] Landig, R., Hruby, L., Dogra, N. et al. *Quantum phases from competing short- and long-range interactions in an optical lattice*. Nature **532**, 476–479 (2016).

[61] Braverman, B., Kawasaki, A., Pedrozo-Peñafiel, E. et al. *Near-Unitary Spin Squeezing in $^{171}Yb$*. Physical Review Letters **122**, 223203 (2019).

[62] Davis, E.J., Bentsen, G., Homeier, L., Li, T. and Schleier-Smith, M.H. *Photon-Mediated Spin-Exchange Dynamics of Spin-1 Atoms*. Physical Review Letters **122**, 010405 (2019).

[63] Samutpraphoot, P., Đorđević, T., Ocola, P.L. et al. *Strong Coupling of Two Individually Controlled Atoms via a Nanophotonic Cavity*. Physical Review Letters **124**, 063602 (2020).

[64] Jaksch, D., Cirac, J.I., Zoller, P. et al. *Fast Quantum Gates for Neutral Atoms*. Physical Review Letters **85**, 2208–2211 (2000).

[65] Lukin, M.D., Fleischhauer, M., Cote, R. et al. *Dipole Blockade and Quantum Information Processing in Mesoscopic Atomic Ensembles*. Physical Review Letters **87**, 037901 (2001).

[66] Urban, E., Johnson, T.A., Henage, T. et al. *Observation of Rydberg blockade between two atoms*. Nature Physics **5**, 110–114 (2009).

[67] Gaëtan, A., Miroshnychenko, Y., Wilk, T. et al. *Observation of collective excitation of two individual atoms in the Rydberg blockade regime*. Nature Physics **5**, 115–118 (2009).

[68] Isenhower, L., Urban, E., Zhang, X.L. et al. *Demonstration of a Neutral Atom Controlled-NOT Quantum Gate*. Physical Review Letters **104**, 010503 (2010).

[69] Wilk, T., Gaëtan, A., Evellin, C. et al. *Entanglement of Two Individual Neutral Atoms Using Rydberg Blockade*. Physical Review Letters **104**, 010502 (2010).

[70] Schauß, P., Cheneau, M., Endres, M. et al. *Observation of spatially ordered structures in a two-dimensional Rydberg gas*. Nature **491**, 87–91 (2012).

[71] Guardado-Sanchez, E., Brown, P.T., Mitra, D. et al. *Probing the Quench Dynamics of Antiferromagnetic Correlations in a 2D Quantum Ising Spin System*. Physical Review X **8**, 021069 (2018).

[72] Maller, K.M., Lichtman, M.T., Xia, T. et al. *Rydberg-blockade controlled-not gate and entanglement in a two-dimensional array of neutral-atom qubits*. Physical Review A **92**, 022336 (2015).

[73] Labuhn, H., Barredo, D., Ravets, S. et al. *Tunable two-dimensional arrays of single Rydberg atoms for realizing quantum Ising models*. Nature **534**, 667–670 (2016).

[74] Bernien, H., Schwartz, S., Keesling, A. et al. *Probing many-body dynamics on a 51-atom quantum simulator*. Nature **551**, 579–584 (2017).

[75] Kim, H., Park, Y., Kim, K., Sim, H.S. and Ahn, J. *Detailed Balance of Thermalization Dynamics in Rydberg-Atom Quantum Simulators*. Physical Review Letters **120**, 180502 (2018).

[76] Lienhard, V., de Léséleuc, S., Barredo, D. et al. *Observing the Space- and Time-Dependent Growth of Correlations in Dynamically Tuned Synthetic Ising Models with Antiferromagnetic Interactions*. Physical Review X **8**, 021070 (2018).

[77] Keesling, A., Omran, A., Levine, H. et al. *Quantum Kibble–Zurek mechanism and critical dynamics on a programmable Rydberg simulator*. Nature **568**, 207–211 (2019).

[78] de Léséleuc, S., Lienhard, V., Scholl, P. et al. *Observation of a symmetry-protected topological phase of interacting bosons with Rydberg atoms*. Science **365**, 775–780 (2019).

[79] Baumgärtner, A. *A new apparatus for trapping and manipulating single Strontium atoms*. Master's thesis, University of Heidelberg (2017).

[80] NIST, P.M.L. *Physical Reference Data*.

[81] Daley, A.J., Boyd, M.M., Ye, J. and Zoller, P. *Quantum Computing with Alkaline-Earth-Metal Atoms*. Physical Review Letters **101**, 170504 (2008).

[82] Goban, A., Hutson, R.B., Marti, G.E. et al. *Emergence of multi-body interactions in a fermionic lattice clock*. Nature **563**, 369–373 (2018).

[83] Saskin, S., Wilson, J.T., Grinkemeyer, B. and Thompson, J.D. *Narrow-Line Cooling and Imaging of Ytterbium Atoms in an Optical Tweezer Array*. Physical Review Letters **122**, 143002 (2019).

[84] Hachisu, H., Miyagishi, K., Porsev, S.G. et al. *Trapping of Neutral Mercury Atoms and Prospects for Optical Lattice Clocks*. Physical Review Letters **100**, 053001 (2008).

[85] Brickman, K.A., Chang, M.S., Acton, M. et al. *Magneto-optical trapping of cadmium*. Physical Review A **76**, 043411 (2007).

[86] Yasuda, M., Kishimoto, T., Takamoto, M. and Katori, H. *Photoassociation spectroscopy of $^{88}$Sr: Reconstruction of the wave function near the last node*. Physical Review A **73**, 011403 (2006).

[87] Sansonetti, J.E. and Nave, G. *Wavelengths, Transition Probabilities, and Energy Levels for the Spectrum of Neutral Strontium (SrI)*. Journal of Physical and Chemical Reference Data **39**, 033103 (2010).

[88] Safronova, M.S., Porsev, S.G., Safronova, U.I., Kozlov, M.G. and Clark, C.W. *Blackbody-radiation shift in the Sr optical atomic clock*. Physical Review A **87**, 012509 (2013).

[89] Cooper, A., Covey, J.P., Madjarov, I.S. et al. *Alkaline-Earth Atoms in Optical Tweezers*. Physical Review X **8**, 041055 (2018).

[90] Steck, D.A. *Quantum and Atom Optics*. Available online at http://steck.us/teaching (2007).

[91] Grimm, R., Weidemüller, M. and Ovchinnikov, Y.B. *Optical dipole traps for neutral atoms*. arXiv:physics/9902072 (1999).

[92] Goodman, J.W. *Introduction to Fourier Optics*. McGraw-Hill, 2nd ed. (1996). ISBN 0070242542.

[93] Born, M. and Wolf, E. *Principles of Optics*. Cambridge University Press, 7th ed. (1999).

[94] Melles-Griot, C. *Gaussian Beam Optics*.

[95] Kim, H., Han, H.S. and Cho, D. *Magic Polarization for Optical Trapping of Atoms without Stark-Induced Dephasing*. Physical Review Letters **111**, 243004 (2013).

[96] Rosenband, T., Grimes, D.D. and Ni, K.K. *Elliptical polarization for molecular Stark shift compensation in deep optical traps*. Optics Express **26**, 19821 (2018).

[97] Norcia, M.A., Young, A.W. and Kaufman, A.M. *Microscopic Control and Detection of Ultracold Strontium in Optical-Tweezer Arrays*. Physical Review X **8**, 041054 (2018).

[98] Ido, T. and Katori, H. *Recoil-Free Spectroscopy of Neutral Sr Atoms in the Lamb-Dicke Regime*. Physical Review Letters **91**, 053001 (2003).

[99] Young, A.W., Eckner, W.J., Milner, W.R. et al. *Half-minute-scale atomic coherence and high relative stability in a tweezer clock*. Nature **588**, 408–413 (2020).

[100] Norcia, M.A., Young, A.W., Eckner, W.J. et al. *Seconds-scale coherence on an optical clock transition in a tweezer array*. Science **366**, 93–97 (2019).

[101] Stellmer, S., Pasquiou, B., Grimm, R. and Schreck, F. *Laser Cooling to Quantum Degeneracy*. Physical Review Letters **110**, 263003 (2013).

[102] Grünzweig, T., Hilliard, A., McGovern, M. and Andersen, M.F. *Near-deterministic preparation of a single atom in an optical microtrap*. Nature Physics **6**, 951–954 (2010).

[103] Carpentier, A.V., Fung, Y.H., Sompet, P. et al. *Preparation of a single atom in an optical microtrap*. Laser Physics Letters **10**, 125501 (2013).

[104] Lester, B.J., Luick, N., Kaufman, A.M., Reynolds, C.M. and Regal, C.A. *Rapid Production of Uniformly Filled Arrays of Neutral Atoms*. Physical Review Letters **115**, 073003 (2015).

[105] Brown, M.O., Thiele, T., Kiehl, C., Hsu, T.W. and Regal, C.A. *Gray-Molasses Optical-Tweezer Loading: Controlling Collisions for Scaling Atom-Array Assembly*. Physical Review X **9**, 011057 (2019).

[106] Akatsuka, T., Takamoto, M. and Katori, H. *Three-dimensional optical lattice clock with bosonic $^{88}$Sr atoms*. Physical Review A **81**, 023402 (2010).

[107] Bakr, W.S., Peng, A., Tai, M.E. et al. *Probing the Superfluid-to-Mott Insulator Transition at the Single-Atom Level*. Science **329**, 547–550 (2010).

[108] Gallagher, A. and Pritchard, D.E. *Exoergic collisions of cold Na*-Na*. Physical Review Letters **63**, 957–960 (1989).

[109] Zelevinsky, T., Boyd, M.M., Ludlow, A.D. et al. *Narrow Line Photoassociation in an Optical Lattice*. Physical Review Letters **96**, 203201 (2006).

[110] Diedrich, F., Bergquist, J.C., Itano, W.M. and Wineland, D.J. *Laser Cooling to the Zero-Point Energy of Motion*. Physical Review Letters **62**, 403–406 (1989).

[111] Monroe, C., Meekhof, D.M., King, B.E. et al. *Resolved-Sideband Raman Cooling of a Bound Atom to the 3D Zero-Point Energy*. Physical Review Letters **75**, 4011–4014 (1995).

[112] Wineland, D.J. and Itano, W.M. *Laser cooling of atoms*. Physical Review A **20**, 1521–1540 (1979).

[113] Mølmer, K., Castin, Y. and Dalibard, J. *Monte Carlo wave-function method in quantum optics*. Journal of the Optical Society of America B **10**, 524 (1993).

[114] Taïeb, R., Dum, R., Cirac, J.I., Marte, P. and Zoller, P. *Cooling and localization of atoms in laser-induced potential wells*. Physical Review A **49**, 4876–4887 (1994).

[115] Ivanov, V.V. and Gupta, S. *Laser-driven Sisyphus cooling in an optical dipole trap*. Physical Review A **84**, 063417 (2011).

[116] Covey, J.P., Madjarov, I.S., Cooper, A. and Endres, M. *2000-Times Repeated Imaging of Strontium Atoms in Clock-Magic Tweezer Arrays*. Physical Review Letters **122**, 173201 (2019).

[117] de Léséleuc, S., Barredo, D., Lienhard, V., Browaeys, A. and Lahaye, T. *Analysis of imperfections in the coherent optical excitation of single atoms to Rydberg states*. Physical Review A **97**, 053803 (2018).

[118] Tarallo, M.G. *Development of a Strontium optical lattice clock*. PhD thesis, University of Pisa (2009).

[119] Levine, H., Keesling, A., Omran, A. et al. *High-Fidelity Control and Entanglement of Rydberg-Atom Qubits*. Physical Review Letters **121**, 123603 (2018).

[120] Di Domenico, G., Schilt, S. and Thomann, P. *Simple approach to the relation between laser frequency noise and laser line shape*. Applied Optics **49**, 4801 (2010).

[121] Savard, T.A., O'Hara, K.M. and Thomas, J.E. *Laser-noise-induced heating in far-off resonance optical traps*. Physical Review A **56**, R1095–R1098 (1997).

[122] Cook, R.J. *Atomic motion in resonant radiation: An application of Ehrenfest's theorem*. Physical Review A **20**, 224–228 (1979).

[123] Martinez-Dorantes, M., Alt, W., Gallego, J. et al. *State-dependent fluorescence of neutral atoms in optical potentials*. Physical Review A **97**, 023410 (2018).

[124] Dörscher, S., Schwarz, R., Al-Masoudi, A. et al. *Lattice-induced photon scattering in an optical lattice clock*. Physical Review A **97**, 063419 (2018).

[125] Chu, S., Hollberg, L., Bjorkholm, J.E., Cable, A. and Ashkin, A. *Three-dimensional viscous confinement and cooling of atoms by resonance radiation pressure*. Physical Review Letters **55**, 48–51 (1985).

[126] Lett, P.D., Watts, R.N., Westbrook, C.I. et al. *Observation of Atoms Laser Cooled below the Doppler Limit*. Physical Review Letters **61**, 169–172 (1988).

[127] Alt, W., Schrader, D., Kuhr, S. et al. *Single atoms in a standing-wave dipole trap*. Physical Review A **67**, 033403 (2003).

[128] Tuchendler, C., Lance, A.M., Browaeys, A., Sortais, Y.R.P. and Grangier, P. *Energy distribution and cooling of a single atom in an optical tweezer*. Physical Review A **78**, 033425 (2008).

[129] Meekhof, D.M., Monroe, C., King, B.E., Itano, W.M. and Wineland, D.J. *Generation of Nonclassical Motional States of a Trapped Atom*. Physical Review Letters **76**, 1796–1799 (1996).

[130] Bergschneider, A., Klinkhamer, V.M., Becher, J.H. et al. *Spin-resolved single-atom imaging of $^6$Li in free space*. Physical Review A **97**, 063613 (2018).

[131] Andor. *iXon Ultra Hardware Guide* (2012).

[132] Araneda, G., Walser, S., Colombe, Y. et al. *Wavelength-scale errors in optical localization due to spin–orbit coupling of light*. Nature Physics **15**, 17–21 (2019).

[133] Gurov, M.G., Gurova, E.G. and Dmitriev, A.K. *Repumping of Strontium Atoms in a Magneto-Optical Trap on Singlet Transitions*. Russian Physics Journal **57**, 1138–1148 (2014).

[134] Hunter, L.R., Walker, W.A. and Weiss, D.S. *Observation of an atomic Stark–electric-quadrupole interference*. Physical Review Letters **56**, 823–826 (1986).

[135] Kim, D., Keesling, A., Omran, A. et al. *Large-scale uniform optical focus array generation with a phase spatial light modulator*. Optics Letters **44**, 3178 (2019).

[136] Qiu, E. *Generation of arbitrary 2D Arrays of Optical Tweezers*. Master's thesis, University of Toronto (2018).

[137] Saleh, B.E.A. and Teich, M.C. *Fundamentals of Photonics*. Wiley-Interscience, 2nd ed. (2007).

[138] Madjarov, I.S., Cooper, A., Shaw, A.L. et al. *An Atomic-Array Optical Clock with Single-Atom Readout*. Physical Review X **9**, 041052 (2019).

[139] Shaw, A.L. *Private communication*.

[140] Santra, R., Christ, K.V. and Greene, C.H. *Properties of metastable alkaline-earth-metal atoms calculated using an accurate effective core potential*. Physical Review A **69**, 042510 (2004).

[141] Taichenachev, A., Yudin, V., Oates, C. et al. *Magnetic Field-Induced Spectroscopy of Forbidden Optical Transitions with Application to Lattice-Based Optical Atomic Clocks*. Physical Review Letters **96**, 083001 (2006).

[142] Boyd, M.M. *High Precision Spectroscopy of Strontium in an Optical Lattice: Towards a New Standard for Frequency and Time*. PhD thesis, University of Colorado (2007).

[143] BIPM. *Recommended values of standard frequencies for applications including the practical realization of the metre and secondary representations of the definition of the second* (2017).

[144] Ovsiannikov, V.D., Derevianko, A. and Gibble, K. *Rydberg Spectroscopy in an Optical Lattice: Blackbody Thermometry for Atomic Clocks*. Physical Review Letters **107**, 093003 (2011).

[145] Origlia, S., Pramod, M.S., Schiller, S. et al. *Towards an optical clock for space: Compact, high-performance optical lattice clock based on bosonic atoms*. Physical Review A **98**, 053443 (2018).

[146] Gibble, K. *Scattering of Cold-Atom Coherences by Hot Atoms: Frequency Shifts from Background-Gas Collisions*. Physical Review Letters **110**, 180802 (2013).

[147] Brusch, A., Le Targat, R., Baillard, X., Fouché, M. and Lemonde, P. *Hyperpolarizability Effects in a Sr Optical Lattice Clock*. Physical Review Letters **96**, 103003 (2006).

[148] Brown, R.C., Phillips, N.B., Beloy, K. et al. *Hyperpolarizability and Operational Magic Wavelength in an Optical Lattice Clock*. Physical Review Letters **119**, 253001 (2017).

[149] Taichenachev, A.V., Yudin, V.I., Ovsiannikov, V.D. and Pal'chikov, V.G. *Optical Lattice Polarization Effects on Hyperpolarizability of Atomic Clock Transitions*. Physical Review Letters **97**, 173601 (2006).

[150] Madjarov, I.S., Covey, J.P., Shaw, A.L. et al. *High-fidelity entanglement and detection of alkaline-earth Rydberg atoms*. Nature Physics **16**, 857–861 (2020).

[151] Kale, A. *Towards High Fidelity Quantum Computation and Simulation with Rydberg Atoms*. Bachelor's thesis, California Institute of Technology (2020).

[152] Ma, L.S., Jungner, P., Ye, J. and Hall, J.L. *Delivering the same optical frequency at two places: accurate cancellation of phase noise introduced by an optical fiber or other time-varying path*. Optics Letters **19**, 1777 (1994).

[153] Dick, G.J. *Local oscillator induced instabilities in trapped ion frequency standards*. Proceedings of the 19th Annual Precise Time and Time Interval Systems and Applications pages 133 – 147 (1987).

[154] Santarelli, G., Audoin, C., Makdissi, A. et al. *Frequency stability degradation of an oscillator slaved to a periodically interrogated atomic resonator*. IEEE Transactions on Ultrasonics, Ferroelectrics and Frequency Control **45**, 887–894 (1998).

[155] Westergaard, P., Lodewyck, J. and Lemonde, P. *Minimizing the dick effect in an optical lattice clock*. IEEE Transactions on Ultrasonics, Ferroelectrics and Frequency Control **57**, 623–628 (2010).

[156] Schulte, M., Lisdat, C., Schmidt, P.O., Sterr, U. and Hammerer, K. *Spin squeezing can only improve clocks with small atom number*. arXiv:1911.00882 (2019).

[157] Numata, K., Kemery, A. and Camp, J. *Thermal-Noise Limit in the Frequency Stabilization of Lasers with Rigid Cavities*. Physical Review Letters **93**, 250602 (2004).

[158] Jiang, Y.Y., Ludlow, A.D., Lemke, N.D. et al. *Making optical atomic clocks more stable with $10^{-16}$-level laser stabilization*. Nature Photonics **5**, 158–161 (2011).

[159] Robinson, J.M., Oelker, E., Milner, W.R. et al. *Crystalline optical cavity at 4 K with thermal-noise-limited instability and ultralow drift*. Optica **6**, 240 (2019).

[160] Nicholson, T., Campbell, S., Hutson, R. et al. *Systematic evaluation of an atomic clock at $2 \times 10^{-18}$ total uncertainty*. Nature Communications **6**, 6896 (2015).

[161] Services, H.T. *Stable32 User Manual* (2008).

[162] UFFC, H..I. *Stable32*.

[163] Grotti, J., Koller, S., Vogt, S. et al. *Geodesy and metrology with a transportable optical clock*. Nature Physics **14**, 437–441 (2018).

[164] Blatt, S., Ludlow, A.D., Campbell, G.K. et al. *New Limits on Coupling of Fundamental Constants to Gravity Using $^{87}$Sr Optical Lattice Clocks*. Physical Review Letters **100**, 140801 (2008).

[165] Pruttivarasin, T., Ramm, M., Porsev, S.G. et al. *Michelson–Morley analogue for electrons using trapped ions to test Lorentz symmetry*. Nature **517**, 592–595 (2015).

[166] Scazza, F., Hofrichter, C., Höfer, M. et al. *Observation of two-orbital spin-exchange interactions with ultracold SU(N)-symmetric fermions*. Nature Physics **10**, 779–784 (2014).

[167] McGrew, W.F., Zhang, X., Leopardi, H. et al. *Towards the optical second: verifying optical clocks at the SI limit*. Optica **6**, 448 (2019).

[168] Kim, K., Chang, M.S., Korenblit, S. et al. *Quantum simulation of frustrated Ising spins with trapped ions*. Nature **465**, 590–593 (2010).

[169] Gross, C. and Bloch, I. *Quantum simulations with ultracold atoms in optical lattices*. Science **357**, 995–1001 (2017).

[170] Kaubruegger, R., Silvi, P., Kokail, C. et al. *Variational Spin-Squeezing Algorithms on Programmable Quantum Sensors*. Physical Review Letters **123**, 260505 (2019).

[171] Koczor, B., Endo, S., Jones, T., Matsuzaki, Y. and Benjamin, S.C. *Variational-state quantum metrology*. New Journal of Physics **22** (2020).

[172] Kómár, P., Kessler, E.M., Bishof, M. et al. *A quantum network of clocks*. Nature Physics **10**, 582–587 (2014).

[173] Pagano, G., Scazza, F. and Foss-Feig, M. *Fast and Scalable Quantum Information Processing with Two-Electron Atoms in Optical Tweezer Arrays*. Advanced Quantum Technologies **2**, 1800067 (2019).

[174] Covey, J.P., Sipahigil, A., Szoke, S. et al. *Telecom-Band Quantum Optics with Ytterbium Atoms and Silicon Nanophotonics*. Physical Review Applied **11**, 034044 (2019).

[175] Huntemann, N., Okhapkin, M., Lipphardt, B. et al. *High-Accuracy Optical Clock Based on the Octupole Transition in* $^{171}Yb^{+}$. Physical Review Letters **108**, 090801 (2012).

[176] Tan, T.R., Kaewuam, R., Arnold, K.J. et al. *Suppressing Inhomogeneous Broadening in a Lutetium Multi-ion Optical Clock*. Physical Review Letters **123**, 063201 (2019).

[177] Al-Masoudi, A., Dörscher, S., Häfner, S., Sterr, U. and Lisdat, C. *Noise and instability of an optical lattice clock*. Physical Review A **92**, 063814 (2015).

[178] Nemitz, N., Jørgensen, A.A., Yanagimoto, R., Bregolin, F. and Katori, H. *Modeling light shifts in optical lattice clocks*. Physical Review A **99**, 033424 (2019).

[179] Leroux, I.D., Scharnhorst, N., Hannig, S. et al. *On-line estimation of local oscillator noise and optimisation of servo parameters in atomic clocks*. Metrologia **54**, 307–321 (2017).

[180] Koller, S.B., Grotti, J., Vogt, S. et al. *Transportable Optical Lattice Clock with $7 \times 10^{-17}$ Uncertainty*. Physical Review Letters **118**, 073601 (2017).

[181] Campbell, S.L., Hutson, R.B., Marti, G.E. et al. *A Fermi-degenerate three-dimensional optical lattice clock*. Science **358**, 90–94 (2017).

[182] Swallows, M.D., Bishof, M., Lin, Y. et al. *Suppression of Collisional Shifts in a Strongly Interacting Lattice Clock*. Science **331**, 1043–1046 (2011).

[183] Chang, D.E., Ye, J. and Lukin, M.D. *Controlling dipole-dipole frequency shifts in a lattice-based optical atomic clock*. Physical Review A **69**, 023810 (2004).

[184] Hutson, R.B., Goban, A., Marti, G.E. et al. *Engineering Quantum States of Matter for Atomic Clocks in Shallow Optical Lattices*. Physical Review Letters **123** (2019).

[185] Riehle, F. *Frequency Standards*. Wiley (2003). ISBN 9783527402304.

[186] Norcia, M.A. *Coupling atoms to cavities using narrow linewidth optical transitions: applications to frequency metrology*. Journal of Physics B: Atomic, Molecular and Optical Physics **52**, 193001 (2019).

[187] Saffman, M., Walker, T.G. and Mølmer, K. *Quantum information with Rydberg atoms*. Reviews of Modern Physics **82**, 2313–2363 (2010).

[188] Browaeys, A. and Lahaye, T. *Many-body physics with individually controlled Rydberg atoms*. Nature Physics **16**, 132–142 (2020).

[189] Zeiher, J., van Bijnen, R., Schauß, P. et al. *Many-body interferometry of a Rydberg-dressed spin lattice*. Nature Physics **12**, 1095–1099 (2016).

[190] Ye, S., Zhang, X., Killian, T.C. et al. *Production of very-high-n strontium Rydberg atoms*. Physical Review A **88**, 043430 (2013).

[191] Couturier, L., Nosske, I., Hu, F. et al. *Measurement of the strontium triplet Rydberg series by depletion spectroscopy of ultracold atoms*. Physical Review A **99**, 022503 (2019).

[192] Ding, R., Whalen, J.D., Kanungo, S.K. et al. *Spectroscopy of $^{87}$Sr triplet Rydberg states*. Physical Review A **98**, 042505 (2018).

[193] Graham, T.M., Kwon, M., Grinkemeyer, B. et al. *Rydberg-Mediated Entanglement in a Two-Dimensional Neutral Atom Qubit Array*. Physical Review Letters **123**, 230501 (2019).

[194] Browaeys, A., Barredo, D. and Lahaye, T. *Experimental investigations of dipole–dipole interactions between a few Rydberg atoms*. Journal of Physics B: Atomic, Molecular and Optical Physics **49**, 152001 (2016).

[195] Choi, J. *Private communication*.

[196] Vaillant, C.L., Jones, M.P.A. and Potvliege, R.M. *Long-range Rydberg–Rydberg interactions in calcium, strontium and ytterbium*. Journal of Physics B: Atomic, Molecular and Optical Physics **45**, 135004 (2012).

[197] Weber, S., Tresp, C., Menke, H. et al. *Calculation of Rydberg interaction potentials*. Journal of Physics B: Atomic, Molecular and Optical Physics **50**, 133001 (2017).

[198] Šibalić, N., Pritchard, J., Adams, C. and Weatherill, K. *ARC: An open-source library for calculating properties of alkali Rydberg atoms*. Computer Physics Communications **220**, 319–331 (2017).

[199] Schauß, P. *High-resolution imaging of ordering in Rydberg many-body systems*. PhD thesis, Ludwig–Maximilians–Universität München (2014).

[200] Seaton, M.J. *Quantum defect theory*. Reports on Progress in Physics **46**, 167–257 (1983).

[201] Gallagher, T.F. *Rydberg Atoms*. Cambridge University Press (1994). ISBN 9780521385312.

[202] Miroshnychenko, Y., Gaëtan, A., Evellin, C. et al. *Coherent excitation of a single atom to a Rydberg state*. Physical Review A **82**, 013405 (2010).

[203] Johnson, T.A., Urban, E., Henage, T. et al. *Rabi Oscillations between Ground and Rydberg States with Dipole-Dipole Atomic Interactions*. Physical Review Letters **100**, 113003 (2008).

[204] Cooke, W.E., Gallagher, T.F., Edelstein, S.A. and Hill, R.M. *Doubly Excited Autoionizing Rydberg States of Sr*. Physical Review Letters **40**, 178–181 (1978).

[205] Xu, E.Y., Zhu, Y., Mullins, O.C. and Gallagher, T.F. *Sr $5p_{1/2}ns_{1/2}$ and $5p_{3/2}ns_{1/2}$ J=1 autoionizing states*. Physical Review A **33**, 2401–2409 (1986).

[206] Aymar, M., Greene, C.H. and Luc-Koenig, E. *Multichannel Rydberg spectroscopy of complex atoms*. Reviews of Modern Physics **68**, 1015–1123 (1996).

[207] Millen, J., Lochead, G., Corbett, G.R., Potvliege, R.M. and Jones, M.P.A. *Spectroscopy of a cold strontium Rydberg gas*. Journal of Physics B: Atomic, Molecular and Optical Physics **44**, 184001 (2011).

[208] Greene, C.H. *Private communication*.

[209] Mukherjee, R., Millen, J., Nath, R., Jones, M.P.A. and Pohl, T. *Many-body physics with alkaline-earth Rydberg lattices*. Journal of Physics B: Atomic, Molecular and Optical Physics **44**, 184010 (2011).

[210] Sansonetti, J.E. *Wavelengths, Transition Probabilities, and Energy Levels for the Spectra of Strontium Ions (Sr II through Sr XXXVIII)*. Journal of Physical and Chemical Reference Data **41**, 013102–013102–119 (2012).

[211] Itano, W.M., Heinzen, D.J., Bollinger, J.J. and Wineland, D.J. *Quantum Zeno effect*. Physical Review A **41**, 2295–2300 (1990).

[212] Zhu, B., Gadway, B., Foss-Feig, M. et al. *Suppressing the Loss of Ultracold Molecules Via the Continuous Quantum Zeno Effect*. Physical Review Letters **112**, 070404 (2014).

[213] Sevinçli, S. and Pohl, T. *Microwave control of Rydberg atom interactions*. New Journal of Physics **16**, 123036 (2014).

[214] Booth, D.W., Isaacs, J. and Saffman, M. *Reducing the sensitivity of Rydberg atoms to dc electric fields using two-frequency ac field dressing*. Physical Review A **97**, 012515 (2018).

[215] Robertson, E., Šibalić, N., Potvliege, R. and Jones, M. *ARC 3.0: An expanded Python toolbox for atomic physics calculations*. Computer Physics Communications **261**, 107814 (2021).

[216] Covey, J.P. *Enhanced Optical and Electric Manipulation of a Quantum Gas of KRb Molecules*. Springer International Publishing (2018). ISBN 978-3-319-98106-2.

[217] Wilson, J., Saskin, S., Meng, Y. et al. *Trapped arrays of alkaline earth Rydberg atoms in optical tweezers*. arXiv:1912.08754 (2019).

[218] Dutta, S.K., Guest, J.R., Feldbaum, D., Walz-Flannigan, A. and Raithel, G. *Ponderomotive Optical Lattice for Rydberg Atoms*. Physical Review Letters **85**, 5551–5554 (2000).

[219] Topcu, T. and Derevianko, A. *Dynamic polarizability of Rydberg atoms: Applicability of the near-free-electron approximation, gauge invariance, and the Dirac sea*. Physical Review A **88**, 042510 (2013).

[220] Porsev, S.G., Ludlow, A.D., Boyd, M.M. and Ye, J. *Determination of Sr properties for a high-accuracy optical clock*. Physical Review A **78**, 032508 (2008).

[221] Topcu, T. and Derevianko, A. *Divalent Rydberg atoms in optical lattices: Intensity landscape and magic trapping*. Physical Review A **89**, 023411 (2014).

[222] Singer, K., Stanojevic, J., Weidemüller, M. and Côté, R. *Long-range interactions between alkali Rydberg atom pairs correlated to the ns–ns, np–np and nd–nd asymptotes*. Journal of Physics B: Atomic, Molecular and Optical Physics **38**, S295–S307 (2005).

[223] Vaillant, C.L. *Long-Range Interactions in One- and Two-Electron Rydberg Atoms*. PhD thesis, Durham University (2014).

[224] Le Roy, R.J. *Long-Range Potential Coefficients From RKR Turning Points: $C_6$ and $C_8$ for $B(3^+_{Ou})$-State $Cl_2$, $Br_2$, and $I_2$*. Canadian Journal of Physics **52**, 246–256 (1974).

[225] Wall, M.L., Hazzard, K.R.A. and Rey, A.M. *Quantum Magnetism with Ultracold Molecules*. In *From Atomic to Mesoscale*, pages 3–37. World Scientific (2015).

[226] Leibfried, D., Knill, E., Seidelin, S. et al. *Creation of a six-atom 'Schrödinger cat' state*. Nature **438**, 639–642 (2005).

[227] Saffman, M. and Walker, T.G. *Analysis of a quantum logic device based on dipole-dipole interactions of optically trapped Rydberg atoms*. Physical Review A **72**, 022347 (2005).

[228] Löw, R., Weimer, H., Nipper, J. et al. *An experimental and theoretical guide to strongly interacting Rydberg gases*. Journal of Physics B: Atomic, Molecular and Optical Physics **45**, 113001 (2012).

[229] Beterov, I.I., Ryabtsev, I.I., Tretyakov, D.B. and Entin, V.M. *Quasiclassical calculations of blackbody-radiation-induced depopulation rates and effective lifetimes of Rydberg nS, nP, and nD alkali-metal atoms with $n \leq 80$*. Physical Review A **79**, 052504 (2009).

[230] Barragán-Gil, L.F. and Walser, R. *Harmonic oscillator thermal density matrix: First-order differential equations for the position representation*. American Journal of Physics **86**, 22–24 (2018).

[231] Lienhard, V., Scholl, P., Weber, S. et al. *Realization of a Density-Dependent Peierls Phase in a Synthetic, Spin-Orbit Coupled Rydberg System*. Physical Review X **10**, 021031 (2020).

[232] Fendley, P., Sengupta, K. and Sachdev, S. *Competing density-wave orders in a one-dimensional hard-boson model*. Physical Review B **69**, 075106 (2004).

[233] Liu, F., Lundgren, R., Titum, P. et al. *Confined Quasiparticle Dynamics in Long-Range Interacting Quantum Spin Chains*. Physical Review Letters **122**, 150601 (2019).

[234] Samajdar, R., Ho, W.W., Pichler, H., Lukin, M.D. and Sachdev, S. *Complex Density Wave Orders and Quantum Phase Transitions in a Model of Square-Lattice Rydberg Atom Arrays*. Physical Review Letters **124**, 103601 (2020).

[235] Celi, A., Vermersch, B., Viyuela, O. et al. *Emerging Two-Dimensional Gauge Theories in Rydberg Configurable Arrays*. Physical Review X **10**, 021057 (2020).

[236] Surace, F.M., Mazza, P.P., Giudici, G. et al. *Lattice Gauge Theories and String Dynamics in Rydberg Atom Quantum Simulators*. Physical Review X **10**, 021041 (2020).

[237] Calabrese, P. and Cardy, J. *Time Dependence of Correlation Functions Following a Quantum Quench*. Physical Review Letters **96**, 136801 (2006).

[238] Calabrese, P. and Cardy, J. *Quantum quenches in 1 + 1 dimensional conformal field theories*. Journal of Statistical Mechanics: Theory and Experiment **2016**, 064003 (2016).

[239] Tan, W.L., Becker, P., Liu, F. et al. *Observation of Domain Wall Confinement and Dynamics in a Quantum Simulator*. arXiv:1912.11117 (2019).

[240] Kaufman, A.M., Tai, M.E., Lukin, A. et al. *Quantum thermalization through entanglement in an isolated many-body system*. Science **353**, 794–800 (2016).

[241] Levine, H., Keesling, A., Semeghini, G. et al. *Parallel Implementation of High-Fidelity Multiqubit Gates with Neutral Atoms*. Physical Review Letters **123**, 170503 (2019).

[242] Kim, M.E., Chang, T.H., Fields, B.M., Chen, C.A. and Hung, C.L. *Trapping single atoms on a nanophotonic circuit with configurable tweezer lattices*. Nature Communications **10**, 1647 (2019).

[243] Barredo, D., Lienhard, V., de Léséleuc, S., Lahaye, T. and Browaeys, A. *Synthetic three-dimensional atomic structures assembled atom by atom*. Nature **561**, 79–82 (2018).

[244] Drever, R.W.P., Hall, J.L., Kowalski, F.V. et al. *Laser phase and frequency stabilization using an optical resonator*. Applied Physics B Photophysics and Laser Chemistry **31**, 97–105 (1983).

[245] Anderson, D.Z., Frisch, J.C. and Masser, C.S. *Mirror reflectometer based on optical cavity decay time*. Applied Optics **23**, 1238 (1984).

[246] Webster, S. and Gill, P. *Force-insensitive optical cavity*. Optics Letters **36**, 3572 (2011).

[247] Sandberg, J. *Research toward laser spectroscopy of trapped atomic hydrogen*. PhD thesis, Massachusetts Institute of Technology (1993).

[248] Porsev, S.G., Rakhlina, Y.G. and Kozlov, M.G. *Electric-dipole amplitudes, lifetimes, and polarizabilities of the low-lying levels of atomic ytterbium*. Physical Review A **60**, 2781–2785 (1999).

[249] Mitroy, J., Safronova, M.S. and Clark, C.W. *Theory and applications of atomic and ionic polarizabilities*. Journal of Physics B: Atomic, Molecular and Optical Physics **43**, 202001 (2010).

[250] Porsev, S.G. *Private communication*.

[251] Richards, B. and Wolf, E. *Electromagnetic diffraction in optical systems, II. Structure of the image field in an aplanatic system*. Proceedings of the Royal Society of London. Series A. Mathematical and Physical Sciences **253**, 358–379 (1959).

[252] Oumarou, B., Picart, J., Tran Minh, N. and Chapelle, J. *New and rapid method for calculation of electric dipole and quadrupole radial integrals between atomic Rydberg states*. Physical Review A **37**, 1885–1894 (1988).